UCLA
UCLA Electronic Theses and Dissertations

Title
Multi-Scale Multi-Species Modeling for Plasma Devices

Permalink
https://escholarship.org/uc/item/38d4h99p

Author
Araki, Samuel Jun

Publication Date
2014

Peer reviewed|Thesis/dissertation

eScholarship.org Powered by the California Digital Library
University of California

University of California
Los Angeles

Multi-Scale Multi-Species Modeling for Plasma Devices

A dissertation submitted in partial satisfaction
of the requirements for the degree
Doctor of Philosophy in Aerospace Engineering

by

Samuel Jun Araki

2014

© Copyright by
Samuel Jun Araki
2014

Abstract of the Dissertation

Multi-Scale Multi-Species Modeling for Plasma Devices

by

Samuel Jun Araki

Doctor of Philosophy in Aerospace Engineering

University of California, Los Angeles, 2014

Professor Richard E. Wirz, Chair

This dissertation describes three computational models developed to simulate important aspects of low-temperature plasma devices, most notably ring-cusp ion discharges and thrusters. The main findings of this dissertation are related to (1) the mechanisms of cusp confinement for micro-scale plasmas, (2) the implementation and merits of magnetic field aligned meshes, and (3) an improved method for describing heavy species interactions.

The Single Cusp (SC) model focuses on the near-cusp region of the discharge chamber to investigate the near surface cusp confinement of a micro-scale plasma. The model employs the multi-species iterative Monte Carlo method and uses various advanced methods such as electric field calculation and particle weighting algorithm that are compatible with a non-uniform mesh in cylindrical coordinates. Three different plasma conditions are simulated with the SC model, including an electron plasma, a sparse plasma, and a weakly ionized plasma. It is found that the scaling of plasma loss to the cusp for a sparse plasma can be similar to that for a weakly ionized plasma, while the loss mechanism is significantly different; the primary electrons strongly influence the loss structure of the sparse plasma. The model is also used, along with experimental results, to describe the importance of the local magnetic field on the primary electron loss behavior at the cusp.

Many components of the 2D/3D hybrid fluid/particle model (DC-ION) are improved from the original version. The DC-ION code looks at the macroscopic structure of the discharge

plasma and can be used to address the design and optimization challenges of miniature to micro discharges on the order of 3 cm to 1 cm in diameter. Among the work done for DC-ION, detailed steps for the magnetic field aligned (MFA) mesh are provided. Solving the plasma diffusion equation in the ring-cusp configuration, the benefit of the MFA mesh has been fully investigated by comparing the solution with a uniform mesh. It is found that the MFA mesh can still produce a relatively large error due to the misalignment at the domain boundary but still provides a significant improvement in the bulk plasma region. The mesh generation routine can be further improved by enhancing the smoothness of the near-boundary grid elements.

The Ion Beam (IB) model is similar to the SC model but primarily focuses on heavy species. The model implements detailed calculation of the heavy species collisions, solving the classical scattering equation with higher order interaction potentials for different collision pairs. A parametric study has been conducted, and the simulation results have shown very good agreement with the experimental results when using an appropriate value for the secondary electron yield. Further study on the elastic collision has shown that the initial atom velocity should not be neglected in order to accurately compute the post-collision CEX ion velocity. The knowledge gained has led to an improvement on the current method by defining an effective elastic collision cross-section and significantly reducing the frequency of the collision calculation. The same method can be applied to collisions between fast and slow atoms.

The dissertation of Samuel Jun Araki is approved.

Troy A. Carter

Jeff D. Eldredge

Xiaolin Zhong

Richard E. Wirz, Committee Chair

University of California, Los Angeles

2014

To my mother,

for her inspiration.

Table of Contents

List of Figures

List of Tables

Acknowledgments

First and foremost, I should express my deepest gratitude to my advisor Professor Richard Wirz for his intellectual guidance and the opportunity. Being one of his first students, the experience at UCLA was exceptionally unique; everything started from an empty lab, and I attained skills and knowledge as the lab was filled with equipments and students. He has let me explore many different research topics and provided me with a good amount of freedom to invest time in my research interest; he has also saved me a countless number of times from falling into endlessly deep holes.

I greatly acknowledge my committee, Professor Xiaolin Zhong, Professor Jeff Eldredge, and Professor Troy Carter for sparing their time to critique my work. Their wisdom also provided me with a deeper insight into my thesis work through their lectures and discussions. Special thanks to Dr. Dan Goebel and Professor Ann Karagozian. Dr. Goebel introduced me to the field of electric propulsion, and Professor Karagozian helped me find a way to pursue the field at UCLA by introducing me to Professor Wirz.

I'm indebted to my fellow members of Wirz Research Group for their friendship and intellectual discussions. In particular, I like to thank Ben Dankongkakul, Perry Roth-Johnson, Phillip Chiu, and Taylor Matlock. Without the amount of drinks we had together, I might have been burnt out before getting this far. Of course, they have been great resources for me, which has influenced me quite a bit during the course of this endeavor. I should also thank other former and current members for their support: Hann-Shin Mao, Marlene Patino, Lauren Chu, Ryan Conversano, Chris Dodson, and Cesar Huerta. Thanks to Yuta Toriyama, Taylor Matlock, and Marlene Patino for proofreading parts of this dissertation.

Finally, I'm very thankful to my family–Yoshiaki, Mari, Shinichi, and Toshiko–for their love and support. This dissertation is dedicated to my mother, Shizue, who would have been the most supportive, understanding, and delighted to my success as a researcher if she still lived in the earthly world.

Vita

2007	B.S. (Aerospace Engineering), *Summa Cum Laude*, UCLA.
2008	Aerospace Engineering Outstanding B.S. Student Award, UCLA.
2008	First-Year Departmental Fellowship, Department of Mechanical and Aerospace Engineering, UCLA.
2009	Teaching Assistant, Department of Mechanical and Aerospace Engineering, UCLA. Taught sections for MAE161B (Spacecraft Technology).
2009	NASA Space Grant - Jet Propulsion Laboratory, research advisory by Dr. John Steven Snyder.
2009–2014	Research Assistant, Department of Mechanical and Aerospace Engineering, UCLA.
2009	M.S. (Aerospace Engineering), UCLA.
2013	Dissertation Year Fellowship, UCLA.

Publications

Araki, S. J. and Wirz, R. E., "Magnetic Field Aligned Mesh for Ring-Cusp Discharge Chambers," *50th AIAA/ASME/SAE/ASEE Joint Propulsion Conference & Exhibit*, Cleveland, Ohio, Jul. 28–30, 2014, AIAA 2014-3830

Araki, S. J. and Wirz, R. E., "Cell-Centered Particle Weighting Algorithm for PIC Simulations in a Non-Uniform 2D Axisymmetric Mesh," *Journal of Computational Physics*, Vol. 272, 2014, pp 218-226

Dankongkakul, B., Araki, S. J., Wirz, R. E., "Magnetic Field Structure Influence on Primary Electron Cusp Losses for Micro-Scale Discharges," *Physics of Plasmas*, Vol. 21, No. 043506, 2014

Araki, S. J. and Wirz, R. E., "Particle Simulation of Near-Surface Cusp Confinement of Weakly Ionized Plasma," *33rd International Electric Propulsion Conference*, Washington D.C., Oct. 6–10, 2013, IEPC 2013-349

Dankongkakul, B., Araki, S. J., Wirz, R. E., "Influence of Upstream Field Structure on Primary Electron Loss for a Permanent Magnet Cusp," *49th AIAA/ASME/SAE/ASEE Joint Propulsion Conference & Exhibit*, San Jose, California, Jul. 14–17, 2013, AIAA 2013-3963

Araki, S. J. and Wirz, R. E., "Ion-Neutral Collision Modeling Using Classical Scattering with Spin-Orbit Free Interaction Potential," *IEEE Transactions on Plasma Science*, Vol. 41, No. 3, 2013

Wirz, R. E., Araki, S. J., and Dankongkakul, B., "Near-Surface Cusp Confinement for Weakly Ionized Plasma," *48th AIAA/ASME/SAE/ASEE Joint Propulsion Conference & Exhibit*, Atlanta, Georgia, Jul. 29–Aug. 1, 2012, AIAA 2012-3948

Wirz R. E., Chu L., Patino M., Mao H., Araki S. J., "Well-Characterized Plasma Experiments for Validation of Computational Models," *32nd International Electric Propulsion Conference*, Kurhaus, Wiesbaden, Germany, Sep. 11–15, 2011

Araki, S. J. and Wirz, R. E., "Collision Modeling for High Velocity Ions in a Quiescent Gas," *42nd AIAA Plasmadynamics and Lasers Conference*, Honolulu, Hawaii, Jun. 27–30, 2011, AIAA 2011-3740

CHAPTER 1

Introduction

Plasma is a system containing mobile charges in which electromagnetic interactions between particles play the dominant role in the dynamics of the system. Such property is necessary in realizing various plasma devices including fusion, plasma processing, plasma propulsion, and microwave devices. The plasma device to be investigated is the electrostatic ion thruster, while the techniques and findings discussed in this dissertation can be extended to other devices with the similar plasma. This chapter first briefly introduces the electric propulsion in Sec. 1.1. Then, the electron-bombardment ion thruster is introduced in Sec. 1.2 with a brief description of ion thruster operations. Section 1.3 provides an extensive survey of numerical models for different regions of an ion thruster. Lastly, Sec. 1.4 describes the organization of this dissertation.

1.1 Electric Propulsion

Electric propulsion (EP) devices use electric power to achieve higher propellant exhaust velocity compared to chemical propulsion devices that are limited by the internal energy stored in their propellant. Therefore, the specific impulse, I_{sp}, for EP devices is typically much higher than for chemical propulsion devices, as compared in Table 1.1 [1–3]. The amount of propellant, m_p, required for a given velocity increment, ΔV, can be calculated using the rocket equation,

$$m_p = m_0 \left[1 - \exp\left(-\frac{\Delta V}{I_{sp} g} \right) \right] \tag{1.1}$$

where m_0 is the initial mass and g_0 is the sea-level gravitational acceleration. From Eq. (1.1), it can be readily seen that a higher I_{sp} leads to less m_p required for a given ΔV. With a

significant reduction in the propellant mass, the launch mass and cost required to deliver the satellite to a given orbit can be reduced significantly, which makes various space missions including interplanetary flights and long-duration missions affordable.

Depending on the propellant acceleration method used to produce thrust, EP devices can be categorized into three principal classes: electrothermal, electrostatic, and electromagnetic [4]. Table 1.2 summarizes the three classes and various EP devices. Different EP devices perform at different ranges of I_{sp} and thrust, T, and their application vary depending on their performance. For example, field emission electric propulsion (FEEP) and colloid thrusters are suitable for low-thrust precision control due to the very low T to power ratio [5]. In contrast, magnetoplasmadynamic (MPD) thrusters perform at large I_{sp} and T and are applicable for large ΔV missions. However, MPD thrusters require high power in their operation, thus they are limited by the current lack of power generation technology. Finally, ion and Hall thrusters are suitable for various missions including attitude control, orbit insertion, and station keeping because of their moderately high I_{sp} and relatively high efficiency [5].

Table 1.1: Typical values of I_{sp}[a] for various thrusters. All thrusters shown below are EP thrusters unless specified as chemical [1–3].

Thruster	Specific Impulse (s)
Chemical (monopropellant)	$150 - 225$
Chemical (bipropellant)	$300 - 450$
Resistojet	$300 - 350$
Arcjet	$500 - 2000$
Ion Thruster	$1000 - 5000$
Hall Thruster	$500 - 3000$
Pulsed Plasma Thruster (PPT)	$850 - 1500$
Field Emission Electric Propulsion (FEEP)	$6000 - 10000$
Magnetoplasmadynamic (MPD) Thruster	$1500 - 6000$

[a] I_{sp} is defined as the ratio of the exhaust velocity to the sea-level gravitational acceleration

Table 1.2: Types of EP devices [4].

Types	Acceleration Method	Devices
Electrothermal	Propellant gas is heated electrically and expanded through a convergent/divergent nozzle	Resistojet, Arcjet
Electrostatic	Ionized propellant gas is accelerated by the application of electric fields	Ion thruster[a], Hall thruster[a], Colloid thruster, FEEP thruster
Electromagnetic	Ionized propellant gas is accelerated by the application of both electric and magnetic fields	PPT[a], MPD thruster[b]

[a] Operated on flight space vehicles

[b] Demonstrated on ground testing facilities

1.2 Ion Thruster

1.2.1 Historical Background

Extensive research and development of ion thrusters began in 1950's, about 40 years after the concept of electric propulsion was first introduced by Goddard in 1906 and independently by Tsiolkovskiy in 1911 [6]. The first flight experiment of ion thrusters was conducted in 1964 through the Space Electric Rocket Test (SERT) 1 program [4]. One of the two thrusters built by the NASA Glenn research center operated successfully in space. Since then, a number of flight experiments were conducted in several countries including the United States, the United Kingdom, Germany, Russia, and Japan. Many advancements were seen in critical components of ion thrusters such as the accelerator grids, the discharge chamber, and the electron bombardment source to achieve longer life and higher power [7]. In 1994, Japan launched the communications satellite, Japanese Engineering Test Satellite (ETS) VI, carrying four xenon ion thrusters intended for north-south station keeping (NSSK) for the first time [8]. The first commercial use of ion thrusters in the United States began in 1997 with the launch of communications satellites employing Xenon Ion Propulsion System (XIPS) for NSSK [7]. The first interplanetary mission using ion engines was NASA Deep Space-1 (DS-1) launched in 1998. The DS-1 spacecraft employed NASA Solar Electric Propulsion

Technology Application Readiness (NSTAR) ion thruster as the primary propulsion system, and successfully encountered the asteroid Braille and the comet Borrelly [1,9]. Ion thrusters have become common options for many space missions including interplanetary flights, orbit insertion, station keeping, and attitude control. As of 2006, a total of over one hundred XIPS ion thrusters had been in orbit for station keeping applications with more than 150,000 accumulated operating hours [10]. Recent interplanetary missions include the Hayabusa asteroid sample return mission, which used a microwave discharge ion engine [11], and NASA's Dawn mission, which used the NSTAR ion thruster [12].

1.2.2 Types of Ion Thrusters

Ion thrusters use three fundamental processes to produce thrust: plasma generation, electrostatic acceleration of ions, and ion beam neutralization. First, a propellant gas is ionized to generate a plasma in an ion thruster discharge chamber. Then, the resulting ions are electrostatically accelerated to high velocities through a set of biased grids to produce thrust. Finally, the ion beam is neutralized by injecting an equal flux of free electrons from a neutralizer cathode.

Different types of ion thrusters exist depending on the plasma generation method. These include the surface contact ion thruster, the microwave ion thruster, the radio frequency (RF) ion thruster, and the direct current (DC) electron-bombardment ion thruster. The type of ion thruster receiving the most research in the United States and England is the DC electron-bombardment ion thruster; a schematic of such a thruster is shown in Fig. 1.1 [13]. Examples of ion thrusters include the NSTAR ion thruster, the NASA Evolutionary Xenon Thruster (NEXT), the Nuclear Electric Xenon Ion thruster System (NEXIS) developed by NASA, the XIPS ion thruster developed by Hughes Aircraft Company in the United States, the Miniature Xenon Ion Thruster (MiXI) developed at California Institute of Technology, and the T5 and T6 Kaufman thrusters manufactured by QinetiQ in England. Radio frequency (RF) and microwave ion thrusters are primarily investigated and developed in Germany and Japan, respectively. The RIT-10 is a RF ion thruster developed by the University of Giessen,

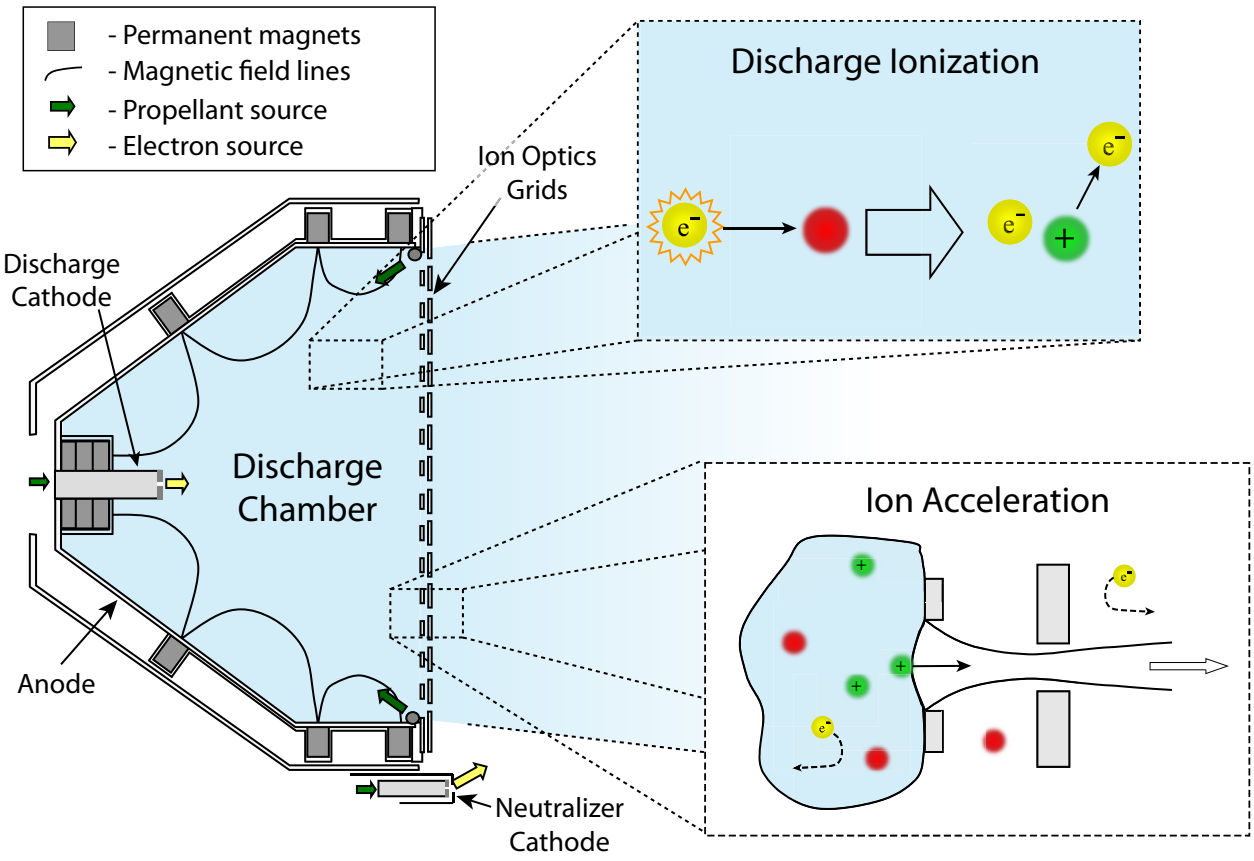

Figure 1.1: Schematic of DC electron bombardment ring-cusp ion thruster (Redrawn from Ref. [13]).

Germany, and is currently flying on ARTEMIS (Acceleration, Reconnection, Turbulence and Electrodynamics of the Moon's Interaction with the Sun). The μ10 microwave ion thruster developed by Mitsubishi has flown on ETS-VI and the Hayabusa asteroid sample return mission. Among all the types of ion thrusters, DC electron-bombardment ion thrusters generally provide better efficiency [1]. The following sections cover the three primary components of a DC electron bombardment ion thruster.

1.2.3 Discharge Chamber

In the discharge chamber of the DC ion thruster, high energy (primary) electrons extracted from a hollow cathode encounter the neutral propellant gas and undergo ionization collisions to generate plasma. Ionization efficiency is improved by applying magnetic fields created by multiple permanent magnets and/or a solenoid to increase electron confinement time and

path length before being lost to the anode surface. The magnetic field configuration most widely used for this type of ion thruster utilizes permanent block magnets placed around the circumference of the discharge chamber to create ring cusp fields. The strong field near the magnet ring causes the primary electrons to reflect, reducing the number of primary electrons lost to the anode and increasing ionization probability in the chamber. The primary electrons also collide with the plasma electrons, raising the plasma electron temperature. As a result, a greater number of the plasma electrons that lies at the tail of the Maxwellian distribution can have energies above the ionization threshold energy and thus contribute to the plasma generation. In Kaufman-type ion thrusters, the strongly diverging axial magnetic field is used to shield an anode electrode placed near the discharge chamber wall. For an improved performance of an ion thruster, it is generally preferred that the plasma generation region is near the ion optics for a greater ion extraction and the plasma density is nearly uniform behind the grid for beam flatness.

1.2.4 Extraction Grids

Through a set of biased extraction grids, the ions created in the discharge chamber are accelerated electrostatically to produce thrust. These grids are usually made of two or three grids as illustrated in Fig. 1.1. The first grid is called the screen grid, which prevents direct impingement of ions to the second grid, the accelerator (accel) grid. The accel grid is biased negatively to accelerate ions and prevents undesirable backstreaming of neutralizer electrons; electron backstreaming causes electrical power losses and overheats the internal components of the discharge chamber. The accel grid also minimizes the loss of neutral atoms from the discharge chamber to maximize the ion thruster discharge propellant utilization; therefore, the accel grid has a smaller hole size than the screen grid. In a three-grid configuration, the decelerator (decel) grid is placed after the accel grid to prevent the erosion of the accel grid downstream surface from secondary ions created by charge-exchange (CEX) interactions between beam ions and neutral atoms [14]. Due to the slow initial speed of the CEX ions, these ions are much more susceptible to the electric field compared to the beam ions. Consequently, the CEX ions are attracted toward the negatively biased accel grid and impact

the grid at high energies, resulting in sputtering of the grid material. The erosion of the accel grid can be the limiting factor of the overall ion thruster life. By the addition of the decel grid, the impingement of the CEX ions to the accel grid downstream surface can be reduced significantly. However, the erosion of the accel grid holes still occurs due to the CEX ions created within the aperture. As a result, the minimum potential within the hole is increased, causing the neutralizer electrons to flow into the discharge chamber while gaining energy through the grids. The electron backstreaming can be prevented by reducing the accel grid voltage during the course of mission while this, in turn, enhances the grid erosion. In order to minimize the grid erosion, the grid is typically made out of materials with low sputtering yield under xenon ion bombardment. These include molybdenum, carbon-carbon composite material, and pyrolytic graphite.

1.2.5 Hollow Cathode

Two hollow cathodes are utilized in a DC electron-bombardment ion thruster (See Fig. 1.1); one of the hollow cathodes placed inside the chamber provides electrons for sustaining plasma discharges, and the other hollow cathode external to the discharge chamber provides electrons to neutralize the ion beam to prevent charge imbalance with the spacecraft. A hollow cathode consists of a cathode tube and an orifice plate at the end of the tube. An insert in the shape of a hollow cylinder is placed inside the cathode tube with one end flushed against the orifice plate, and a heater is wrapped around the cathode tube. The hollow cathode is started by applying electric power to the heater to raise the insert temperature. Then, thermionic emission of electrons occurs at the surface of the insert. In order to reduce the power required for this process, the insert is made out of a material with a low work function, such as Barium-oxide and lanthanum hexaboride. The electrons from the insert surface ionize the neutral gas injected through the cathode tube to create a plasma. Once the cathode is started, the external heater is turned off as the heating of the insert can be maintained by the plasma bombardment. The hollow cathode also consists of a keeper, an electrode that encloses the heater and cathode tube. The keeper eases the start up of the cathode discharge, helps in maintaining the cathode temperature, and protects the enclosing components from

ion bombardment [1]. The plasma created inside the cathode diffuses through the orifice dominantly by the means of collisions. The electrons are then accelerated toward the bulk plasma in the chamber at a higher potential. The energy gain is approximately the difference between the anode and cathode potentials.

1.3 Survey of Numerical Models for a DC Cusped Ion Thruster

In simulations of ion thrusters, three types of computational models are often employed: a kinetic model, a fluid model, and a hybrid model in which one species is solved via fluid equations and the other species is solved by the particle method. At very low neutral pressures of interest, the mean free path of the ions becomes comparable to or larger than the length of a domain so that the effective Knudsen (Kn) number becomes on the order of unity or greater. In this regime, the continuum assumption in the fluid equation is violated [15] so that it becomes necessary to use a kinetic model to solve the problem. On the other hand, the fluid approximation is typically used for the continuum regime where the collisions between particles are very frequent. Fluid models are, in general, faster than kinetic models but cannot capture the local plasma structure (i.e. near a wall within a sheath). In contrast, kinetic models are statistically noisy and require large computational run-time, while it is relatively straightforward to add more physics. In this section, we provide a brief review of the numerical models that are developed specifically for the different parts or regions of a DC cusped ion thruster including the discharge chamber, the ion optics, and the plume. Although the hollow cathode is an important component of an ion thruster, a review of hollow cathode models is not given herein since the models developed for this thesis work are not relevant to hollow cathode models.

1.3.1 Discharge Chamber Models

To date, several models have been developed to improve the understanding of the plasma inside a DC ion thruster discharge chamber that utilizes permanent magnets. Among these models, computational models that only track primary electrons have been developed by

various groups. These models are, of course, not capable of revealing all the physics but focus on the most important species in the discharge chamber; the plasma production is primarily maintained by ionization collisions between the primary electrons and background neutral atoms. Many of these models have been extended later to include other species either by treating them as particles or by using the fluid approximation. Arakawa and Yamada [16] developed a Monte Carlo model called PRIMA in which macro-particles representing fractions of the total primary electron current from the cathode were tracked in magnetic fields of the cusped discharge chamber. The model also used the Monte-Carlo collision method to determine if an electron collided with a background neutral atom. The primary electron utilization factors predicted by PRIMA were generally in fair comparison with experimental data when the anomalous collision accounting for the plasma oscillation was used. The original version of PRIMA was improved by Mahalingam and Manart [17] at Wright State University; the improvements included parallel tracking, adoption to any discharge chamber configuration, and a fix for the numerical heating problem. The improved version of PRIMA was used by other researchers in the same group to perform sensitivity studies on primary electron confinement with different design parameters [17–21]. Results from these investigations led to several rules-of-thumbs for initial design of the discharge chamber field configuration. Several other models [13, 22–30] also incorporated the primary electron tracking routine, but results solely from this routine were not reported since these models were capable of simulating more species.

The first computational model to simulate the plasma in the discharge chamber was developed by Arakawa and Ishihara [22]. In this model, their primary electron tracking routine, PRIMA, was combined with other tools that solved the plasma diffusion equation for ion and plasma electron densities in the plasma [31] and predicted the discharge performance using Brophy's analytical model [32, 33]. Their model was demonstrated for ion thrusters of different sizes (7 and 30 cm in diameters), and the results showed qualitative agreement with experimental results for ion production cost versus propellant utilization. Wirz and Katz [13, 23, 24] developed a 2D/3D hybrid fluid/particle model (DC-ION) specifically for ring-cusp DC ion thrusters. Similar to Arakawa and Ishihara's model, DC-ION treated

primary electrons as particles and other species as fluids. However, the model was much more sophisticated than Arakawa and Ishihara's model in that the DC-ION model self-consistently obtained the solutions for neutral atom density and plasma electron temperature in addition to the other species densities, species generation rates, and discharge performance parameters. The model was largely developed and validated using data from the 30-cm NSTAR ion thruster, and was successfully applied to a 3-cm MiXI ion thruster. These hybrid models assumed quasi-neutrality in the fluid approximation, thus could not resolve the near-wall and magnetic cusp regions where charge separation occurred.

Mahalingam and Menart [25–27] developed a 2D full particle-in-cell Monte Carlo collision model (PIC-MCC), treating five different species–primary and plasma electrons, single and double ions, and neutral atoms–as particles. The species trajectories were coupled by the electrostatic force acting on each other. Collisions between different species were incorporated in the model; these included collisions between electron-atom (elastic, excitation, and ionization), electron-single ion (excitation, ionization, and recombination), electron-double ion (excitation and recombination), single ion-atom (elastic and charge exchange), and double ion-atom (charge exchange) collisions. Also, the static magnetic field produced by the permanent magnets was obtained with MAXWELL-2D developed by Ansoft Corporation. Full particle simulation of such devices was an extremely difficult task because of the limit in computational power, allowable number of simulation particles, and unstable nature of the numerical method due to the species in the opposite charge. They managed to obtain converged solutions for both the NSTAR [26] and NEXT ion thrusters [27, 34] by starting from an increased value for the permittivity in electric potential calculation and gradually reducing the artificial permittivity value to the physical value. At each stage, a solution was obtained after a simulation time of 2 to 3 ns and then used as a starting point for the simulation with the next permittivity value that is closer to the physical permittivity. In the simulation with the correct permittivity, the simulation was run until the solution became fully convergent. Furthermore, the particle tracking and the potential solver were parallelized using multiple CPUs. A few other groups developed full particle models for the ring-cusp DC ion thruster. Hirakawa and Arakawa [28, 29] developed a 2D PIC model for

ions and plasma electrons for simulations of very small regions near the magnetic cusp in the discharge. Various simplifying assumptions were made, and these assumptions were likely inaccurate for the actual discharge chamber. In particular, they assumed no collisions, did not include primary electrons, and used ion-to-electron mass ratio that was different for the actual simulation condition. Due to the limitation in the computational power at the time of research, this model was not capable of simulating the entire discharge chamber.

Brophy and Wilber [32, 33] developed a simple 0D analytical model for cusped ion thrusters, using the conservation of particles and energy for the discharge plasma. This model used several simplifying assumptions such as uniform species densities and the average of the ion production and loss in the discharge chamber. Even with the simplifications, the results from the model were in good agreement with various experimental data for cusped ion thrusters for different propellant gases. Furthermore, the model led to an improved understanding of the operation of the ion thruster discharge and helped with the optimization of the various thruster designs [35,36]. Goebel et al. [37] further expanded the 0D analytical model by closing the set of equations and calculating various parameters self-consistently. With a small number of inputs such as the thruster geometry, ion-optics performance, and electrical inputs, the model was capable of predicting discharge loss as a function of mass utilization efficiency for the NSTAR, NEXT, and NEXIS ion thrusters at various throttle conditions. Although the analytical model is a strong tool for a ion thruster discharge design, the computational models are still necessary to obtain detailed information of the plasma inside the discharge chamber.

1.3.2 Ion Optics Models

In contrast to the discharge chamber models, the primary species in the ion optics simulation is the high energy beam ions extracted from the discharge chamber. These ions can experience momentum exchange (MEX) and charge exchange (CEX) collisions with the neutral atoms escaping the chamber. The CEX ions created from the CEX interaction is responsible for grid erosion; therefore, the CEX ions need to be included for the prediction of the thruster

life. The electrons are confined within the discharge chamber due to the plasma sheath that develops behind the grids. The variation of the electron density from the chamber to the screen grid is often described by the Boltzmann relations.

$$n_e = n_i \exp\left(\frac{\phi - \phi_p}{T_e}\right) \tag{1.2}$$

where n is the density, ϕ is the electric potential, T is the temperature, and the subscripts i and e denote ions and electrons, respectively. The same equation can be applied downstream of the grids where the ions are neutralized by the electrons from the neutralizer cathode. Depending on how precise the modelers decide to capture these collisions, two distinctive modeling techniques–the Monte Carlo and the PIC methods–have been used for the ion optics models.

The Monte Carlo approach, also referred to as a gun model, simply traces the the beam ions while the electric potential is frozen during each iteration. Then, the electric potential is updated using the computed density from the particle tracking. These calculations are repeated until the steady-state solution is obtained at a given time. The neutral density is computed independently from the beam ions, using the analytical equation or the Monte Carlo approach and assuming that the neutral density is not significantly affected by the CEX interactions. Based on the neutral density, the CEX ion current at any location is computed, and the CEX ions are tracked in the same manner as the beam ions to determine the trajectories. The final impact location and energy are used to predict the amount of sputtered grid material. With the updated geometry, all of these calculations are repeated for the next successive time-step.

The gun-type method was incorporated in many models including CEX2D and CEX3D developed at Jet Propulsion Laboratory [14, 38–40], FFX and IGX developed at Colorado State University [41, 42], OPT originally developed at University of Tokyo [22, 43, 44] and extended by other Japanese institutions to be named as OPT-J [45–47], and IGUN adapted to ion optics simulations in Germany [48, 49]. While all of these models were structured in a similar way, a noticeable difference could be found in the computation method for the

neutral density. CEX2D and CEX3D as well as FFX and IGX used analytical formulas to approximate the neutral atom density. In order to use these formulas, a transmission factor for the grid system needed to be known; this was computed using the Monte Carlo approach in CEX2D and CEX3D and using an analytical formula in FFX and IGX. In IGUN, the Monte Carlo approach was used to find the density in the entire region, assuming that the collisional effect was negligible and using a straight path approximation between walls. OPT-J used the Direct Simulation Monte Carlo (DSMC) method for the atom-atom elastic collisions. In the DSMC method, nearby particles are chosen to be the collision partners, and the collisions are applied to every collision pair, while the counterpart method, the MCC method, uses the target species density information to determine the probability of the collisional event. Furthermore, among all the other ion optics models, only OPT-J incorporated the effect of redeposition of the grid material.

Another method commonly used for ion optics simulations is the PIC method. Similar to the Monte Carlo method, the heavy species are treated as particles. The plasma electrons can also be treated as particles, while many PIC models simply apply the Boltzmann distribution for the electron density. In a PIC model, all the particles are advanced by a small time-step in the electric field fixed at the given time. The advanced particle position is then used to update the field. These calculations are repeated until the solution becomes steady-state. Unlike the Monte Carlo model, all the species are moved simultaneously within the simulation time-step; this feature of the PIC model allows the inclusion of the species interactions in a more direct manner. More specifically, the collisions between particles of the same or different species are computed at each time-step, and as a result, the particle trajectories are altered. Therefore, the PIC models generally require fewer assumptions compared to the Monte Carlo models. For this reason, the PIC model is considered to be more accurate. The drawback of the PIC method is in computational intensity. PIC simulations typically require very small time-steps. Consequently, a large number of iterations is needed to reach the converged solution. Due to the nature of the model, a large degree of statistical noise is typically seen in the results, which can be reduced by running the simulation for a longer time after convergence. Furthermore, the electric potential is computed much more frequently due

to the structure of the model. The overall simulation may take days to obtain useful results as opposed to minutes to hours for the Monte Carlo models.

The PIC method was used in several ion optics models. For example, Okawa and Takegahara [50, 51] developed 2D PIC code called IBEX-T. This model only considered the beam ions and plasma electrons, and the collisional effect between the particles was not taken into account. Unlike other PIC models, IBEX-T treated the plasma electrons as particles. The code was used to show the transient phenomena of the ion beam immediately after applying the accel grid voltage; the transient phenomena could not be captured by the Monte Carlo models. Kafafy and Wang [52–54] developed the 3D PIC model that used the immersed finite element method for potential calculation (IFE-PIC). The IFE-PIC model used two sets of computational grids and interpolated the values between the grids. Both the IBEX-T and IFE-PIC codes did not incorporate the neutral atoms and CEX ions, and thus the erosion rate of the grids could not be computed. The 2D PIC code (ERODE) developed at University of Michigan simulated all the important species including the neutral atoms and CEX ions [55–57]. This code used the DSMC method for the collisions between particles. Furthermore, ERODE was capable of computing the erosion rate of the grids and finding the electron back-streaming limit.

The results from the two types of ion optics codes have been compared by a few researchers. Farnell [42, 56] looked at the accel grid-to-beamlet current ratio and the minimum centerline potential as a function of the beamlet current computed by five different ion optics models–ERODE, FFX, IGX, CEX2D, and CEX3D. The direct impingement currents were generally in good agreement except that the CEX2D over-predicted by approximately 10 mA. In contrast, FFX and IGX predicted a lower saddle point potential compared to the other models. Nevertheless, the discrepancy was acceptable. Funaki et al. [46] compared their OPT-J model with a full-PIC model and showed that the results were in excellent agreement except within the region after the decel grid. In particular, the two models provided very similar results for the potential distribution, upstream sheath positions, ion trajectories, and even the accel grid-to-beamlet current.

The development of the ion optics code has led to a better understanding of different

grid systems. The study done by Wirz et al. [40] using CEX3D showed that the addition of the decel grid led to a significant reduction in the pits-and-grooves erosion, the erosion that occurred at the downstream surface of the accel grid. However, the aperture wall erosion of the accel grid was generally comparable for both the 2-grid and 3-grid systems. The CEX3D code was also used to design the grids for a miniature ion thruster [14]. The computational and experimental analyses yielded the Small Hole Accelerator Grid (SHAG) design that reduced the neutral atom transparency while providing sufficient ion transparency. With this grid design, the neutral atom density could be kept high with the same source flow rate, allowing a high enough ionization rate necessary for the miniature discharge. Many of these ion optics models were also capable of predicting the time that an ion thruster failed due to the erosion of the grids.

1.3.3 Plume Models

The beam ions extracted from the discharge chamber are accelerated through the grids. These high-energy ions are the primary species that contribute to thrust. In contrast, slow ions are created from the CEX interactions between the beam ions and neutrals. While the beam ions are nearly unaffected by the electric field within the plume, the CEX ion trajectories can be altered significantly. The beam ions are neutralized by electrons from a neutralizer cathode to avoid charge imbalance with the spacecraft. The neutral atoms also leave the discharge chamber through the grids and the neutralizer cathode. Therefore, the electric propulsion plume consists of high energy ions, electrons, neutral atoms, and slow CEX ions. The plume may also consist of a small fraction of sputtered atoms from the grids.

An understanding of the plume physics is very important from many aspects. Information obtained from direct measurements of the plume can yield determination of thruster performance [1]. While the knowledge of the thruster performance is necessary from the mission design perspective, accurate determination of ion and sputtered atom trajectories diverging from the plume is extremely important from the spacecraft design perspective; the placement of spacecraft components is restricted by the location and orientation of thrusters.

The divergence half-angles of plumes are within 20° for the NEXIS ion thruster and are typically larger for Hall thrusters, about twice the angle compared to ion thrusters [1]. Even when the spacecraft component is placed outside the plume cone, the component can still be subjected to sputtering by the high energy ions and contamination by the sputtered atoms either from the thruster or other components of the spacecraft. The beam ions may experience momentum exchange (MEX) collisions with neutral atoms, deflecting at larger angles. While their momentum is partially lost to the neutral atoms, their energies can still be high enough to cause significant sputtering of the impinging surface, as observed in the collimated retarded potential analyzer data for the BPT-4000 thruster [58]. In contrast, the CEX ions created by the CEX collision are likely to be initially at low energies. These ions gain energies from the plume electric field and can impinge the spacecraft components, such as solar arrays and payloads placed even behind the thruster exit plane, at significant energies. Therefore, it is important that the plume models include accurate models in treating the two collisions for an analysis of the plume-thruster interaction.

Although the focus of this thesis is the ion thrusters, plume models developed for Hall thrusters are also mentioned herein, because the models for the two devices are very similar. The analysis of the plume began with a semi-empirical approach, using the experimentally measured ion current density profile data to extrapolate the profile at any location [59]. While the agreement was very good in the core of the plume, the model could not capture the current at larger angles due to the CEX ions. Since then, more detailed computational models have been developed for simulations of the plume, revealing how the plume plasma interacts with the spacecraft. All of these models deal with four different plume species: high energy beam ions, plasma electrons, neutral atoms, and CEX ions.

Roy et al. [60,61] extended the semi-empirical model for the beam ions by adding the other important species. In this computational model, the CEX ions and plasma electrons were treated as particles and fluids, respectively. The electric potential and field were computed based on the charged species densities. The CEX ion trajectories were computed via the PIC method while the electron density was obtained by the Boltzmann relation. An analytical equation derived from a simple point source model was evaluated to obtain the neutral

density, and using both the beam ion and neutral densities, the CEX ion generation rate was calculated. The MEX collision between ions and neutral atoms was not incorporated in this model. The model was further extended by Wang et al. [62], implementing the immersed finite element (IFE) potential solver in place of the finite difference solver. The IFE method was also incorporated in the 3D PIC ion optics model [52–54]. This method enabled the use of the body-fitted unstructured mesh with tetrahedral elements, allowing simulations with complex spacecraft geometries without sacrificing accuracy in the electric field calculations. Kafafy and Cao [63] used the model to examine the plume interactions with spacecraft in formation flight.

The IFE method was incorporated in a 3D PIC model called DRACO originally developed at Virginia Polytechnic Institute and State University [64–66]. The IFE potential solver was later replaced with the solver using the Boltzmann inversion with a "quasi-neutral" switch that allowed mesh sizes greater than the Debye length [67]. Unlike the model developed by Roy et al. [60, 61], DRACO solved both the beam and CEX ions via the PIC method. The model was also capable of solving electrons as particles while the fluid treatment was still incorporated and could be used instead. The neutral atoms were not treated as particles, and their density was precomputed using the projection function. The CEX ion current was computed by the MCC method; however, the MEX collision was not implemented in this model.

The effect of the MEX collisions was incorporated in a few other plume models: AQUILA developed at Massachusetts Institute of Technology [68–71] and MONACO developed at Cornell University [72] and extended at University of Michigan [73–75]. These models treated all the heavy species as particles and performed the MEX collision calculation using the DSMC method. The post-collision velocity of the neutral atoms due to the collisions with the same species was computed using the variable hard sphere (VHS) method. The difference in the two models was in the way that the CEX collision was handled. AQUILA assumed no momentum transfer for the CEX collision whereas MONACO used the differential cross-section computed by the classical scattering theory with the more accurate ion-atom interaction potential [73, 76, 77]. In addition, MONACO used a more accurate representation of the

electron fluid instead of the Boltzmann relation. Finally, AQUILA was capable of handling a very complex geometry, like DRACO, by utilizing an unstructured tetrahedral grid.

All of these models were incorporated in a software package called COLISEUM led by the Air Force Research Laboratory (AFRL) [78]. The software simulated the electric propulsion plume and predicted the plume-surface interactions. It was also capable of predicting the rates of surface sputtering and redeposition. The COLISEUM framework was designed to be flexible, usable, and expandable; COLISEUM could take complex surface meshes generated by 3D solid modeling packages and contained all the methodologies described above that could be selected by users.

Unlike the models that treated heavy species as particles, there exists the 2D Lagrangian fluid model developed at Jet Propulsion Laboratory (JPL), in which both the ions and electrons were treated as fluids [79]. The simplified electron fluid equation led to the Boltzmann relation that could be used to extract the electric potential. Then, the electric potential and the ion fluid equation were used to solve the expansion of the beam ions based on a Lagrangian approach. This model utilized the differential cross-section computed by the classical scattering theory with only the repulsive part of the potential in an effort to capture the larger angle scattered ion currents. The CEX ion fluxes were automatically considered in the differential cross-section. The neutral density from the thruster was computed analytically and was superimposed with the background neutral density approximated to be uniform. Their results suggested that the MEX ions were responsible for relatively high energy ions observed at angles greater than 25°.

1.4 Organization of Dissertation

This dissertation covers three independent computational models that the author has developed or contributed for his thesis work. Chapter 2 provides descriptions of the multi-species iterative Monte-Carlo model, the Single Cusp (SC) model, developed to investigate the plasma loss behavior at an anode wall in a cusp field created by a single permanent magnet. The understanding of the plasma loss at a magnetic cusp is particularly of interest

for a miniature DC electron bombardment ion thruster. Component level validations of the code are performed for the numerical methods implemented in the model. The model is also validated in a simple condition with an electron plasma. Then, the model is applied to a relatively more complex simulation condition to gain further understanding of the cusp physics.

Chapter 3 discusses the improvements that have been implemented in the DC-ION code developed primarily by Wirz [13, 24]. The goal for the effort is to use the model for a design of a micro-ion thruster on the order of 1 cm in diameter. While several methods described in Chapter 2 can be directly applied to DC-ION for improved accuracy in the particle portion of the code, the focus of this chapter is the methods for the fluid portion of the code. This chapter provides an extensive study of the magnetic field aligned (MFA) mesh, describing the detailed mesh generation method and comparing the accuracy in numerical results obtained with the MFA and uniform meshes. This chapter also provides a description of a numerical method for solving the plasma diffusion equation in a MFA mesh. Furthermore, this chapter discusses the improvements made to the routine to compute the neutral atom density.

Chapter 4 describes the details of the iterative Monte Carlo model, the Ion Beam (IB) model, similar to the SC model given in Chapter 2. The objective of the effort is to use the model to improve the understanding of the electrode current results from the ion beam experiment conducted by UCLA researchers [80]. Unlike the SC model, appropriate handling of heavy species collisions is necessary to simulate such an experiment. Both the ion-atom and atom-atom elastic collisions are computed by the fundamental equations of the classical scattering theory. Electrons are introduced by heavy species impact onto electrode surfaces. Therefore, four different species including high energy beam ions, CEX ions, high energy neutrals, and secondary electrons are tracked as particles. A parametric study on a secondary electron yield is performed using the model, and the electrode current results are compared with the experimental data and analytical calculations.

While all the models can easily be applied to different gases, we use a xenon gas throughout this dissertation. Therefore, when referred as ions and neutral atoms, they imply that they are xenon ions and xenon atoms, respectively.

CHAPTER 2

Numerical Investigation of Near-Surface Cusp Confinement of Micro-Scale Plasma

The Single Cusp (SC) model described in this chapter is developed in an attempt to capture the plasma loss behavior in a magnetic cusp field at an anode wall. Therefore, the model needs to resolve the micro-scale structure of the plasma and sheath very near the wall while simulating the entire domain of a system. This chapter begins with survey of experiments and numerical methods used specifically for the investigation of the cusp physics (Sec. 2.2). Then, the details of the SC model are provided in Sec. 2.3. Many of the numerical methods used in the model can also be incorporated in the discharge chamber models such as DC-ION. These methods are validated independently in Sec. 2.4. Finally, the SC model is used to simulate various configurations in Sec. 2.5.

The general structure and content of this chapter follow the article *Particle Simulation of Near-Surface Cusp Confinement of Weakly Ionized Plasma* presented at 33rd International Electric Propulsion Conference, while much details are added for this thesis. Some of the results given in this chapter are from the articles *Magnetic Field Structure Influence on Primary Electron Cusp Losses for Micro-Scale Discharges* published in Physics of Plasmas, *Influence of Upstream Field Structure on Primary Electron Loss for a Permanent Magnet Cusp* presented at 49th AIAA/ASME/SAE/ASEE Joint Propulsion Conference, and *Near-Surface Cusp Confinement for Weakly Ionized Plasma* presented at 48th AIAA/ASME/SAE/ASEE Joint Propulsion Conference. Furthermore, the SC model implements the particle weighting algorithm developed by the author found in the article *Cell-Centered Particle Weighting Algorithm for PIC Simulations in a Non-Uniform 2D Axisymmetric Mesh* published in Journal of Computational Physics.

2.1 Introduction

The magnetic field configurations for the conventional (13–30 cm) and the 3-cm Miniature Xenon Ion (MiXI) thrusters are similar in that both devices use a permanent magnet cusp field; however, the primary driver of the discharge ionization is different. In the MiXI thruster, the ionization is almost entirely caused by the high energy primary electrons while both the primary and plasma electrons contribute to the ionization in the conventional ion thrusters [24]. The negligible plasma electron ionization for the MiXI discharge chamber is a result of poor electron confinement. A significant fraction of primary electrons are lost to the anode walls too quickly to experience any collision event to produce plasma electrons. The low plasma electron temperature caused by the poor confinement also prevents plasma electrons from significantly contributing to ionization. Higher magnetic fields can be used to achieve a better confinement of electrons, but this causes discharge instabilities due to overly high magnetic field strengths near the cusp. Magnetic cusp confinement of plasma at conducting surfaces involves interactions between a divergent magnetic field, multiple plasma species, and the sheath conditions near the surface [81]. The behavior of plasma near the cusp is especially important for small discharges since the cusp field represents a large percentage of the overall discharge volume. Therefore, it is necessary to gain improved knowledge of the near-surface cusp region needed for optimization of the MiXI and for design of a stable and efficient discharge for micro-ion thrusters on the order of 1 cm in diameter.

Small-scale ($\leq$ 3 cm diameter) ion thrusters are attractive for many applications. First, small-scale ion thrusters can be used as a primary propulsion system for large ΔV missions that use small spacecrafts. Small spacecrafts such as CubeSats [82, 83] are easy to construct and, more importantly, inexpensive to develop and launch [84]. Scientific missions to the Moon using a 10×10×30 cm CubeSat are feasible with the MiXI propulsion system, but are impossible with a chemical propulsion system due to the size constraint and the large volume of chemical propellants [82]. Second, small-scale ion thrusters can be used for precise attitude control and maneuver for larger spacecrafts. The MiXI ion thruster is a critical component in the proposed Terrestrial Planet Finder (TPF) project. The MiXI propulsion

system would provide precision pointing of mirrors and supply motive forces for formation rotations and maneuvers [85, 86].

The objective of this investigation is to develop a computational model (SC model) to improve the understanding of cusp confinement very near the anode surface for a single permanent magnetic cusp. The expression for leak width provides a crude estimate of the leak area, but a much more accurate description is necessary to achieve our goal. Since probing of the sheath and near the cusp is extremely difficult using conventional probes, it is necessary to develop an accurate computational model of this region. The overall goal of this research is to develop a 1-cm micro-ion thruster that provides a stable and efficient discharge. The knowledge gained from the SC model on the cusp physics is to be incorporated in the DC-ION code developed by Wirz and Katz [13,24], which will be used to optimize the design of the micro-discharge.

2.2 Survey of Literature

2.2.1 Experimental and Theoretical Studies on Leak Width

Experimental and theoretical investigations on a plasma leak width at a magnetic cusp have been conducted extensively in the past. Experiments considered the magnetic cusp field created either by electromagnets or permanent magnets in various configurations. In the experiments with cusp fields created by electromangets, two different configurations were primarily studied: the spindle cusp and the picket fence configuration. The spindle cusp device consists of two identical circular coils placed in parallel, which creates a point cusp at the center of each coil and a ring cusp on the mid-plane between the coils by running currents in opposite directions. In contrast, the picket fence device commonly consists of a number of elongated coils placed side-by-side. Between the coils, line cusp fields are created by alternating current directions from coils to coils. The line and ring cusps are very similar except that the ring cusp goes around a circle and does not terminate. Many cusp experiments also used permanent magnets to study plasma loss in the similar cusp fields.

Multiple magnets can be placed in parallel with the same pole direction to create a line cusp. Similarly, a ring cusp is created by placing the magnets around a circumference of a cylindrical chamber. It should be noted that the cusp fields created by the two types of magnets are not the same. Along the cross-sectional plane of the electromagnet cusp field, the field strength decreases as approaching the center of the cusp. The variation is different for the permanent magnet cusp; the field strength increases toward the magnet.

Despite the extensive research on cusp confinement, the plasma leak through a magnetic cusp is not fully understood. Many experimental and theoretical works focused on finding the plasma leak width through the cusp. Knowledge of the plasma leak width is particularly important as it is directly comparable to the plasma loss rate in cusp confinement devices. Until the 1970's, the plasma loss width was believed to be on the order of an ion Larmor radius [87]. However, Kitsunezuki et al. [88] and Hershkowitz et al. [89] independently reported that the leak width was much smaller than the local ion gyroradius for a high-β high density plasma and a low-β low density plasma, respectively, where β is the ratio of the plasma pressure to the magnetic pressure. Hershkowitz et al. [89] concluded that the plasma leak half-width should be on the order of a hybrid gyroradius that was always smaller than the ion gyroradius. Here, the hybrid gyroradius is defined as $2\sqrt{\rho_e \rho_i}$ where ρ_e and ρ_i are the gyroradii for electrons and ions, respectively. Leung et al. [90] provided additional data that leakage half-widths were about the hybrid gyroradii in an experiment similar to the one by Hershkowitz et al. [89]. In a spindle cusp configuration, Bosch and Merlino [91, 92] also observed the same scaling with the magnetic field for a low β plasma under the condition where the Debye length is much smaller than the loss width. In spite of the dissimilarity between the electromagnet and permanent magnet cusp fields, the hybrid gyroradius scaling was also observed in various experiments using permanent magnets in line cusp [93–95] and ring cusp configurations [96, 97] for low-β plasmas. On the contrary to these experiments, several other researchers still reported that the scaling of the loss width was on the order of ion Larmor radius in spindle cusp experiments with high-β and highly ionized plasma [98,99] and even for low-β plasma [100]. Horiike et al. [101] also observed the leak width through the permanent magnet cusp to be twice the size of the ion Larmor radius for low-β plasma

in a strong magnetic field.

Many theoretical attempts were made to explain the contradiction in the experimental results. In the 1977 review paper by Haines on plasma cusp confinement, he noted that the hybrid gyroradius scaling can be interpreted in terms of either ion-acoustic instability, modified two-stream turbulence, or a visco-resistive sheath [102]. Koch and Matthieussent [103] developed a collisional diffusion model and showed that the leak width scaled as B^{-1} under a highly collisional condition (i.e. mean free paths were much shorter than the characteristic length for the variation of the plasma parameters). If the anomalous diffusion in a perpendicular direction was taken into account, then the leak width scaled as $B^{-1/2}$. The same scaling law with the magnetic field was obtained by Bosch and Merlino [91, 92]. Similar to Koch and Matthieussent [103], they derived the leak width using the plasma diffusion equation but in a simpler manner. For a ring-cusp in the spindle cusp configuration, the leak width was expressed as [92],

$$w_l = \sqrt{\frac{2\bar{D}R}{C_s}} \tag{2.1}$$

where w_l is the leak width, $\bar{D}$ is the effective diffusion coefficient, R is the coil radius, and C_s is the ion acoustic speed. A similar formula was also obtained for a point cusp. Note that these formulas still scaled as the hybrid gyroradius if the classical ambipolar diffusion was to be considered. The main difference from the derivation by Koch and Matthieussent was the collisionality along the magnetic field; Bosch and Merlino assumed non-collisional flow of plasma along the field. This difference yielded different leak width scaling with the neutral pressure [104]. Morishita et al. [105] applied the expression obtained by Bosch and Merlino and showed good agreement with experiment for the range of pressure in their multi-cusp negative ion source. Fukano et al. [106] extended the work by Bosch and Merlino by applying the leak width formula to different ranges of plasmas.

The theoretical works described above used the plasma diffusion equation where the underlying assumption was the quasi-neutrality (i.e. $n_i \approx n_e$) even near the cusp. Bosch and Merlino [91, 92] argued that the condition should be true at sufficiently high densities where the Debye length was much smaller than the leak width; the quasi-neutral condition

was maintained by the self-consistent electric fields that inhibited perpendicular motion of ions, which was evident from the similar current profiles of ions and electrons. However, the much lower electric potential at the cusp also suggests that there should be a slight charge separation effect locally while the ion and electron densities are approximately the same. Knorr and Willis [107] performed a theoretical study using a Vlasov-Poisson model and self-consistently solved the electric potential without assuming charge neutrality. The other important assumption that they made was a collisionless plasma, while the collisional effect was the dominant mechanism to explain the hybrid gyroradius scaling for theories derived from the diffusion equation. Even by solely considering the electrostatic effect, their model suggested that the hybrid gyroradius scaling was possible. They also noted that their unpublished experiments suggested the presence of primary electrons was necessary to observed the hybrid gyroradius scaling for the leak width. Later, Knorr and Merlino [108] attempted to theoretically explain the influence of the primary electrons on the leak width. They found that, without primary electrons, plasma electrons would diffuse further outward to compensate the electric potential, thus resulting in the leak width on the order of ion gyroradius. They argued that the diffusion length across the magnetic field was reduced through collisions between primary and plasma electrons, causing the plasma electrons to gain energies and enhancing the loss.

The recent paper by Martinez-Sanchez and Ahedo [81] used a kinetic model to analytically investigate the plasma characteristics in a cusp magnetic field near an electron repelling wall, the similar geometry as we study through a computational model in this chapter. Their model ignored the collisional effect as Knorr and Merino [107] while including the sheath due to the solid wall. Note that all the other theories did not consider the sheath effect. They studied two different cases with magnetized and unmagnetized ions. Their analytical solutions yielded several important findings for the magnetized ion case;

1. Electric potential dropped on the order of 0.7 times the electron temperature in a presheath.
2. Ions satisfied the Bohm criterion, entering a sheath at an ion sound speed.
3. Ion flux to the wall was not reduced through the cusp.

For the unmagnetized ion case, they argued that the ions were electrostatically confined through converging equipotential tube; the ions bounced back and forth the surface, eventually turning back toward the bulk plasma. This mechanism is analogous to a confinement through a magnetic mirror. They concluded that the quantity, $h \langle m_i w_\perp^2 \rangle^{(2+n)/2n}$, is an electrostatic adiabatic invariant where h is the half-width of the potential channel, m_i is the ion mass, and $w_\perp$ is the perpendicular component of ion velocity.

2.2.2 Computational Models for Cusp Confinement Devices

Previous researchers have developed computational models that can be utilized to predict electron and ion losses at the cusp. For example, Arakawa and Ishihara [22] developed a 2D hybrid fluid/particle model for a cusped ion thruster. In their model, primary electrons were treated as particles while other species were modeled as fluids. The discharge chamber performances predicted by the model and measured in experiments were compared for 7 cm and 30 cm diameter ion thrusters. Both the diffusion coefficients by the classical and Bohm diffusion were used in the fluid approximation for comparison. The results suggested that the model was capable of predicting ion production cost vs. propellant utilization behavior that qualitatively agreed with the experimental result. The underlying assumption for the fluid approximation was charge neutrality. This assumption was generally valid even in the cusp region but cannot include the charge separation effect to more accurately predict the detailed plasma loss structure and dynamics. Wirz et al. [13, 23, 24] also developed a 2D/3D hybrid particle/fluid model for discharge chamber simulations. This model was more sophisticated than Arakawa and Ishihara's model; in that, more detailed plasma diffusion equation was used to self-consistently compute many different parameters. Nevertheless, the fluid approximation was again not suitable for our objective.

In comparison to these models, full particle models have also been developed for simulations of devices utilizing magnetic cusps. Marcus et al. [109] developed a PIC model to study plasma behavior and confinement in a "picket fence" magnetic cusp device. Although their model did not assume charge neutrality, all charged particles were assumed to be generated

in the cusp region. In a discharge chamber, the charged particles are mostly created in the bulk plasma region away from the walls. Therefore, their results are not applicable for our experimental condition or for micro discharges. Furthermore, the type of magnetic cusp that they investigated is different from a cusp created by a permanent magnet. More specifically, the magnetic field is weaker at the cusp compared to the field near the coil for a picket fence device, whereas the field is the strongest near the permanent magnet cusp. For this reason, the detail of the plasma loss behavior could be different. A similar computational domain was used in a PIC model developed by Hirakawa and Arakawa [28], while applying a permanent magnet cusp field. Unlike the model by Marcus et al., the plasma was assumed to be created away from the wall. Therefore, uniform fluxes of plasma species were applied at the bulk plasma boundary of the computational domain. The trends obtained from the model showed qualitative agreement, and the plasma loss width agreed fairly well with the existing theory. However, these results were obtained with a simplified cusp field and a different mass ratio of ion to electron compared to the actual discharge condition, mainly due to the lack of computer power.

More recently, Takekida and Nanbu [110] developed a PIC-MCC model for optimizing the design of a large multi-cusp confinement of plasma discharge. This model simulated not only the cusp region but also the entire domain of the device. The model also included many different types of collisions. Using the model, they were able to determine an optimum number of magnetic poles for a better primary electron confinement and trends important in improving the design. However, their focus was on macroscopic structure of the plasma instead of the small structure very near the cusp. Finally, Mahalingam and Menart [25–27] developed a more extensive PIC-MCC model to simulate the discharge chamber of an ion thruster. Their model was used to obtain the current density distribution along the wall and clearly showed the charge separation effect, while detailed study of the plasma loss behavior is still required for developing a more accurate theory and applying it to a design of a micro discharge.

2.3 Description of Single Cusp Model

2.3.1 Overview

The SC model developed herein to investigate the cusp physics employs the multi-species iterative Monte Carlo method. A simplified flowchart of the model is shown in Fig. 2.1. This model is similar to the standard PIC model that tracks charged species in the electric field and weights particles to the computational grid for calculations of the electric field. However, the major difference from the PIC model is that the electric field is frozen during the particle tracking phase. In this way, the interactions between the charged species are decoupled, and the different species can be tracked independently, whereas the PIC model requires tracking of all the species simultaneously. After all the particles are tracked independently, the electric potential is updated. These calculations are repeated until the potential and species densities attain convergence. The benefits of these features are the simpler structure of code and the ease of parallelization without significant changes to the code structure. In the SC model, the particle tracking is parallelized using the message passing interface (MPI). Furthermore, the model can be faster than the PIC model if the potential solution converges smoothly, which is often the case for low density plasmas. However, at higher plasma densities, the

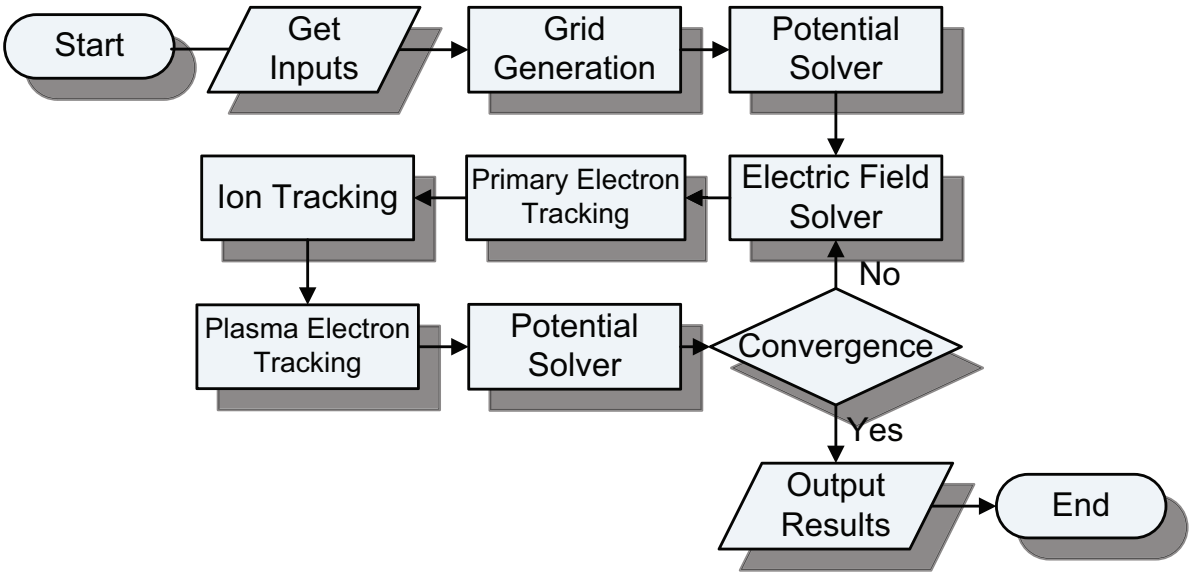

Figure 2.1: Simplified flowchart of the SC model.

convergence can be a critical issue as discussed later in this chapter.

The model treats all the important charged species such as the primary electrons, ions, and plasma electrons as particles. A particle model is required due to a large range of collisionality for the densities and energies that are used in this effort and to resolve species interactions and dynamics in the cusp region. The important components of the code include:

- Analytical equations for fields induced by permanent magnets
- Modified Boris method for particle tracking
- Generalized weighting scheme for particle weighting
- 2nd order methods for electric potential and field

In addition to these components, this chapter covers the collision calculation method and mixing and smoothing methods that are implemented to improve the convergence. Further details on geometric algorithms, data structure for the computational mesh, and particle injection and loading methods are provided in appendices.

The SC model takes both the regular and adaptive meshes. The adaptive mesh was used during the initial investigations to resolve only the cusp region by increasing the resolution with the field strength of the magnet of interest. In later simulations, the adaptive feature of the grid generation was turned off to apply the charge density smoothing method for a regular mesh. The weighting scheme and the methods for the electric potential and field calculations implemented in the SC model are compatible with the adaptive mesh and the MFA mesh discussed in Sec. 3.2.

2.3.2 Analytical Equations for Magnetic Fields

The SC model utilizes analytical equations to solve magnetic fields induced by magnetic dipoles, permanent magnets, and current loops. All of these equations are given in Appendix C. Among the permanent magnet equations available in the literature, the analytical equations for axially magnetized cylindrical magnets [111, 112], block magnets [113], and axially and radially magnetized ring magnets [112, 114] are implemented in the SC model. These equations were found relatively recently within the past 10 years. The underlying

assumption for the permanent magnet equations is the uniform magnetization within the magnets. The validity of the assumption is dependent on the hysteresis characteristic of the type of permanent magnet. Samarium cobalt magnets are used mostly in the experiment; the assumption of constant magnetization is reasonable for these magnets as they have a low dependence of magnetization with the applied magnetic field such that the magnetization is not affected significantly by the surrounding magnets. Samarium cobalt magnets also have a very high coercivity such that they are not easily subjected to demagnetization.

The fast and accurate magnetic field solver is one of the key features of the model since the particle trajectories are directly affected by the magnetic fields. These analytical equations are faster to evaluate compared to existing magnetic field simulation software and accurate even very near the permanent magnets. Nevertheless, the computation of the magnetic field can be the bottleneck of the overall run-time since the equations are evaluated for all the particles at every time-step. In order to mitigate the large computational run-time, interpolation of the field at particle locations was also considered during the course of code development. This method requires a separate grid that stores the magnetic field, and the field can be interpolated to the particle location using the stored values. However, for magnetic configurations used in our experiments, the accuracy of the interpolation method was not sufficient when using a 2D magnetic field grid, due to the configuration azimuthally asymmetric about the domain axis. We also considered approximating the permanent magnet equations with multiple dipoles, but again the accuracy was not sufficient.

The equations for the cylindrical and ring magnets are relatively complex, expressed in terms of complete elliptic integrals of the first, $K(m)$, and second kind, $E(m)$, and incomplete elliptic integrals of the first, $F(\theta, m)$, and second kind, $E(\theta, m)$. Here, m is the square of the elliptic modulus k and ϕ is the amplitude. The complete elliptic integrals also appear in the current loop equation. The preliminary version of the model first evaluated Carlson's elliptic integrals (R_F, R_D, and R_J) and applied the simple relationship with standard elliptic integral [115] (Appendix C.7). This method worked very well for wide ranges of input arguments of elliptic integrals. However, the computation methods were later replaced with Fukushima's fast computation methods for $K(m)$ [116], $E(m)$ [116], and $F(\theta, m)$ [117] in

the standard domain of elliptic parameters, $0 < m < 1$ (and $0 < \theta < \pi/2$ for an incomplete elliptic integrals). These methods are also briefly described in Appendix C.7. Fukushima also provided a method for $E(\theta, m)$ [118], which has not been implemented at this moment. The reductions in the wall time for $K(m)$, $E(m)$, and $F(\theta, m)$ were approximately 74, 88, and 48 percents, respectively.

2.3.3 Particle Tracking Method

In addition to the magnetic field calculation discussed above, the numerical method used to integrate particles' equation of motion is critical in any particle simulation due to the large number of integrations required to determine particle trajectories. For this reason, the integration method has to be fast while retaining sufficient accuracy. This requirement is extremely important for low energy plasma electrons in cusp confinement devices; unacceptable gain of energy from the integrator enhances the loss of electrons, masking the actual species dynamics and structure at the magnetic cusp.

The motion of charged particles between collisions is described by Lorentz equation and Newton's Second Law,

$$\frac{d\mathbf{v}}{dt} = \frac{q}{m}(\mathbf{E} + \mathbf{v} \times \mathbf{B}) = \mathbf{f} \tag{2.2}$$

$$\frac{d\mathbf{x}}{dt} = \mathbf{v} \tag{2.3}$$

where $\mathbf{v}$ is the particle velocity, q is the particle charge, m is the particle mass, $\mathbf{E}$ is the electric field, and $\mathbf{B}$ is the magnetic field. In electrostatic PIC simulations, Boris method [119, 120] is commonly used to integrate Eqs. (2.2) and (2.3). In the Leapfrog method, the velocity and the position are calculated on a staggered grid in time. Although the number of function evaluation per step is identical to first-order accurate Euler method, the staggered-grid feature of the Leapfrog integrator allows the method to be second-order accurate. The Boris method uses this feature of the Leapfrog method while providing additional accuracy to the particle gyration calculation; the Lorentz forces on the particle are decomposed into electric and magnetic forces. The electrostatic force is assumed to act half at the beginning,

and half at the end of a given time step. This allows the circular motion of the particle due to the magnetic field to be treated in the absence of the electric field. Consequently, the velocity after one time-step is computed in three steps.

$$\mathbf{v}_- = \mathbf{v_n} + \left(\frac{q\Delta t}{2m}\right)\mathbf{E} \tag{2.4}$$

$$\frac{\mathbf{v}_+ - \mathbf{v}_-}{\Delta t} = \frac{q}{m}\left(\frac{\mathbf{v}_+ - \mathbf{v}_-}{2} \times \mathbf{B}\right) \tag{2.5}$$

$$\mathbf{v_{n+1}} = \mathbf{v}_+ + \left(\frac{q\Delta t}{2m}\right)\mathbf{E} \tag{2.6}$$

where Δt is the time-step and subscript n denotes nth time-step.

The SC model uses a modified version of Boris method proposed by Wirz [13]. In this method, the staggered-grid feature of the Leapfrog integrator is removed, and the position and velocity are evaluated on an aligned temporal grid. Instead, better estimations of the magnetic fields are obtained by using a predictor-corrector algorithm in solving a simple circular gyromotion of the particle given by Eq. (2.5) [13]. The predictor-corrector algorithm determines the particle trajectory for each time step by first predicting the midpoint of the trajectory assuming the magnetic field at the starting position. The magnetic field at the "predicted" midpoint is calculated and then used to determine a "corrected" final position and velocity orientation. Another feature of this method is that the rotation is done in the cylindrical coordinate referenced at particle's guiding center. The rotation of velocity vector is expressed as

$$\mathbf{v}_+ = (\mathbf{v}_-)_\parallel + |(\mathbf{v}_-)_\perp|\left(\cos(\Delta\theta)\hat{h}_\perp - \sin(\Delta\theta)\hat{h}_r\right) \tag{2.7}$$

where $\Delta\theta$ is the change in angle determined by $2\pi/\omega_c\rho$, ω_c is the cyclotron frequency, and ρ is the number of steps per cycle specified as an input. Here, $\hat{h}$ represents the coordinate system aligned with the magnetic field [121].

$$\hat{h}_\parallel = \frac{\mathbf{B}}{|\mathbf{B}|}; \quad \hat{h}_\perp = \frac{\mathbf{v} - (\mathbf{v}\cdot\hat{h}_\parallel)\hat{h}_\parallel}{|\mathbf{v} - (\mathbf{v}\cdot\hat{h}_\parallel)\hat{h}_\parallel|}; \quad \hat{h}_r = \frac{q}{|q|}(\hat{h}_\parallel \times \hat{h}_\perp) \tag{2.8}$$

The position after one time-step in the field-aligned coordinate system is then given as [121]

$$\begin{aligned} \Delta x_{\parallel} &= \Delta t(\mathbf{v} \cdot \hat{h}_{\parallel})\hat{h}_{\parallel} \\ \Delta x_{\perp} &= r_L \sin(\Delta\theta)\hat{h}_{\perp} \\ \Delta x_r &= -r_L[1 - \cos(\Delta\theta)]\hat{h}_r \end{aligned} \tag{2.9}$$

where r_L is the Larmor radius given as $r_L = m\mathbf{v}_{\perp}/|q||\mathbf{B}|$.

In the SC model, three time-step values are computed separately based on the local grid size, electric field, and ρ.

$$dt_G = \gamma \frac{\min(\Delta z_{\text{cell}}, \Delta r_{\text{cell}})}{|\mathbf{v}|}, \quad dt_E = \gamma \frac{|\mathbf{v}|m}{e|\mathbf{E}|}, \quad dt_B = \frac{2\pi}{\omega_c \rho} \tag{2.10}$$

where γ is a fraction specified as an input. The first time-step, dt_G, prevents the particle to skip between cells, so the particle can at most move to one of the surrounding cells. The second time-step, dt_E, limits the change in velocity in one time-step. Lastly, the third time-step, dt_B, limits the rotation angle for gyromotion. The smallest of the three time-steps is used to advance a particle.

$$\Delta t = \min(dt_G, dt_E, dt_B) \tag{2.11}$$

In the standard Boris method, a constant time-step has to be used to maintain its accuracy because of the symmetry required in the Leapfrog feature. This requirement leads to an unreasonably small time-step in a bulk region of a ring-cusp discharge device where the magnetic field is very low, because the time-step has to be set based on the maximum field strength in the domain. Therefore, the modified Boris method with variable time-step is suitable for the ring-cusp discharge device where the range of magnetic field strength is large.

Mao and Wirz [121] have made comparisons of charged particle tracking methods in three different configurations: uniform field, Earth's dipole field, and magnetic mirroring on a small scale. The second and third test cases involve magnetic cusps and are relevant to the ring-cusp discharge chamber. It was shown that the gain in the relative energy was minimal

while the wall time was comparable to the Boris method.

The procedure in advancing a particle by one time-step with the modified Boris method is provided below. Here, the subscript $*$ denotes the predicted mid-point in this procedure.

1. Given $\mathbf{B}_n$ and $\mathbf{v}_n$ at nth time-step.
2. Choose a time-step (Eq. (2.11)).
3. Compute $\mathbf{v}_-$ by applying half the electric impulse (Eq. (2.4)).
4. Obtain the field-aligned coordinates using $\mathbf{v}_-$ and $\mathbf{B}_n$ (Eq. (2.8)).
5. Calculate $\Delta\theta_n$ and r_{Ln} using $\mathbf{v}_-$ and $\mathbf{B}_n$.
6. Advance position by $\Delta\theta_n/2$ and $\Delta t/2$ to get predicted midpoint, $\mathbf{x}_*$ (Eq. (2.9)).
7. Obtain $\mathbf{B}_*$ at $\mathbf{x}_*$.
8. Recalculate the field-aligned coordinates using $\mathbf{v}_-$ and $\mathbf{B}_*$ (Eq. (2.8)).
9. Calculate $\Delta\theta_*$ and r_{L*} using $\mathbf{v}_-$ and $\mathbf{B}_n$.
10. Advance velocity vector by $\Delta\theta_*$ using $\hat{h}_*$ (Eq. (2.7)).
11. Compute $\mathbf{v}_{n+1}$ by applying another half the electric impulse (Eq. (2.6)).
12. Advance position by a full step using $\mathbf{v}_{n+1}$ and $\hat{h}_*$ (Eq. (2.9)).

2.3.4 Particle Weighting Algorithm

The PIC method involves the exchange of information between particles and a computational grid. In particular, weighting of particles to the grid is necessary to compute electric potential and field at discrete grid points, while interpolation of the field is required to obtain the electrostatic force at the particle locations. Although regular grids are most commonly used in PIC simulations for simplicity, many researchers have applied PIC methods to more complex grids such as adaptive meshes [122, 123], structured non-orthogonal grids [124, 125], and unstructured finite element meshes [126]. Standard weighting schemes (e.g. first order area weighting in two dimensions) work very well in Cartesian coordinates [120]. However, in cylindrical coordinates, these weighting methods produce systematic errors in particle densities at boundary nodes when a regular mesh is used [127–129]. For a rectilinear mesh with varying spacing in the r-direction, the errors become more severe; in that, the errors

occur at the interior grid points in addition to the nodes at the boundaries.

Several authors have proposed corrections to the density calculation for 2D rectilinear meshes in cylindrical coordinates. For example, Larson et al. [127] suggested applying the correction factors to the calculated densities at the grid points. On the other hand, Ruyten [128] proposed density-conserving shape factors to distribute particles to the grid. More recently, Verboncoeur [129] proposed a generalized weighting scheme, employing a corrected volume calculated with the same shape factor as applied in particle weighting. All of these methods remove the systematic errors in the density calculations while conserving the particle density. In particular, with a uniform current density as an input, a uniform particle distribution on the grid is produced. However, it is difficult to apply the weighting schemes by Larson et al. and by Ruyten to more complex meshes such as adaptive, non-orthogonal, and unstructured meshes in cylindrical coordinates. The generalized weighting scheme suggested by Verboncoeur can be applied fairly easily once the corrected cell volumes are calculated properly. In the work by Vazquez and Castellanos [126], the corrected volumes were applied successfully in a triangular mesh. Although they set up equations for the weighted volumes for quadrilateral elements, the equations were not solved and applied to a quadrilateral mesh. In the work by Kwok and Cornet [122, 123], the generalized weighting scheme has been applied to an adaptive regular mesh in cylindrical coordinates. However, their algorithm is difficult to apply in even more complex meshes such as a non-orthogonal adaptive grid.

The SC model implements the cell-centered particle weighting algorithm discussed herein. The weighted volume calculation is extended for non-uniform 2D axisymmetric meshes, enabling the application of Verboncoeur's generalized weighting scheme to adaptive regular meshes used in the SC model and even to the MFA meshes discussed in Sec. 3.2.

2.3.4.1 Mapping Quadrilateral and Triangular Elements in Natural Coordinates

For an element of 3 or 4 vertices, the weighting factors and the corrected volumes can be calculated in either physical or natural coordinates. However, the calculation in the physical coordinates is not always straightforward, especially for the case with quadrilateral elements of arbitrary shapes. For this reason, the expressions for the weighting factors and the corrected volumes are derived in natural coordinates, in which, the arbitrarily shaped triangle or quadrilateral is mapped into a reference polygon of right triangle or square, respectively. As shown in Fig. 2.3, the reference polygons have two sides lying along the two natural coordinate axes with both lengths equal to one. In mapping r-z cylindrical coordinates to natural coordinates, the following interpolation function is used.

$$g(\xi,\eta) = \sum_{k}^{N_v} g_k W_k(\xi,\eta) \tag{2.12}$$

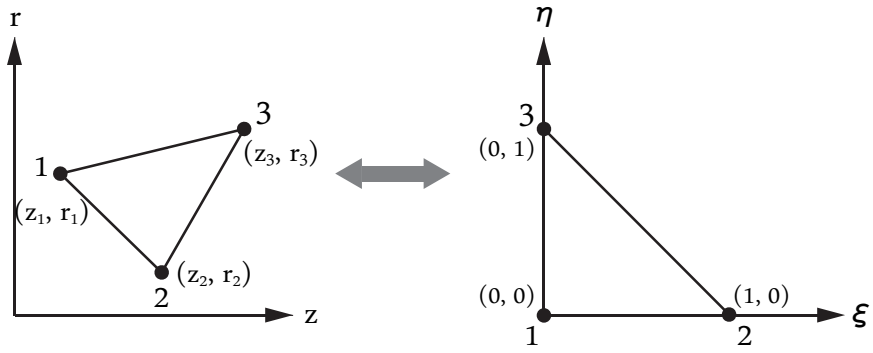

Figure 2.2: Mapping of a triangular element in natural coordinates.

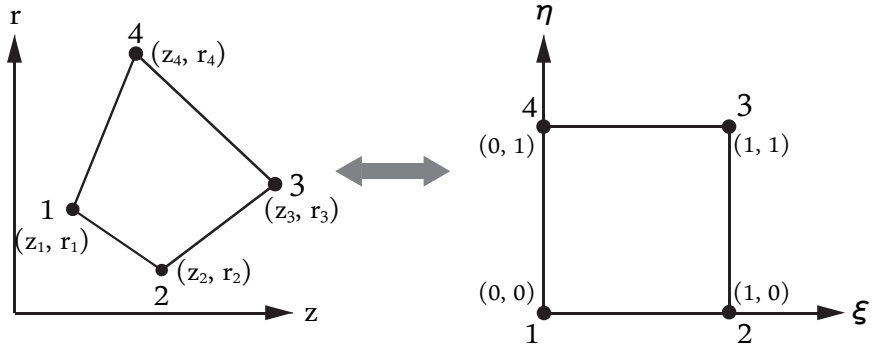

Figure 2.3: Mapping of a quadrilateral element in natural coordinates.

where g is some function, W is the weighting factor, N_v is the number of vertices, and the subscript k denotes the vertex number. The numbering of vertices starts at $(0,0)$ in natural coordinates and is incremented in a counterclockwise direction as shown in Fig. 2.3. The weighting factors are given as,

$$\begin{array}{llllll} \text{Triangle:} & W_1 = 1-\xi-\eta & W_2 = \xi & W_3 = \eta & & \\ \text{Quadrilateral:} & W_1 = (1-\xi)(1-\eta) & W_2 = \xi(1-\eta) & W_3 = \xi\eta & W_4 = (1-\xi)\eta \end{array} \tag{2.13}$$

These weights are used to assign particles to the vertices. From Eq. (2.12), z and r components for the triangular element are found in terms of ξ and η in natural coordinates.

$$\begin{aligned} z(\xi,\eta) &= a_1 + a_2\xi + a_3\eta \\ r(\xi,\eta) &= b_1 + b_2\xi + b_3\eta \end{aligned} \tag{2.14}$$

where

$$\begin{pmatrix} a_1 \\ a_2 \\ a_3 \end{pmatrix} = \begin{pmatrix} z_1 \\ z_2 - z_1 \\ z_3 - z_1 \end{pmatrix} \qquad \begin{pmatrix} b_1 \\ b_2 \\ b_3 \end{pmatrix} = \begin{pmatrix} r_1 \\ r_2 - r_1 \\ r_3 - r_1 \end{pmatrix} \tag{2.15}$$

Similarly for the quadrilateral element, z and r components in cylindrical coordinates are found in terms of ξ and η in natural coordinates using Eq. (2.12).

$$\begin{aligned} z(\xi,\eta) &= c_1 + c_2\xi + c_3\eta + c_4\xi\eta \\ r(\xi,\eta) &= d_1 + d_2\xi + d_3\eta + d_4\xi\eta \end{aligned} \tag{2.16}$$

where

$$\begin{pmatrix} c_1 \\ c_2 \\ c_3 \\ c_4 \end{pmatrix} = \begin{pmatrix} z_1 \\ z_2 - z_1 \\ z_4 - z_1 \\ z_1 - z_2 + z_3 - z_4 \end{pmatrix} \qquad \begin{pmatrix} d_1 \\ d_2 \\ d_3 \\ d_4 \end{pmatrix} = \begin{pmatrix} r_1 \\ r_2 - r_1 \\ r_4 - r_1 \\ r_1 - r_2 + r_3 - r_4 \end{pmatrix} \tag{2.17}$$

2.3.4.2 Weighting of Particles

Given the particle position (z, r), ξ and η in naturals coordinates are computed in order to determine the weighting factors. For the triangular element, ξ and η are determined from Eq. (2.14).

$$\begin{pmatrix} \xi \\ \eta \end{pmatrix} = \frac{1}{a_2 b_3 - a_3 b_2} \begin{bmatrix} b_3 & -a_3 \\ -b_2 & a_2 \end{bmatrix} \begin{pmatrix} z - z_1 \\ r - r_1 \end{pmatrix} \tag{2.18}$$

where a_i and b_i are defined in Eq. (2.15). In Eq. (2.18), $a_2 b_3 - a_3 b_2$ is equivalent to twice the area of the triangular element, and the weighting factors obtained from Eq. (2.18) are the same as the area ratios calculated directly in r-z cylindrical coordinates. For the quadrilateral element, the interpolants in natural coordinates are found by solving for ξ and η in Eq. (2.16).

$$\xi = \begin{cases} \dfrac{-B \pm \sqrt{B^2 - 4AC}}{2A} & \text{for } A \neq 0 \\ -C/B & \text{for } A = 0 \end{cases} \tag{2.19}$$

$$\eta = \frac{c_1' - c_2 \xi}{c_3 + c_4 \xi} = \frac{d_1' - d_2 \xi}{d_3 + d_4 \xi} \tag{2.20}$$

where $A = c_4 d_2 - c_2 d_4$, $B = c_1' d_4 - c_4 d_1' - c_2 d_3 + c_3 b_2$, and $C = c_1' d_3 - c_3 d_1'$. Here, c_1' and d_1' are defined as $c_1' = z - z_1$, $d_1' = r - r_1$, and c_i and d_i are defined in Eq. (2.17). Once ξ and η are calculated from Eqs. (2.18) to (2.20), weighting factors for the vertices are found using Eq. (2.13). Then, the number of particles assigned to a vertex, k, is simply given as

$$N_k = N_p W_k(\xi, \eta) \tag{2.21}$$

where N_p is the number of particles that a macro-particle represents.

2.3.4.3 Weighted Volume Calculation

In applying the generalized weighting algorithm, the particle density at the grid is calculated with the cell volume weighted using the same interpolation function applied in the particle weighting. As described above, the corrected volume calculation is done in natural coordinates for the reference polygons as described in Ref. [126]. The differential volume element, dV, can be expressed in terms of natural coordinates.

$$dV = 2\pi r dz dr = 2\pi r(\xi,\eta)|J(\xi,\eta)|d\xi d\eta \tag{2.22}$$

where $|J(\xi,\eta)|$ is a Jacobian or a determinant of a Jacobian matrix for the mapping shown in Fig. 2.3.

$$[J] = \begin{bmatrix} \dfrac{\partial x}{\partial \xi} & \dfrac{\partial x}{\partial \eta} \\ \dfrac{\partial y}{\partial \xi} & \dfrac{\partial y}{\partial \eta} \end{bmatrix} \tag{2.23}$$

Using Eqs. (2.22) and (2.23), the corrected volume can be calculated by solving the following integrals.

$$V_k = \int\int W_k(\xi,\eta) 2\pi r(\xi,\eta)|J|\, d\xi d\eta \tag{2.24}$$

where the limits of the integrals are $\xi = 0 \rightarrow 1-\eta$ and $\eta = 0 \rightarrow 1$ for the triangular element and $\xi = 0 \rightarrow 1$ and $\eta = 0 \rightarrow 1$ for the quadrilateral element. Also, the Jacobian, $|J|$, for the triangular and the quadrilateral elements are $|J| = a_2 b_3 - a_3 b_2$ and $|J| = (a_2 b_3 - a_3 b_2) + \xi(a_2 b_4 - a_4 b_2) + \eta(a_4 b_3 - a_3 b_4)$, respectively. For the triangular element, the corrected volumes are as follows.

$$\begin{aligned} V_1 &= \pi(2r_1 + r_2 + r_3)(a_2 b_3 - a_3 b_2)/12 \\ V_2 &= \pi(r_1 + 2r_2 + r_3)(a_2 b_3 - a_3 b_2)/12 \\ V_3 &= \pi(r_1 + r_2 + 2r_3)(a_2 b_3 - a_3 b_2)/12 \end{aligned} \tag{2.25}$$

Note that the sum of the volumes corresponds to the physical volume of the triangular element. Similarly, for the quadrilateral element, the weighted volumes are as follows.

$$\begin{aligned}
V_1 &= \pi\left[(8r_1+4r_2+2r_3+4r_4)s_1\right. \\
&\quad \left.+(2r_1+2r_2+r_3+r_4)s_2+(2r_1+r_2+r_3+2r_4)s_3\right]/36 \\
V_2 &= \pi\left[(4r_1+8r_2+4r_3+2r_4)s_1\right. \\
&\quad \left.+(2r_1+6r_2+3r_3+r_4)s_2+(r_1+2r_2+2r_3+r_4)s_3\right]/36 \\
V_3 &= \pi\left[(2r_1+4r_2+8r_3+4r_4)s_1\right. \\
&\quad \left.+(r_1+3r_2+6r_3+2r_4)s_2+(r_1+2r_2+6r_3+3r_4)s_3\right]/36 \\
V_4 &= \pi\left[(4r_1+2r_2+4r_3+8r_4)s_1\right. \\
&\quad \left.+(r_1+r_2+2r_3+2r_4)s_2+(2r_1+r_2+3r_3+6r_4)s_3\right]/36
\end{aligned} \tag{2.26}$$

where $s_1 = c_2d_3 - c_3d_2$, $s_2 = c_2d_4 - c_4d_2$, and $s_3 = c_4d_3 - c_3d_4$. The sum of the volumes corresponds to the physical volume of the quadrilateral element. These formulas for corrected volumes can be used for any grid with arbitrary quadrilaterals or triangles including uniform, adaptive regular, non-orthogonal, and unstructured meshes in r-z cylindrical coordinates.

2.3.4.4 Implementation

For every node element, the weighted volumes are calculated using Eqs. (2.25) and (2.26) and distributed to corresponding vertices (cell centroids). The sum of the volumes distributed to one cell is the corrected volume used for the density calculations for the cell. Then, the volumes assigned to the boundary cells are re-assigned to the nearest interior cells since the volumes of the boundary cells are essentially zero. Therefore, the effective weighting between the boundary cells and the neighboring interior cells are the nearest-grid-point weighting as shown by the interpolation function in Fig. 2.4. At every time-step during the tracking of particles, fraction of particles that a macro-particle represents is distributed to three to four vertices of a node element in which the particle is located. The particles weighted to the vertices are determined from Eqs. (2.13) and (2.18) to (2.21), depending on the element shape, and these particles are accumulated at cell centroids until the end of

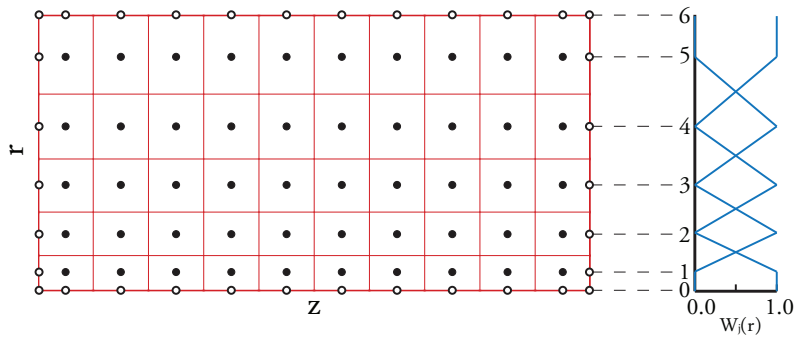

Figure 2.4: Orthogonal mesh with variable spacing in radial direction. Closed and open dots represent interior and boundary cells, respectively. Radial interpolation function, $W_j(r)$, is shown to the right of the mesh.

the particle tracking. Again, the particles distributed to the boundary cells are re-assigned to the nearest interior cells. Finally, the particle density at a cell is computed by dividing the particles assigned to each cell centroid by the corrected cell volume. The Verboncoeur's approach allows a significant reduction in the computational cost since it does not require complex weighting factor calculation that is performed at every particle position while the weighted cell volumes are computed only once when the computational grid is generated.

2.3.5 Collisions

Atomic collision is a non-collective process that involves exchange of energy between the same or different species. For most of the simulations, the background neutral density is several orders of magnitude higher than the densities of other species. Therefore, we mainly consider collisions of primary electrons, ions, and plasma electrons with background neutral atoms. The collision process can be categorized by the types of energy exchange: elastic, inelastic (excitation and ionization), superelastic, radiative and charge-reactive collisions [4]. The types of collisions included in the SC model are listed below.

- Electron-atom elastic collision
- Electron-atom ionization
- Electron-atom excitation
- Ion-atom elastic collision

The relative importance of different collision types can be determined by examining mean free path, λ, for each collision type. The mean free path is related to collision cross-section, σ, and density of target gas, n, by $\lambda = 1/\sigma n$. Collision cross-section is an effective cross-sectional area that a collision event may take place and is a measure of the collision probability. The larger the cross-section and the density, the shorter the collision path length is, thus collisions occur more frequently within the total path length that a particle travels. For electron-atom collisions, elastic and inelastic collisions are considered to be important for the simulation conditions because of the much larger cross-sections compared to those for other collision types. For ion-atom collisions, only elastic (i.e. MEX) collision is included in the SC model. Due to the low energy of ionized particles, inelastic collision is neglected as ions only have energies below the threshold energy of the collision. The symmetric CEX collision is also neglected because the resulting effect is similar to the MEX collision at the ion and neutral energies. The primary electron-plasma electron collision is not implemented in a direct manner but is incorporated by considering the equilibration (slowing) rate.

2.3.5.1 Elastic Collision

In an elastic collision, velocity vectors of the collision pair are altered while the total kinetic energy is conserved, and no charge exchange occurs between the collision pair. After the collision event, a charged particle initially gyrating about a magnetic field line is confined by a different field line. The individual particles undergo a random walk as a result of multiple elastic collisions, and the net effect is the diffusion of the particles across magnetic fields. With a higher collision frequency, the diffusion across the fields is enhanced while the diffusion along the fields is impeded.

The elastic collision is approximated using the Monte Carlo collision (MCC) method. During a time-step, Δt, the probability that a particle experiences an elastic collision is expressed as

$$P_{\mathrm{el}} = 1 - \exp(-\Delta t \sigma_{\mathrm{el}} v n_o) \tag{2.27}$$

where v is the velocity and n_o is the neutral density. Equation (2.27) gives a positive value

that is always less than or equal to 1. Whether an elastic collision event takes place is determined by comparing P_{el} with a uniformly probable number between 0 and 1 generated by the random number generator, U. The random number is updated for every instance it appears in different equations. If $P_{\text{el}} > U$, then the particle experiences an elastic collision at the given time-step. Once it is determined that the particle experiences an elastic collision, we need to compute the post-collision velocity. The calculation of the velocity involves four steps: (1) transformation of the pre-collision velocity to the center of mass (CM) frame, (2) computation of the CM deflection angle, (3) determination of the CM post-collision velocity, and (4) transformation of the post-collision back to the laboratory (LAB) frame. The transformation between the two frames are provided in Appendix D.2.

Deflection Angle Calculation In applying the MCC method, it is necessary to obtain a functional form of scattering angle χ as functions of the relative energy E_r and the random number U. This can be achieved by finding the differential cross-section, $I = d\sigma/d\Omega$, and then determining the probability that the particle is scattered at χ.

$$P(E_r, \chi) = \frac{\int_0^{\chi} I(E_r, \chi')d\chi'}{\int_0^{2\pi} I(E_r, \chi')d\chi'} \tag{2.28}$$

After solving the integrals in Eq. (2.28), the resulting equation can be manipulated to obtain an expression for χ as functions of E_r and P. In the MCC method, the probability, P, is replaced by U in determining the scattering angles.

While the process of determining χ is relatively simple, it requires a knowledge of the differential cross-section that can be applied for a range of relative energy values. Experimental data for differential cross-section for elastic collisions between electrons and xenon atoms are obtained by many authors [130–134], and these data agree fairly well with theoretical calculations [135, 136] as shown in Fig. 2.5. Figure 2.5 also plots the differential cross-sections for the scattering models [137, 138] applied in many computational models. As seen in Fig. 2.5, the pattern of the differential cross-section varies dramatically as incident energy changes. For this reason, it is difficult to obtain a single curve-fit equation representing the differential

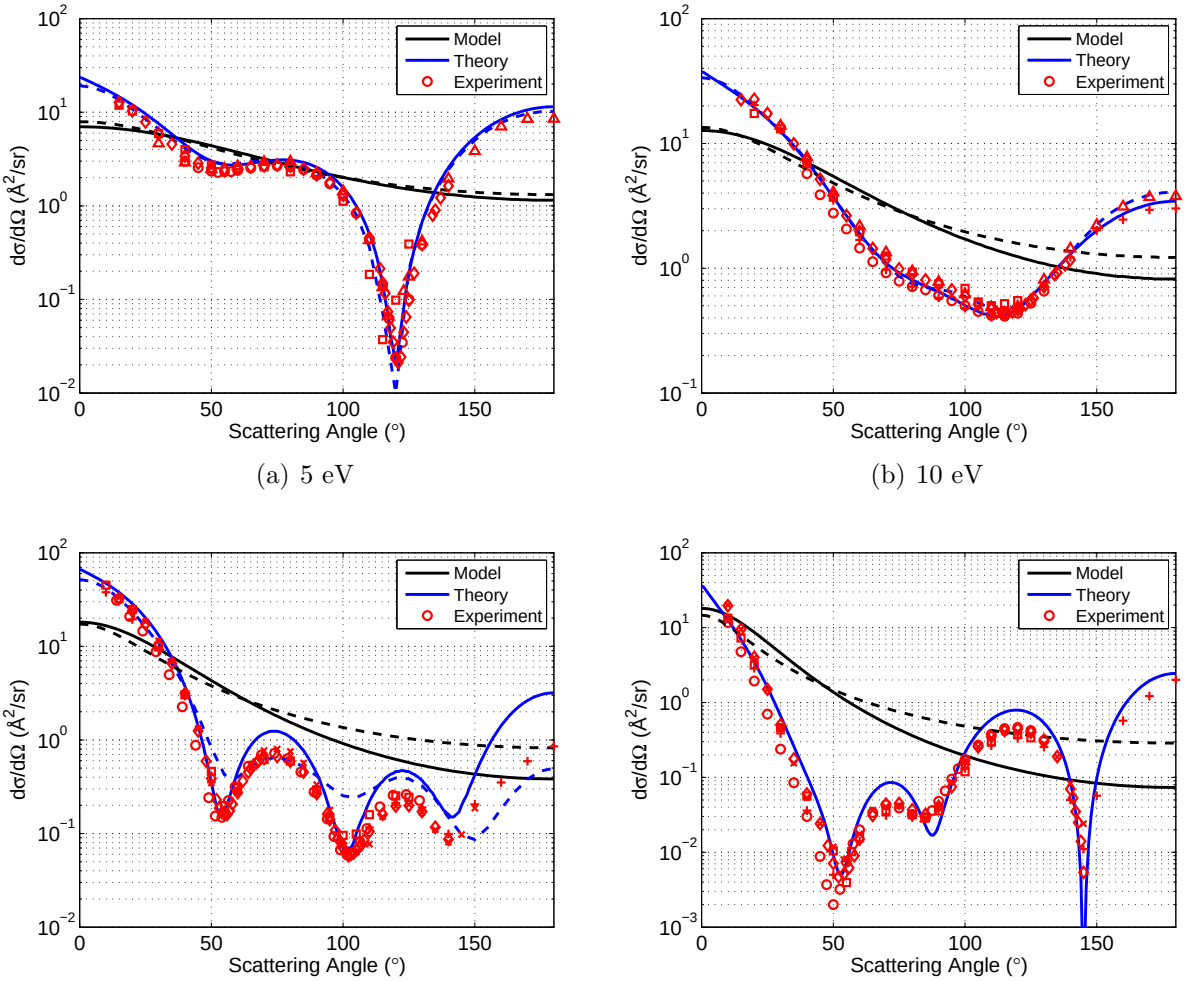

(a) 5 eV

(b) 10 eV

(c) 20 eV

(d) 50 eV

Figure 2.5: Differential cross-sections at different impact energies. Experimental measurements are shown by red markers (○ [130], □ [131], ◊ [132], △ [133], + [134], and × [134]). Blue lines represent the theoretical results (solid [135] and dashed [136]). Black lines represent the models often implemented in computational models (solid [137] and dashed [138]).

cross-section for the range of energy values. The theoretical calculations of the differential cross-section may be implemented to accurately predict the scattering angles. However, it would result in much longer computational run-time as the calculation has to be performed for every incidence of elastic collision.

In the SC model, we use a simple formula derived by Okhrimovskyy et al. [137] for the CM deflection angle calculation. This method is not perfectly accurate as shown in Fig. 2.5 but takes into account that the scattering is more forward-peaked with increasing energy.

More importantly, the determination of the deflection angle is very quick. Approximating the electron-atom interaction potential by the screened Coulomb potential and using the first Born approximation of quantum scattering, Okhrimovskyy et al. derived an expression for the differential cross-section.

$$I(E_r, \chi) = \frac{1}{4\pi} \frac{1 + 8\varepsilon}{(1 + 4\varepsilon - 4\varepsilon \cos\chi)^2} \tag{2.29}$$

where $\varepsilon = E_r/E_0$ is the dimensionless energy and E_0 is the atomic unit of energy ($E_0 = 27.21$ eV). Equation (2.29) is used in Eq. (2.28) to find the probability that an electron is scattered at χ. Finally, a formula for the deflection angle can be derived by replacing P with U and solving for χ.

$$\cos\chi = 1 - \frac{2U}{1 + 8\varepsilon(1 - U)} \tag{2.30}$$

For ion-atom elastic collision, the computational model employs the variable hard sphere (VHS) molecular model [139]. Although the scattering characteristic of the model is not completely realistic, the VHS model has been used in various simulations for rarefied gases at relatively low energies and produced very accurate results. Also, the simple model allows quick calculations of collision mechanics. In this model, the scattering is determined in the same way as the hard sphere model, while the cross section is determined by the following formula given by Dalgarno et al. [140] instead of using the physical cross section.

$$\sigma_i = \frac{64200}{v_r} \text{Å}^2 \tag{2.31}$$

The deflection angle is given as follows

$$\chi = 2\cos^{-1}\sqrt{U} \tag{2.32}$$

Since the scattering is isotropic in the CM frame, the transformation between the CM and LAB frames is not necessary; thus the method requires significantly less operations compared to the other counterpart methods. The IB model described in Chapter 4 implements a more detailed method, which was necessary due to the high energy of incident ions.

Inelastic Collision Inelastic collisions (i.e. ionization, excitation, etc.) between primary electrons and background neutral atoms result in production of other species such as ions and plasma electrons. In a single ionization event, the incident primary electron energy is used to eject the bound electron of the atom. Since the threshold energy for a single ionization collision is 12.13 eV, the primary electron loses an energy corresponding to the threshold energy for every ionization event. Although the primary electron of 25 eV have a sufficient energy to experience two ionization events, we assume for simplicity that the primary electron join the plasma electron population after the event. Thus, every ionization event results in one ion and two plasma electrons. In an excitation event, the kinetic energy of the primary electron is transferred into some internal mode to create an atom in an excited bound state. Similar to the ionization event, we assume that the primary electrons join the plasma electron population after an excitation collision. The equilibration of primary electrons interacting with the plasma electron population by Coulomb collisions is treated similarly to the inelastic collisions. The equilibration rate is much faster after an inelastic collision because of the reduced energy. If this equilibration rate is faster than the rate of inelastic collision, then the assumption of primary electrons joining the plasma electron population after a single inelastic collision would not be too far off from the reality.

In approximating inelastic collisions by the MCC method, a macro-particle current, J, is reduced at every time-step. A current of particles traveling for a given time-step, Δt, through a collection of species densities, n, is given as [141]

$$J(t + \Delta t) = J(t) \exp\left(-\Delta t \sum (Kn)\right) \tag{2.33}$$

where K is the rate constant for different types of inelastic collisions. Effects of all the types of inelastic collisions are included in $\sum (Kn)$ such that

$$\sum (Kn) = n_o \left(K_{\text{iz}} + K_{\text{ex}}\right) + n_s \left(K_{\text{slow}}\right) \tag{2.34}$$

where subscripts *iz*, *ex*, and *slow* denote ionization, excitation, and equilibration processes, respectively. The rate constants, K_{iz} and K_{ex}, are simply calculated by $K = v\sigma$, and K_{slow} is

calculated using Spitzer particle-field slowing time as given in Appendix D.3. The percentage of current lost due to all types of inelastic collisions is then expressed as

$$P_{\text{inel}} = 1 - \exp\left(-\Delta t \sum (Kn)\right) \tag{2.35}$$

The percentage of current lost due to each type of inelastic collision is obtained by the similar equation.

$$\begin{aligned} P_{\text{iz}} &= 1 - \exp\left(-\Delta t (K_{\text{iz}} n_o)\right) \\ P_{\text{ex}} &= 1 - \exp\left(-\Delta t (K_{\text{ex}} n_o)\right) \\ P_{\text{slow}} &= 1 - \exp\left(-\Delta t (K_{\text{slow}} n_s)\right) \end{aligned} \tag{2.36}$$

With these percentages of current lost, the reduction in the primary electron current by each type of inelastic collision can be determined. The reduction in the primary electron current at each time-step is computed by multiplying P_{inel} by the current before the time-step.

$$\Delta J = J(t) P_{\text{inel}} \tag{2.37}$$

The current lost by each inelastic collision at each time-step is then given by

$$\Delta J_{\text{iz}} = \Delta J \frac{P_{\text{iz}}}{\sum P}, \quad \Delta J_{\text{ex}} = \Delta J \frac{P_{\text{ex}}}{\sum P}, \quad \Delta J_{\text{slow}} = \Delta J \frac{P_{\text{slow}}}{\sum P} \tag{2.38}$$

where $\sum P = P_{\text{iz}} + P_{\text{ex}} + P_{\text{slow}}$ is the sum of the percentages of the current lost. The amount of representative current lost for each inelastic collision during the time step is added to the local cell until the end of particle tracking. The total current loss due to the ionization event, $\sum(\Delta J_{\text{iz}})$, is related to the ion generation rate density.

$$\dot{n}_i = \frac{\sum(\Delta J_{\text{iz}})}{e V_{\text{cell}}} \tag{2.39}$$

where V_{cell} is the volume of the cell in which the particle predominantly resides during the

time step. Similarly, the plasma electron generation density of the local cell is given by

$$\dot{n}_e = \frac{\sum(2\Delta J_{\text{iz}} + \Delta J_{\text{ex}} + \Delta J_{\text{slow}})}{eV_{\text{cell}}} \tag{2.40}$$

These generation rate densities are used to determine the currents for macro-particles representing numbers of ions and plasma electrons from the local cells.

2.3.5.2 Collision Cross-Sections

A collision cross-section is an effective area that a given type of collisional reaction occurs and is directly related to a probability of the collisional event. By comparing cross-sections for different reactions, relative importance of the specific collision type can be determined. A collision cross-section depends on the types of particles involved and the relative energy of the collision pair. Therefore, the data for the cross-sections as a function of energy have to be gathered for every type of collision for the specific combination of the collision pair. For electron-atom collisions, we consider three types of collisions: elastic, ionization, and excitation collisions.

Numerous data for these collision cross-sections for the combination of electron and xenon atom have been obtained by previous researchers. Among the cross-section data, we have chosen the relatively recent experimental data as well as the data used the most commonly in other computational models that are applicable for the energy range of interest. The elastic collision cross-section data are obtained by Hayashi [142] and Register et al. [132]. The two data agree fairly well, while we choose to use the more recent data by Hayashi to find the curve-fit equation for the type of collision. The ionization cross-section data are obtained by Hayashi [142], Kobayashi et al. [147], Rejoub et al. [148], and Rapp and Englander-Golden [149]. Although the data obtained by Rapp are the oldest among the four data sets, we use Rapp's data because the data set is the most commonly used in other computational models. The excitation cross-section data are obtained by Hayashi [142, 150], Mason and Newell [151], de Heer et al. [152], Kaur et al. [153], and Ester and Kessler [154]. The excitation cross-section data are sparse in that none of the data sets agrees to each

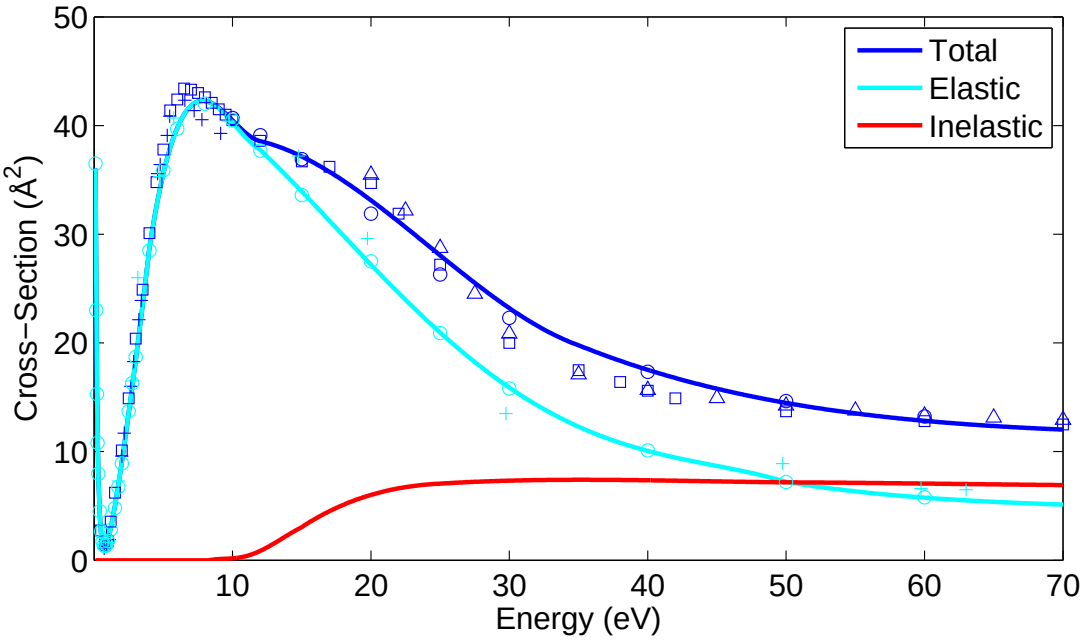

Figure 2.6: Cross-sections for total (○ [142], + [143], □ [144], × [145], and △ [146]), elastic (○ [142] and + [132]), and inelastic collisions. The solid lines represent the curve-fit equations used in the SC model.

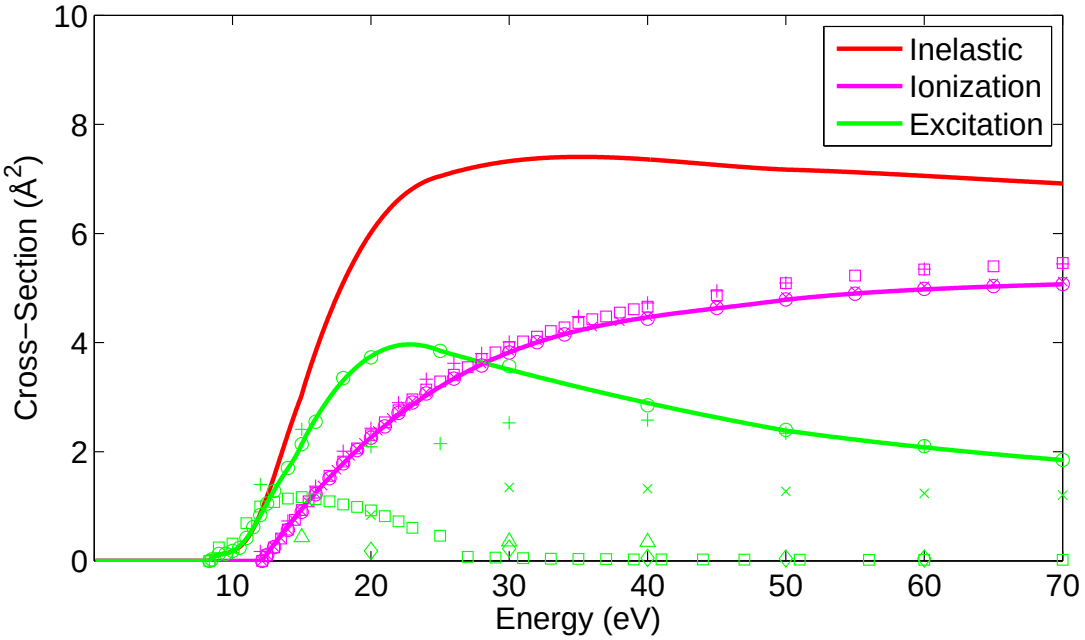

Figure 2.7: Cross-sections for inelastic, ionization (○ [147], + [148], □ [142], and × [149]), and excitation (○ [150], + [142], □ [151], × [152], ◊ [153] and △ [154]) collisions. The solid lines represent the curve-fit equations used in the SC model.

other. We use the data obtained by Hayashi [150] because the sum of cross-sections for all the collision types agreed best with the total cross-section data for the energy of 25 eV when using his excitation cross-section data.

The cross-section data and the curve-fit equations used in the model for different types of collisions are shown in Figs. 2.6 and 2.7. These data sets for total, elastic, inelastic, ionization, and excitation collision cross-sections are fitted with piecewise polynomials of order 3 to 6. These fitting equations are formulated to cover the energy range of 0.1 to 1000 eV while a better fitting is obtained by using smaller segments for the range of energy applicable to our simulation conditions.

2.3.6 Potential Solver

All the charged particles are tracked independently, yielding the charge density distribution in the computational domain. This information is used to update the electric potential, computed by applying the finite volume method to the integral form of Gauss's equation.

$$\oint \mathbf{E} \cdot d\mathbf{S} = \iiint_V \frac{\rho_f}{\varepsilon_0} dV \tag{2.41}$$

where $\mathbf{E}$ is the electric field given as $\mathbf{E} = -\nabla\phi$, $d\mathbf{S}$ is the differential surface vector pointing outward, ρ_f is the free charge density, and ε_0 is the permittivity of free space. Equation (2.41) is solved via control volume formulation for each cell.

$$\oint_{\text{cell}} \mathbf{E} \cdot d\mathbf{S} = -\oint_{\text{cell}} \nabla\phi \cdot d\mathbf{S} = \frac{\rho_f V_{\text{cell}}}{\varepsilon_0} \tag{2.42}$$

The left hand side of Eq. (2.42) is evaluated along the cell edges. The standard way of approximating $\nabla\phi$ is to take a difference equation with the values at the cell of interest and its neighboring cell as described in Sec. 2.3.6.1. For a uniform mesh, this method works very well, and the solution is globally second order accurate. However, when applying the simple method to an adaptive mesh, the accuracy drops locally across coarse/fine grid interfaces. Several researchers have addressed the problem and proposed a method performing

an interpolation to obtain a value inside a coarse cell and applying the difference equation [155–157]. The SC model uses a similar but more general method that can be used even for non-uniform meshes. The method is introduced by Batishchev [158] and applied by Fox [159] in his fully-kinetic PIC model. Details of the method are provided in Sec. 2.3.6.2.

2.3.6.1 First Order Potential Solver

In the first-order accurate method, the electric field across a cell face is approximated using a finite difference equation. Consider the cells shown in Fig. 2.8 where the cell of interest and the cell across the face, i, are denoted by s and n, respectively. Note that the cell vertices are numbered to coincide with the cell face number so that the vertices of the cell face are always i and $i+1$. The electric field across the cell face i is

$$\mathbf{E}_i = -\nabla\phi = -\frac{\phi_n - \phi_s}{\sqrt{(z_n - z_s)^2 + (r_n - r_s)^2}}\hat{i}_{sn} \tag{2.43}$$

where $\hat{i}_{sn}$ is the unit vector from cell center location of cell s to cell n expressed as,

$$\hat{i}_{sn} = \frac{(z_n - z_s)\hat{z} + (r_n - r_s)\hat{r}}{\sqrt{(z_n - z_s)^2 + (r_n - r_s)^2}} \tag{2.44}$$

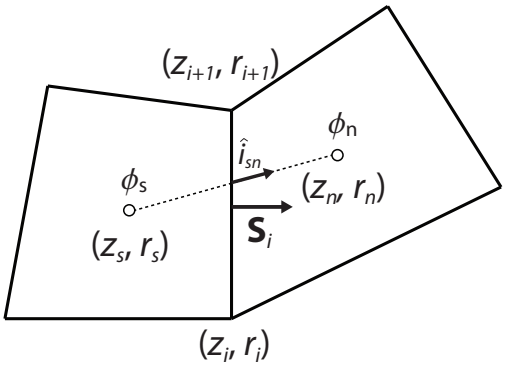

Figure 2.8: Electric flux across the cell face i is determined with the nodal and cell-centered coordinates and cell-centered potential values.

Assuming that $\mathbf{E} = -\nabla\phi$ is constant along the cell face, the flux across the cell face i becomes

$$\int_i \mathbf{E}_i \cdot d\mathbf{S} = \mathbf{E}_i \cdot \int_i d\mathbf{S} = \mathbf{E}_i \cdot \mathbf{S}_i \tag{2.45}$$

where $\mathbf{S}_i$ is the cell face vector pointing outward and is given as $\mathbf{S}_i = \pi(r_i + r_{i+1})(\Delta r\hat{z} - \Delta z\hat{r})$. Here, $\Delta r = r_{i+1} - r_i$, and $\Delta z = z_{i+1} - z_i$. Combining Eqs. (2.43) to (2.45), the flux across the cell face is expressed as,

$$\mathbf{E}_i \cdot \mathbf{S}_i = C_i\phi_s - C_i\phi_n \tag{2.46}$$

where

$$C_i = -\pi(r_i + r_{i+1})\frac{(z_n - z_s)\Delta r - (r_n - r_s)\Delta z}{(z_n - z_s)^2 + (r_n - r_s)^2} \tag{2.47}$$

Every cell has four to eight faces in an adaptive regular mesh, depending on refinement of adjacent cells. Summing the fluxes across all the cell faces, Gauss's law for each cell can be expressed in terms of potentials at the cell of interest and the neighboring cells.

$$\sum_{i=1}^{N_f} \mathbf{E}_i \cdot \mathbf{S}_i = \sum_{i=1}^{N_f} (C_i\phi_s - C_i\phi_{ni}) = \frac{\rho_f V_{\text{cell}}}{\varepsilon_0} \tag{2.48}$$

where N_f is the number of cell faces. For a uniform mesh, this method is globally second order accurate since the Laplacian in Poisson's equation is a second derivative operator, and the finite difference equation to the Laplacian is inherently second order accurate.

2.3.6.2 Second Order Potential Solver

Using the simple method described above, the accuracy drops to first order when the line between two cell-centered locations and the cell face are not orthogonal. This situation arises at coarse/fine grid interface of an adaptive mesh as well as in a non-uniform unstructured mesh. Therefore, a more sophisticated method has to be implemented to retain the second-order accuracy. The second-order method approximates the local variation in ϕ across a cell face with the 2D quadratic equation [159].

$$\phi = \phi_s + a\Delta z_s + b\Delta r_s + c\Delta z_s^2 + d\Delta z_s\Delta r_s + e\Delta r_s^2 \tag{2.49}$$

where $\Delta z_s = z - z_s$, $\Delta r_s = r - r_s$, and a, b, c, d, and e are the coefficients to be solved. Since Eq. (2.49) has five unknown coefficients, determining the coefficients require five independent equations of ϕ; therefore, five different cell-centered points closest to the cell face are chosen in addition to the current element. Let the neighboring cells be donated by 1 to 5, then the linear system of equations can be packed into matrix and vector form.

$$Ax = f \tag{2.50}$$

where

$$A = \begin{bmatrix} \Delta z_{s1} & \Delta r_{s1} & \Delta z_{s1}^2 & \Delta z_{s1} r_{s1} & \Delta r_{s1}^2 \\ \vdots & \vdots & \vdots & \vdots & \vdots \\ \Delta z_{s5} & \Delta r_{s5} & \Delta z_{s5}^2 & \Delta z_{s5} r_{s5} & \Delta r_{s5}^2 \end{bmatrix}, \quad x = \begin{pmatrix} a \\ b \\ c \\ d \\ e \end{pmatrix}, \quad f = \begin{pmatrix} \Delta\phi_{s1} \\ \vdots \\ \Delta\phi_{s5} \end{pmatrix}$$

and $\Delta\phi_s = \phi - \phi_s$. By finding inverse matrix of A, the coefficients can be expressed in terms of potentials of the neighboring cells, $x = A^{-1} f$.

Along a cell face, the line between the two cell nodes (i and $i+1$) is taken to be a straight line. Thus, the relation between z and r is simply

$$r = \alpha z + \beta \qquad z = \frac{r - \beta}{\alpha} \tag{2.51}$$

where

$$\alpha = \frac{r_{i+1} - r_i}{z_{i+1} - z_i} \qquad \beta = r_i - \alpha z_i \tag{2.52}$$

With the quadratic approximation to ϕ given in Eq. (2.49), we can solve Eq. (2.42) for each cell. The electric field $\mathbf{E}$ can be expressed in terms of the coefficients, the position of the cell of interest, and the position along the cell face.

$$\mathbf{E} = -\nabla\phi = -\left(\frac{\partial\phi}{\partial z}\hat{z} + \frac{\partial\phi}{\partial r}\hat{r}\right) \tag{2.53}$$

where

$$\frac{\partial \phi}{\partial z} = a + 2c(z - z_s) + d(r - r_s)$$
$$\frac{\partial \phi}{\partial r} = b + d(z - z_s) + 2e(r - r_s)$$

Also, the differential area along the cell surface is given by $d\mathbf{S} = 2\pi r(dr\hat{z} - dz\hat{r})$. Unlike the case described in Sec. 2.3.6.1, $\mathbf{E}$ across the cell face is not taken to be constant in this method, so the integration along the cell face is done analytically.

$$\begin{aligned}\int \mathbf{E} \cdot d\mathbf{S} &= 2\pi \left[\int -r\frac{\partial \phi}{\partial z} dr + \int r\frac{\partial \phi}{\partial r} dz \right] \\ &= 2\pi \begin{bmatrix} \left(-\frac{2}{3}\frac{a}{\alpha} - \frac{1}{3}d + \frac{2}{3}\frac{e}{\alpha} + \frac{1}{3}\frac{d}{\alpha^2}\right)(r_2^3 - r_1^3) \\ + \left(-\frac{1}{2}a + c(\beta/\alpha + z_s) + \frac{1}{2}dr_s\right)(r_2^2 - r_1^2) \\ + \left(\frac{1}{2}\frac{b}{\alpha} - \frac{e}{\alpha}r_s - \frac{1}{2}\frac{d}{\alpha}(\beta/\alpha + z_s)\right)(r_2^2 - r_1^2) \end{bmatrix}\end{aligned} \tag{2.54}$$

Finally, summing the fluxes across all the cell faces, Gauss's law for each cell can be expressed in terms of potentials at the cell of interest and the neighboring cells.

$$\sum_{i=1}^{N_f} \int_i \mathbf{E}_i \cdot d\mathbf{S}_i = \sum_{i=1}^{N_f} (D_{si}\phi_s + D_{1i}\phi_{1i} + D_{2i}\phi_{2i} + D_{3i}\phi_{3i} + D_{4i}\phi_{4i} + D_{5i}\phi_{5i}) = \frac{\rho_f V_{\text{cell}}}{\varepsilon_0} \tag{2.55}$$

One thing to note is that this method can only applied if matrix A in Eq. (2.50) is non-singular and well-conditioned. For an adaptive regular grid, singularity occurs in a uniform region where all the neighboring cells are the same size as the current element. Whether the matrix A is singular is checked by finding its eigenvalues; if any of the eigenvalue is nearly zero, then A is singular. In addition, A can be ill-conditioned under some specific geometry; this is determined by computing the inverse of the condition number and checking if the value is larger than some tolerance value. If the matrix A is singular or ill-conditioned, the simple method described in Sec. 2.3.6.1 is used instead. Equation (2.54) can also be singular if a cell face is parallel to $\hat{z}$ or $\hat{r}$ as the coefficient α becomes zero or infinity for those cases. This is always true for the regular grid. Instead of using Eq. (2.54), we use the following equations depending on the axis that the cell face is parallel to.

Element face parallel to $\hat{z}$ ($\Delta r = dr = 0$, $r = r_i = r_{i+1}$)

$$\begin{aligned}\int_i \mathbf{E} \cdot d\mathbf{S} &= 2\pi \left[\int_i -r \frac{\partial \phi}{\partial z} \cancel{dr} + \int_i r \frac{\partial \phi}{\partial r} dz \right] \\ &= 2\pi \int_i [b + 2e(r - r_s) + d(z - z_s)] r dz \\ &= 2\pi r \left[(b + 2e(r - r_s) - dz_s)(z_{i+1} - z_i) + \frac{1}{2} d(z_{i+1}^2 - z_i^2) \right] \end{aligned} \tag{2.56}$$

Element face parallel to $\hat{r}$ ($\Delta z = dz = 0$, $z = z_i = z_{i+1}$)

$$\begin{aligned}\int_i \mathbf{E} \cdot d\mathbf{S} &= 2\pi \left[\int_i -r \frac{\partial \phi}{\partial z} dr + \int_i r \frac{\partial \phi}{\partial r} \cancel{dz} \right] \\ &= -2\pi \int_i [a + 2c(z - z_s) + d(r - r_s)] r dr \\ &= -2\pi \left[(a + 2c(z - z_s) - dr_s) \frac{1}{2} (r_{i+1}^2 - r_i^2) + \frac{1}{3} d(r_{i+1}^3 - r_i^3) \right] \end{aligned} \tag{2.57}$$

2.3.6.3 Solving Linear System of Equations

After setting up the equations for all the cells, the linear system of equations may be written in matrix form,

$$My = g \tag{2.58}$$

where the components of M are the coefficients of ϕ, y is an array of ϕ values at all the cell-centers, and g is an array consisting of the boundary potentials and space charges. Equation (2.58) is solved using the Parallel Direct Sparse Solver (PARDISO) built in Intel Math Kernel Library (MKL). PARDISO requires that nonzero components of M are stored using the compressed sparse row format. This format uses three separate arrays that contain all the nonzero components of M and indices that locate corresponding column and row numbers in the matrix.

2.3.7 Electric Field Solver for Non-Uniform Mesh

An accurate computation of electric field is necessary in calculating an accurate particle trajectory since the electric field is directly proportional to the force acting on a particle. Once electric potential is computed at the grid points using the method described above, the electric field is calculated by solving $\mathbf{E} = -\nabla\phi$. The electric field is solely dependent on the gradient of potential; therefore, the computation of electric field is analogous to finding a slope ($\mathbf{E}$) on a surface described by potential values stored on the grid.

In an orthogonal mesh, the gradient operator can be approximated using a three-point finite difference equation.

$$E_s = -\frac{\partial\phi}{\partial s} = -\left(C_{i+1}\phi_{i+1} + C_i\phi_i + C_{i-1}\phi_{i-1}\right) \tag{2.59}$$

where s is the coordinate (r or z for cylindrical coordinate system) and C is the coefficient given by,

$$\begin{aligned} C_{i+1} &= \frac{\Delta s_{i-1/2}}{\Delta s_{i+1/2}(\Delta s_{i-1/2} + \Delta s_{i+1/2})} \\ C_i &= \frac{\Delta s_{i+1/2} - \Delta s_{i-1/2}}{\Delta s_{i+1/2}\Delta s_{i-1/2}} \\ C_{i-1} &= \frac{-\Delta s_{i+1/2}}{\Delta s_{i-1/2}(\Delta s_{i-1/2} + \Delta s_{i+1/2})} \end{aligned} \tag{2.60}$$

Here, $\Delta s_{i+1/2} = s_{i+1} - s_i$ and $\Delta s_{i-1/2} = s_i - s_{i-1}$. Note that Eq. (2.59) reduces to the central difference equation if the mesh is uniformly spaced ($\Delta s_{i+1/2} = \Delta s_{i-1/2}$). It can be shown that Eq. (2.59) gives the second order accurate solution for the orthogonal mesh. In the case with a non-orthogonal mesh, Eq. (2.59) becomes first order accurate as the error depends on both Δz and Δr. Therefore, Eq. (2.59) cannot be applied to an adaptive mesh where the cell-centers are not aligned with axes at the grid interface.

2.3.7.1 First Order Electric Field Solver

In determining electric field, Fox [159] first used the incomplete 2D quadratic equation in his fully-kinetic PIC model. For non-adaptive quadrilateral mesh, there are four cells adjacent to the current cell. The complete 2D quadratic equation given in Eq. (2.49) has five coefficients, requiring five independent equations to determine the coefficients. For this reason, he was forced to use a slightly less accurate representation.

$$\phi = \phi_s + a\Delta z_s + b\Delta r_s + c\Delta z_s^2 + e\Delta r_s^2 \tag{2.61}$$

Then, the electric field can be computed by taking a gradient once the coefficients are obtained. Unfortunately, this method did not produce accurate results as the spline matrix A becomes ill-conditioned under some conditions, resulting in inaccurate solution of the coefficients.

The method he ultimately used utilizes the 2D linear equation which is only first order accurate. The 2D linear equation is given by

$$\phi = \phi_s + a\Delta z_s + b\Delta r_s \tag{2.62}$$

By taking a gradient of Eq. (2.62), the z- and r-components of the electric field simply depends on the two coefficients, a_s and b_s.

$$E_z = \frac{\partial \phi}{\partial z} = -a, \quad E_r = \frac{\partial \phi}{\partial r} = -b \tag{2.63}$$

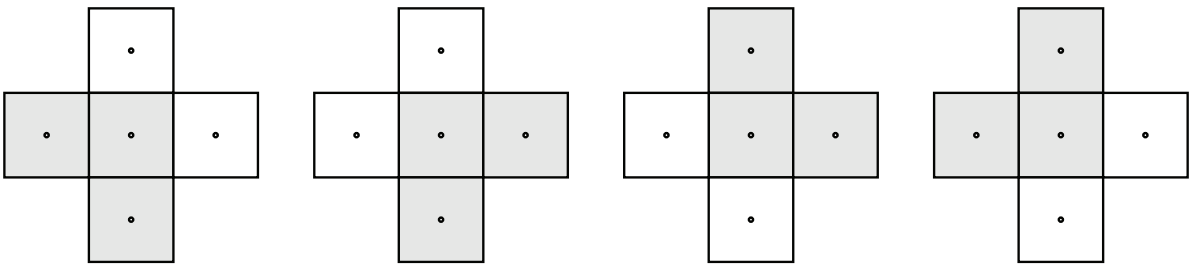

Figure 2.9: Four combinations of cells are used to determine the electric field when using the 2D linear equation.

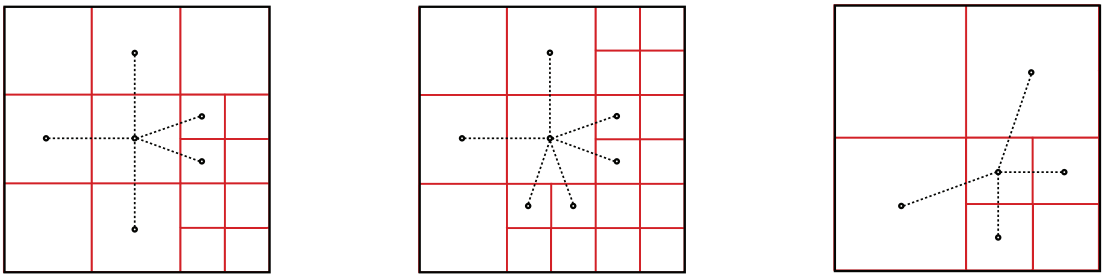

Figure 2.10: Examples of cell combinations used in the first order electric field calculation.

In determining the coefficients in Eq. (2.62), two neighboring cells have to be chosen while there are total of four neighboring cells. The unique approach he made was to compute the electric field with four different combinations of the neighboring cells and simply take the average. The four combinations of points are shown in Fig. 2.9. This method can easily be extended to an adaptive mesh. In an adaptive regular mesh, the number of neighboring cells varies from four to eight, depending on the refinement of the neighboring cells as illustrated in Fig. 2.10. Since we use the second-order accurate method in the potential calculation, the electric field calculation is required to be second-order accurate in order to maintain the overall order of accuracy. Therefore, the first order method is not used in the SC model, while it is used to compare with the second-order method in Sec. 2.4.3.

2.3.7.2 Second Order Electric Field Solver

In determining the electric potential at the grid points, six cells including the current cell are appropriately chosen for each cell face to determine the coefficients for the 2D quadratic equation. A combination of cells is easily chosen since, in most of the cases, there are six cells touching a cell face. The electric field calculation method described here uses the same 2D quadratic equation as the one used for potential calculation, providing the second order accurate solution.

$$\phi = \phi_s + a\Delta z_s + b\Delta r_s + c\Delta z_s^2 + d\Delta z_s \Delta r_s + e\Delta r_s^2 \tag{2.49}$$

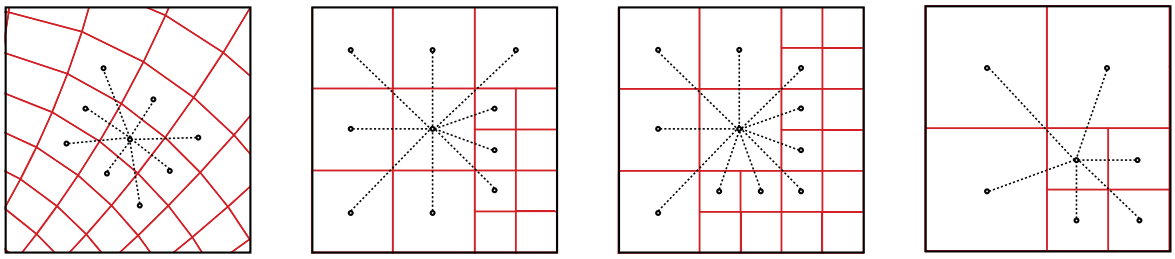

Figure 2.11: Examples of cell combinations used in the second-order electric field calculation.

In contrast to the potential calculation, the local variation of potential is determined within a cell instead of across a cell face. Around the cell of interest, the number of neighboring cells (cells with one or two common nodes) can vary between 6 and 12 as shown in Fig. 2.11, which is always larger than the number of coefficients for the 2D quadratic equation. Therefore, we use the least squares approach, in which, the best fitted 2D quadratic potential surface through all the neighboring cells and current cell is determined. In this approach, the same equation can be applied for any number of cells greater than the number of coefficients. Once the coefficients are obtained by the least squares method, the electric field is determined by

$$E_z = -\frac{\partial \phi}{\partial z} = -\left[a + 2c(z - z_s) + d(r - r_s)\right] \tag{2.64}$$

$$E_r = -\frac{\partial \phi}{\partial r} = -\left[b + d(z - z_s) + 2e(r - r_s)\right] \tag{2.65}$$

There are a unique set of coefficients for each cell, and Eqs. (2.64) and (2.65) can be used to determine electric field at any point within the cell. If the coefficients for all the cells are stored, then we can compute the electric field at any point within the domain. This is useful in obtaining the electric field value at a particle position at any time step.

Formulation The least squares approach best approximates the local variation of the electric potential by minimizing the squares of deviation from the computed potential values. The error of the quadratic equation at cell k is expressed as

$$R_k = \phi_s + a\Delta z_{sk} + b\Delta r_{sk} + c\Delta z_{sk}^2 + d\Delta z_{sk}\Delta r_{sk} + e\Delta r_{sk}^2 - \phi_k \tag{2.66}$$

where $\Delta z_{sk} = z_k - z_s$ and $\Delta r_{sk} = r_k - r_s$. Then, the square of the error over N neighboring cells is,

$$R^2 = \sum_k^N R_k^2 = \sum_k^N \left[\phi_s + a\Delta z_{sk} + b\Delta r_{sk} + b\Delta z_{sk}^2 + d\Delta z_{sk}\Delta r_{sk} + e\Delta r_{sk}^2 - \phi_k\right]^2 \tag{2.67}$$

The error of the quadratic equation through all the cells is minimized when the partial derivatives of Eq. (2.67) with respect to the coefficients are all zero.

$$\frac{\partial R^2}{\partial a} = 0, \quad \frac{\partial R^2}{\partial b} = 0, \quad \frac{\partial R^2}{\partial c} = 0, \quad \frac{\partial R^2}{\partial d} = 0, \quad \frac{\partial R^2}{\partial e} = 0 \tag{2.68}$$

The five equations from Eq. (2.68) can be expressed in matrix/vector form, and the coefficients can be computed by solving the linear system of equations.

Alternatively, the matrix from Eq. (2.68) can be directly derived from the overdetermined linear system of equations. For N number of cells, the linear system of equations becomes

$$Ax = f \tag{2.69}$$

where

$$A = \begin{bmatrix} \Delta z_{s1} & \Delta r_{s1} & \Delta z_{s1}^2 & \Delta z_{s1} r_{s1} & \Delta r_{s1}^2 \\ \vdots & \vdots & \vdots & \vdots & \vdots \\ \Delta z_{sN} & \Delta r_{sN} & \Delta z_{sN}^2 & \Delta z_{sN} r_{sN} & \Delta r_{sN}^2 \end{bmatrix}, \quad x = \begin{pmatrix} a \\ b \\ c \\ d \\ e \end{pmatrix}, \quad f = \begin{pmatrix} \Delta\phi_{s1} \\ \vdots \\ \Delta\phi_{sN} \end{pmatrix}$$

Here A is a 5-by-N matrix, and x is an array containing the coefficients for the 2D quadratic equation, f is an array containing $\Delta\phi = \phi_s - \phi_k$ where $k = 1, ..., N$. A unique solution for the coefficients in an array x can be determined by multiplying both sides by the transpose of matrix A from the left and finding the inverse of $A^T A$.

$$x = [A^T A]^{-1} A^T f \tag{2.70}$$

Instead of applying Eq. (2.70) directly, the least squares problem is solved using the routine, *gels*, available in Intel MKL.

Boundary Conditions for Electric Field The upstream, side wall, and downstream plates of the cylindrical domain are either grounded or biased at fixed potential. Therefore, the electric field along any electrode should always be zero. In addition, the radial component of the electric field along the axis of symmetry is zero because of the symmetry. These boundary conditions for the electric field is shown in Fig. 2.12. Although the potential is input accordingly for the boundary cells, the boundary condition for the electric field is not always satisfied by the least squares approach. In other words, the potential surface described by the 2D quadratic equation does not necessarily go through the potential values at the boundaries when the least squares method is used. In order to increase the accuracy near the boundaries, the 2D quadratic equation is refined to ensure that the boundary conditions are satisfied. Along the axis of symmetry, the expression for the radial component of the electric field is given as

$$E_r|_{r=0} = -\{b + d(z - z_s) - 2er_s\} = 0 \tag{2.71}$$

Since Eq. (2.71) has to be satisfied for any value of z along the axis, d has to be zero. Then, Eq. (2.71) reduces to $-b + 2er_s = 0$. Along the electrodes, similar approach can be used to obtain additional constraints for the coefficients of the 2D quadratic equation. These equations are summarized in Table 2.1.

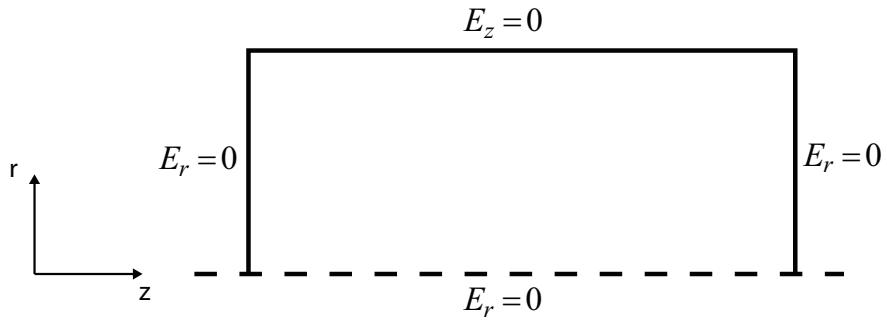

Figure 2.12: Boundary conditions for electric field.

Table 2.1: Constraint equations for the 2D quadratic equation to enforce the boundary conditions for electric field.

Boundary	Constraints for Coefficients
Axis of symmetry, $r = 0$	$d = 0$, $-b + 2er_s = 0$
Upstream end, $z = 0$	$e = 0$, $b - dz_s = 0$
Downstream end, $z = z_b$	$e = 0$, $b + d(z_b - z_s) = 0$
Side wall of cylindrical domain, $r = r_b$	$c = 0$, $a + d(r_b - r_s) = 0$

2.3.8 Mixing and Smoothing

Due to the structure of the SC model, charged species at thermal velocity (i.e. ions and plasma electrons) overly respond to the small potential well resulted from a slight imbalance of the positive and negative charges. For example, if there is a potential well that exceeds the energy of ions, all the ions created near the region stays in the well while the plasma electrons are quickly repelled from the region. This brings up the electric potential significantly higher than a realistic value. In the next iteration, the potential peak then attracts the electrons and repel the ions, again resulting in a large well. The alternation of the potential structure continues, and the potential never converges to a final solution. In order to mitigate this effect, the SC model mixes the computed species densities for the current iteration with the values in the previous iterations. Let the subscripts *in* and *out* denote the species densities used to compute the electric potential and obtained directly after the particle tracking routines at iteration k, respectively. The species density used to compute the potential for the next iteration is determined by

$$n_{in}^{k+1} = (1 - \xi) \sum_{j=k-N_k}^{k} n_{in}^{j} + \xi \sum_{j=k-N_k}^{k} n_{out}^{j} \tag{2.72}$$

where ξ is the mixing factor and N_k is the number of previous iterations to mix. Also, the change in the density from the previous iteration is limited to be within an order of magnitude such that $n_{out}^{k} = \min(n_{out}^{k*},\ 10\ n_{in}^{k-1})$ where the superscript $*$ denotes the raw output value from the particle tracking.

The mixing technique smooths the behavior of the solution in the iteration space. On the other hand, the smoothing technique reduces the statistical fluctuations in the physical space at each iteration. Smoothing is done by mixing the charge densities of nearby cells while keeping the total number of particles the same. Since the cell volumes are constant in the axial direction in a uniform mesh, a simple binomial filter function can be applied.

$$\begin{aligned}
\rho_0^{k+1} &= \frac{3}{4}\rho_0^k + \frac{1}{4}\rho_1^k \\
\rho_i^{k+1} &= \frac{1}{4}\rho_{i-1}^k + \frac{1}{2}\rho_i^k + \frac{1}{4}\rho_{i+1}^k, \quad 0 < i < N_z \\
\rho_{N_z}^{k+1} &= \frac{1}{4}\rho_{N_z-1}^k + \frac{3}{4}\rho_{N_z}^k
\end{aligned} \tag{2.73}$$

where ρ is the charge density, i is the cell index in the axial direction, and N_z is the number of cells along the z-axis. Note that Eq. (2.73) is the smoothing for the cell-centered quantity so that the smoothing for the node-centered quantities is slightly different. In the radial direction, the coefficients need to be derived by considering the variation in cell volume [160].

$$\begin{aligned}
\rho_0^{k+1} &= (1-\alpha_0)\rho_0^k + \alpha_0\rho_1^k \\
\rho_j^{k+1} &= \alpha_j\rho_{j-1}^k + (1-2\alpha_j)\rho_j^k + \alpha_j\rho_{j+1}^k, \quad 0 < j < N_r \\
\rho_{N_r}^{k+1} &= \alpha_{N_r}\rho_{N_r-1}^k + (1-\alpha_{N_r})\rho_{N_r}^k
\end{aligned} \tag{2.74}$$

where

$$\alpha_0 = \frac{1}{4},\ \alpha_1 = \frac{\alpha_0 V_0}{V_1},\ \alpha_j = \frac{2\alpha_{j-1}V_{j-1}}{V_j} - \frac{\alpha_{j-2}V_{j-2}}{V_j},\ \alpha_{N_r} = \frac{\alpha_{N_r-1}V_{N_r-1}}{V_{N_r}} \tag{2.75}$$

Here, i is the cell index in the radial direction and N_r is the number of cells along the radius. For the node-centered quantities, α_0 is replaced with $\frac{1}{2}$. Therefore, for an interior cell, the charge density is mixed with values at the cell of interest and eight surrounding cells with coefficients as in Eq. (2.76)

$$\begin{bmatrix} \alpha_j \\ 1-2\alpha_j \\ \alpha_j \end{bmatrix} \begin{bmatrix} \frac{1}{4} & \frac{1}{2} & \frac{1}{4} \end{bmatrix} = \begin{bmatrix} \frac{1}{4}\alpha_j & \frac{1}{2}\alpha_j & \frac{1}{4}\alpha_j \\ \frac{1}{4}(1-2\alpha_j) & \frac{1}{2}(1-2\alpha_j) & \frac{1}{4}(1-2\alpha_j) \\ \frac{1}{4}\alpha_j & \frac{1}{2}\alpha_j & \frac{1}{4}\alpha_j \end{bmatrix} \tag{2.76}$$

Packing all the coefficients and charge densities for all the cells in the vector-matrix form, a single pass smoothing is done by applying $P^1 = AP^0$ where P is the array containing all the ρs and A is the matrix containing the coefficients for all the cells. This can be extended for multiple passes by

$$P^k = A^M P^0 \tag{2.77}$$

where M is the number of passes. A^M can be precomputed before the main program. While the technique reduces the number of completely unrealistic trajectories of charged species due to the unphysical potential wells and peaks, it may mask the important characteristic in the plasma structure. Therefore, the degree of mixing is reduced by decreasing M as reaching the final solution.

2.3.9 Convergence

Convergence of the solution is determined by the change in the electric potential and species densities between the iterations. Two different vector norms are used for the convergence criteria: the 2-norm and the maximum norm. The 2-norm provides information on how much the potential structure has changed from the previous iteration.

$$||\delta\phi||_2 = \sqrt{\sum_i^N \frac{(\phi_i^{k+1} - \phi_i^k)}{\phi_i^{k+1}}} \tag{2.78}$$

where i denotes the cell number, N is the number of cells, and k is the iteration step. On the other hand, the maximum norm tells the percentage change in the maximum potential value.

$$||\delta\phi||_\infty = \max_i \left\{ \frac{(\phi_i^{k+1} - \phi_i^k)}{\phi_i^{k+1}} \right\} \tag{2.79}$$

Similar norms can be obtained for species densities. When these norms are smaller than some tolerance, ϵ, specified as an input, then the solution is considered to be converged.

2.4 Component Level Validations

2.4.1 Particle Weighting in Cylindrical Coordinates

2.4.1.1 Numerical Assessment of Density Errors

Density errors arising from the cell-centered weighting algorithm are computed for different radial density profiles in an adaptive regular mesh and a unstructured mesh as shown in Fig. 2.13. The adaptive regular grid allows for testing of mixed quadrilateral and triangle node elements at the coarse/fine grid interface. The unstructured mesh contains quadrilateral node elements that are shaped differently throughout the test domain. Three different radial density profiles are used to investigate their effects to the density errors: 1) uniform, 2) linearly decreasing, and 3) Bessel function. For the case of a uniform density, the computed density profile should be exact if the corrected volume formulas are applied properly. The Bessel function profile is chosen since this can physically arise in glow discharges; the solution can be obtained by solving the diffusion equation ($-D_{\perp}\nabla^2 n = \beta n$) in cylindrical coordinates [161]. The functional form of the exact density profiles are given in Table 2.2. In the test program, radial positions of the macro-particles are determined by finding the radius that satisfy the equations provided in Table 2.2 for a given random number, U, between 0 and 1. Then, macro-particles are advanced in a direction perpendicular to the downstream end. At every time-step, fraction of particles that a macro-particle represents is distributed to three to four vertices of a node element in which the particle is located. The particles weighted to the vertices are determined from Eqs. (2.13) and (2.18) to (2.21), depending on the element shape, and these particles are accumulated at cell centroids until the end of the particle tracking. Again, the particles distributed to the boundary cells are re-assigned to the nearest interior cells. Finally, the particle density at a cell is computed by dividing the particles assigned to each cell centroid by the corrected cell volume. For all the test cases, computational results are obtained with $1,000,000$ macro-particles and $2,000$ time-steps before reaching the downstream end.

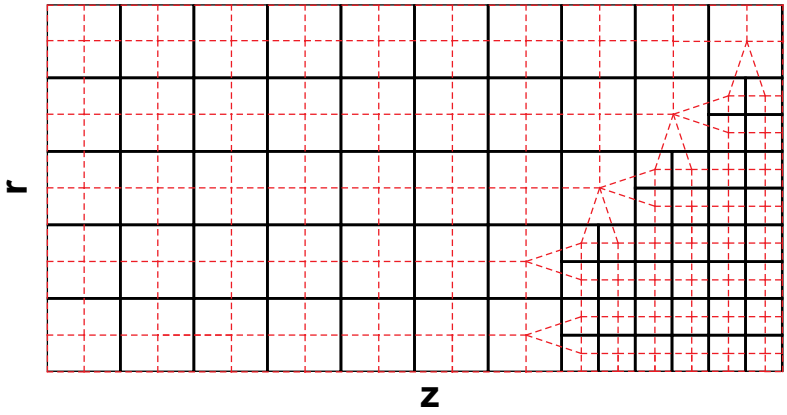

(a) Adaptive regular mesh

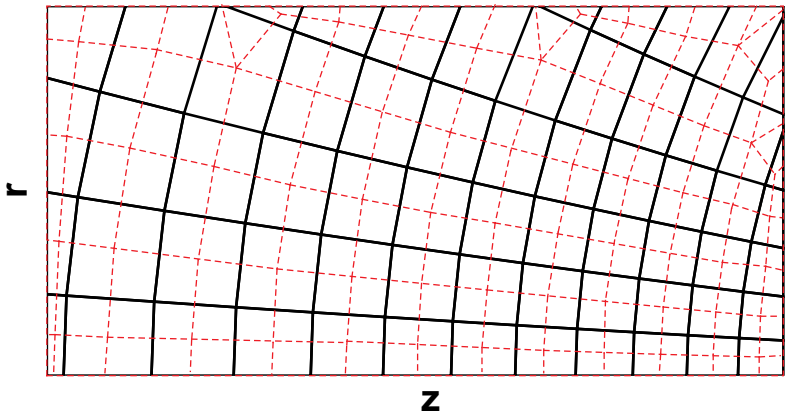

(b) Unstructured mesh

Figure 2.13: Two meshes used in the numerical test for particle weighting algorithm. The solid line corresponds to cell boundaries, and the dashed line corresponds to node element boundaries.

Table 2.2: Equations for exact solution and particle injection position for different density profiles examined. Here, n_0 is the centerline density, R is the normalized radius ($R = r/r_{max}$), U is the random number between 0 and 1, J_0 is the zeroth-order Bessel function of the first kind, and k_1 is the first root of J_0.

Density profile	Exact solution	Particle injection
Uniform	$n(R) = n_0$	$U = R^2$
Linear	$n(R) = n_0(1 - R)$	$U = 3R^2 - 2R^3$
Bessel	$n(R) = n_0 J_0(k_1 R)$	$U = RJ_1(k_1 R)/J_1(k_1)$

Adaptive regular mesh Figures 2.14 to 2.16 show the relative error for uniform, linearly decreasing, and Bessel function density profiles, respectively, when using the standard area weighting and the generalized weighting scheme in an adaptive regular mesh. In Fig. 2.14(a), the errors at top and bottom cells apart from the grid interface are 9.3×10^{-3} and 8.3×10^{-2}, respectively. These errors are consistent with the results provided in Ref. [129] for one dimensional radial grid; the errors can be derived analytically by using nearest-grid-point weighting between boundary cells and the neighboring interior cells. At the grid interface, the error becomes more severe, reaching a value of 0.47. As shown in Fig. 2.14(b) for the case of uniform density profile, all of these systematic errors are removed by using the generalized weighting scheme. The systematic errors at the top and bottom cells are eliminated completely, and the densities at cells along the grid interface almost perfectly match the expected values with errors of less than 3.3×10^{-6}, thus showing that the cell-centered weighting algorithm has been implemented properly. Using the standard area weighting for the cases with non-uniform density profiles (Figs. 2.15(a) and 2.16(a)), the errors along the grid interface are still dominant. These errors are reduced significantly when the generalized weighting scheme is used (Figs. 2.15(b) and 2.16(b)). Although the errors in outermost interior cells have slightly increased, it is insignificant compared to the reduction in errors at the grid interface. Furthermore, Figs. 2.15(b) and 2.16(b) clearly show the reduction in density errors in the region of a finer grid size; thus, the benefit of using the adaptive regular mesh can be realized.

Unstructured mesh Figures 2.17 to 2.19 show the relative error for uniform, linearly decreasing, and Bessel function density profiles, respectively, when using the two weighting algorithm in a non-uniform mesh. As shown in Fig. 2.17, density errors are, again, reduced drastically when using the generalized weighting scheme, and the density profile is almost exactly uniform. For all the density profiles with the standard weighting scheme (Figs. 2.17(a), 2.18(a) and 2.19(a)), the distribution of the density error is comparable. The errors are generally smaller away from the boundary, and very large errors are seen in the triangular cells and quadrilateral cells with large aspect ratio that touch the boundaries. The maxi-

mum density errors are 1.4, 3.9, and 4.0 for uniform, linearly decreasing, and Bessel function density profiles, respectively. One of the primary reasons for the large errors are the poor smoothness of the grid; the change in cell size is very large from those cells to the neighboring cells. When connecting the cell centroids, the midpoint of the line does not lie sufficiently close to the cell edge. This indicates that the effective cell shape is significantly different from the actual shape for those cells near boundaries. The large errors at those cells can be alleviated by using a mesh that covers, in addition to the domain, a region outside the domain. In this way, the cell centroid locations are not affected by the domain boundaries. To apply the generalized weighting scheme, the limits in the corrected volume calculation, Eq. (2.24), have to be modified to exclude the region outside the domain. The modifications to the boundary treatment have not implemented herein since it is beyond the scope of this paper. Another primary reason for the large errors is the non-uniform profile of density, as indicated by increased errors at cells touching the boundary with $R = 1$ (or $r = r_{max}$). When using the area weighting, the region where the particle is distributed to a cell centroid is larger than the actual cell area. If the density value is greater at a neighboring cell, a larger number of particles are weighted to the cell of interest. This is the main reason that density errors at the cells touching the boundary with $R = 1$ persist even when using the generalized weighting scheme, while the errors at all the cells near both ends are corrected and become comparable to the neighboring cells (Figs. 2.18(b) and 2.19(b)). Note that the density profile is uniform in axial direction for all cases. A further discussion for the density errors near the boundary at $R = 1$ are provided in Sec. 2.4.1.2. In spite of the relatively larger density errors, the maximum errors for generalized weighting scheme are reduced significantly, by more than 50%.

2.4.1.2 Effect of Near-Boundary Density Error in Potential Solution

A further analysis for the Bessel function density profile has been conducted in order to examine the effect of the grid size and the relatively large errors near the boundary to electric potential solution. In this analysis, the electric potential is computed on a uniform radial grid with number of interior cells of $N = 5$, 10, 20, and 40. Given the density profile provided

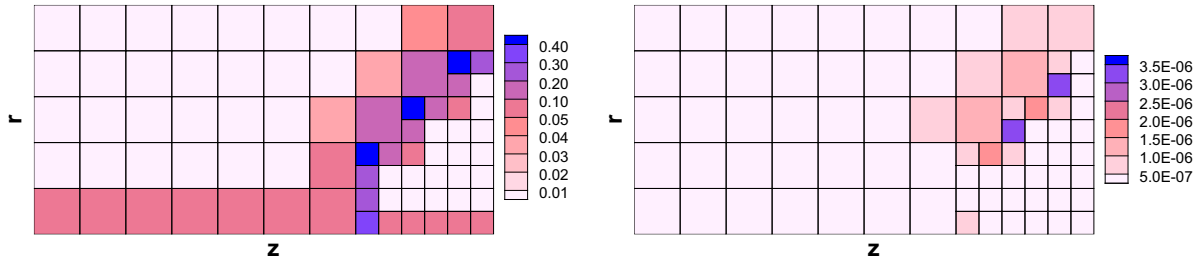

(a) Standard weighting scheme (b) Generalized weighting scheme

Figure 2.14: Relative error in density computed for uniform density profile in an adaptive regular mesh.

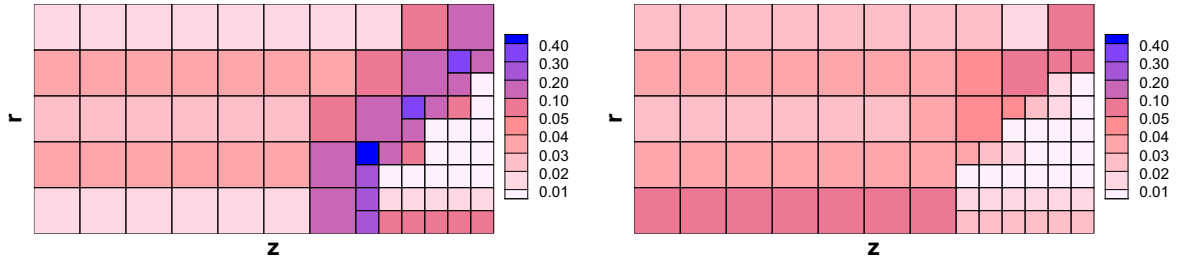

(a) Standard weighting scheme (b) Generalized weighting scheme

Figure 2.15: Relative error in density computed for linearly decreasing density profile in an adaptive regular mesh.

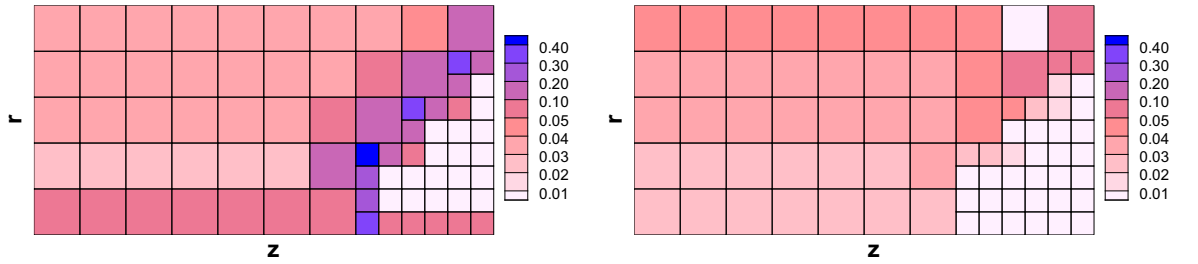

(a) Standard weighting scheme (b) Generalized weighting scheme

Figure 2.16: Relative error in density computed for Bessel function density profile in an adaptive regular mesh.

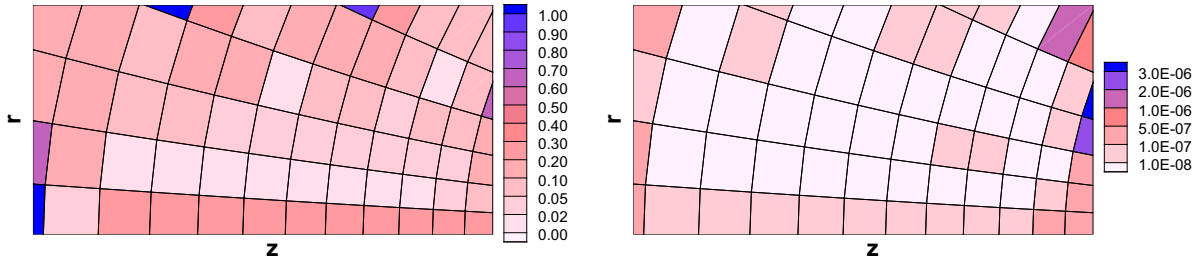

(a) Standard weighting scheme (b) Generalized weighting scheme

Figure 2.17: Relative error in density computed for uniform density profile in a non-uniform mesh.

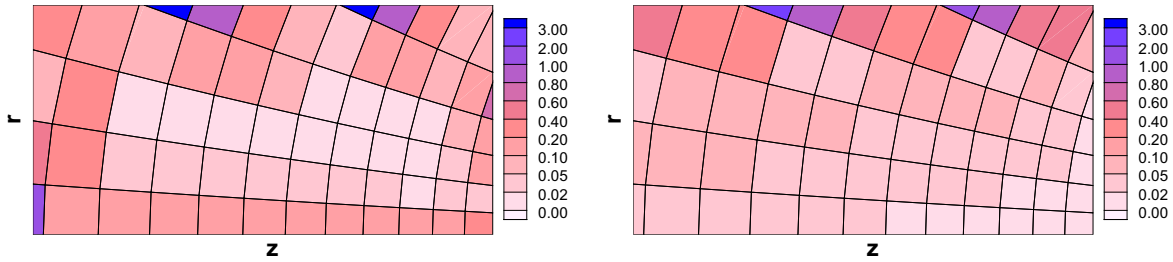

(a) Standard weighting scheme (b) Generalized weighting scheme

Figure 2.18: Relative error in density computed for linearly decreasing density profile in a non-uniform mesh.

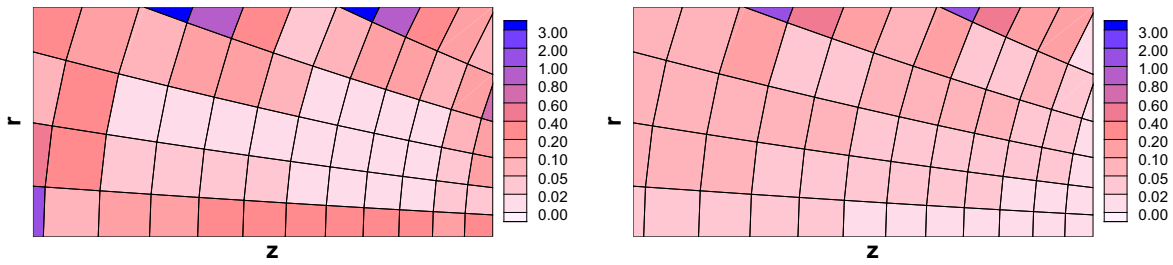

(a) Standard weighting scheme (b) Generalized weighting scheme

Figure 2.19: Relative error in density computed for Bessel function density profile in a non-uniform mesh.

in Table 2.2, the exact solution for potential can be solved analytically.

$$\phi(R) = \phi_0 J_0(k_1 R) \tag{2.80}$$

where ϕ_0 is the potential at the centerline. Note that both Eq. (2.80) and the density profile given in Table 2.2 are simply a function of the zeroth-order Bessel function of the first kind and that the normalized profiles are identical. Macro-particles distributed properly along the radius are weighted to cell centroids using the same weighting algorithm described in Sec. 2.3.4; the particles are distributed to the cell-centroids, then the particles distributed to the boundary cells are re-assigned to the nearest interior cells. Once the particle densities at the cells are determined, the finite volume method is used to compute the potential at the cells. Neumann ($\frac{\partial \phi}{\partial r} = 0$) and Dirichlet ($\phi = 0$) boundary conditions are applied at $R = 0$ and $R = 1$, respectively. Finally, the computed electric potential is compared with the exact solution.

Figure 2.20 shows the normalized density profile obtained from the analytical solution given in Table 2.2 and computed for four different mesh sizes. Although it is difficult to see the degree of accuracy, it is readily seen that the computed density agrees, to the first order, with the exact solution for all the meshes. Figure 2.21 plots the relative error along the radial grid. Note that the relative error for the case of $N = 5$ is consistent with the coarse mesh region in Fig. 2.16(b). For all the meshes, the error is the minimum for the innermost cell. This is expected since the density profile is closest to uniform, and the corrected volume is derived for the uniform density profile. With the increasing radius, the error monotonically increases, reaching the maximum error at the outermost cell. The density error away from the boundary at $R = 1$ is proportional to the square of the cell size (the second order accuracy), while the maximum error value located at the outermost appears to increase with finer mesh, as shown in Figs. 2.21 and 2.23. The increasing error with radius can be explained by the monotonically decreasing density profile. For the density profile, the area weighting results in a larger number of particles to be weighted to cell centroids from location below when compared to nearest-grid-point weighting, and less particles from location above. For

interior cells, particle distribution from below and above the cell centroid can cancel out to some degree. For the outermost cell, the number of weighted particles is always greater when compared to the nearest-grid-point weighting. Furthermore, since the density is the minimum at the outermost cell, the relative error is sensitive to the inaccuracy of weighting, causing an apparent inflation of the error by orders of magnitude. Although the density errors at outermost cells persist with smaller grid size, the potential solution converges with grid size and is the second order accurate, as shown in Figs. 2.22 and 2.23. At the outermost cell, the relative error is large; however, the magnitude of the density is small, so the density in the cell has only a small effect to the solution in electric potential.

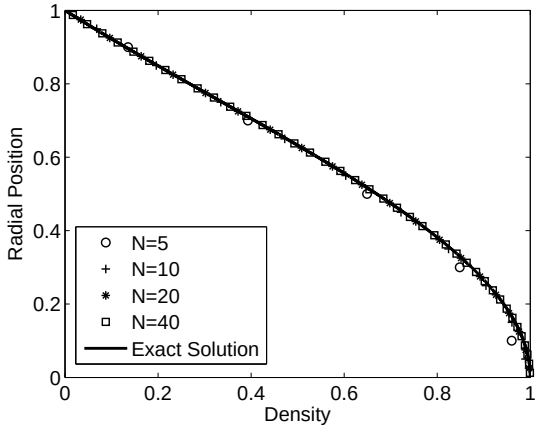

Figure 2.20: Normalized density profile

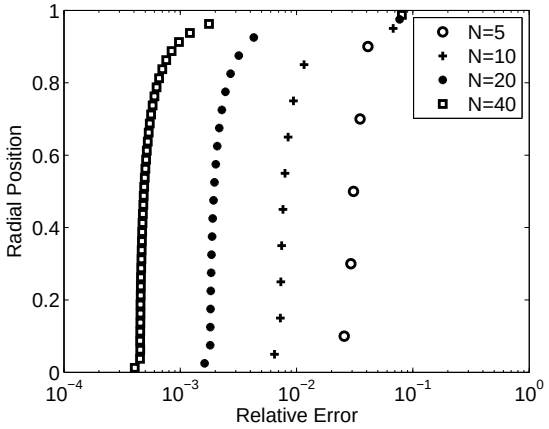

Figure 2.21: Relative error in density

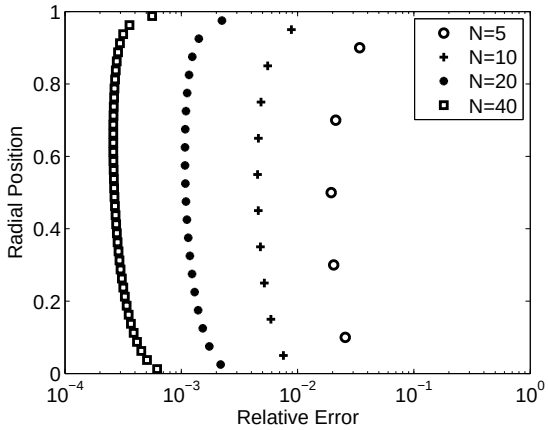

Figure 2.22: Relative error in potential solution

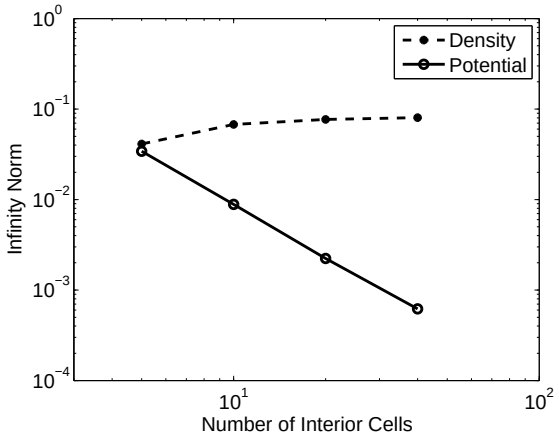

Figure 2.23: Infinity norm for density and potential solutions

2.4.2 Potential Calculation

A numerical test on the potential solver described in Sec. 2.3.6.2 has been performed to check the implementation and to show the second-order accuracy. The standard method described in Sec. 2.3.6.1 is also implemented for comparison. In this test, electric potential is calculated on a cylindrical domain with the end wall biased at 100 V and the other walls grounded (0 V). The solutions computed with the two methods are compared with an analytical solution obtained by solving the Laplace equation in cylindrical coordinates.

$$\nabla^2\phi(r,\theta,z) = \frac{1}{r}\frac{\partial\phi}{\partial r} + \frac{\partial^2\phi}{\partial r^2} + \frac{1}{r^2}\frac{\partial\phi}{\partial\theta} + \frac{\partial^2\phi}{\partial z^2} = 0 \tag{2.81}$$

The general solutions for the Laplace equation is obtained by applying separation of variable [162].

$$\begin{aligned}\phi(r,\theta,z) = \sum_{m=0}^{\infty}\sum_{n=1}^{\infty} &[A_{mn}J_m(k_nr) + B_{mn}Y_m(k_nr)] \\ &\times [C_{mn}\sin(m\theta) + D_{mn}\cos(m\theta)]\,[E_{mn}\sinh(k_nz) + F_{mn}\cosh(k_nz)]\end{aligned} \tag{2.82}$$

or

$$\begin{aligned}\phi(r,\theta,z) = \sum_{m=0}^{\infty}\sum_{n=1}^{\infty} &[A_{mn}I_m(k_nr) + B_{mn}K_m(k_nr)] \\ &\times [C_{mn}\sin(m\theta) + D_{mn}\cos(m\theta)]\,[E_{mn}\sin(k_nz) + F_{mn}\cos(k_nz)]\end{aligned} \tag{2.83}$$

where A, B, C, D, E, and F are some constants, J_m and Y_m are the mth order Bessel function of first and second kind, I_m and K_m are the mth order modified Bessel function of first and second kind, k_n is constant, and m and n are integers. In this specific problem, we use Eq. (2.82) to find the analytical solution. In Eq. (2.82), m has to be 0 to satisfy axisymmetric condition, and a few terms can be eliminated based on the boundary conditons. Then, Eq. (2.82) is simplified as

$$\phi(r,z) = \sum_{n=1}^{\infty} G_n \sinh(k_nz) J_0(k_nr) \tag{2.84}$$

where G_n are constants, k_n is determined by setting $J_0(k_na) = 0$ which corresponds to k_na=2.4048, 5.5201, 8.6537, $\cdots$, and a is the radius of the domain. G_n can be determined

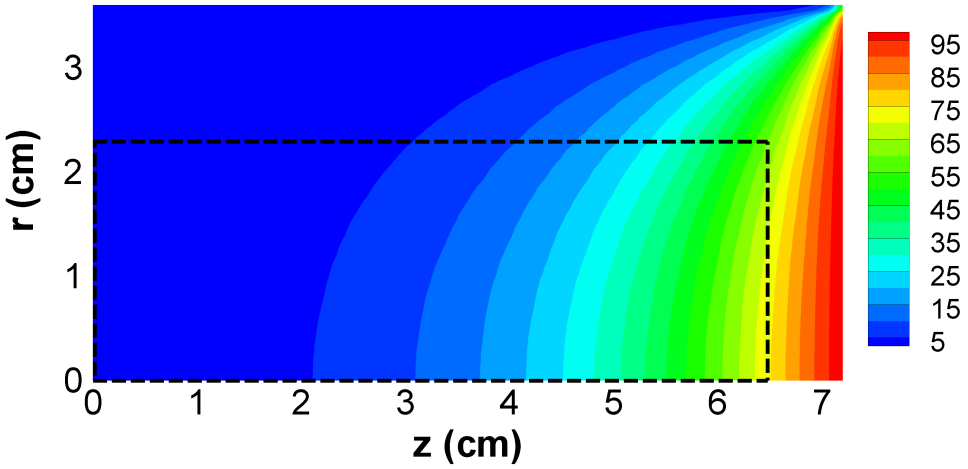

Figure 2.24: Contour plot of potential (V) calculated with the analytical solution for the case with a cylindrical domain with end plate biased at 100 V. The solutions are compared for the cells inside the dashed box.

using orthogonal property of J_0 and sinh functions.

$$G_n = \frac{2V_0}{k_n a J_1(k_n a)\sinh(k_n L)} \tag{2.85}$$

The analytical solution given in Eq. (2.84) involves infinite sum of sinh J_0. For this numerical test, 1000 terms are added; the number of terms is determined so that the solution is computed reasonably accurately within an acceptable amount of time. A plot of potential contour for the test problem is shown in Fig. 2.24. Even with the number of terms used to compute the solution, the lower accuracy at the circumference of the end plate is inevitable because of the sudden change of the boundary condition from the end plate to the cylinder wall. Therefore, the solutions are only compared within the dashed box shown in Fig. 2.24.

Figures 2.25 and 2.26 show the relative errors for the solutions computed by the first-order and the second-order methods in a non-uniform mesh. The first-order method produces relatively larger errors at the cells near the coarse/fine grid interface when compared to errors in the uniform region. This is expected since the method becomes second order in a uniform mesh. These errors at the grid interface are removed when using the second-order method as seen in Fig. 2.26. Figure 2.27 shows the change in the maximum relative error for three different grid resolutions. By finding the slope of the lines, the order of convergence can be

determined. As seen in Fig. 2.27, the standard method provides a second-order accurate solution when using a uniform mesh. However, the order of accuracy drops by one order for an adaptive mesh. The accuracy is recovered when using the spline method for the same mesh.

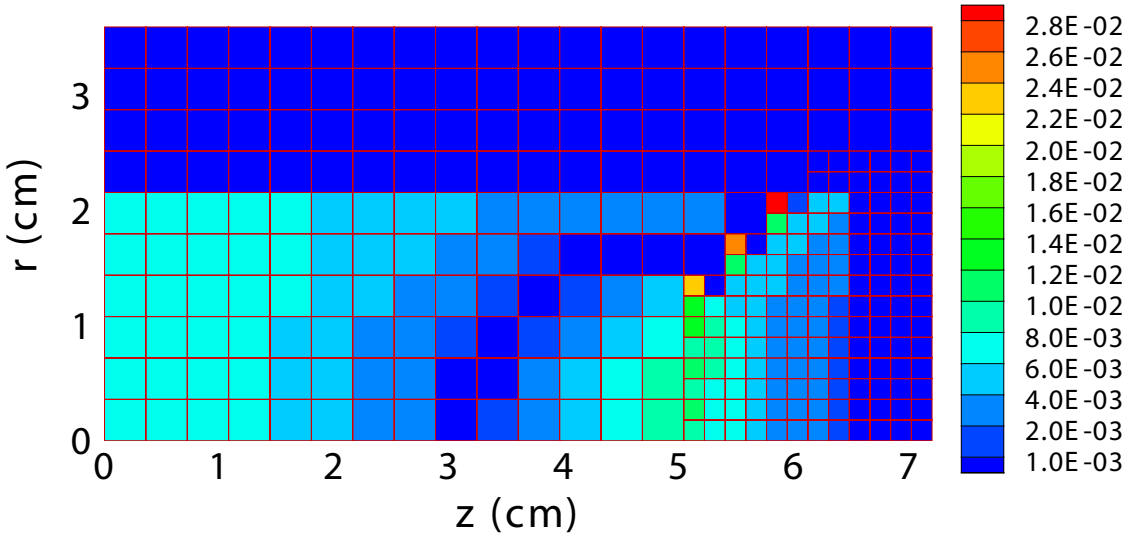

Figure 2.25: Plot of relative error in electric field solution using the first order method.

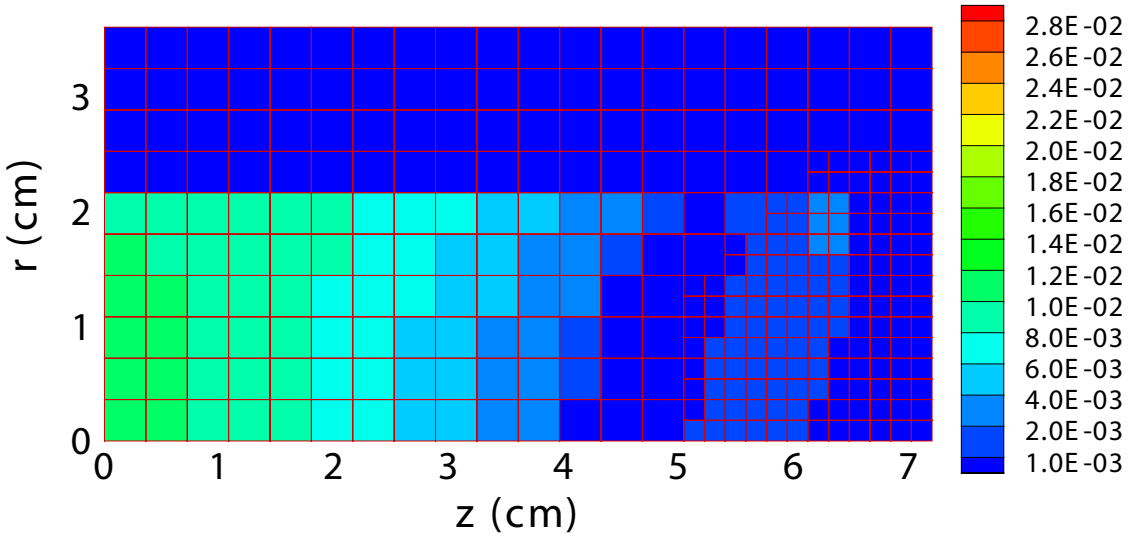

Figure 2.26: Plot of relative error in electric field solution using the least squares approach.

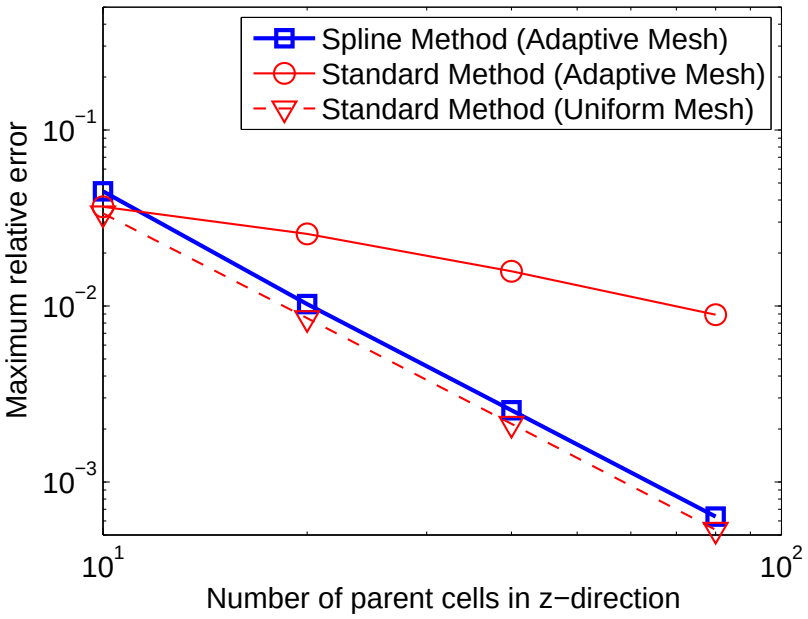

Figure 2.27: Convergence of potential solutions computed with the first- and second-order methods in an adaptive regular mesh.

2.4.3 Electric Field Calculation

The same test condition studied in Sec. 2.4.2 is used for the numerical test of electric field calculation. The analytical solution for the electric field can be computed by simply taking the gradient of ϕ given in Eq. (2.84).

$$E_r(r,\theta,z) = \sum_{n=1}^{\infty} k_n G_n \sinh(k_n z) J_1(k_n r) \tag{2.86}$$

$$E_z(r,\theta,z) = -\sum_{n=1}^{\infty} k_n G_n \cosh(k_n z) J_0(k_n r) \tag{2.87}$$

where J_1 is the first order Bessel function of the first kind. In this test, the potential obtained from Eq. (2.84) is used to compute the electric field with Fox's first-order method [159] described in Sec. 2.3.7.1 and the least squares (second-order) method described in Sec. 2.3.7.2.

Similar to the test result for potential described in Sec. 2.4.2, the errors from the first-order method are greater at the coarse/fine grid interface compared to uniform grid region as shown in Fig. 2.28. These errors are removed when using the least squares approach as shown

in Fig. 2.29. Figure 2.30 shows the convergence of the electric field solutions. By comparing the slope, it is clearly seen that the difference in the order of accuracy obtained from Fox's method and least squares method in an adaptive mesh. Although the Fox's method provides the second-order accurate solution in a uniform mesh, the order of accuracy drops to first-order when using the adaptive mesh, and the accuracy is recovered to second-order when using the least squares method. Furthermore, examining Fig. 2.28, less errors are found in the region of finer grid, thus the benefit of the adaptive mesh has been demonstrated.

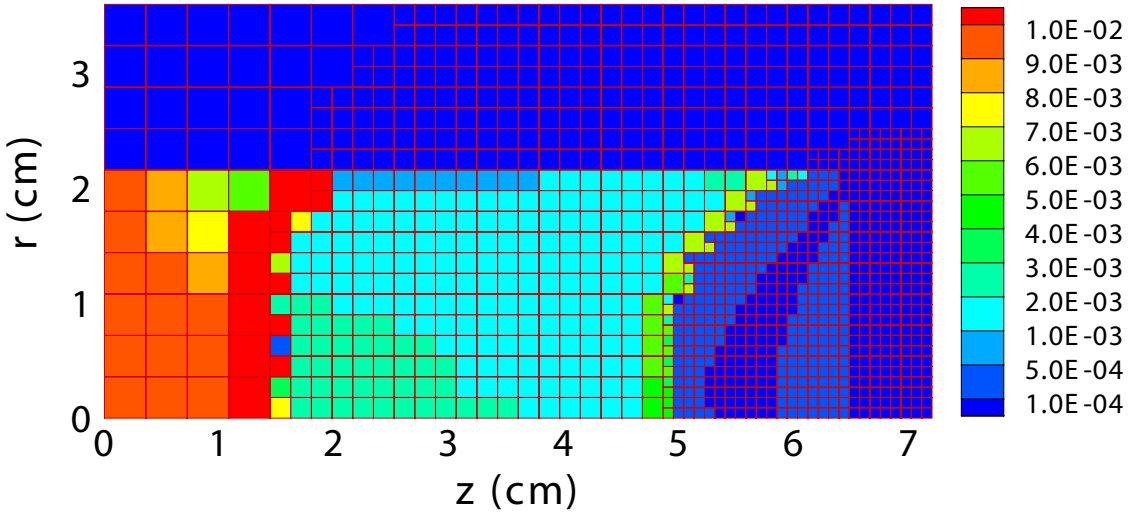

Figure 2.28: Plot of relative error in potential solution using the standard method.

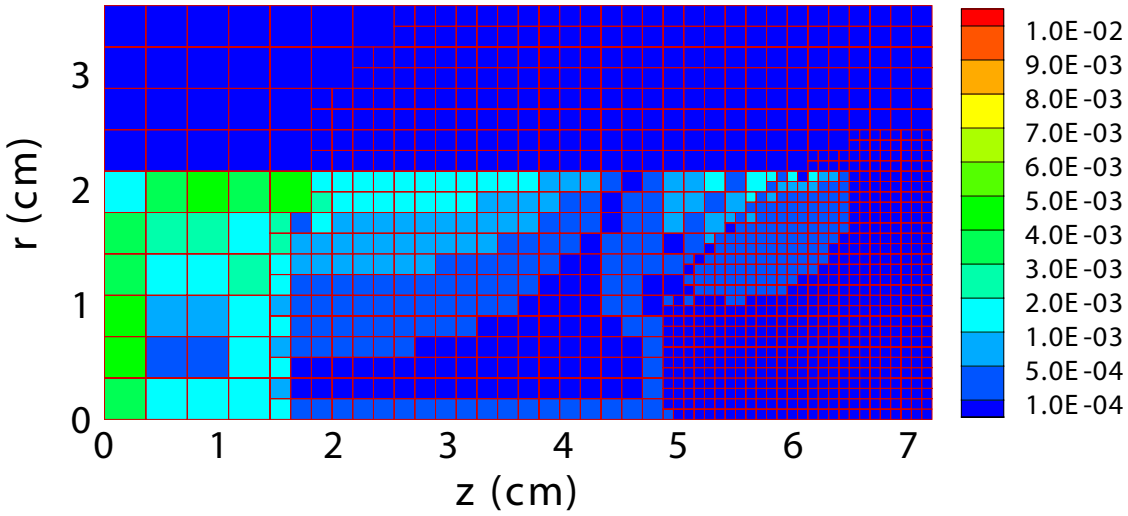

Figure 2.29: Plot of relative error in potential solution using the spline method.

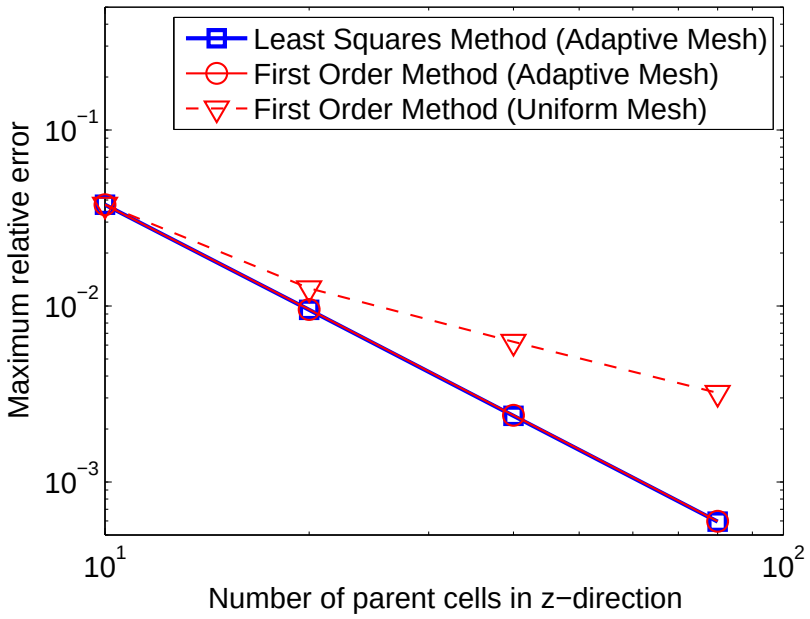

Figure 2.30: Convergence of electric field solutions computed with Fox's method and the least squares approach in an adaptive regular mesh.

2.5 Simulation Results

The SC model is used to simulate a variety of plasmas with increasing complexity of the system. The simulation starts from an electron plasma that contains only the primary electrons in a magnetic field created by a single cylindrical permanent magnet (Sec. 2.5.1). An electron flood gun is used as the source of the nearly mono-energetic primary electrons. This simulation is mainly to validate important components of the computational model, most critically the electron tracker and magnetic field calculations. Then, the neutral gas is introduced in the system, yielding a sparse plasma with four different species: primary electrons, ions, plasma electrons, and neutral atoms (Sec. 2.5.2). Here, the sparse plasma refers to a plasma with very low density such that the Debye length is comparable to the plasma volume. Multiple block magnets are used in addition to the cylindrical magnet to increase the primary electron confinement. In the ring-cusp configuration, the sparse plasma as a whole is simulated to study the loss behavior of plasma species (Sec. 2.5.2.1). Then, the confinement is improved by adding another ring-cusp; a close-up study of the primary electrons was necessary to obtain a comparable result with the experiment. While

the electron gun was used in the simulations for the primary electron confinement and the sparse plasma due to its well-known gun characteristic, the gun was later replaced with a hollow cathode to achieve a higher ionization rate and a plasma condition that is more applicable to ion thrusters (Sec. 2.5.3).

2.5.1 Primary Electron Confinement

The simulation using the SC model starts from an examination of the 25 eV primary electron structure near the cusp in the absence of other species, mainly to validate important components of the computational model. As shown in the primary electron trajectories (black lines in Fig. 2.31), the primary electrons are ejected from the left along the axis of the discharge domain, toward the cylindrical magnet placed downstream, at a divergence angle of 10–15° and a beam radius of 0.5 mm. Initially, the electrons are effectively not magnetized, and their trajectories are approximately straight until the magnetic field strength becomes sufficiently strong. Then, the electrons start to gyrate about the field lines and their gyroradii become smaller as the magnetic field becomes stronger toward the magnet, with increasing likelihood of magnet mirroring as they approach the cusp. Figure 2.32 compares the wire scan results obtained from the experiment [163] and the computational model at the locations shown in Fig. 2.31. These results show a good quantitative and qualitative agreement, indicating that the particle tracking technique and the magnetic field calculations are fairly accurate. One of the causes of the slight disagreement is likely the misalignment of the magnet and electron gun axes during the experiment, as seen in the asymmetric scan profile obtained during the experiment. Another reason for the disagreement is that the distance from the magnet can only be obtained within certain accuracy in the experiment, and the uncertainty is comparable with the step-size of position for the wire scan.

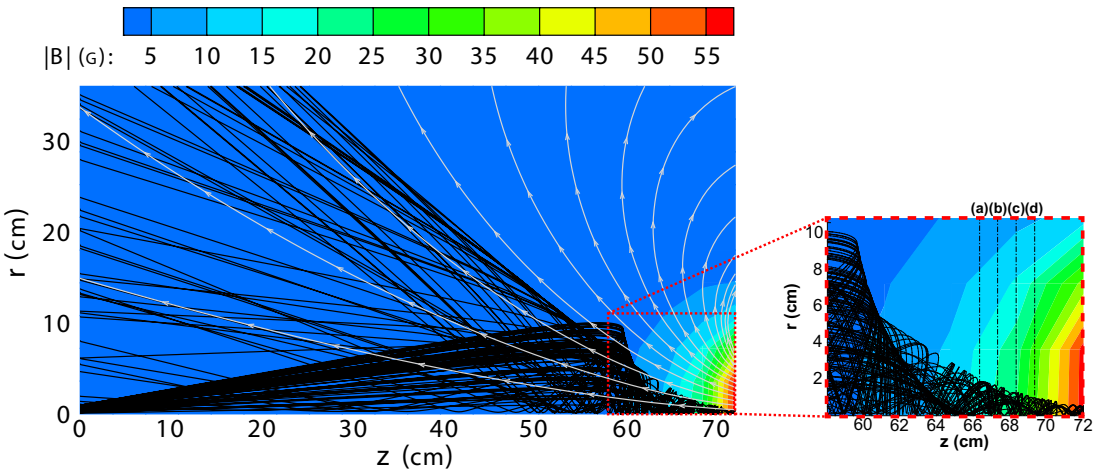

Figure 2.31: Primary electron trajectories (black lines) in 2D. The white lines represent the magnetic field lines. The dash-dot lines represent the wire scan locations.

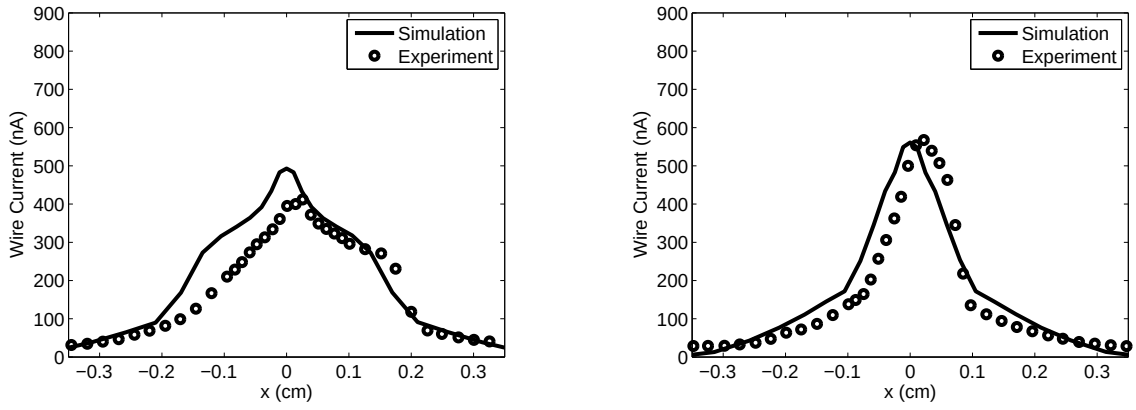

(a) 1.05 cm

(b) 0.95 cm

(c) 0.85 cm

(d) 0.75 cm

Figure 2.32: Comparison of wire scan results from the simulation and the experiment. The distances from the magnet surface to the wire scan locations are given in the sub-figure captions.

2.5.2 Sparse Plasma

2.5.2.1 Structure and Leak Mechanism of Sparse Plasma

The confinement of the primary electrons is not sufficient to cause enough ionization by simply introducing a neutral gas in the single cusp configuration. In addition, the other plasma species such as ions and plasma electrons are lost to the walls too quickly and are not maintained in the domain. For this reason, multiple block magnets are placed around the circumference of the test cell and the electron gun to increase the confinement. A schematic of the experiment simulated by the SC model is shown in Fig. 2.33. The detailed description of the experimental apparatus is provided in Ref. [163]. The plasma is obtained by shooting the 25 eV primary electron beam of 50 μA into the test cell at the base pressure of 5×10^{-8} Torr and at the xenon gas pressure of 1×10^{-3} Torr. The electron gun is placed upstream of the test cell in order to account for its limit in the neutral pressure. The dimension of the test cell is 4 cm in length and 1.78 cm in radius. Since the mean free path of the ionization collision is $\lesssim$ 1.0 m, the primary electrons need to experience a number of reflection at magnetic cusps before ionizing the neutral atom. While the other plasma species are generated by

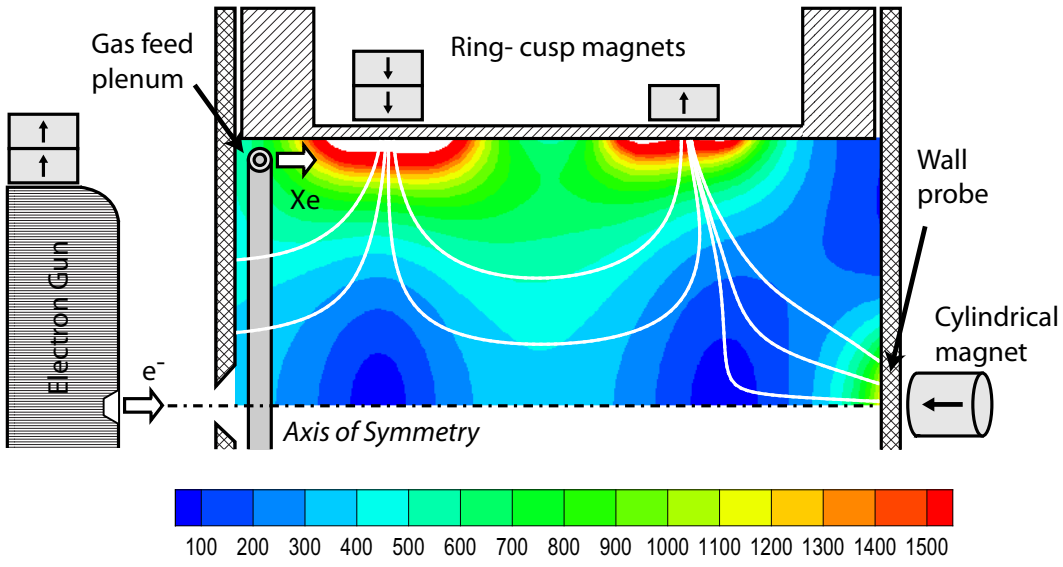

Figure 2.33: Schematic of the discharge experiment for a sparse plasma. The contour plot of magnetic field strength (Gauss) is shown inside the test cell. The white lines represent magnetic field lines. The SC model is used to simulate the same domain.

the inelastic collisions, the achievable plasma density remains low due to the low primary electron current. The electron density is on the order of $10^{12} to 10^{14}$ m^{-3}. Here, we call our plasma a sparse plasma, in which the Debye length is comparable to the plasma volume such that the plasma is not quasi-neutral.

Figures 2.34 and 2.35 show the experimental results for the current densities in front of the cylindrical magnet at the base pressure and at the pressure of 1×10^{-3} Torr. The white "$\times$" and dotted circle indicate the center and edge of the cylindrical magnet face, respectively. It is readily noticeable that the current densities are not peaked at the center of the magnet. This is due to the difficulty in perfectly aligning the electron gun with the magnet center. At the scale of the species loss, even 1 mm of the misalignment can have a significant impact on the loss pattern. At the base pressure, distinct ridges are present in the results, whereas the ridges are slightly smoothed out when introducing the xenon gas. On the other hand, the ion current density contour does not exhibit the ridge structure. The cause of these loss patterns will be explored in Sec. 2.5.2.2.

A simulation of the experiment is carried out by the SC model. In this simulation, it is assumed that 300 K xenon atoms are filled uniformly within the domain. The plasma electron temperature is assumed to be 3 eV. Figure 2.36 shows the electric potential computed by the SC model. All the electrodes are grounded, so the Dirichlet boundary condition of $\phi = 0$ are applied in the simulation. The highest potential value is seen close to the center of the cylindrical domain while the potential drops rapidly towards the boundaries. This potential structure pushes ions toward the walls. Figure 2.37 shows the contour plot of primary electrons. The density is relatively higher at the single magnetic cusp. By design, the stronger magnetic field strength at the ring-cusps reflect the electrons, while a larger number of electrons reach the downstream electrode because of the relatively weaker field at that surface. The contours for ion and plasma electron generation rate density are similar to the primary density contour; thus, the vast majority of ions and plasma electrons are created very near the cusp for plasma condition created by the electron gun. The ion and plasma electron density contours are shown in Figs. 2.38 and 2.39. While the ion density is peaked near the magnetic cusp, the plasma electron density is higher in the two regions of

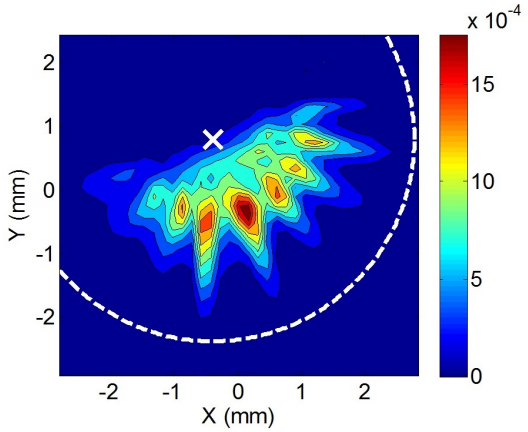

Figure 2.34: Contour plot of the electron current density measured during the experiment at base pressure of 5×10^{-8} Torr.

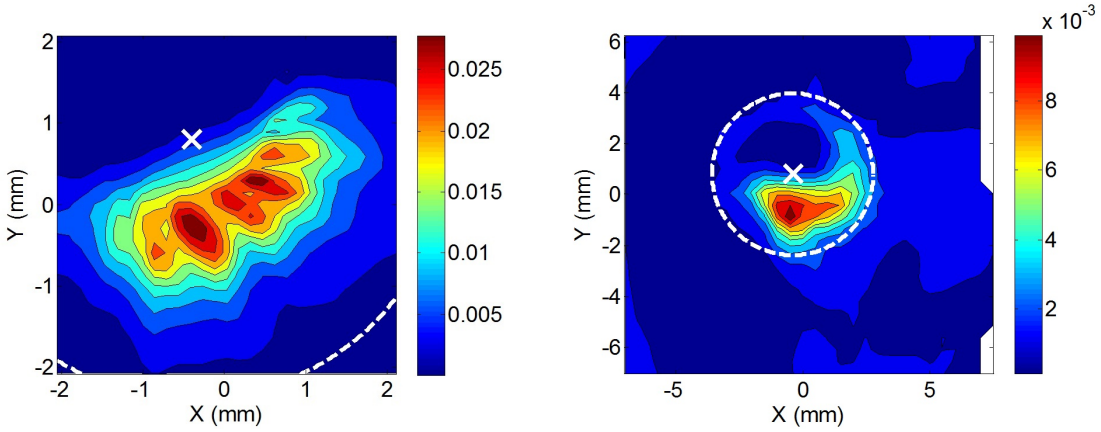

(a) Electrons (b) Ions

Figure 2.35: Contour plot of the current densities measured during the experiment at pressure of 1×10^{-3} Torr.

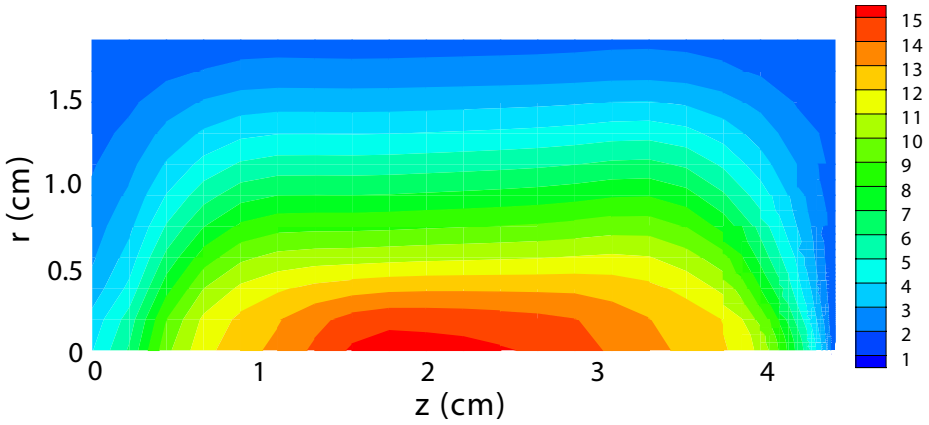

Figure 2.36: Electric potential (V) calculated by the SC model.

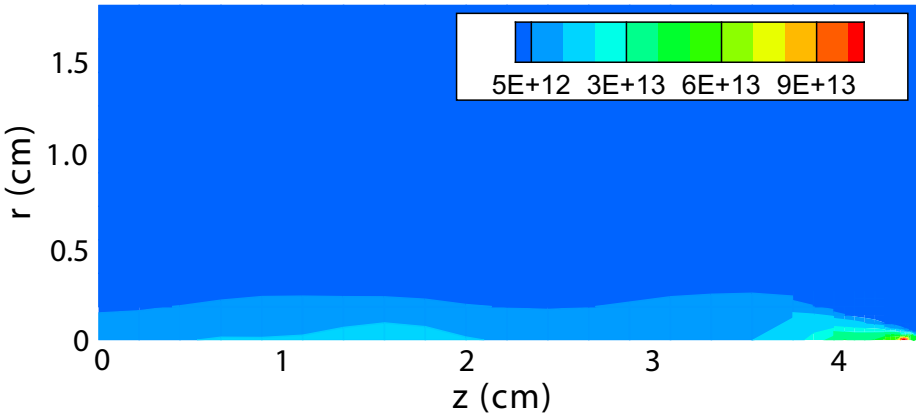

Figure 2.37: Primary electron density (m^{-3}).

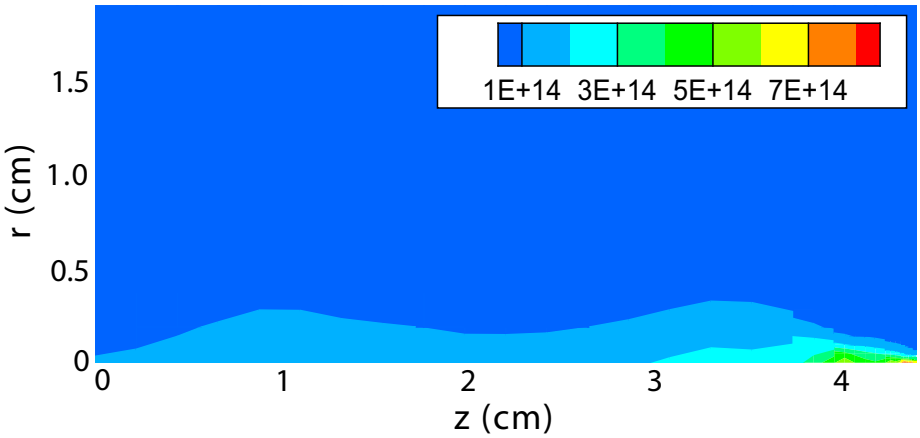

Figure 2.38: Ion density (m^{-3}).

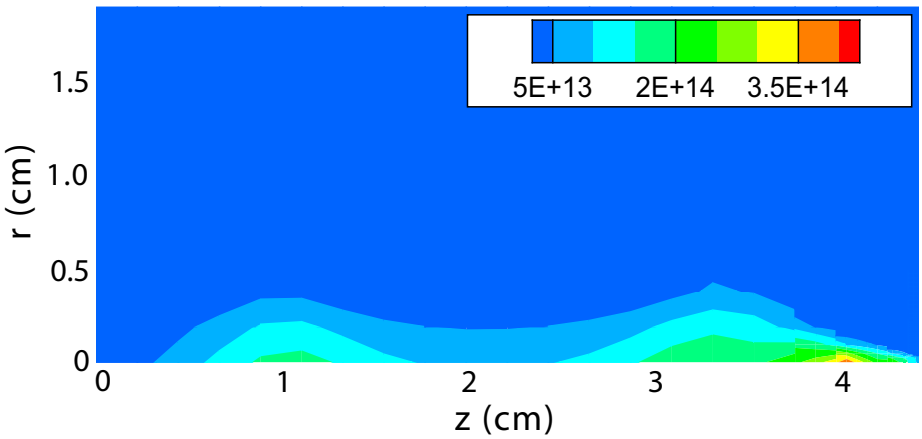

Figure 2.39: Plasma electron density (m^{-3}).

weaker magnetic fields within the domain. The plasma electrons are confined by both the electrostatic force and the magnetic field, remaining in the domain and moving between the upstream and the downstream electrodes.

Figure 2.40 shows current density profiles at the downstream plate after the initial particle tracking calculation and at the end of simulation. These data are normalized to the maximum values for each species to show the proportionality of the current density. During the initial calculation, particles are tracked in zero electric field. Then, the electric potential is updated based on the space charge computed from the particle tracking results. Therefore, the result at the end of simulation is produced by tracking particles in the converged electric field.

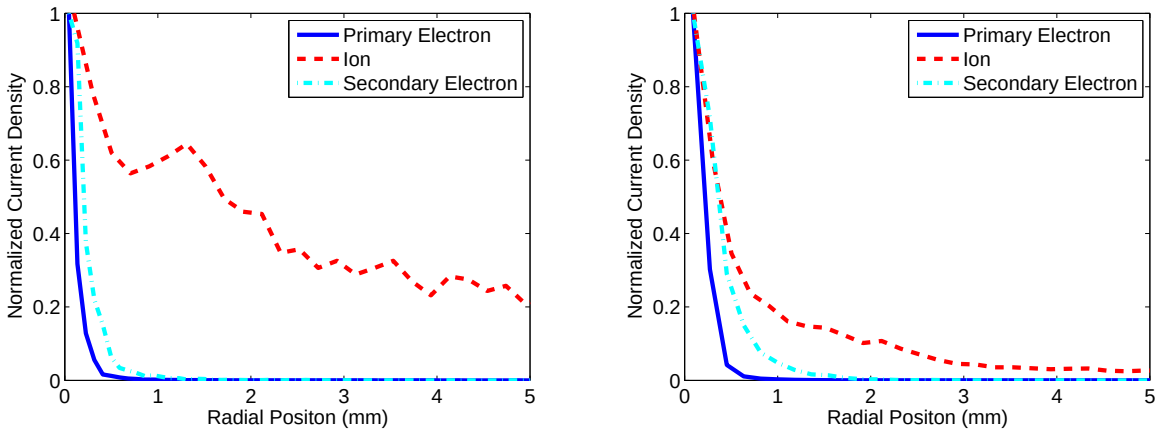

(a) After the first iteration.

(b) At the end of simulation.

Figure 2.40: Normalized current density profile along the radius of the downstream plate. The data are normalized to the maximum values for each species.

Table 2.3: Characteristic radii (mm) for the discharge experiment.

	Primary Electrons	Ions	Plasma Electrons
Leak Radius (Exp.)[a]	0.62	0.77	0.59
Leak Radius (Model)[a]	0.08	0.35	0.30
Gyroradius[b]	0.14	2.50	0.055
Hybrid Gyroradius	1.18[c]	1.18[c]/0.74[d]	0.74[d]

[a] Leak radii determined for full width at half maximum (FWHM)

[b] Gyroradius calculated for each species using local magnetic field and assumed perpendicular energies

[c] Hybrid gyroradius estimated using primary electrons and ions is 1.18 mm (i.e. $\rho_h \approx 2\sqrt{\rho_p \rho_i}$)

[d] Hybrid gyroradius estimated using plasma electrons and ions is 0.74 mm (i.e. $\rho_h \approx 2\sqrt{\rho_e \rho_i}$)

Comparing Fig. 2.40(b) with Fig. 2.40(a), it is clearly seen the electric field affects the loss of ions and plasma electrons; a higher concentration of ions is seen close to the center while the loss area for plasma electrons expands when they are moved in electric field. By taking full width at half maximum (FWHM) of profiles shown in Fig. 2.40(b), leak radii (summarized in Table 2.3) for individual species are obtained. These leak radii are on the same order as the theoretical hybrid radii and the experimental results except for the primary electrons.

The computed primary loss radius is on the order of its Larmor radius, which is much smaller than the value obtained from the experiment. This disagreement is somewhat expected since, in the model, the electron gun is perfectly aligned with the cylindrical magnet, which results in primary electron velocities nominally directed largely along the axis. The primary electron tracking model has shown that the misalignment of the electron gun in the experiment reduces the electron population near the centerline field, resulting in relatively lower current density peaks shown in the experimental data. As described above, ions and plasma electrons are mostly created close to the cusp. Because of the axial electrostatic force in this region, the ions are pushed toward the downstream wall as shown in Fig. 2.41, resulting in high ion current density near the cusp. This behavior results in ion loss radii much smaller than the ion gyroradius and comparable to the hybrid gyroradius evaluated for plasma electrons and ions. The plasma electron loss radius on the order of hybrid loss radius is explained by the potential and the magnetic field structures near the permanent magnet cusp. Unlike a spindle cusp, the permanent magnet creates a weakly convergent cusp field as shown in Fig. 2.33, and cross-section of plasma electron volume remains large even very near the cusp. The plasma electrons created near the cusp and initially moving toward the downstream wall are pulled toward the higher potential regions. For this reason, the overall confinement time for the plasma electrons is greater, resulting in greater number of elastic collisions and enhanced diffusion across the magnetic fields. The expansion of plasma electron volume is clearly seen from the plasma electron trajectories shown in Fig. 2.42 for the initial particle tracking calculation and at the end of simulation. By these observations, we see that the sparse plasma conditions used in this experiment do not exhibit the same mechanisms that are used to explain the hybrid gyro behavior for a weakly ionized plasma.

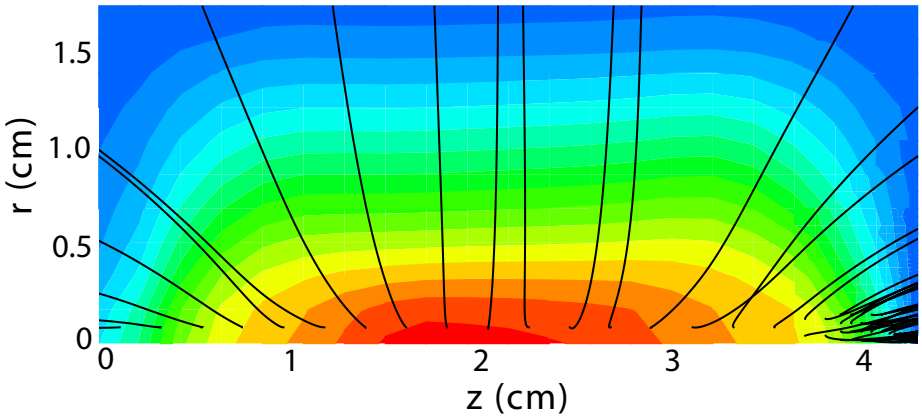

Figure 2.41: Examples of ion trajectories with potential contour shown in background.

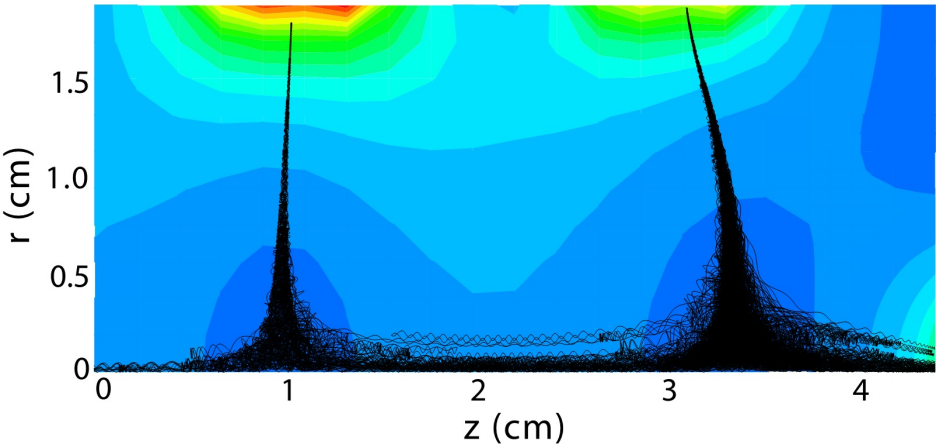

(a) During the first iteration in no electric field.

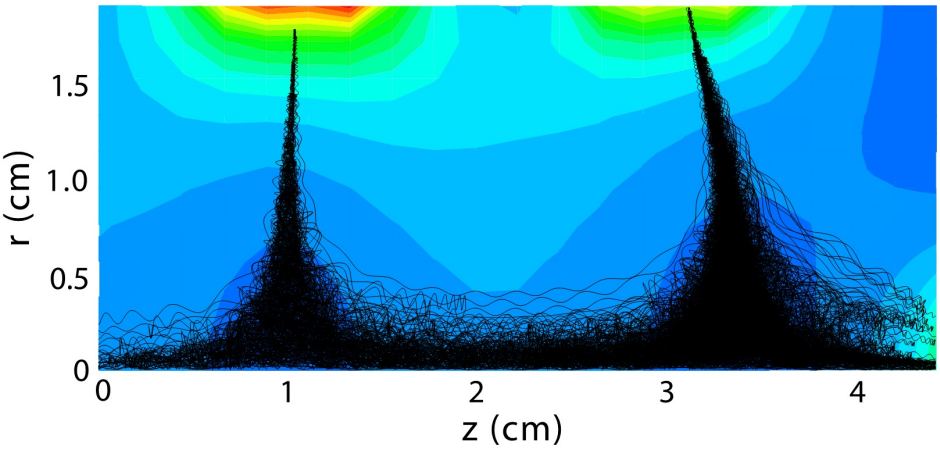

(b) At the end of simulation

Figure 2.42: Examples of plasma electron trajectories with magnetic field strength contour shown in background. With an electric field, the plasma electrons are more confined, yielding a larger electron volume.

2.5.2.2 Behavior of Primary Electrons

The experimental results shown in Figs. 2.34 and 2.35 exhibited asymmetric loss patterns caused by the misalignment of the electron gun and the magnet. In order to reduce the effect of the electron gun misalignment with the loss structure, another set of ring-cusp magnets are added in an attempt to randomize the motion of electrons before being lost to the electrodes (Fig. 2.43). The addition of the magnets decreases the strength of the magnetic field in the bulk plasma region, expanding the region of low magnetic field much further outward. Therefore, the electrons are more likely to lose their invariance. The detailed description of the experiment is provided in Refs. [164, 165].

Figure 2.44 shows the current densities at the base pressure of 3×10^{-8} Torr and at the xenon gas pressure of 5×10^{-4} Torr. Unlike the case for the previous ring-cusp configuration, the current density is peaked at a point at the base pressure while still possessing the ridge structure similar to the previous experiment. The peak location does not necessarily coincide with the center of the cylindrical magnet. Once the neutral gas is introduced in the system, the spatial distribution of current is signicantly altered while the azimuthal position and total number of the ridges remain unchanged from the base pressure result. The highest current

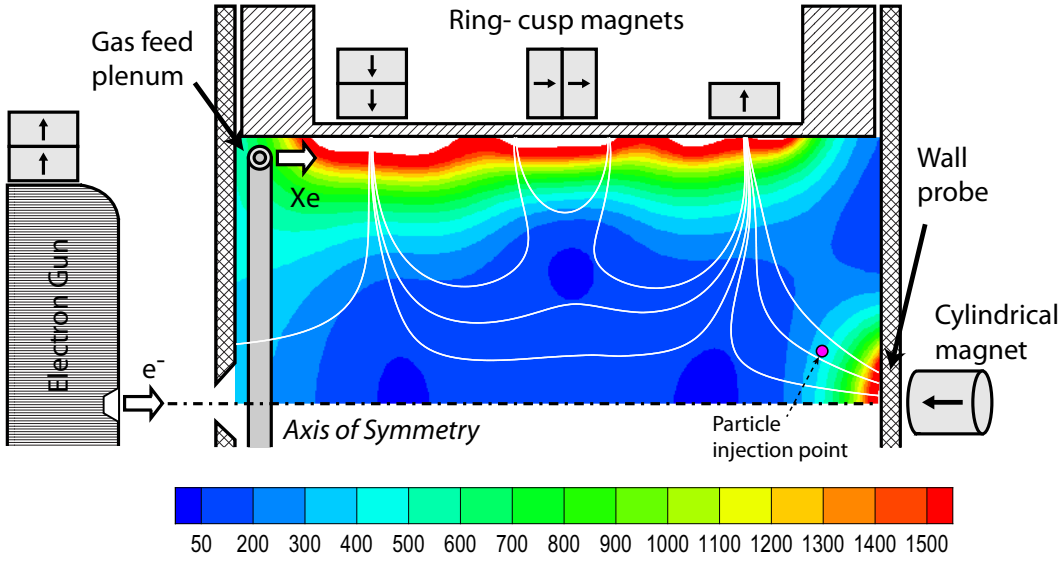

Figure 2.43: Schematic of the improved discharge experiment for a sparse plasma. The contour plot of magnetic field strength (Gauss) is shown inside the test cell. The white lines represent magnetic field lines. The SC model is used to simulate the same domain.

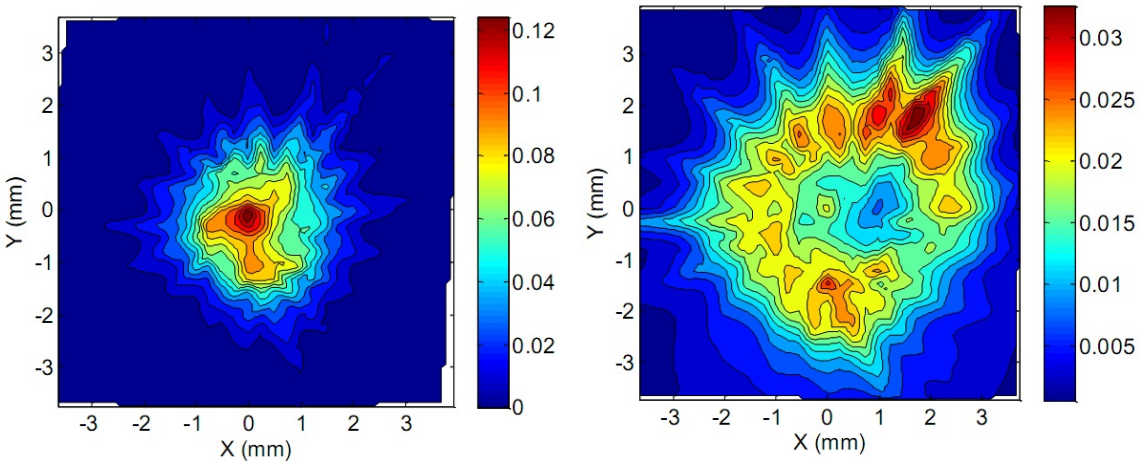

(a) Base pressure.

(b) Pressure of 5×10^{-4} Torr.

Figure 2.44: Contour plot of the current densities measured during the experiment. Origins of the plots are set at the location of peak current for the base pressure case. Orientation is from the perspective of the cylindrical magnet viewing upstream.

density is located off-axis at a radius of 2 mm with a general trend of decreasing current density in counterclockwise direction. The angle between each of the ridges range from 16° to 27°, which does not exactly correspond to the average angular spacing for the number of block magnets used (20° for 18 block magnets). This angular spacing and the azimuthal orientation of the ridges is similar for experimental conditions over a range of election energies and xenon pressures. For all data taken, there are 17 ridges in the loss pattern which does not equal to the 18 block magnets around the circumference of the device. This discrepancy is later discussed in light of the forthcoming simulation results.

In gaining a better understanding in the loss behavior in Fig. 2.44, the SC model is applied to provide a phenomenological investigation for the same operating conditions. The primary electron current is assumed to be uniform at the inlet of the test cell. The angle between the velocity vector and the test cell axis is assumed to increase uniformly with the radial position so that the maximum angle at the edge of the electron beam matches with the divergence angle for the electron gun. Figure 2.45 shows the simulation results for particle loss positions and current density at the collection plane at base pressure. The loss structure from the simulation agrees with the experimental result. The large peak near the center of the magnet is due to the large fraction of primary electrons that are confined

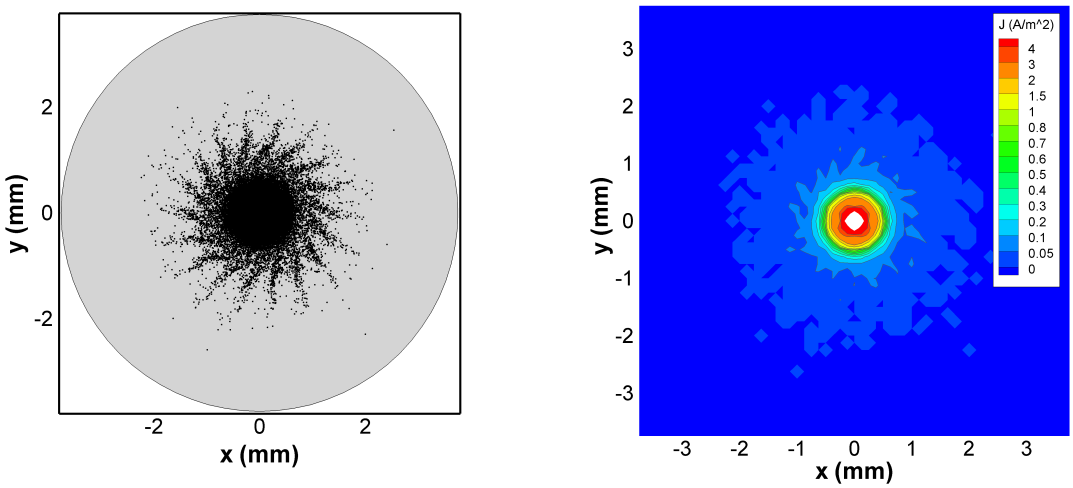

(a) (b)

Figure 2.45: Simulation results for (a) primary electron loss positions and (b) contour of current density at the plane 2 mm upstream of the cylindrical magnet face. The primary electron current density exceeds 10 A/m^2 within the white contour.

very near the centerline. These electrons stream directly toward the center of the point cusp without experiencing reflection at the ring cusp field. The simulation result for the case with xenon pressure of 5×10^{-4} Torr is similar to Fig. 2.45 except that the ridges are still observable but not as distinctive as the base pressure case and that the particle loss positions and current density distribution spread radially outward. This loss structure disagrees with the experimental result seen in Fig. 2.44. By introducing a xenon gas, primary electrons can undergo elastic, single and multiple ionization, and excitation collisions with the background neutrals. If the primary electrons are initiated very close to centerline, they tend to remain within a small radius and be collected close to the center of the point cusp. They are unlikely to experience collisions as their path lengths are much shorter than the collision mean free path. Therefore, the concentrated current near the center should be seen even for the case of 5×10^{-4} Torr if the electron gun and the cylindrical magnet are perfectly aligned. In contrast, the primary electrons confined by the field lines further away from the centerline are more susceptible to collisions as their effective path length is increased by the multiple reflections at the cusps. From these observations, it is possible that elastic collision causes the significant alternation of the particle guiding center and Larmor radius, and the

overall effect is the diffusion in the radially outward direction. The simulation result is obtained for perfect alignment of the electron gun, test cell, and the downstream cylindrical magnet: a condition difficult to achieve experimentally. The misalignment can easily cause the primary electrons that impact at slightly greater radial positions at the collection plane, and the loss position can move further out due to the radial diffusion once the neutral gas is introduced. Furthermore, the electric field from the non-quasi-neutral plasma can affect the primary electron trajectories according to the simulation in Sec. 2.5.2.1. Evidence to the effect is the substantial increase of total electron current collected inside the discharge by the introduction of a neutral gas. Unfortunately, the drastic change in the loss structure could not be self-consistently predicted by the SC model when a degree of misalignment possible during the experiment was applied.

In order to computationally investigate the ring shape loss structure, primary electrons are artificially injected with isotropic velocity distribution at the location (z, r) = (40 mm, 3 mm) as illustrated in Fig. 2.43. The simulation focuses on the interaction between the point cusp magnet and the discrete ring cusp magnets. The purpose is to understand the cause of the loss structure instead of attempting to determine the exact misalignment conditions in the experimental data. The effect of other species is neglected in this simulation. Simulations are conducted by changing the number of block magnets that form the ring cusp immediately upstream of the point cusp while maintaining constant total magnet volume. Figure 2.46 shows the simulation results for the current density at the collection plane for the case of 10, 18, and 30 block magnets and a radially magnetized ring magnet. The results show that the ridge structure at the point cusp is caused by the discretation of the upstream ring cusp as the number of ridges and block magnets correlates. For all the cases, the highest current density is seen at (x, y) = ($\sim$ 1.4 mm, 0 mm), where the current density is two orders of magnitude greater than the other peak current density values. This is due to the isotropic injection of particles at the azimuth angle of 0° leading to a large fraction of electrons with high parallel velocity that are lost at first incidence to the cusp. Therefore, the peaks are partially an artifact of the initial velocity distribution and do not influence the interpretation of the results.

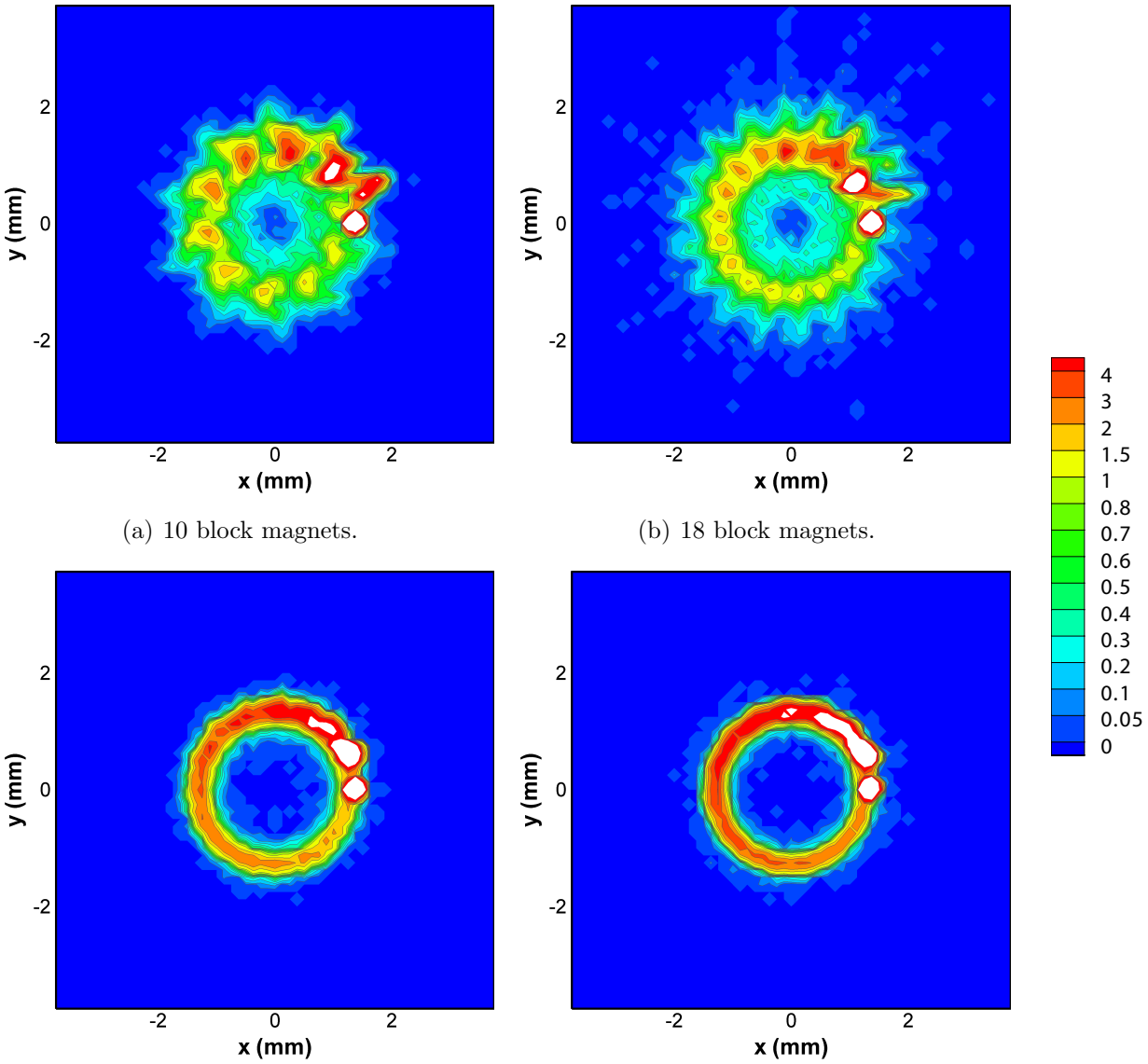

(a) 10 block magnets.

(b) 18 block magnets.

(c) 30 block magnets.

(d) Continuous ring magnet.

Figure 2.46: Simulation result for current density (A/m^2) for upstream ring cusp magnets comprising of different number of block magnets and a complete ring magnet. In this simulation, particles are injected at (z, r) = (40 mm, 3 mm) with isotropic velocity distribution. Within the white contour, the current density value exceeds 7 A/m^2.

Numerical and analytical analyses are carried out to explain the loss structure. A counter clockwise reduction of the current density around the point cusp is seen in both the experimental and computational results shown in Figs. 2.44 and 2.46, respectively. This behavior is caused by a combination of guiding center drifts in the azimuthal direction and the continuous electron loss to the cusps upon the localized injection of the particles. Among the various guiding center drifts, curvature and grad B drifts are found to be the most dominant types of drift. The velocities for the curvature and grad B drifts are given as

$$\mathbf{v_R} = \frac{mv_\parallel}{q}\frac{\mathbf{R_c}\times\mathbf{B}}{R_c^2B^2}, \quad \mathbf{v_{\nabla B}} = \frac{mv_\perp^2}{2qB}\frac{\mathbf{B}\times\nabla\mathbf{B}}{B^2} \tag{2.88}$$

where $\mathbf{R_c}$ is the curvature of the field lines. Based on the result obtained by the SC model, E×B drift is found to be at least an order of magnitude smaller than these drifts. Figure 2.47 shows the azimuthal precession caused by the combination of curvature and grad-B drifts within each grid region. In this calculation, the gradient of the magnetic field and the radius of curvature are obtained computationally. Each drift is calculated assuming a pitch angle of 15°. At the pitch angle, the curvature drift is an order of magnitude greater than the grad-B drift, while the effect of grad-B drift becomes more dominant with increasing pitch angle.

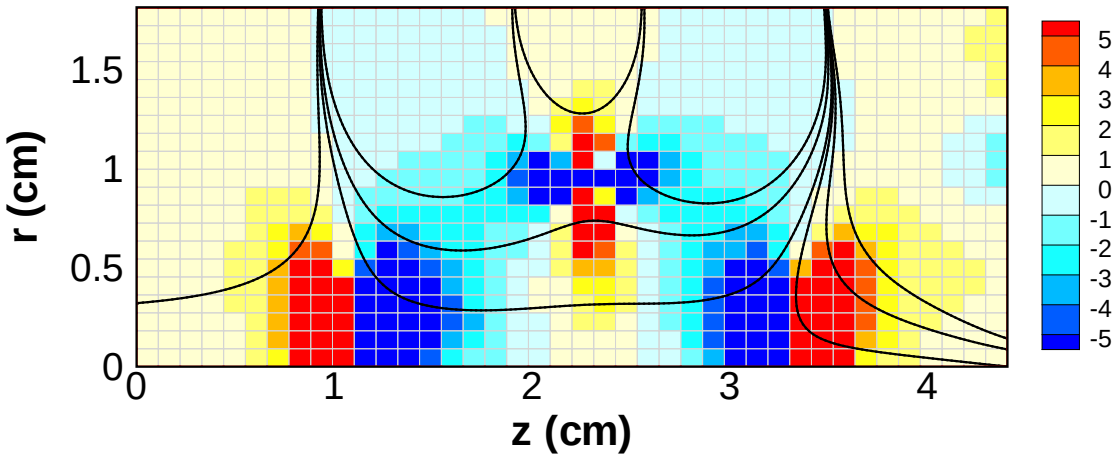

Figure 2.47: Azimuthal precession caused by the combination of curvature and grad-B drifts. Positive sign indicates the direction out the paper, and vise versa. Contour values represent the maximum drift in degrees that an electron can undergo within each grid region. Each drift is computed assuming a pitch angle of 15°.

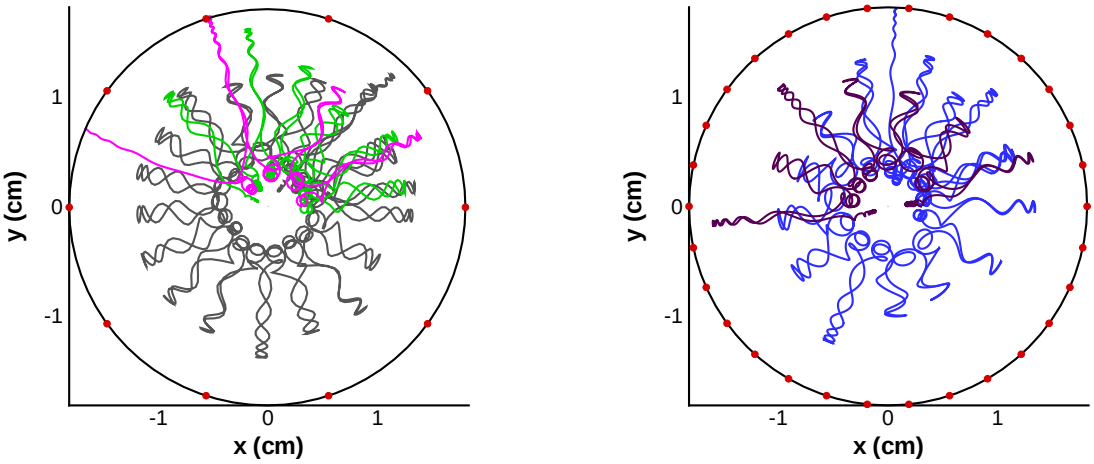

(a) 10 block magnets

(b) 30 block magnets

Figure 2.48: Particle trajectories of electrons confined between the point cusp and the directly upstream ring cusp comprising of different number of block magnets. Dots around circumference represent location of block magnet center. Particles travel along magnetic field lines and undergo an impulsive turning event at the high drift region.

In Fig. 2.47, electrons confined to the magnetic field lines in between the point cusp and the directly upstream ring cusp traverse a local region of high curvature and grad-B drift. As seen in Figure 2.48, confined particles generally travel along the magnetic field lines and only experience a short azimuthal turning event within the high drift region shown in Fig. 2.47. Particles that reside radially further and therefore in the regions of lower drift experience a smaller angular precession per reflection event.

Although it has been shown that the drifts are responsible in the ring loss structure, they are inadequate to explain the details of the loss structure, particularly the peak and ridge structure. Here, we will provide a summary of findings that cause such structure; the detailed explanation is given in Ref. [165]. The peak and ridge structure is caused by a combination of independent dynamics of electrons. First, the electrons are more susceptible of losing invariance in the low field regions, becoming less confined when passing through these regions. The condition for the 1st invariant is assessed using the following equation:

$$\xi = r_L \left| \frac{\nabla B}{B} \right| \ll 1 \tag{2.89}$$

Figure 2.49 highlights the regions where the 1st invariant is the least applicable and consequently where the particles are most likely to become unconfined. In a configuration with a continuous ring magnet and a cylindrical point cusp magnet, electrons gradually lose their invariance and are lost to the cusps after experiencing a number of reflections. The region with higher loss of invariance is still not adequate to explain the peaks for the case of discrete ring magnets. Indeed, the azimuthal asymmetry of the discrete ring magnets is responsible in leading the electrons into the low field region. Slight azimuthal gradients in the magnetic field very near the magnets cause electron drifts in both the positive and negative axial direction. Since the field lines are highly concentrated near the ring magnets, a slight drift causes a significant radial translation near the point cusp. The backward axial drift results in a further penetration of the electron trajectory into the low field region; this causes a larger degree of loss of invariance and thus leads to the peaks in the loss structure. On the other hand, forward axial drift translates into significantly larger radius at the point cusp; this leads to the ridge structure of the loss pattern.

Several possible experimental inaccuracies were investigated to examine the reason for the discrepancy between the 18 blocks ring magnet and the observed 17 ridges in the results.

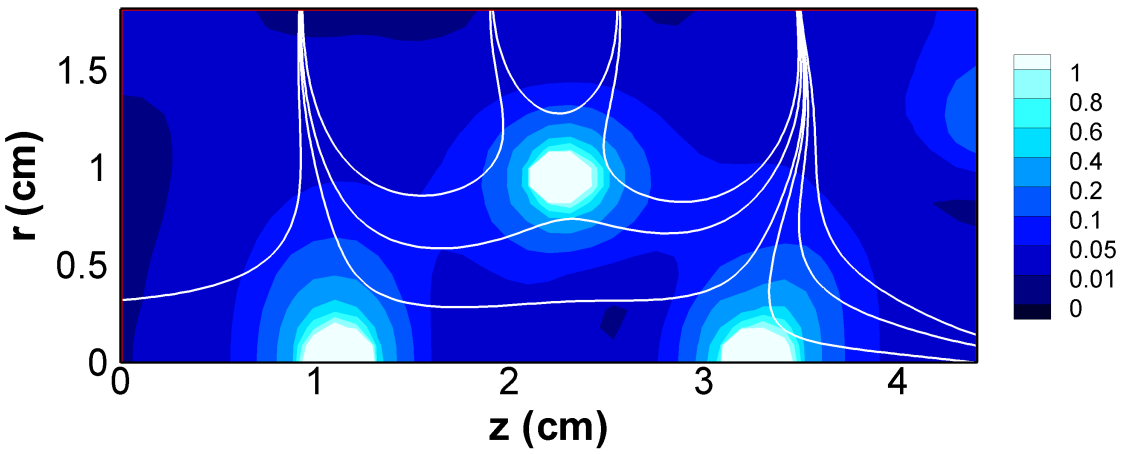

Figure 2.49: Validity equation for the 1st adiabatic condition plotting left hand side of Eq. (2.89) for electrons with a 15° pitch angle. Values for different pitch angles are proportional to the particle's perpendicular velocity and thus the Larmor radius. Locations of greater numerical value are in greater degree of violation of the invariant condition.

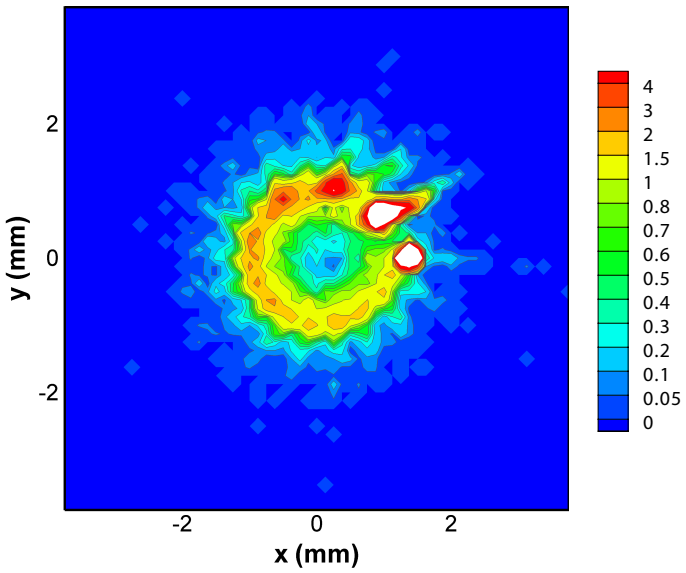

Figure 2.50: Simulation results for 18 block magnets with the magnet in line with the positive x-axis at 75% magnetization. Results show 17 ridge structures similar to the observation in the experiment.

One probable explanation is a weakened field at a local azimuthal location. Demonstrated in Fig. 2.50, the demagnetization of a single block magnet in the array can cause the disappearance of a ridge structure. The variation of angular separation and length of the ridge structure in the experimental results indicates a non-uniform spacing and/or magnetization of the block magnets. This uncertainty, coupled with the possibility of a small gap between the block magnet face and the cylindrical chamber, can potentially create a magnetic field deficit adequate for similar behavior with the simulation result.

These analyses suggest that the primary electron loss structure is strongly influenced by the magnetic field upstream of the magnetic cusp. If there is any similarity in the plasma loss mechanism between a weakly ionized plasma and a sparse plasma, it ultimately suggests that the loss structure of the weakly ionized plasma may also be affected by the upstream magnetic field configuration; the conventional theory suggests that the loss width is only a function of the local magnetic field.

2.5.3 Weakly Ionized Plasma

Simulation condition For the simulations described in Secs. 2.5.1 and 2.5.2, the electron gun was used as a source of high energy primary electrons; the required operating condition for the gun limited the achievable neutral density and thus the ionization level. For this reason, the source is replaced with a hollow cathode that is commonly used for the ring-cusp discharge chamber. The hollow cathode with an orifice of 1 mm in radius is assumed to operate at 0.4 A discharge current. At the exit of the cathode, it is also assumed that mono-energetic (8 eV) primary electrons enter the domain uniformly with a cosine distribution for their velocity directions. As shown in Fig. 2.51, the simulation domain is again inside of a cylindrical test cell, with a conducting mesh and a plate at the boundaries. The length of the test cell is determined to ensure that the primary electrons experience sufficient ionization collision with neutrals. The downstream end plate is biased at 25 V and mesh wall is grounded. Instead of using the discrete ring magnets, the magnetic field configuration is made azimuthally symmetric by replacing them with multiple current coils. The magnetic cusp in front of the cylindrical magnet is still the region of interest. In this simulation, The neutral flow rate through the hollow cathode orifice is assumed to be 0.6 sccm. The flow rate and the background chamber pressure of 3 mTorr are used to compute the neutral density (Fig. 2.52). Neutrals are free to escape through the mesh boundaries, while the sheath near

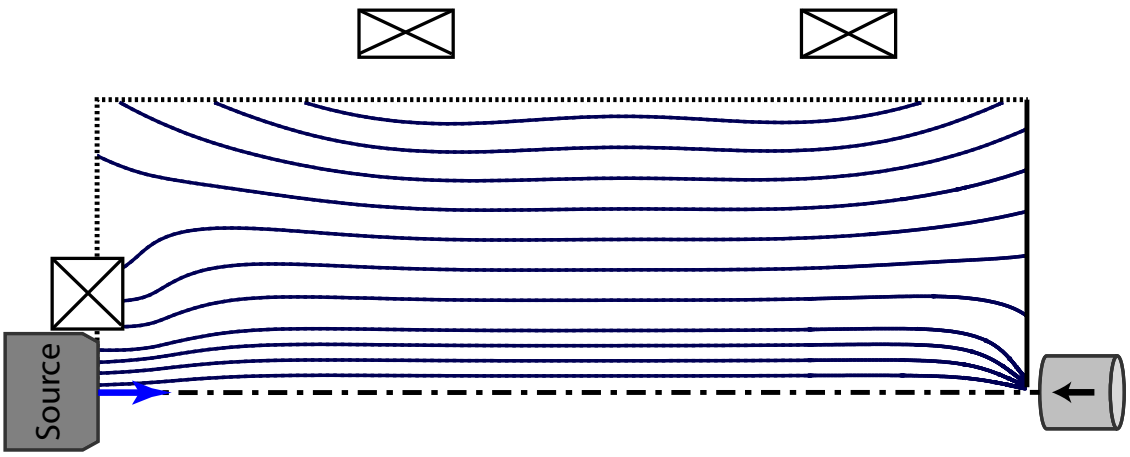

Figure 2.51: A slice of a cylindrical test cell to be simulated. The region of interest is in front of the cylindrical magnet placed downstream. Current coils are used to guide the electrons near the centerline.

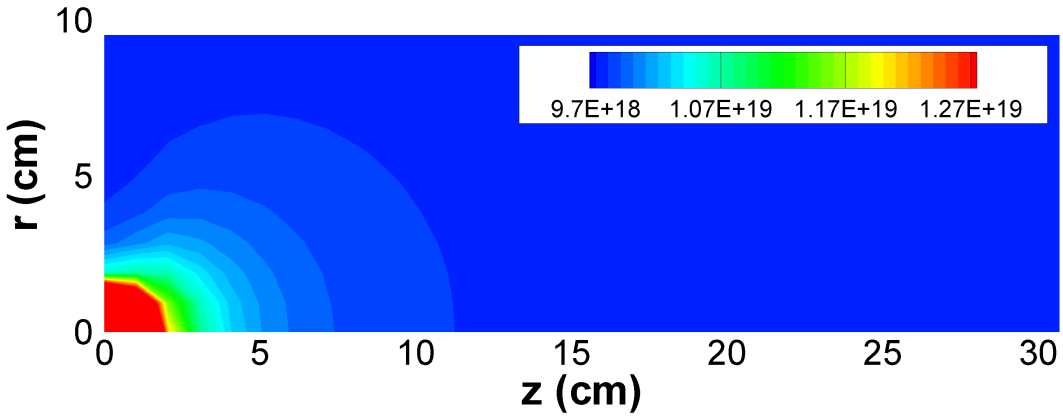

Figure 2.52: Contour plot of neutral density (m^{-3}). The highest neutral density is at the origin with the density of $> 2.2 \times 10^{19}$ m^{-3}

the mesh wall prevents plasma electrons from escaping. The neutral density is assumed to remain constant throughout the simulation since the ion density is a few orders of magnitude lower than the neutral density, and the reduction in neutral density due to ionization collision is insignificant.

Analytical Solution for Bulk Density Profile A simple analytical model is developed to approximate the density profile along the radius where the field is approximately aligned with the centerline axis. The result from the analytical model described herein is compared with the computational result for model validation. Assuming that the domain is much longer compared to the radius, the density profile along the radius can be estimated with the diffusion equation.

$$\frac{\partial n}{\partial t} - D\nabla^2 n = \dot{n}(r) \tag{2.90}$$

The first term in Eq. (2.90) is neglected since the solution of interest is steady-state. In this formulation, it is assumed that the magnetic field is homogeneous away from the magnetic cusp in the direction parallel to the axis. Assuming that the ion generation rate density profile along the radius can be expressed by a polynomial of degree N_d, the equation to be solved becomes,

$$-D_\perp \frac{1}{r}\frac{\partial}{\partial r}\left(r\frac{\partial n}{\partial r}\right) = \dot{n}(r) = \sum_{s=1}^{N_d} p_s r^{N_d - s} \tag{2.91}$$

where p is the polynomial coefficients. At the edge of the sheath near the side wall, the characteristic loss velocity of ions, u_w is assumed to satisfy the Bohm criterion for a positive sheath, $u_w = u_{\text{Bohm}} = \sqrt{kT_e/m_i}$. Thus, the boundary conditions are,

$$n(r = r_{\max}) = n_w, \quad \Gamma = -D_\perp \left.\frac{\partial n}{\partial r}\right|_{r=r_{\max}} = n_w u_w \tag{2.92}$$

The solution of Eq. (2.91) is then,

$$n(r) = \sum_{s=1}^{N_d} \frac{p_s}{(N_d - s + 2)^2} \left[\frac{r_{\max}^{(N_d - s + 2)} - r^{(N_d - s + 2)}}{D_\perp} + \frac{r^{(N_d + s + 1)}}{u_w}(N_d - s + 2) \right] \tag{2.93}$$

A similar solution can be derived using a boundary condition with $n(r = r_{\max}) = 0$, yielding Eq. (2.93) without the second term in the parentheses. Equation (2.93) is dependent on the perpendicular diffusion coefficient, $D_\perp$, which is difficult to obtain for our specific problem. The classical ambipolar diffusion across a magnetic field can be obtained by equating the ion and electron fluxes perpendicular to the direction of magnetic field. [166]

$$D_\perp = \frac{\mu_{i\perp} D_{e\perp} - \mu_{e\perp} D_{i\perp}}{\mu_{i\perp} - \mu_{e\perp}} \tag{2.94}$$

The diffusion coefficient given in Eq. (2.94) is appropriate in a infinitely long cylindrical plasma with uniform magnetic field along the axis. When the domain is finite and is bounded by conducting walls, the diffusion coefficient should be modified to take into account of Simon's "short-circuit" effect [167].

$$D_\perp = \frac{\mu_i D_{e\perp} - \mu_e D_{i\perp}}{\mu_i - \mu_e} \tag{2.95}$$

Unlike the case with the classical ambipolar diffusion, the particle flux is no longer at the same equilibrium value in each direction, but rather the total flux for each species should be maintained. In our problem, strong and weak cusps are placed at the downstream and upstream ends, respectively. In this magnetic field configuration, electrons are not freely lost to the ends if they are confined near the centerline. In contrast, the electrons are easily lost

at the ends away from the centerline due to the low field strength. Therefore, the diffusion coefficient applicable for our problem is likely between Eq. (2.94) and Eq. (2.95), and the density solutions obtained using the two diffusion coefficients should provide the upper and lower bounds for the computational result.

Numerical Results Unfortunately, the solution did not converge at the end of simulation as shown in Figs. 2.53 and 2.54. The species densities were nearly steady-state, but the ion and plasma electron densities did not meet the convergence criteria near the end of

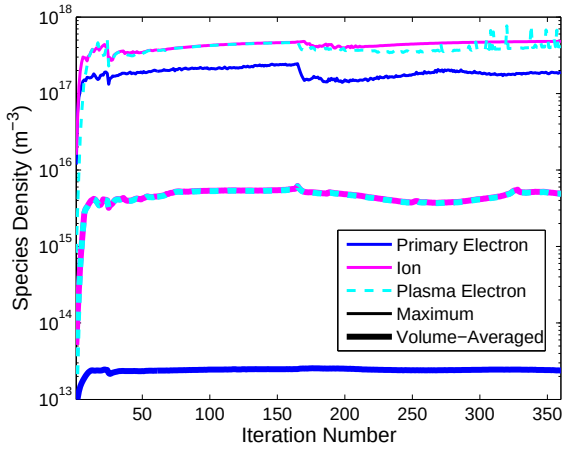

Figure 2.53: Maximum and volume averaged densities versus iteration. The densities were mixed with values from 25 previous iterations.

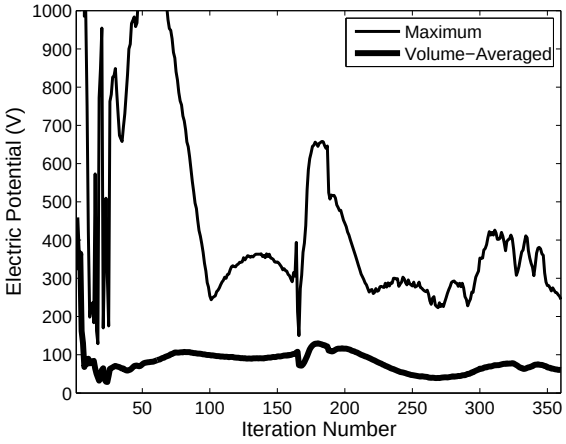

Figure 2.54: Maximum and volume averaged electric potential versus iteration. The values were obtained directly from potential solver (before performing mixing with potential values from 25 previous iterations).

simulation. Note that the simulation was restarted at iteration 163. The electric potential was far from convergence; the max potential was greater than 200 V, while we expected that the maximum and volume averaged potential should be close to the expected plasma potential of ~ 33 V.

Figure 2.55 compares the computational and analytical results for a density profile along the radius at $z = z_{\max}/2$. The profile for ion generation rate density is obtained by the computational model and is fitted with a polynomial of degree $N_d = 9$. As seen in Fig. 2.55, the computational result does not agree well with the analytical solution; we expect that the computational result would be bounded by the profiles predicted using ambipolar and Simon's diffusion coefficients. One of the reasons for the disagreement may be that the electric potential has not been developed completely at the end of simulation. For the profile shown in Fig. 2.55, a converged solution for the electric field is expected to act to push the ions near the centerline further radially outward, so the density profile is flattened. Comparing the computational results in the middle and at the end of simulation, the slope of the density profile became closer to the analytical solution; however, further iterations did not result in the expected density profile. Another source of the error can be the finite dimension of the domain. The transport in the axial direction is neglected in the analytical

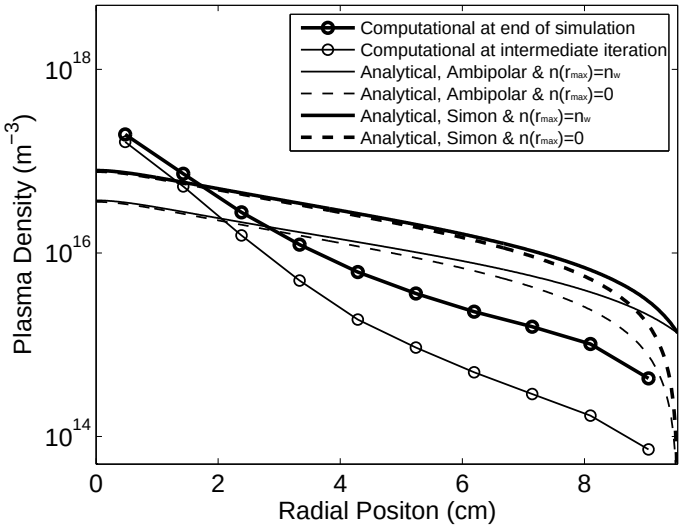

Figure 2.55: Comparison of density profiles from computational and analytical models along the radius at $z = z_{\max}/2$.

model; however, a finite diffusion in axial direction must be present even at $z = z_{\max}/2$ since the domain radius is only a third of the length. The computational model predicted slight variation of density axially near the axis while relatively larger density variation was seen further away from the axis. Finally, azimuthal inertia terms in the diffusion equation are neglected in the analytical formulation which may be significant.

Since the solution did not converge at the end of the simulation, the results are inaccurate but do exhibit some physical consistencies when comparing the potential structure and the relative species density distributions. Figure 2.56 shows the potential structure near the cusp. The contour level is omitted as the magnitude is not of importance here, but red corresponds to high potential and blue corresponds to low potential. It is clearly seen that there is a sheath along the anode wall as represented by the steep drop of the potential toward the wall. Figure 2.57 compares the species densities near the cylindrical magnet cusp. The right hand side of the domain shown in Fig. 2.57 represents the anode wall at the magnetic cusp; the magnet face is 3 mm downstream of this surface. The general and relative structure of the density profiles shown in these plots remained unchanged toward the end of simulation.

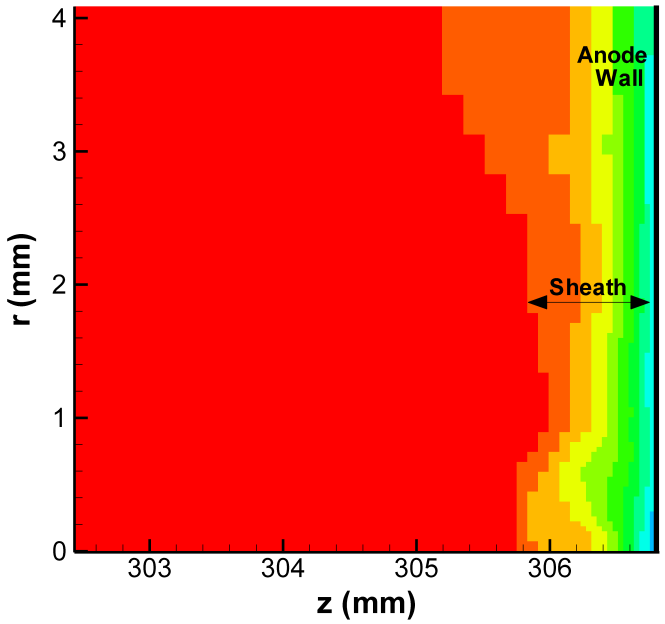

Figure 2.56: Electric potential near the anode wall at the magnetic cusp. Magnet face is at $z = 310$ mm. Sheath is developed along the anode wall.

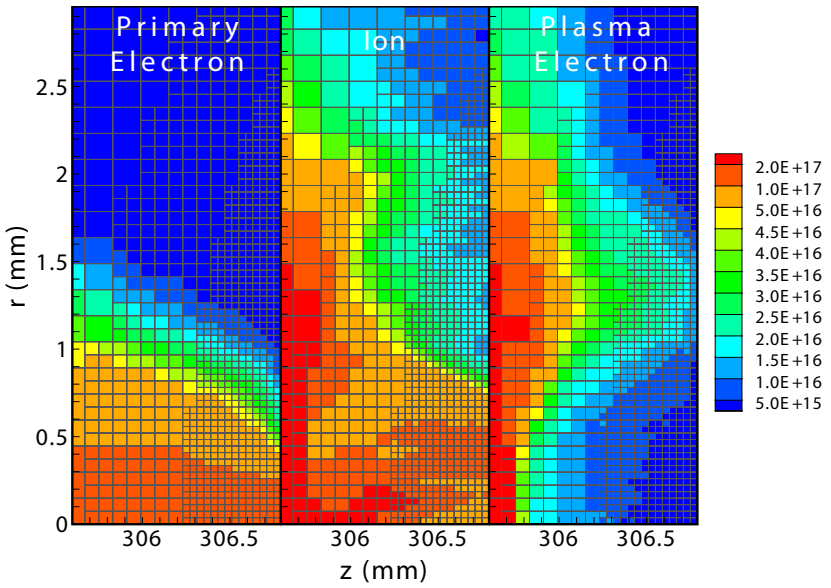

Figure 2.57: Species densities (m^{-3}) very near the cusp. Magnet face is at $z = 310$ mm. Primary electrons are confined very near the centerline.

Since the hollow cathode is placed along the same axis as the cylindrical magnet, the primary electrons are directed toward the cusp and are confined very near the centerline. Primary electrons are not as confined by magnetic mirroring and sheath as plasma electrons, so the residence time of primary electron is a few orders of magnitude less than that of plasma electron. Therefore, it is much more difficult for the primary electrons to diffuse across the magnetic field. Because of the concentrated primary electron population near the centerline, the potential is developed to attract ions radially inward. The radial component of the electric field interacts with the axial magnetic field to create an azimuthal E×B drift for the highly confined plasma electrons. Ions and plasma electrons are predominately created by inelastic collisions between primary electrons and neutrals, so their generation rate density is high in the region of high primary electron density. Ions created very near the magnetic cusp are immediately accelerated toward the wall whereas plasma electrons are repelled from the wall. As the plasma electrons are strongly confined by the magnetic field and sheath, these results suggest that their path length is to be over 50 times longer than that for primary electrons. The plasma electrons diffuse much further radially outward due to multiple elastic collisions with neutrals and eventually gain enough parallel velocity to reach the anode wall.

As a result, it appears that they are mainly collected in an annular region surrounding the axis near the cusp. Consequently, these results suggest that in the near-sheath and sheath region near the axis may be dominated by the primary electrons and ions while the plasma electrons and ions occupy the outer region at low primary electron density. These results do not agree with measurements in spindle cusp and picket fence experiments [89–92] and may be attributable in part to the current lack of a converged solution. We wish to note, however, that in contrast to the experiments mentioned the cusp here occurs at a current collecting wall. The electric field at the wall must be such that a sufficient current of electrons is drawn to maintain the discharge. If the electron current near the cusp is ample, one may expect the normal sheath formation as electrons are lost rapidly along the field lines. The different boundary conditions here may reasonably be expected to result in different distributions.

Figure 2.58 shows the local degree of quasi-neutrality, η, obtained by the computational result where η is given as,

$$\eta = \frac{n_i - n_e}{\max(n_i, n_e)} \tag{2.96}$$

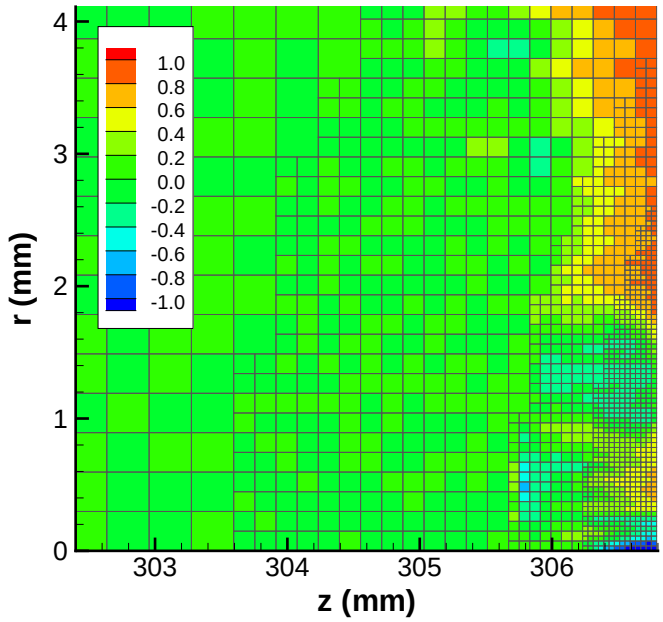

Figure 2.58: Degree of quasi-neutrality obtained by $\eta = (n_i - n_e)/\max(n_i, n_e)$. Magnet face is at $z = 310$ mm. Positive and negative contours indicate regions dominated by ions and electrons, respectively.

Here, $\eta = 0$, $\eta > 0$, and $\eta < 0$ indicate quasi-neutral, ion-dominated, and electron-dominated plasma, respectively. As shown in Fig. 2.58, ions dominate the near-wall region at $r \gtrsim 1.6$ mm. This is, again, due to the sheath potential that accelerate ions toward the wall and repel plasma electrons away from the wall. Within the near-wall region at $r \lesssim 1.6$ mm, the positive sheath is still present, but the difference between the plasma and anode potential is not large enough to prevent primary electrons from being lost at the wall. As a result, ions in this simulation respond to the potential structure caused by the high primary electron concentration. However, they do not reside in the region long enough to completely counteract charge imbalance, being accelerated toward the wall by the sheath. Therefore, the region very near the centerline is dominated by the primary electrons.

2.6 Chapter Summary

The SC model that uses an iterative Monte Carlo technique has been developed to investigate the important structure and dynamics of the cusp confined plasma species. The model uses various numerical techniques that are necessary for our objective. These include implementations of analytical equations for magnetic fields induced by permanent magnets together with the fast computation methods for elliptic integrals (Sec. 2.3.2 and Appendix C) and the modified Boris method for integration of particle motion (Sec. 2.3.3). In addition, we have developed the particle weighting algorithm (Sec. 2.3.4) and the second order electric field solver (Sec. 2.3.7) that work for any type of mesh including an adaptive regular and a MFA mesh during the course of the model development. Furthermore, advanced methods for calculations of collisions (Sec. 2.3.5) and electric potential (Sec. 2.3.6) and also a method for smoothing (Sec. 2.3.8) are implemented in the SC model. All of these methods have been validated independently in simple test cases, while this chapter has provided extensive validation studies for the particle weighting algorithm, the potential solver, and the electric field calculation.

The simulation using the SC model began with the simplest system that involves a magnetic cusp: 25 eV primary electrons from an electron flood gun shot toward a point-

cusp cylindrical magnet placed downstream. The simulation result showed good qualitative and quantitative agreement with the experimental data, thus further validating the particle tracking and magnetic field calculations.

Then, the simulation was extended to include multiple species (primary electrons, neutrals, ions, and plasma electrons) to examine their interactions, especially in the cusp region very near the anode wall. The sparse plasma condition was achieved by adding multiple ring cusps in an effort to confine primary electrons and the other plasma species. The results from the multi-species computational simulations provided insight into the dynamics and structure of sparse plasma in the cusp region and showed that the sparse plasma conditions used in this experiment do not exhibit the same mechanisms that are used to explain the hybrid gyro behavior for a more highly ionized plasma. In particular, the reduction of ion loss width was due to the high rate of generation near the cusp and the potential structure that immediately accelerated ions toward the electrode. On the other hand, the plasma electrons immediately repelled from the wall due to the electric field are confined by the potential and the magnetic field, experiencing multiple elastic collisions with neutral atoms and thus resulting in the expansion of plasma electron volume and the increase in the loss area.

The next simulation for the sparse plasma in the multi-cusp configuration focused on the dynamics of the primary electrons. The experimentally measured loss pattern exhibited an interesting pattern with the peak and ridge structure with decreasing current density in the counter clockwise direction. The SC model was applied to provide a phenomenological investigation of the loss pattern by injecting the primary electrons between the point cusp magnet and the ring magnets directly upstream of the point cusp. Ignoring the peaks near the injection point that are artifacts of the initial velocity distribution, all the important features of the experimentally measured loss pattern were captured by the model, leading to the conclusion that the unique pattern was indeed due to the upstream discrete block magnets creating the ring cusp. Analytical study was carried out, and it was found that the loss structure was due to a combination of azimuthal drift in the low field region, forward and backward axial drifts very near the ring cusp, and the loss of invariance in the low field

region. This indicated that the primary electron loss structure was strongly affected by the upstream magnetic field configuration. Tying with the results from the full simulation for the sparse plasma, the loss of the sparse plasma should be altered by changing the upstream magnetic field configuration, while this does not necessarily apply to a weakly ionized plasma.

The SC model was also used to simulate a weakly ionized plasma in a field configuration created by multiple current coils and a cylindrical magnet. Due to the structure of the model, it was found that the convergence condition was extremely difficult to satisfy due to the opposite charges of ions and electrons. Even by implementing a high degree of mixing between iterations, the electric potential still oscillates from iteration to iteration. The quasi-neutral condition for a weakly ionized plasma requires the charge density to be within $\sim 10^{11}$ m^{-3} which corresponds to $\sim 10^{-4}$ % of the species density for this specific simulation condition. Since the solution did not converge at the end of the simulation, the results were inaccurate but did exhibit some physical consistencies when comparing the potential structure and the relative species density distributions. In particular, the sheath structure near the anode wall was captured, and the plasma species distribution very near the magnetic cusp was resolved.

CHAPTER 3

Techniques for a Ring-Cusp Discharge Chamber Modeling for a Micro-Discharge Design

The objective of this effort is to use the ring-cusp discharge chamber model developed by Wirz and Katz [13, 24] (DC-ION) to address the design and optimization challenges of miniature to micro discharges on the order of 3 cm to 1 cm in diameter. To this end, significant improvements to the model are necessary due to the scaled-down dimension of the domain. The SC model and the related experiments discussed in Chapter 2 have revealed important phenomenological primary electron loss behavior that is strongly affected by the upstream magnetic field, which needs to be extended for a weakly ionized plasma. While the SC model has provided a qualitative description of plasma structure near the cusp, it still requires many improvements to obtain a fully converged solution and thus provide a precise and quantitative picture. With the lack of accurate descriptions, the formulation of a theory that could be easily included in DC-ION was not possible. Nevertheless, improved techniques and routines that can be incorporated in DC-ION have been developed to achieve better accuracy and computational speed. Some of these are also necessary to enable simulations for small scale discharges. Several components of the SC model can be used in DC-ION such as the analytical equations for permanent magnets, the particle weighting algorithm, and the electron-atom elastic scattering. This chapter discusses the other improved techniques and routines to be incorporated in DC-ION. First, a brief description of DC-ION is provided in Sec. 3.1. Section 3.2 gives the details of the magnetic field aligned (MFA) mesh generation process. Section 3.3 describes the numerical method for solving the plasma diffusion equation in such a complex mesh and compares the solutions obtained with the MFA and uniform meshes. Finally, Sec. 3.4 discusses the improvement made to the neutral density calculation

method in terms of computational efficiency. Both Secs. 3.2 and 3.3 are taken from the article *Magnetic Field Aligned Mesh for Ring-Cusp Discharge Chambers* presented at 50th AIAA/ASME/SAE/ASEE Joint Propulsion Conference.

3.1 General Description of a Ring-Cusp Discharge Model

The discharge chamber model developed by Wirz and Katz [13, 24], DC-ION, is the 2D/3D hybrid fluid/particle model that self-consistently includes effects of primary electrons along with other plasma species. The model has been validated against the data for the NSTAR ion thruster with 30 cm chamber diameter and also applied to the simulation of 3 cm MIXI thruster. The general structure of the model is shown in Fig. 3.1. As shown in Fig. 3.1, the model consists of the Internal Mesh Generator and four sub-models. In the Electron Collision Sub-Model, the Monte Carlo approach is used for primary electrons, tracking many macro-particles representing a number of electrons in 3D domain. This sub-model is similar to

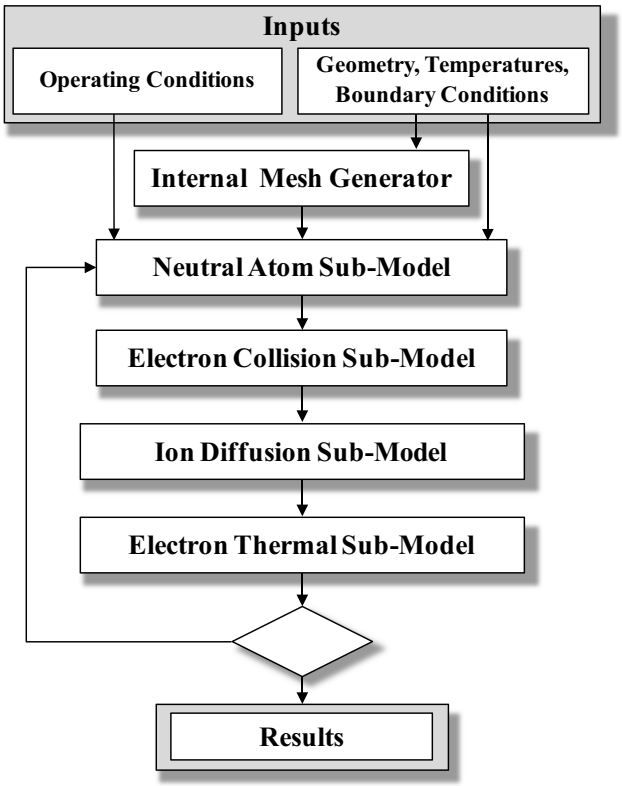

Figure 3.1: General structure of DC-ION. Reproduced from Ref. [24].

the SC model discussed in Chapter 2; thus, the more sophisticated numerical techniques and methods can be directly applied to the sub-model for improvements. The Ion Diffusion Sub-Model solves the plasma diffusion equation derived from the conservation equations for mass and momentum for ions and plasma electrons. Then, the electron energy equation is computed in the Electron Thermal Sub-Model to obtain the electron temperature. The neutral density is computed using the zonal method in the Neutral Gas Sub-Model. In this model, a regular grid with uniformly sized rectangular elements is generated by the Internal Mesh Generator. The techniques and routines discussed in this chapter are related to the Internal Mesh Generator, the Ion Diffusion Sub-Model, and the Neutral Atom Sub-Model.

3.2 Magnetic Field Aligned Mesh

3.2.1 Introduction

In a magnetized plasma, rates of transport in directions parallel and perpendicular to a magnetic field are different. According to the classical plasma transport theory, the perpendicular electron transport coefficient is scaled with B^{-2} and is always smaller, and often at least an order of magnitude smaller, than the parallel transport coefficient [141]. This is also commonly the case even when one considers more Bohm-like (B^{-1}) diffusion. When computationally solving the transport equation for such systems, a numerical error arises due to the anisotropicity of the transport coefficients if the computational grid is unaligned with the magnetic field; this is called the numerical diffusion. For example, Anderson [168] demonstrated an artificial diffusion of the temperature by solving the heat conduction equation on a 2D Cartesian grid with the magnetic field at 45° with respect to the grid edge. Even by setting the perpendicular conductivity to zero (anisotropy ratio of ∞), the temperature field after 35 time-step showed a finite perpendicular heat flow, which resulted in the effective anisotropy ratio of $\sim$4. A similar but more extensive study was performed by Meier et al. [169] by solving the heat conduction equation with a high-order finite element code. They found that even a small misalignment can cause a significant numerical error and that the error can be reduced by using a finer resolution and a higher-order polynomial

basis expansion in the finite element method. They also noted that the accuracy is slightly better if the misalignment between the field and the grid was 45° as opposed to some other non-zero angles.

One of the methods to remedy the numerical diffusion error is to use a computational grid that is aligned with the magnetic field. The generation of the magnetic field aligned (MFA) mesh is most commonly done by simply tracing the field lines [23, 170–179]. Given the data or the functional form of the field lines, the lines parallel and orthogonal to the magnetic field are determined by the direct numerical integration; the integration can be executed using commercially available graphics software [170, 171] or an explicit method such as 5th order Adams-Bashforth method [177–179]. Once the intersections of those lines are determined, the computational mesh can be generated by connecting the intersections such that each grid element consists of facets parallel and perpendicular to the field lines. The direct numerical integration is very easy to perform and can be applied to a complex system where a transformation between the magnetic flux coordinate and inertial coordinate cannot be defined. However, the method is often too time-consuming as the step-size has to be very small to obtain enough accuracy in the line integration. For 3D plasma edge modeling of toroidal fusion devices, the time required in generating a MFA mesh is significantly reduced by using mapping techniques after a block of 3D mesh covering some toroidal angles is generated [174–180]. These mapping techniques are not applicable for the field configuration in a ring-cusp discharge chamber. In contrast to the numerical integration method, the lines of magnetic field can be determined directly if there exists an appropriate transformation between the magnetic flux coordinate and inertial coordinate. Magnetic field lines are simply represented by the lines of constant flux function, ψ, which can be computed numerically. This method has been applied by Brieda and Keidar [181] for Hall-effect thruster simulations and by Marchand and Dumberry [182, 183] for 2D edge plasma modeling. The mapping method described by Abdullaev [184] may also be applied for a toroidal system.

In a DC ring-cusp ion thruster, the magnetic field topology is fairly complex. The magnetic field is created by multiple block magnets that are placed along the circumference of the discharge chamber to create a ring-cusp field. Near the magnetic cusp, the magnetic

field is highly convergent, and the gradient of the field is very high. Furthermore, the field configuration typically consists of a null point where the magnetic field cancels out to zero. Considerably large difference between the maximum and the minimum magnetic field strengths generally makes the task of MFA mesh generation more difficult. In addition, two field lines intersect at the null point; therefore, a special treatment of the null point may be required. Wirz and Katz [23, 172] successfully generated and applied the MFA mesh for the simulation of NSTAR discharge chamber. The MFA mesh generation was accomplished by tracing the magnetic field lines starting from the boundary near a magnet. In later simulations, they switched to a uniform mesh due to the inability of their MFA mesh algorithm to quickly adapt to changing magnetic field structures [185].

This section provides the detailed descriptions of a 2D axisymmetric MFA mesh generation method. The algorithm is significantly robust to automatically mesh a wide range of magnetic field geometries without the need for significant user input. Existing commercial meshing software is not adequate in accomplishing the task because much control in mesh generation is necessary; the MFA mesh with a fair grid quality typically requires adjustment of grid especially in the near-boundary region, and the appropriate technique may differ from configuration to configuration.

3.2.2 Process of MFA Mesh Generation

The procedure in the generation of a MFA mesh used in this section involves primarily six steps: (1) solve for stream function and scalar potential, (2) identify null points, (3) select contour levels, (4) extract node points, (5) create cell elements, and (6) improve the mesh quality. Each mesh generation step is discussed in detail here. Instead of directly tracing the magnetic field lines and lines orthogonal to the field, we solve for the stream function and scalar potential directly from the appropriate relations between the two functions and the magnetic field. This method is computationally much less expensive than tracing the field lines. The transformation from the physical coordinate to the flux coordinate is greatly simplified if the problem is two dimensional or three dimensional with some symmetry.

Therefore, the ring-cusp block magnets are approximated as a single ring magnet. The error in the field strength associated with this approximation was investigated by Mao [186] for a configuration with three ring-cusps. The largest error was seen near the magnets at the off-face place due to the lack of magnet material, but the error was within 5 % while the error away from the magnet was well below 1 %. Furthermore, the numerical method described in Sec. 3.3 does take into account the misalignment of the grid with the field, so the exact alignment of the mesh with the field throughout the domain is not required. The MFA mesh generation method described herein requires a fine uniform mesh so that the stream function and scalar potential values can be numerically evaluated on the grid points. The accuracy in the alignment and the speed in the grid generation are dependent on the resolution of the uniform mesh. In this study, we use the number of cells in the range of 100 to 400 in each direction. This provides a reasonably accurate calculations with an acceptable computational run-time.

3.2.2.1 Stream Function and Scalar Potential

Knowing the magnetic field at the nodes of the fine uniform mesh, the stream function and the scalar potential can be determined computationally from the equations derived in this section. This step can be skipped if one can derive functional forms of the stream function and the scalar potential that describe their variations within the computational domain. However, such functions are nearly impossible to obtain for the magnetic field created by the permanent magnets as the field equations are relatively complex. Therefore, we evaluate the two functions digitally onto the fine uniform mesh. This idea came from the work by Mao [186] but with a slightly different formulation. Since the magnetic field is divergence-free ($\nabla \cdot \mathbf{B} = 0$), there exists a vector field $\mathbf{A}$ such that $\mathbf{B} = \nabla \times \mathbf{A}$. For the axisymmetric magnetic field ($\mathbf{B} = B_z\hat{z} + B_r\hat{r}$), $\mathbf{A}$ must be in $\hat{\theta}$-direction and is expressed as $A_\theta = \psi/r$. Taking the curl of $\mathbf{A}$ and equating with $\mathbf{B}$, the relation between the stream function and magnetic field can be obtained.

$$B_z\hat{z} + B_r\hat{r} = \frac{1}{r}\frac{\partial\psi}{\partial r}\hat{z} - \frac{1}{r}\frac{\partial\psi}{\partial z}\hat{r} \tag{3.1}$$

By replacing the magnetic field with the flow velocity, Eq. (3.1) becomes the well-known relation for the Stokes stream function that is used to describe the streamlines and flow velocity in a 3-D incompressible flow in a cylindrical coordinate system. Finally, by multiplying both sides by r in Eq. (3.1) and taking the curl from both sides, the equation becomes the Poisson's equation.

$$\frac{\partial^2 \psi}{\partial z^2} + \frac{\partial^2 \psi}{\partial r^2} = -\frac{\partial}{\partial z}(rB_r) + \frac{\partial}{\partial r}(rB_z) \tag{3.2}$$

Similar approach can be made to deduce the equation for the scalar potential. In the absence of external currents and time-varying electric field, $\nabla \times \mathbf{B} = 0$ according to the Maxwell equation. This implies that the scalar potential, ϕ, can be employed such that $\mathbf{B} = \nabla\phi$. Taking the divergence from both sides, the equation becomes the Poisson's equation similar to Eq. (3.2).

$$\frac{\partial^2 \phi}{\partial z^2} + \frac{\partial^2 \phi}{\partial r^2} = -\frac{1}{r}\frac{\partial \phi}{\partial r} = -\frac{B_r}{r} \tag{3.3}$$

The stream function and scalar potential values at the fine uniform grid points can easily be obtained by solving Eqs. (3.2) and (3.3) using the standard finite difference method. The stream function can be used to compute the volume flux through the flux surface bounded by a constant value of ψ by $2\pi\psi$. On the other hand, the scalar potential values do not have any direct physical meaning. The zero value can be set arbitrarily as for the electric and gravitational potentials. We typically choose the zero value to be at the location where the magnitude of the radial magnetic field is the minimum along the side wall of the cylindrical domain.

3.2.2.2 Null Point

Before proceeding to the actual construction of the grid, all the null points within the discharge chamber are determined by finding the local minima of the magnetic field strength. The number of null points is usually less than or equal to the number of ring magnets. Therefore, the speed in determining the null points is not an issue as long as a reasonable number of ring magnets is used. The local minima are determined by the method of steepest descent [187]. Given an initial position as an input, the position is simply advanced in the

direction of the magnetic field strength gradient until the gradient becomes effectively zero.

$$\mathbf{x_{h+1}} = \mathbf{x_h} - t\frac{\nabla|B|}{|\nabla|B||} \tag{3.4}$$

where $\mathbf{x}$ is the position and t is the step size. The gradient of the magnetic field strength is approximated by the difference equation.

$$\nabla|B(z,r)| = \frac{|B(z+\epsilon,r)| - |B(z,r)|}{\epsilon}\hat{z} + \frac{|B(z,r+\epsilon)| - |B(z,r)|}{\epsilon}\hat{r} \tag{3.5}$$

where ϵ is a very small number which we set to the square root of the machine epsilon. When the position reaches the domain boundary, the gradient in the direction normal to the boundary is set to zero to ensure that the advanced position is always within the domain. The step size, h, is initially set to a relatively large number, e.g. 1/20 of the maximum dimension of the domain, to increase the speed of convergence. When the position is sufficiently close to the location of the local minimum, the position starts to oscillate, going back and forth and never reaching the exact location of the minimum. Therefore, the step-size is gradually reduced by an order of magnitude every time the positions at hth and h-2th steps are too close (i.e. $|\mathbf{x_h} - \mathbf{x_{h-2}}| < 0.1t$) until the advancement in position is less than the machine epsilon. This ensures an accurate determination of the null points.

3.2.2.3 Selection of Contour Levels

The lines of constant stream function represent the magnetic field, while the lines of constant scalar potential represent the lines orthogonal to the magnetic field. A set of these lines are chosen to generate the MFA mesh. In a contour plot, contour lines correspond to lines of constant function values, and the process discussed here can be thought to be simply adjusting the contour levels. The selection of the contour levels for the stream function and the scalar potential is directly related to the resolution and the quality of the MFA mesh. The element size near the magnet is generally finer than the elements in other regions because of the very strong field strength and the converging field structure. On the other hand, the

element size near the null point is always the largest. The large element in the region can affect the overall accuracy of the solution. Therefore, the method for choosing the contour level can be critical. Different functions can be used for the contour level selection, while the choice of the appropriate function strongly depends on the magnetic field configuration: particularly, the ratio of the maximum strength to the minimum strength.

Given the number of contour levels for the stream function n_ψ, we first determine the index, p_0, so that p_0-th level corresponds to $\psi = 0$.

$$p_0 = \text{int}\left(n_\psi \frac{\psi_{\min}}{\psi_{\max} - \psi_{\min}}\right) \tag{3.6}$$

where $\psi_{\max}$ and $\psi_{\min}$ are the maximum and the minimum stream function values. The level indices greater and lower than p_0 are for positive and negative ψ levels, respectively. Then, the contour levels are chosen based on the exponentially stretching function from $\psi = 0$ to positive and negative ψ. Even with the function, the jump in the contour level from $\psi = 0$ to the next level is too large for most of the configurations tested. In other words, the smoothness of the grid from the innermost element to the adjacent element in the radial direction would not be preferable. Therefore, we add another level after the level of $\psi = 0$. This is done by first determining the levels ψ_{p_0+2} and ψ_{p_0-2} that correspond to the first levels if we were to only use the exponential stretching function.

$$\psi_{p_0+2} = \psi_{\max} \frac{\exp\left(\frac{1}{n_\psi - p_0}\alpha_\psi\right) - 1}{\exp\left(\alpha_\psi\right) - 1}, \quad \psi_{p_0-2} = \psi_{\min} \frac{\exp\left(\frac{1}{p_0 - 1}\alpha_\psi\right) - 1}{\exp\left(\alpha_\psi\right) - 1} \tag{3.7}$$

where α_ψ is the stretching parameter for ψ specified as an input. Then, ψ_{p_0+1} and ψ_{p_0-1} are chosen simply by taking a fraction of ψ_{p_0+2} and ψ_{p_0-2}, respectively.

$$\psi_{p_0+1} = \gamma_+ \psi_{p_0+2}, \quad \psi_{p_0-1} = \gamma_- \psi_{p_0-2} \tag{3.8}$$

where γ_+ and γ_- are less than 1 and are also specified as inputs. The rest of the contour

levels are determined by the exponentially stretching function.

$$\begin{cases} \psi_p = \psi_{p_0+2} + (\psi_{\max} - \psi_{p_0+2}) \dfrac{\exp\left(\frac{p-p_0-2}{n_\psi - p_0 - 2}\alpha_\psi\right) - 1}{\exp(\alpha_\psi) - 1} & \text{if } p > p_0 + 2 \\ \psi_p = \psi_{p_0-2} + (\psi_{\min} - \psi_{p_0-2}) \dfrac{\exp\left(\frac{p_0-2-p}{p_0-3}\alpha_\psi\right) - 1}{\exp(\alpha_\psi) - 1} & \text{if } p < p_0 - 2 \end{cases} \tag{3.9}$$

For the scalar potential, q_0 is determined in the same manner as Eq. (3.6) such that $\phi_{q_0} = 0$. However, the contour levels are determined solely with the exponentially stretching function.

$$\begin{cases} \phi_q = \phi_{\max} \dfrac{\exp\left(\frac{q-q_0}{n_\phi - q_0}\alpha_\phi\right) - 1}{\exp(\alpha_\phi) - 1} & \text{if } q > q_0 \\ \phi_q = \phi_{\min} \dfrac{\exp\left(\frac{q_0-q}{q_0-1}\alpha_\phi\right) - 1}{\exp(\alpha_\phi) - 1} & \text{if } q < q_0 \end{cases} \tag{3.10}$$

where α_ϕ is the stretching parameter for ϕ specified as an input. In order to reduce the element size at a null point, we choose the null point to be a node. This is ensured by replacing the ψ and ϕ contour levels that are the closest to the values at the null point (ψ_{null} and ϕ_{null}) with those values. Even with the determination of contour levels by Eqs. (3.8) and (3.9), the resolution near the domain axis may still be undesirable. This condition occurs when the ratio of the maximum to the minimum magnetic field strength is large: more specifically, when a magnet is placed too close to the boundary in a ring-cusp discharge chamber. In this case, we simply manipulate those large elements rather than trying to control them directly by Eqs. (3.8) and (3.9). The mesh is first constructed with a simple stretching function for ψ similar to Eq. (3.10), which results in an even larger element size near the domain axis. After the baseline mesh is constructed, the near-axis elements are split into multiple elements.

3.2.2.4 Determination of Node Points

The nodes are simply placed at the intersections between the stream function and the scalar potential contour lines that are determined based on the set of levels we specified previously. Based on ψ and ϕ that are computed using Eqs. (3.2) and (3.3) on the uniform mesh, we use the marching squares algorithm to approximate the contour lines. Each cell of the uniform mesh has four corners with ψ and ϕ values stored. The locations where the ψ and ϕ contour lines intersect with each cell boundary are determined by linear interpolation using the ψ and ϕ values stored at the ends of the cell facet (Fig. 3.2(a)). The number of intersections with the cell of the uniform mesh is always an even number (most likely two) as a contour line cannot terminate within a cell. All the segments of the contour lines within a cell are approximated as straight lines (Fig. 3.2(b)). If the contour lines for both ψ and ϕ are through the cell, there is a possibility that the two lines intersect within the cell. The intersection condition is checked by comparing the location of the four points and then utilizing the cross-product. Once we find that the two lines intersect, the determination of the intersection point is trivial (Fig. 3.2(c)). This process is repeated for all the cells in the uniform mesh. After all the interior nodes are located, then the nodes at the domain boundaries are determined. Unlike the case for the interior cells, the intersection with any contour line with a domain boundary is located using linear interpolation. Finally, additional information such as the indices for ψ and ϕ levels and the connectivity between nodes is stored to be utilized in the creation

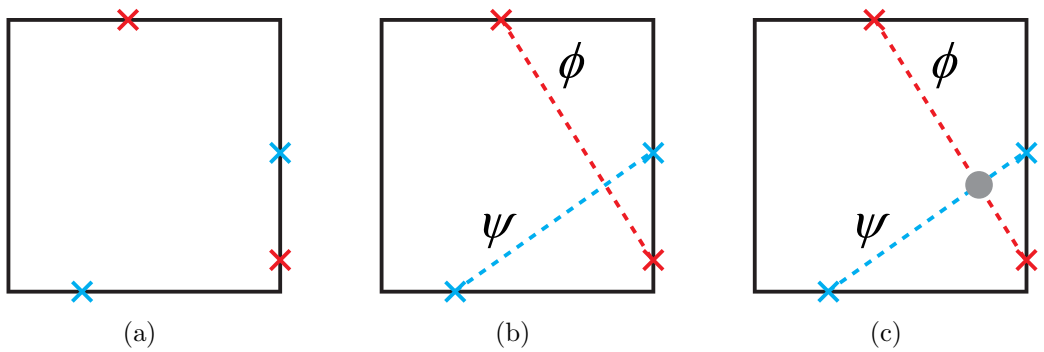

Figure 3.2: Process of node creation. (a) The intersections of the ψ and ϕ contour lines with the cell boundaries are determined using linear interpolation. (b) The contour lines within the cell are approximated as straight lines. (c) A node is placed at the intersection of the contour lines.

process of the MFA mesh elements. The connectivity information is based on the levels for the ψ and ϕ contours and the distance. Any interior node, except the null node, with contour levels of (ψ_p,ϕ_q) has four adjacent nodes with levels of (ψ_p,ϕ_{q+1}), (ψ_{p+1},ϕ_q), (ψ_p,ϕ_{q-1}), and (ψ_{p-1},ϕ_q). In many configurations, there exist multiple nodes with the same ψ and ϕ levels within the entire domain, and the appropriate adjacent node is chosen by comparing the distances between the nodes.

3.2.2.5 Creation of Cell Elements

Once all the node points are determined, these nodes need to be connected properly to create the MFA mesh elements. The process of the element creation involves tracing of the node points based on the node connectivity information to find a polygon that does not enclose any other node point. Starting from one interior node that does not correspond to a null node, we move along the adjacent nodes in the counterclockwise direction in ψ-ϕ coordinate system (e.g. in the order of (ψ_p,ϕ_q), (ψ_p,ϕ_{q+1}), (ψ_{p+1},ϕ_{q+1}), and (ψ_{p+1},ϕ_q)) until reaching the initial node of each tracing (Fig. 3.3(a)). As there are four adjacent nodes associated with the interior node, the tracing for one interior node is done four times, each time first going to a different adjacent node. Although tracing four times for each interior node is often redundant and results in multiple-counting of the same element, this ensures no miscounting of the MFA mesh element. Special treatment has to be made for the case of the null node and the boundary node during the process of node tracing. At the null node, there are always two possible choices for the next node; there is a total of eight nodes adjacent to the null node with four pairs of nodes at the same level of ψ and ϕ (Fig. 3.3(b)). For boundary nodes, simply going along the nodes with the four combinations of ψ and ϕ levels cannot be applied because the domain boundary typically cuts through the quadrilateral MFA cell element, resulting in irregular elements with the number of facets ranging from three to six. Therefore, we take into account the physical location of nodes in addition to the ψ and ϕ levels. Starting from a node $j-1$ during the node tracing process, let the first adjacent node be a null node or a boundary node j. Then the next node $j+1$ is determined by choosing an adjacent node that gives the smallest positive angle in counterclockwise direction between

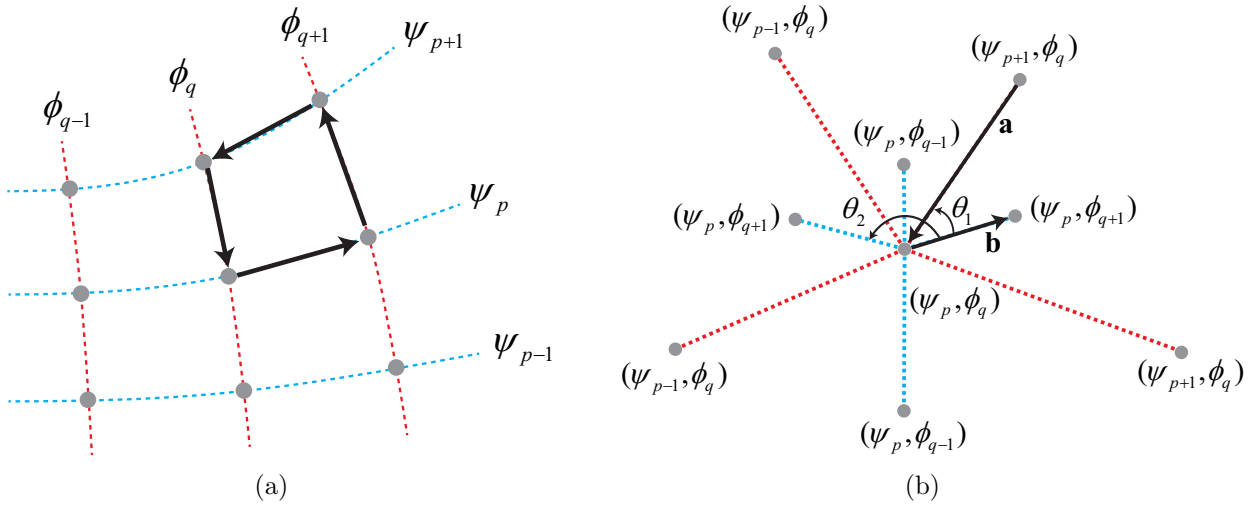

Figure 3.3: Creation process of a MFA mesh element. (a) Nodes are traced in the counterclockwise direction in ψ-ϕ coordinate system. (b) Choosing the appropriate next node from a null node by comparing the angles.

two vectors, $\mathbf{a} = \mathbf{x_j} - \mathbf{x_{j-1}}$ and $\mathbf{b} = \mathbf{x_{j+1}} - \mathbf{x_j}$. The angle can easily be determined by utilizing the dot product and the cross product.

After creating the MFA mesh elements with appropriate nodes associated with them, the rest is a matter of cleaning up the information stored in the element data structure and obtaining additional information that can be useful in the actual computation of a solution with the mesh. The node numbers stored in each element is reordered in the counterclockwise order. First, we find the node that is the closest to the origin. Then, the next node is chosen by the smallest positive angle in counterclockwise direction using the dot product and the cross product between the vectors, $\mathbf{a}$ and $\mathbf{b}$, as defined previously. When the second node is to be determined, vector $\mathbf{a}$ is chosen to be $\mathbf{a} = -\epsilon\hat{z} - \epsilon\hat{r} - \mathbf{x_1}$ where ϵ is a very small number greater than zero; this ensures $\mathbf{a} \neq 0$ when at the origin. The additional information to be stored includes elements attached to a node and elements adjacent to an element. The information can easily be obtained by the node numbers stored for each element. For example, an element adjacent to the element of interest can be found by finding an element that shares the same two nodes. Finally, boundary elements are added at the midpoints of two adjacent boundary nodes. The boundary elements are used to simplify the numerical procedure in computing the solution.

3.2.2.6 Post Processing: Improvements on Mesh Quality

The procedure described above is sufficient to generate a MFA mesh that can be used for a plasma simulation in a magnetic field. However, the MFA mesh does not always produce a result that is more accurate than a solution obtained with a uniform mesh, especially for a complex magnetic field configuration. The accuracy of the numerical solution is dependent on many factors including the problem to be solved, the mesh quality, and the alignment of the mesh [188]. The quality of a mesh is often determined by geometric factors such as smoothness, aspect ratio, and skewness [189, 190]. The smoothness describes the degree of change in element sizes. A large jump in size from an element to its neighboring element is typically not preferable. On the other hand, the aspect ratio is simply the ratio of the maximum to the minimum element edge length, and the skewness is based on the maximum and the minimum interior angles of an element. Mesh elements with the similar edge lengths and the similar interior angles are often preferable for a better mesh quality. The MFA mesh sacrifices the mesh quality to achieve the alignment with the magnetic field. The inaccuracy in the numerical solution using the MFA mesh is likely caused by the poor mesh quality near the simulation boundaries. The domain boundary always cuts through a quadrilateral element that has two facets parallel to and the others perpendicular to the magnetic field. While the elements near the boundary can have the number of facets more or less than four, this typically results in poor smoothness of the grid. In addition, these elements may have undesirable aspect ratio and skewness.

There are many ways to improve the quality of the MFA mesh. The current version of the routine simply relocates the boundary nodes and the nodes adjacent to the boundaries. The boundary nodes are moved such that the element edges intersecting with the boundaries are orthogonal to the boundary. This process can result in three-sided elements to be two-sided, and these elements are removed from the grid (Fig. 3.4(a)). Then, the five-sided elements are split into two elements with three and four facets (Fig. 3.4(b)). The interior node adjacent to the boundary is relocated to the centroid of the polygon consisting of all the elements

attached to the node (Fig. 3.4(c)).

$$\mathbf{x_c} = \frac{\sum_{k=1}^{N} \mathbf{x_k} A_k}{\sum_{k=1}^{N} A_k} \tag{3.11}$$

where $\mathbf{x_c}$ is the location of a centroid, A is the area of an element, N is the number of attached elements, and the subscript k denotes the index for the attached element. Meanwhile, the boundary nodes are moved to maintain the orthogonality. The relocation of a node affects the attached element shapes and the centroid locations for the neighboring nodes. Therefore, the process is repeated until the locations are consistent for all the interior nodes adjacent to the boundary nodes. The grid quality improvement method in this study is still preliminary and can be improved much further. However, a further improvement is beyond the scope of this thesis.

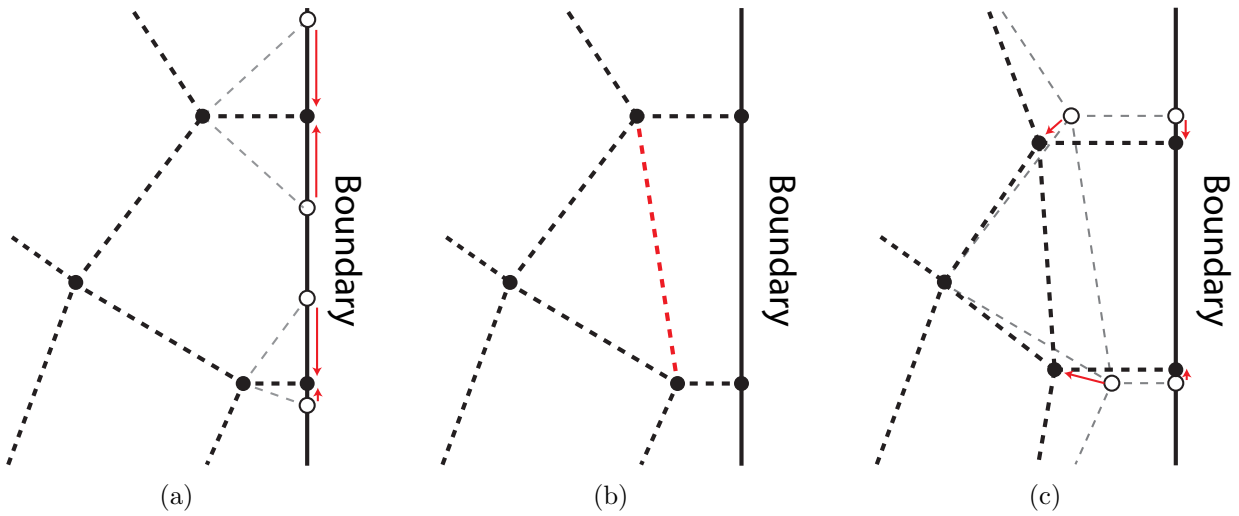

Figure 3.4: Grid quality improvement method used in the model. Opened circles are at the original node locations. (a) Boundary nodes are relocated so the element edge is orthogonal to the boundary. Then, the two-sided elements are removed. (b) Five-sided elements are split into two elements. (c) Interior nodes adjacent to the boundary nodes are relocated to the centroids of the polygons consisting of elements attached to the nodes.

3.2.2.7 Visualization of Generation Process

Some intermediate steps in the mesh generation are shown here to help readers visualize the process. We start with the magnetic field configuration similar to the configuration in a ring-cusp discharge chamber as shown in Fig. 3.5. Using the magnetic field information, the stream function and the scalar potential are numerically evaluated by Eqs. (3.2) and (3.3) on a fine uniform mesh (Figs. 3.6(a) and 3.6(b)). Then, the contour levels are adjusted based on the exponentially stretching function given in Eqs. (3.8) to (3.10) (Figs. 3.7(a) and 3.7(b)). In this example, we have used $n_\psi = 21$, $n_\phi = 21$, $\alpha_\psi = 2$, and $\alpha_\phi = 1$. Although the spacing of the ϕ contour levels is not significantly altered, it is readily seen that the ψ contour levels have become more uniformly distributed in radial direction. Since both the two null points are located along the domain axis, the contour level is not altered based on the contour levels at the null points. Figures 3.8(a) and 3.8(b) plot the overlay of the contour lines for ψ and ϕ shown in Figs. 3.6 and 3.7, respectively. Using the exponentially stretching function, the maximum element size is reduced significantly, which aids in improving the overall mesh quality. The intersections of the contour lines are assigned as the nodes for the MFA mesh, which is evaluated using the combination of the marching squares algorithm and efficient intersection calculation method (Fig. 3.9(a)). Finally, all the nodes are connected properly to create the MFA mesh elements (Fig. 3.9(b)).

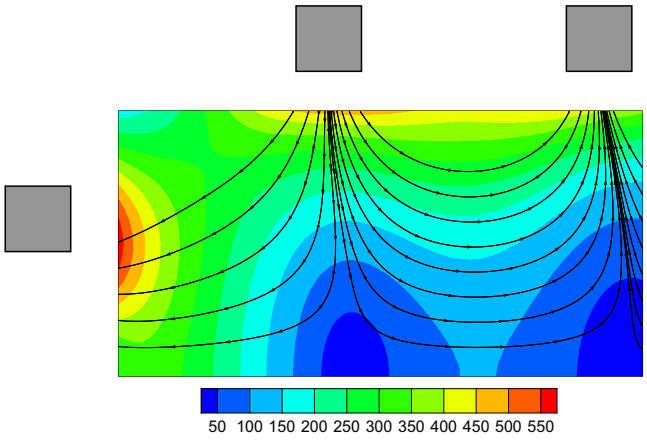

Figure 3.5: A magnetic field configuration similar to the configuration in a ring-cusp discharge chamber. The figure plots the contour of the magnetic field strength in Gauss, overlaid with the magnetic field lines.

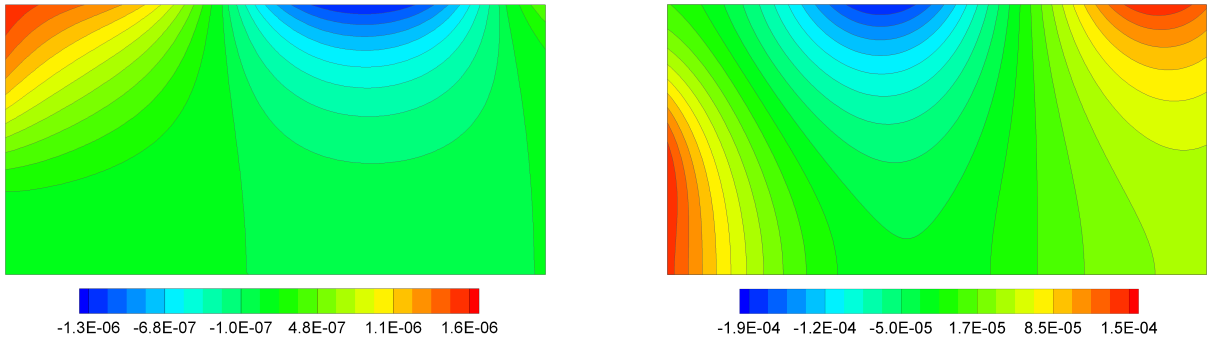

(a) (b)

Figure 3.6: (a) Stream function and (b) scalar potential computed on a very fine uniform mesh. Contour levels are distributed uniformly.

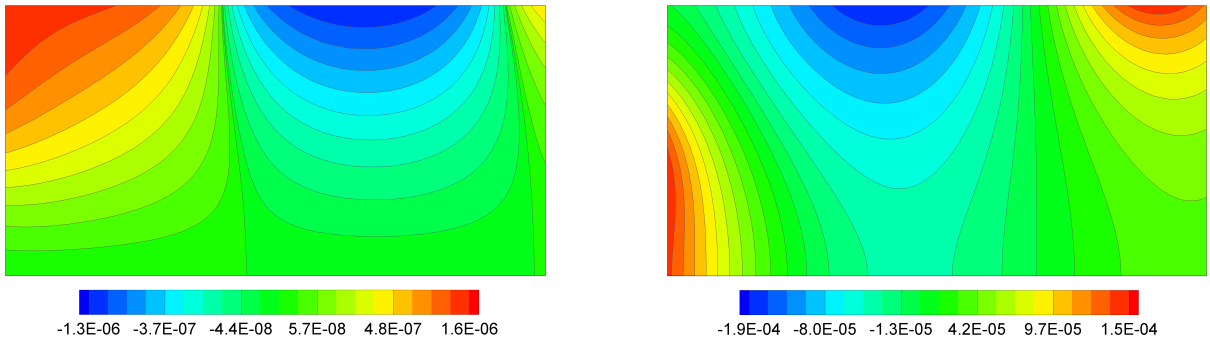

(a) (b)

Figure 3.7: (a) Stream function and (b) scalar potential computed on a very fine uniform mesh. Contour levels are adjusted based on the exponentially stretching function.

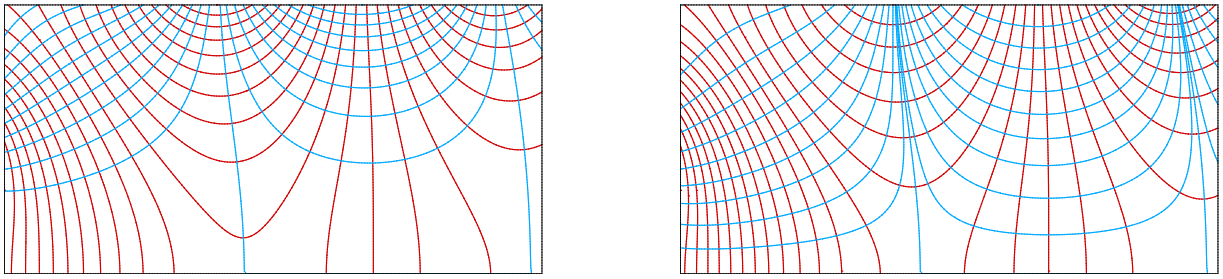

(a) (b)

Figure 3.8: Overlay of contour lines for contour levels that are (a) uniformly distributed and (b) determined based on exponentially stretching function.

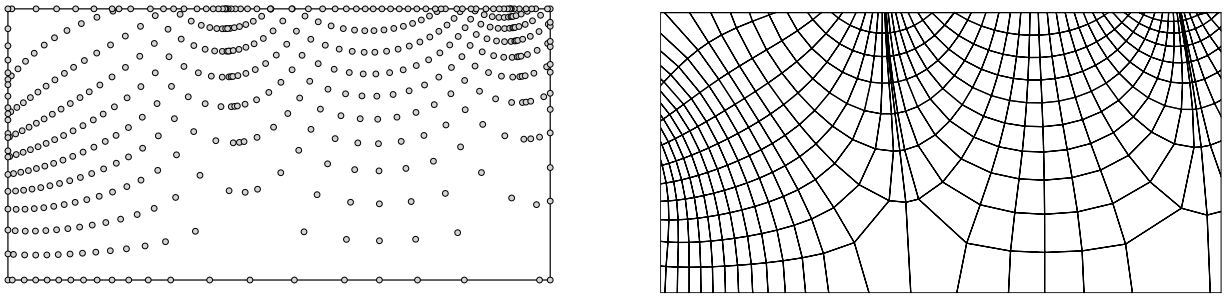

(a) (b)

Figure 3.9: (a) Node points determined by finding the intersections of the contour lines shown in Fig. 3.8(b). (b) These nodes are properly connected to create the baseline MFA mesh.

3.2.3 MFA Meshes for Various Field Configurations

The mesh generation routine has been benchmarked against various magnetic field configurations. In this test, the number and the placement of magnets are varied to see when the routine succeeds in the MFA mesh generation. Manipulation of the near-boundary elements to improve the mesh quality is not performed, so the MFA meshes shown here are not intended to be used for the actual numerical investigation. Under many different field configuration that are applicable to the ring-cusp discharge, meshes are generated successfully. These include configurations shown in Fig. 3.10. In general, the routine works very well with fewer magnets (i.e. two or three magnets), as long as appropriate input parameters controlling the mesh are used. The number of contour levels, n_ψ and n_ϕ, has to be sufficient that an element near the null point is small enough. In addition, the stretching factors, α_ψ and α_ϕ, need to be greater than one when the ratio of the maximum to the minimum magnetic field is large for the same reason. The lines corresponding to $\psi = 0$ originate right at the magnetic cusps, while the axis of the domain also corresponds to the line of $\psi = 0$. These lines can connect at the null point along the centerline (Figs. 3.10(a) to 3.10(c)). A field line originated at a location slightly off from $\psi = 0$ line near the cusp may not approach nearly close to the axis. This means that the element size near the domain axis is inevitably large, which prevents the routine from properly connecting the nodes when creating mesh elements. A larger value for the stretching parameter α_ψ tends to push the line toward the

line of $\psi = 0$. However, the parameter also result in elements with very high aspect ratio near the magnets (Figs. 3.10(b) to 3.10(d)). Even if the mesh generation succeeds with a larger value for α_ψ, the elements in the region are typically still too large and require further refinement (Figs. 3.10(a) to 3.10(c)). With increasing number of magnets, it becomes even harder for the routine to correctly generate a MFA mesh. This is likely attributed to the number and location of the null points. In a configuration in which null points lie on the domain axis and are close to each other, the mesh elements in those regions tend to be even larger. Furthermore, it is more difficult to identify the appropriate lines of ψ and ϕ that correspond to an element. More specifically, the lines of $\psi = 0$ can be next to each other,

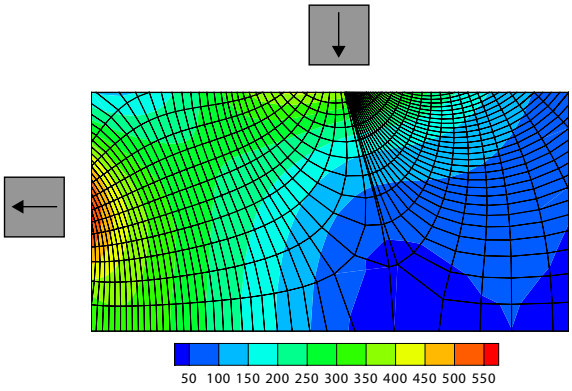

(a) 2-magnet configuration.

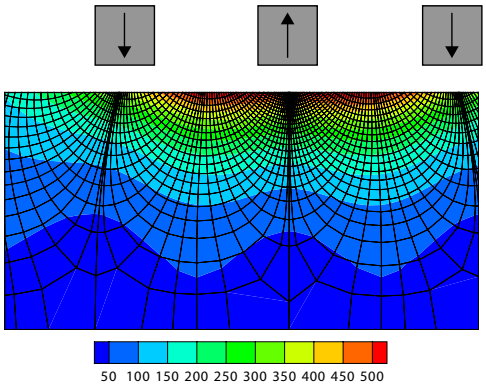

(b) 3-magnet configuration without an upstream magnet.

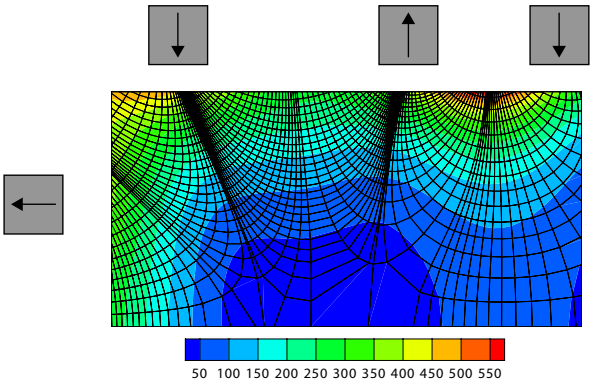

(c) 4-magnet configuration.

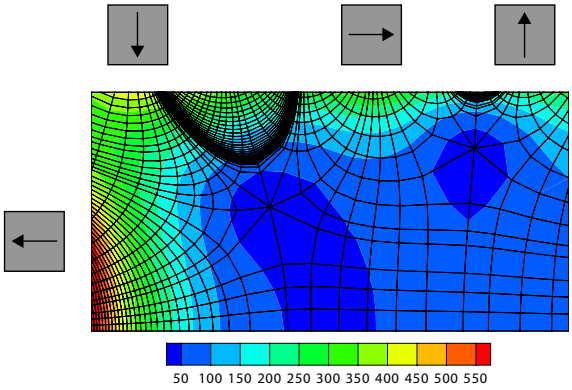

(d) 4-magnet configuration.

Figure 3.10: MFA meshes generated for various ring-cusp discharge-like magnetic field configurations. The length and the radius of the domain are set to two and one centimeter, respectively. The contours represent the magnetic field strength in Gauss. Mesh improvement on the near-boundary elements is not performed.

and choosing nodes in the order of contour levels of (ψ_p,ϕ_q), (ψ_p,ϕ_{q+1}), (ψ_{p+1},ϕ_{q+1}), and (ψ_{p+1},ϕ_q) can be impossible with the current version. It should be noted that the current routine always works up until determining the connectivity between nodes, and the rest should be relatively easy to refine for more rigorous MFA mesh generation routines.

3.3 Numerical Method for Solving Plasma Diffusion Equation in a MFA Mesh

3.3.1 Introduction

The MFA meshes for ring-cusp discharge configurations are typically irregular due to the null node and the domain boundaries cutting through the quadrilateral elements in the flux-aligned coordinate. The number of element facets can vary from three to six, and the number of elements attached to a node can be greater than four. The mesh quality improvement method for near-boundary elements discussed in Sec. 3.2.2.6 removes the elements with more than four edges, while the method creates additional nodes that are attached to more than four elements. In order to use such complex meshes to evaluate the plasma diffusion equation, it was necessary to refine the method described in Ref. [13]. The following sections introduce the plasma diffusion equation to be solved (Sec. 3.3.2) and the numerical method used to solve the equation in a MFA mesh (Sec. 3.3.3). Then, the plasma diffusion equation is numerically solved in a uniform mesh for a simple configuration to validate the numerical method (Sec. 3.3.4). Finally, the combination of the MFA mesh and the numerical method is applied to single-cusp and discharge-like configurations to show the order of convergence and discuss the benefit of the MFA mesh (Sec. 3.3.5).

3.3.2 Plasma Diffusion Equation

The plasma diffusion equation to be solved is based on the formulation by Koch and Matthieussent [103]. In this formulation, the conservations of mass and momentum equations for singly charged ions and electrons are combined, assuming the same diffusion rates

for singly charged ions and electrons due to the ambipolar field [13, 185]. It also assumes a quasi-neutral ($n_i = n_e$), diffusive ($\mathbf{u} \cdot \nabla \mathbf{u} = 0$), and ideal plasma ($\nabla p = k\nabla(nT)$) where n is the density, $\mathbf{u}$ is the velocity, p is the pressure, T is the temperature, k is the Boltzmann constant, and the subscripts i and e denote ions and electrons, respectively. Further assumptions are made such that ions dominate the mass and momentum diffusion, and the perpendicular electric field is "short-circuited," yielding an approximation of $E_\perp = 0$. With all of these assumptions, the governing equations reduce to the Poisson's equation.

$$\dot{n}_i = -\nabla \cdot (\mathbf{M_i} \nabla(nT_i) + \mathbf{M_e} \nabla(nT_e)) \tag{3.12}$$

where

$$\mathbf{M_i} = \begin{bmatrix} M_i & 0 \\ 0 & M_i^\perp \end{bmatrix}, \quad \mathbf{M_e} = \begin{bmatrix} M_e & 0 \\ 0 & M_{e,\text{eff}}^\perp \end{bmatrix}$$

$$M_i = \frac{\mu_e \mu_{ii} + \mu_i \mu_{ei}}{\mu_e + \mu_i}, \quad M_i^\perp = \frac{\mu_e \mu_{ii}^\perp + \mu_i \mu_{ei}^\perp}{\mu_e + \mu_i}, \quad M_e = \frac{\mu_e \mu_{ie} + \mu_i \mu_{ee}}{\mu_e + \mu_i}, \quad M_e^\perp = \frac{\mu_e \mu_{ie}^\perp + \mu_i \mu_{ee}^\perp}{\mu_e + \mu_i}$$

$$M_{e,\text{eff}}^\perp = \frac{\nu_{e-o}}{\nu_{e-o} + \gamma_{nc}\nu_{e-i}} M_e^\perp + \frac{\gamma_{nc}\nu_{e-i}}{\nu_{e-o} + \gamma_{nc}\nu_{e-i}} M_B^\perp$$

Here, $\dot{n}_i$ is the ion generation rate density, μ and ν are the mobility and frequency, respectively, defined in Ref. [13]. The mobility tensor, $\mathbf{M}$, is defined here in the field aligned coordinate, and the superscript $\perp$ denotes the direction perpendicular to the field while the superscript $\parallel$ is dropped for simpler expressions. Note that the expression for mobilities are dependent on the plasma density, n. The effective perpendicular mobility coefficient for electron, $M_{e,\text{eff}}^\perp$, includes the effect of non-classical mobility ($M_B^\perp$=k/(16eB)) with the mixing parameter γ_{nc} of 1/4 to better approximate the plasma behavior in the weakly ionized regime applicable to the ion thruster. At any wall boundary, it is assumed that the plasma is lost at the ion acoustic speed, $u_w = \sqrt{kT_e/m_i}$. This assumption may not be completely applicable at a boundary with a magnetic field at a finite angle with respect to the direction normal to the boundary surface, as the electron motion should greatly be impeded in the perpendicular direction. However, the precise plasma loss condition is not well-known in an oblique magnetic field; thus, we simply use the assumption for the entire domain boundary.

3.3.3 Numerical Method

The final plasma density solution is obtained iteratively when the 2-norm of the difference in the density solutions between previous and current steps becomes smaller than some tolerance, ϵ. The iterative calculation is necessary since the mobility tensors are dependent on the plasma density to be determined. Starting from an initial guess for the plasma density, the mobility tensors are computed, and then the density is updated by solving Eq. (3.12) using the finite volume method. These calculations are repeated until the density converges to a solution.

In numerically solving Eq. (3.12), the computational method has to be compatible with many unique features of the MFA mesh. As discussed above, a domain boundary cuts through a quadrilateral element in the flux aligned coordinate, resulting in poor mesh quality near the boundary. In order to improve the mesh, splitting of the five-sided cell is performed, which can result in irregular number of elements attached to a node (greater than four). In addition, the number of elements attached to an interior null node is always eight. Therefore, a variable number of stencils is needed to be used in setting up the difference equations. Furthermore, the method has to work with both the aligned and unaligned mesh elements due to the elements near the boundary; the grid quality improvements of those elements often result in element edges that are unaligned with the field. Therefore, the numerical method is set up for an unaligned mesh, which automatically reduces to the method for an aligned mesh in the limit that the angle between the field and the element face normal, θ, is zero.

For simplicity, consider a model equation similar to Eq. (3.12),

$$\dot{n}_i = -\nabla \cdot [\mathbf{M} \nabla Q] = -\nabla \cdot \mathbf{\Gamma} \tag{3.13}$$

where $Q = nT$ and $\mathbf{\Gamma}$ is the flux given as $\mathbf{\Gamma} = \mathbf{M}\nabla Q$. Equation (3.13) will be used in derivation of the numerical method, which can easily be extended for Eq. (3.12).

3.3.3.1 Mobility Tensor

The mobility tensor defined in the field aligned coordinate, $\mathbf{M_b}$, needs to be expressed in terms of the grid aligned coordinate, $\mathbf{M_g}$, where the subscripts b and g denote the magnetic field and the grid, respectively. Starting from the relations between the flux and ∇Q in the field aligned coordinate ($\mathbf{\Gamma_b} = \mathbf{M_b}\nabla_b Q$), this can be accomplished by the rotation of the coordinate system utilizing the rotation matrix, $\mathbf{R}$, defined as

$$\mathbf{R} = \begin{bmatrix} \cos\theta & \sin\theta \\ -\sin\theta & \cos\theta \end{bmatrix} \tag{3.14}$$

Here, θ is the angle from the element face normal to the magnetic field in the clockwise direction. The transformation between the two coordinates is simply performed as $\mathbf{\Gamma_b} = \mathbf{R}\mathbf{\Gamma_g}$ and $\nabla_b Q = \mathbf{R}\nabla_g Q$ so that the relationship between $\mathbf{\Gamma}$ and Q can be expressed in the grid aligned coordinate.

$$\begin{pmatrix} \Gamma_n \\ \Gamma_s \end{pmatrix} = -\begin{bmatrix} M_A & M_B \\ M_B & M_C \end{bmatrix} \begin{pmatrix} \dfrac{\partial Q}{\partial n} \\ \dfrac{\partial Q}{\partial s} \end{pmatrix} \tag{3.15}$$

where

$$\begin{aligned} M_A &= M_{\parallel}\cos^2\theta + M_{\perp}\sin^2\theta \\ M_B &= (M_{\parallel} - M_{\perp})\sin\theta\cos\theta \\ M_C &= M_{\parallel}\sin^2\theta + M_{\perp}\cos^2\theta \end{aligned} \tag{3.16}$$

Here, n and s are the unit vectors in the direction normal and tangent to the element face of interest, respectively. When the grid is aligned with the magnetic field, $\theta = 0$ so that the off-diagonal terms in the mobility tensor vanish.

3.3.3.2 Finite Volume Method

The finite volume method is used to solve Eq. (3.13). Integrating Eq. (3.13) over a control volume and applying the divergence theorem on the right hand side, the equation becomes

$$\int_V \dot{n}_i dV = \oint_A \mathbf{\Gamma} \cdot \mathbf{dA} = -2\pi \left(M_A \oint_A r \frac{\partial Q}{\partial n} ds + M_B \oint_A r \frac{\partial Q}{\partial s} ds \right) \tag{3.17}$$

where ds is in the counterclockwise direction along the control volume. Equation (3.17) is applied to each MFA mesh element with the control volume boundary corresponding to the element facets. By taking an element facet to be a straight line, the location on the element boundary (z,r) can be parametrized.

$$\begin{pmatrix} z \\ r \end{pmatrix} = \begin{pmatrix} z_1 \\ r_1 \end{pmatrix} + t \begin{pmatrix} \Delta z \\ \Delta r \end{pmatrix} \tag{3.18}$$

where $\Delta z = z_2 - z_1$, $\Delta r = r_2 - r_1$, the subscripts 1 and 2 denote the beginning and the end of the element facet in counterclockwise direction, respectively, and t is a parameter ranging between 0 and 1. Using this parametrization, the differential element along the element facet can be expressed as $ds = ldt$ where l is the length of the element facet. Then, Eq. (3.17) can be rewritten as

$$\dot{n}_i V_k = -2\pi l \sum_{i=1}^{N} \left[M_{A,i} \int_i (r_1 + t\Delta r) \frac{\partial Q}{\partial n} dt + M_{B,i} \int_i (r_1 + t\Delta r) \frac{\partial Q}{\partial s} dt \right] \tag{3.19}$$

Here, N is the number of facets and the subscripts k and i denote the element of interest and the index of a facet associated with the kth element, respectively. The mobilities, M_A and M_B, are evaluated at the midpoint of the facet and are assumed to be constant along the facet.

3.3.3.3 Gradient across Element Facet

The gradient across the element facet, $\partial Q/\partial n$, is approximated with the first-order difference equation. Let the mth element be the element directly across the facet as illustrated in Fig. 3.11. The unit vector from the kth to mth element centroids, $\hat{i}_{km}$, does not necessarily align with the vector normal to the element facet, $\hat{n}$. Therefore, the finite difference equation has to take into account this misalignment.

$$\frac{\partial Q}{\partial n} = \frac{Q_m - Q_k}{l_{km}} \cos\alpha \tag{3.20}$$

where l_{km} is the distance between the kth and mth element centroids. The angle, α, between $\hat{n}$ and $\hat{i}_{km}$ is determined by taking the dot product of the two unit vectors.

$$\cos\alpha = \hat{n} \cdot \hat{i}_{km} = \frac{\Delta r \Delta z_{km} - \Delta z \Delta r_{km}}{l \cdot l_{km}} \tag{3.21}$$

with $\Delta z_{km} = z_m - z_k$ and $\Delta r_{km} = r_m - r_k$. The angle α is nearly zero when the MFA mesh is perfectly aligned with the magnetic field except near the domain boundaries. Assuming that $\partial Q/\partial n$ is constant along the facet, one of the two integral terms in Eq. (3.19) simply reduces to

$$\int_0^1 (r_1 + t\Delta r)\frac{\partial Q}{\partial n} dt = \frac{r_1 + r_2}{2}\frac{Q_m - Q_k}{l_{km}} \cos\alpha \tag{3.22}$$

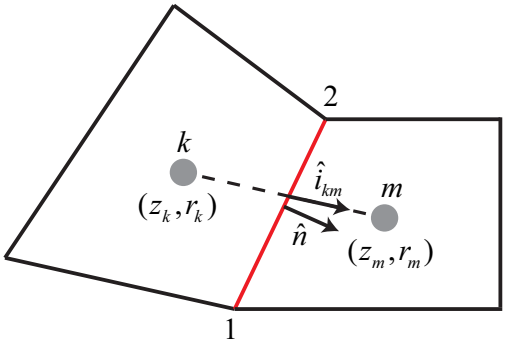

Figure 3.11: Stencils for obtaining a partial derivative in a direction normal to the facet of interest.

During the initial development, dropping the cosine term in Eq. (3.22) produced a slightly more preferable result, although the reason for this is still under investigation. Note that the results given in Sec. 3.3.5 were obtained without the cosine term.

3.3.3.4 Gradient along Element Facet

The difficulty comes in when approximating the gradient along the element facet, $\partial Q/\partial s$. Technically, $\partial Q/\partial s$ can also be approximated by the first-difference equation if the quantity Q at the nodes 1 and 2 is known (see Fig. 3.11). In the original model developed by Wirz [13], the quantity at a node was calculated by a simple bilinear interpolation from the values at the four elements attached to the node. However, this method can no longer be applied if the number of attached elements is more than four. The method developed herein utilizes the 2D quadratic equation to approximate the variation in the quantity, Q, along the element facet.

$$Q = Q_k + a\Delta z_k + b\Delta r_k + c\Delta z_k^2 + d\Delta z_k \Delta r_k + e\Delta r_k^2 \tag{3.23}$$

where the subscript k again denotes the element of interest, $\Delta z_k = z - z_k$, and $\Delta r_k = r - r_k$. Equation (3.23) has also been used by Fox [159] in his electric potential solver. By taking the partial derivative with respect to tangent direction $\hat{s}$ and using the chain rule, an expression for $\partial Q/\partial s$ can be obtained.

$$\begin{aligned}\frac{\partial Q}{\partial s} &= -\sin\beta \frac{\partial Q}{\partial \Delta z} + \cos\beta \frac{\partial Q}{\partial \Delta r} \\ &= -\sin\beta(a + 2c\Delta z_k + d\Delta r_k) + \cos\beta(b + d\Delta z_k + 2e\Delta r_k)\end{aligned} \tag{3.24}$$

where β is the angle from the axis of symmetry to the grid aligned coordinate in the clockwise direction.

$$\begin{pmatrix} \hat{z} \\ \hat{r} \end{pmatrix} = \begin{bmatrix} \cos\beta & -\sin\beta \\ \sin\beta & \cos\beta \end{bmatrix} \begin{pmatrix} \hat{n} \\ \hat{s} \end{pmatrix} \tag{3.25}$$

Equation (3.24) describes the variation in the gradient along the element facet and can be integrated analytically.

$$\begin{aligned}\int_0^1 (r_1 + t\Delta r)\frac{\partial Q}{\partial s}dt = &\left(r_1 + \frac{1}{2}\Delta r\right)(-a\sin\beta + b\cos\beta) \\ &+ \left(r_1(z_1 - z_k) + \frac{1}{2}\left[\Delta r(z_1 - z_k) + \Delta z r_1\right] + \frac{1}{3}\Delta r\Delta z\right)(-2c\sin\beta + d\cos\beta) \\ &+ \left(r_1(r_1 - r_k) + \frac{1}{2}\left[\Delta r(2r_1 - r_k)\right] + \frac{1}{3}\Delta r^2\right)(-d\sin\beta + 2e\cos\beta) \qquad (3.26)\end{aligned}$$

Note that both Eqs. (3.22) and (3.26) reduce to zero along the axis of symmetry, thus automatically satisfying the boundary condition of $\Gamma = 0$. The boundary elements are placed along the line of the facet. Therefore, we simply use the first order difference equation to approximate $\partial Q/\partial s$ at the wall boundary. Here, let m be the boundary element number that is placed at the midpoint of the facet. Then, the gradient at the mth boundary element is given as

$$\begin{aligned}\frac{\partial Q}{\partial s} = &\frac{\Delta s_{m-1/2}}{\Delta s_{m+1/2}(\Delta s_{m-1/2} + \Delta s_{m+1/2})}Q_{m+1} \\ &+ \frac{\Delta s_{m+1/2} - \Delta s_{m-1/2}}{\Delta s_{m+1/2}\Delta s_{m-1/2}}Q_m - \frac{\Delta s_{m+1/2}}{\Delta s_{m-1/2}(\Delta s_{m-1/2} + \Delta s_{m+1/2})}Q_{m-1} \qquad (3.27)\end{aligned}$$

where $\Delta s_{m+1/2}$ is the distance between the boundary elements $m+1$ and m, $\Delta s_{m-1/2}$ is the distance between the boundary elements m and $m-1$, and the boundary elements are counted in the counterclockwise direction. Assuming $\partial Q/\partial s$ is constant along the element facet, the other integral term in Eq. (3.19) becomes

$$\int_0^1 (r_1 + t\Delta r)\frac{\partial Q}{\partial s}dt = \frac{r_1 + r_2}{2}\frac{\partial Q}{\partial s} \qquad (3.28)$$

where $\partial Q/\partial s$ is given by Eq. (3.27). Solving Eqs. (3.22),(3.26) and (3.28) for each facet, an equation for each element can be obtained from Eq. (3.19). During the initial development of the model, the 2D quadratic equation Eq. (3.23) was also applied in the evaluation of $\partial Q/\partial n$. However, this resulted in an unstable method, causing the solution to be less convergent in some magnetic configurations. Therefore, the order of the method in the direction normal

to the facet had to be reduced.

In order to solve Eq. (3.26), the coefficients (a, b, c, d, and e) in Eq. (3.23) have to be expressed as a function of Q at different elements. There are five unknowns in Eq. (3.23), so we need to choose at least five elements in addition to the kth element, the element of interest, in order to obtain a unique solution for those coefficients. For the most typical case, there are exactly five additional elements ($m = 1, ..., N$, $N = 5$) attached to an element facet as illustrated in Fig. 3.12(a). The other possible cases with more than five additional elements ($m = 1, ..., N$, $N > 5$) are illustrated in Figs. 3.12(b) and 3.12(c). For any case, we begin by setting up a linear system of equations for the kth element by applying Eq. (3.23)

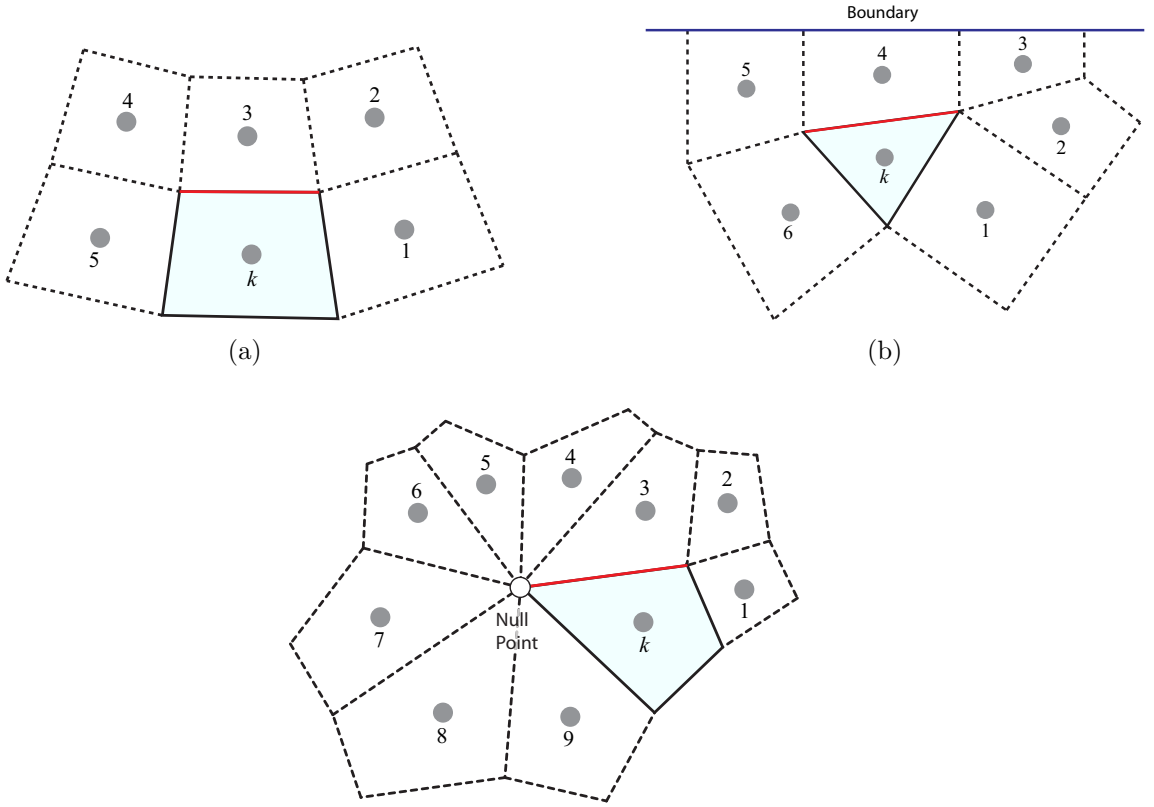

Figure 3.12: The gradient along the element facet (solid line in red) is computed using all the elements attached to the facet. The number of attached elements in addition to the element of interest is (a) $N = 5$ in most cases, (b) $N = 6$ for some elements in near-boundary region, and (c) $N = 9$ near the null point. The case with $N = 7$ is also possible.

at all the other N elements attached to the element facet.

$$Ax = f \tag{3.29}$$

where

$$A = \begin{bmatrix} \Delta z_{k1} & \Delta r_{k1} & \Delta z_{k1}^2 & \Delta z_{k1} r_{k1} & \Delta r_{k1}^2 \\ \vdots & \vdots & \vdots & \vdots & \vdots \\ \Delta z_{kN} & \Delta r_{kN} & \Delta z_{kN}^2 & \Delta z_{kN} r_{kN} & \Delta r_{kN}^2 \end{bmatrix}, \quad x = \begin{pmatrix} a \\ b \\ c \\ d \\ e \end{pmatrix}, \quad f = \begin{pmatrix} \Delta Q_{k1} \\ \vdots \\ \Delta Q_{kN} \end{pmatrix}$$

Here A is a 5-by-N matrix, and x is an array containing the coefficients for the 2D quadratic equation, f is an array containing ΔQ with N elements, and ΔQ is defined in a similar manner as Δz and Δr. The problem reduces to manipulating Eq. (3.29) to express as

$$x = Df \tag{3.30}$$

where D is a N-by-5 matrix. For the regular case where $N = 5$, the matrix A can be directly inverted such that $D = A^{-1}$. However, there are some occasions where the matrix A is ill-conditioned, meaning that accurate calculation of A^{-1} is not possible. The condition always occurs when using a uniform mesh. For this case, we use the singular value decomposition to find a pseudo-inverse [115]. First, the matrix A is decomposed as $A = U\Sigma V^T$ where the 5-by-5 matrices U and V are each orthogonal, and Σ is a 5-by-5 diagonal matrix with diagonal entries w_j. The matrices U, V, and Σ are found using Intel Math Kernel Library (MKL). The singular values are contained in Σ with entries w_j being (numerically) zero. The inverse of Σ is also a diagonal matrix containing $1/w_j$ on the diagonal entries. If Σ contains a diagonal entry with $w_j = 0$, the diagonal entry $1/w_j$ of the inverse matrix blows up approaching ∞; this entry is simply replaced with zero in this method. Let Σ^+ be the inverse of Σ with a singular entry set to zero, then the matrix D (the pseudo-inverse of A)

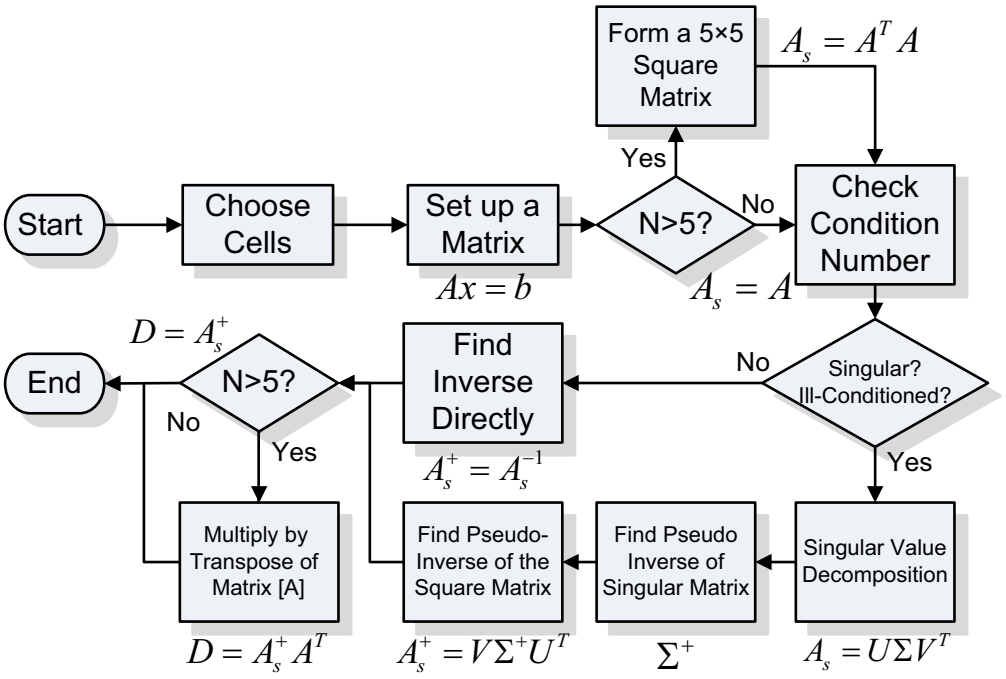

Figure 3.13: A flowchart describing the algorithm to obtain the coefficients for the 2D quadratic equation as a function of element quantities.

is simply calculated by

$$D = V\Sigma^+ U^T \tag{3.31}$$

For other cases where $N > 5$, Eq. (3.29) becomes an over-determined system, and there exists no inverse matrix for the matrix A. In this case, we use the least squares approach, converting the matrix A into a square matrix by multiplying both sides of Eq. (3.29) by A^T. Then, the matrix D to be computed becomes

$$D = (A^T A)^{-1} A^T \tag{3.32}$$

For the case $A^T A$ is not invertible, we again use the singular value decomposition. The methods used to compute the coefficients in Eq. (3.23) are summarized in Fig. 3.13.

3.3.3.5 Boundary Conditions

By utilizing the boundary elements, we can directly compute the densities at the boundaries without using any extrapolation technique afterward. Note that the density at a wall is technically the density before the sheath. The method described above is applied to all the interior elements without considering the boundary conditions. In other words, a flux through an element facet of each interior element is expressed in terms of quantities at neighboring elements, instead of forcing a condition applicable to the specific boundary. Meanwhile, the boundary condition is enforced by the equations set up for the boundary elements. Different boundary conditions are applied at the axis of symmetry and the wall boundary. Across the axis of the domain, a flux should be zero due to axisymmetry. The expression for a flux from the element of interest (denoted by k) to the boundary element (denoted by m) is obtained using the difference equation given by Eq. (3.24) and is equated to zero.

$$\begin{aligned} \Gamma_r = 0 = -M_A \frac{\partial Q}{\partial n} = -M_A \frac{Q_m - Q_k}{l_{km}} \cos\alpha \\ \Rightarrow M_A(Q_m - Q_k) = 0 \end{aligned} \tag{3.33}$$

At the wall boundary, it is assumed that the plasma is lost at the ion acoustic speed, $u_w = \sqrt{kT_e/m_i}$, in a direction perpendicular to the wall. Therefore, the flux normal to the wall is expressed as $\mathbf{\Gamma} \cdot \hat{n} = u_w n_w$. The flux can be approximated in terms of Q at the mth element and two elements directly adjacent to the mth element.

$$\mathbf{\Gamma} \cdot \hat{n} = -\left(M_A \frac{\partial Q}{\partial n} + M_B \frac{\partial Q}{\partial s} \right) = u_{w,m} n_m \tag{3.34}$$

where the partial derivatives are given in Eqs. (3.20) and (3.27).

3.3.3.6 Solving Linear System of Equations

After setting up the equations for all the elements with Eq. (3.19), the linear system of equations can be written in a matrix form such that $Ax = b$ where the components of A are the coefficients of Q, x is an array consisting of the values Q, and b is an array consisting of $\dot{n}V$ at all the element centroids. The linear system equation is solved by the Parallel Direct Sparse Solver Interface (PARDISO) provided in Intel MKL.

3.3.4 Validation in a Simple Configuration

The numerical method for solving the plasma diffusion equation has been validated in a simplified plasma condition and domain so that the numerical solution can be compared with an analytical solution. The analytical solution is extremely difficult to derive in a configuration similar to the ring-cusp discharge; therefore, the domain with no magnetic field is assumed. Note that the solution for a uniform axial magnetic field is exactly in the same form as the solution derived herein except that the density becomes higher. The ionization rate density is taken to be proportional to plasma density to emulate a more realistic condition. The steady-state diffusion equation to be solved is given by

$$D\nabla^2 n = \dot{n} = -\nu_{iz} n \tag{3.35}$$

where D is the diffusion coefficient, and ν_{iz} is the ionization frequency. In order to simplify the problem, we will simply assume that the diffusion coefficient is constant throughout the domain. For an anisotropic diffusion with an axial magnetic field, the diffusion coefficient D can be replaced with $D_{\parallel}$ and $D_{\perp}$ applied to the directions parallel and perpendicular to the magnetic field, respectively. Equation (3.35) is solved using separation of variables, assuming that solutions in both directions are independent.

$$n(z, r) = n_0 J_0\left(\chi_{01}\frac{r}{R}\right)\sin\left(\pi\frac{z}{L}\right) \tag{3.36}$$

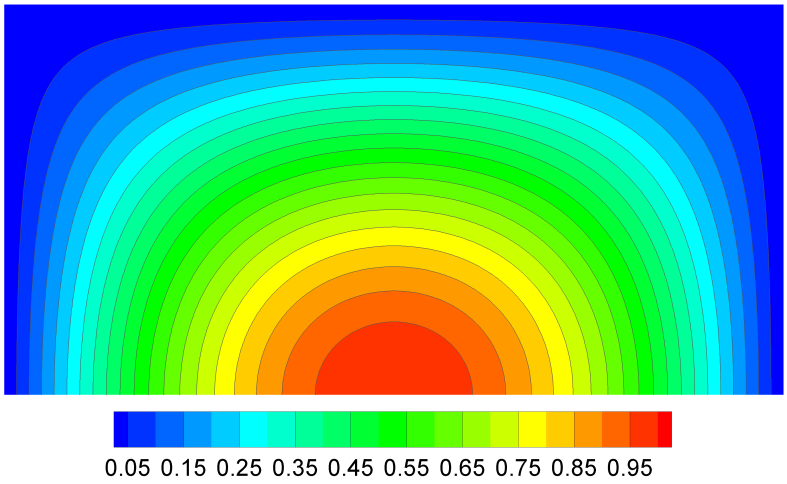

Figure 3.14: Normalized density solution in no magnetic field. The normalized solution is exactly the same for the case with a uniform axial field.

where n_0 is the maximum density, J_0 is the zeroth order Bessel function of the first kind, χ_{01} is the first zeroth of J_0 where $\chi_{01} \approx 2.4048$, R is the radius of the domain, and L is the length of the domain. Here, the boundary condition of zero density is used along the wall boundary, providing a simpler expression for the analytical solution. The normalized density solution of Eq. (3.36) is plotted in Sec. 3.3.4. In order to compare Eq. (3.36) with the computational solution, the same condition is enforced in the model. The maximum density in Eq. (3.36) is obtained from the computational model. The ion generation term in Eq. (3.12) is chosen to be proportional to $J_0(\chi_{01} r/R)\sin(\pi z/L)$, while the maximum ion generation rate is used to compute the diffusion coefficient. All the other plasma parameters used to compute the diffusion coefficient are also taken to be constant throughout the domain. The values for the plasma parameters are omitted here since those are not of importance; we are not comparing the magnitude of the solutions but rather the relative changes in space. The order of convergence is computed using both the infinity norm $||\tilde{n}||_\infty$ and the 2-norm $||\tilde{n}||_2$.

$$||\tilde{n}||_\infty = \frac{||n_\mathrm{c} - n_\mathrm{a}||_\infty}{||n_\mathrm{a}||_\infty} = \frac{\max(|n_c - n_a|)}{\max(|n_a|)}, \quad ||\tilde{n}||_2 = \frac{||n_\mathrm{c} - n_\mathrm{a}||_2}{||n_\mathrm{a}||_2} = \sqrt{\frac{\sum_k^N (n_c - n_a)^2}{\sum_k^N (n_a)^2}} \tag{3.37}$$

where the subscripts c and a denote computational and analytical solutions. Figure 3.15 plots the convergence of the numerical solution with the resolution of the uniform grid. It

is clearly seen that the numerical method is second order accurate; this order of accuracy would be expected in a uniform mesh.

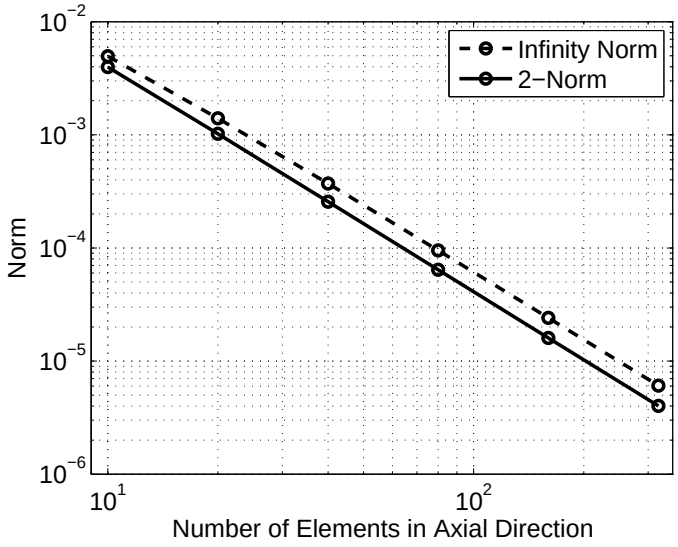

Figure 3.15: Infinity norm and 2-norm of error in the computational solution.

3.3.5 Comparison of Errors in MFA and Uniform Mesh

3.3.5.1 Perfectly Anisotropic Diffusion in a Single Cusp Configuration

The complexity of the magnetic field is slightly increased from the study in Sec. 3.3.4 by adding a cylindrical magnet at the downstream end. The cylindrical magnet creates a diverging field toward the upstream of the domain as shown in Fig. 3.16. The degree of divergence is adjusted by the distance from the downstream end of the domain to the magnet. The field equation for the magnet is obtained from the axially magnetized ring-magnet equation [112] in the limit that the inner radius is zero. Similar to the previous numerical investigation, the parallel mobilities for ions and electrons are assumed constant. However, the perpendicular mobility is set to be zero ($M_\perp = 0$) so that the error propagating in the perpendicular direction can be clearly observed. Instead of deriving an analytical solution for this problem, the numerical solution (Fig. 3.17) obtained with the 300×300 uniform mesh is compared with the numerical solutions from both the unform mesh and the MFA mesh at different resolutions. As there should not be any diffusion in the perpendicular

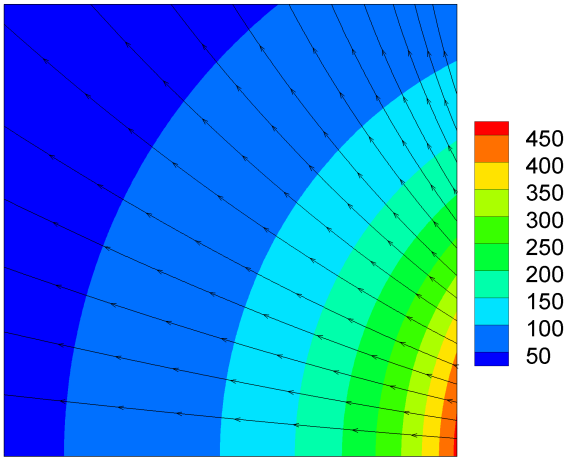

Figure 3.16: Magnetic field in Gauss. The solid lines represent the field lines.

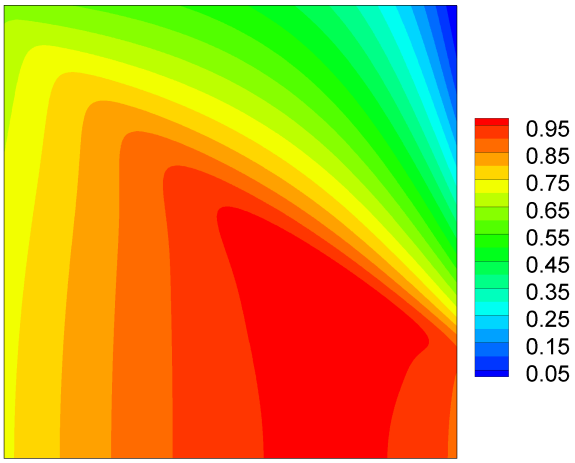

Figure 3.17: Numerical solution of the plasma density. The density is normalized by the maximum density value.

direction, the density profile is purely dependent on the length along the magnetic field within the computational domain. Therefore, the maximum density is seen at a finite radius where the path length along the field line is the maximum. In a real situation where the perpendicular mobility coefficient is finite, the maximum density location tends to lie on the axis of symmetry.

Figure 3.18 shows the errors in the numerical solutions obtained with a uniform and a MFA meshes. The error is normalized by the maximum density. As seen in Fig. 3.18(a), errors are generally larger when the degree of misalignment is larger. The result is mostly in agreement with the observations made by Meier et al. [169] except that there are two regions along the magnetic field with lower errors. This may be attributed to the cancellation of the numerical diffusion from both directions perpendicular to the field. When using a MFA mesh, the error structure is strongly dependent on the mesh. In Fig. 3.18(b), relative large errors are found along the line of the maximum density. The large errors in this region can be suppressed by slightly adjusting the grid spacing, while this can introduce another region with relative larger errors. Furthermore, the maximum errors are typically seen near the upper-right corner of the domain for all the meshes tested in the specific field configuration. All the elements in the row along the direction of the magnetic field touch the domain boundary

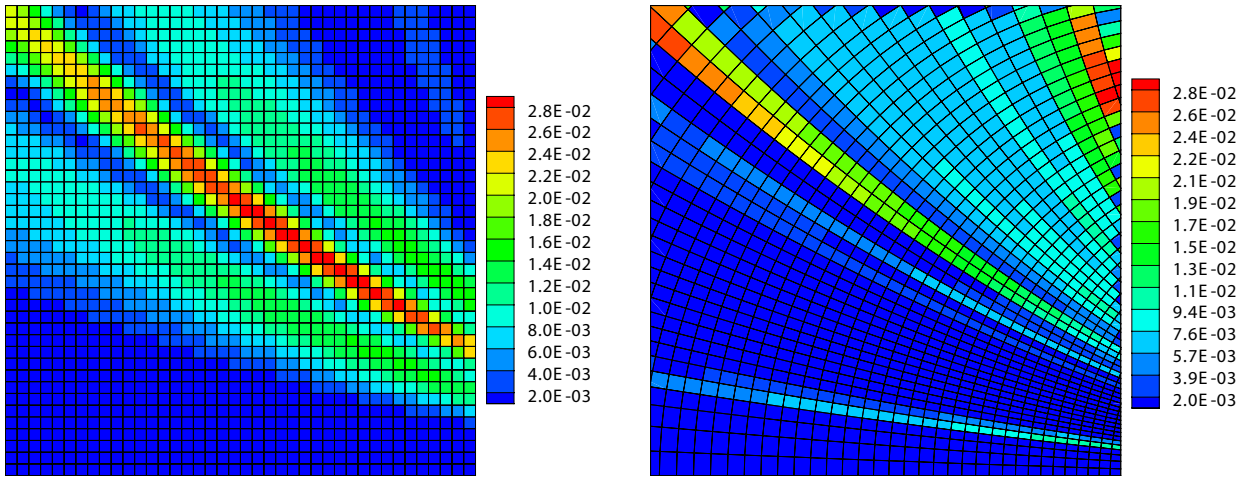

(a) Uniform mesh (b) MFA mesh

Figure 3.18: Relative difference between the numerical solutions compared to the solution with the 300×300 uniform mesh. The difference values are normalized by the maximum density value.

in the upper-right corner region, while less elements touch the boundary as moving toward the lower-left corner region. Accordingly, the errors generally decrease in the direction from upper-right to lower-left regions. Therefore, the MFA mesh provides a more accurate solution in a larger region near the centerline for the specific field configuration. In an effort to reduce the error in the MFA mesh, manipulation of the near-boundary elements has been performed; however, the method based on Sec. 3.2.2.6 turns out to worsen the numerical solution for the configuration, while the improvement in the solution for a discharge-like configuration has been significant as discussed below.

Figure 3.19 plots the norms computed by Eq. (3.37) that are based on the numerical solutions obtained with uniform and MFA meshes at different resolutions. The order of convergence for the uniform mesh is not very clear but seems to be approximately first order, while increasing the number of elements results in slightly increasing convergence rate due to the mesh resolution approaching the resolution of the reference mesh. On the other hand, the order of convergence for the MFA mesh cannot be determined due to the non-monotonic profile. The profile is caused by the change in the mesh quality near the domain boundary. With different numbers of contour levels, n_ψ and n_ϕ, the contour lines intersect with the boundary differently so the degrees of smoothness and skewness can change

drastically between the specified number of contour levels. As seen in Fig. 3.19(a), the infinity norm is always larger for the MFA meshes tested. This is due to the large error elements near the upper-right corner. In contrast, the 2-norm for the MFA mesh can be smaller than the 2-norm obtained with the uniform mesh especially when the large number of elements cannot be used (Fig. 3.19(b)). Finally, comparing the solution from MFA meshes with two different grid stretching parameters, the norms are significantly altered between the two, indicating that an adjustment to the MFA mesh can improve the solution significantly.

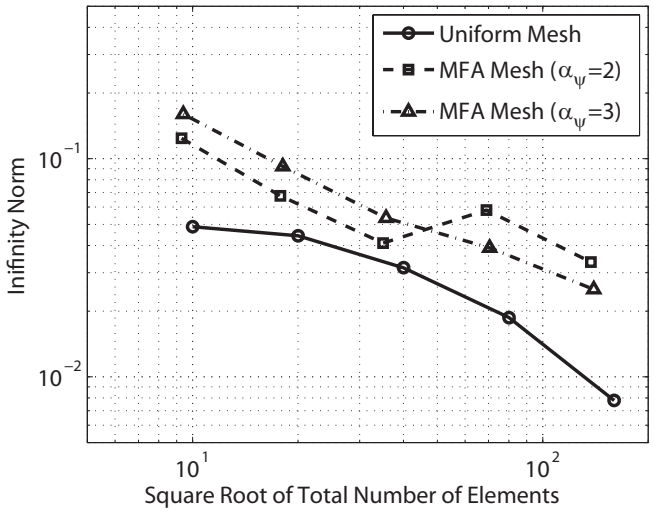

(a) Infinity norm

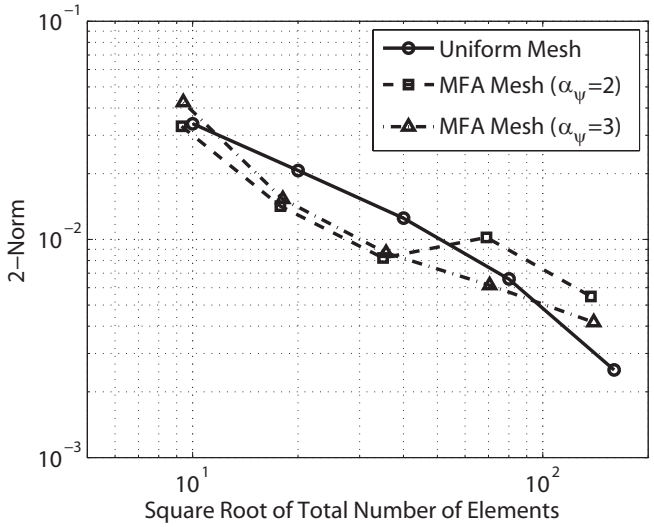

(b) 2-norm

Figure 3.19: Inifinity norm and 2-norm of error in the numerical solution.

3.3.5.2 Plasma Diffusion in a Multi-Cusp Configuration

The final numerical study is performed for a ring-cusp discharge like configuration shown in Fig. 3.5. The length and the radius of the domain are 2 cm and 1 cm, respectively. Unlike the previous studies, the mobilities are no longer taken to be constant but rather a function of the plasma density. Therefore, an iterative procedure is used until the plasma density solution converges as discussed in Sec. 3.3.2. In this study, plasma parameters similar to those for a miniature discharge are used to compute mobilities for both species; these parameters are provided in Table 3.1. The ratio of the electron perpendicular to parallel mobility values is generally on the order of 10^{-4}. Also, the plasma density of 1.5×10^{16} m^{-3} is assumed initially for the calculation of mobilities during the first iteration. The solution obtained from a 400×200 uniform mesh (Fig. 3.20) is compared with numerical solutions obtained with coarser uniform and MFA meshes for error estimations.

Table 3.1: Plasma parameters used to compute mobilities for ions and electrons.

Parameter	Symbol	Unit	Value
Neutral Density	n_o	m^{-3}	2×10^{18}
Ion Generation rate Density	$\dot{n}_i$	$m^{-3}s^{-1}$	2×10^{21}
Electron Generation rate Density	$\dot{n}_e$	$m^{-3}s^{-1}$	2×10^{21}
Ion Temperature	T_i	eV	0.4
Electron Temperature	T_e	eV	4

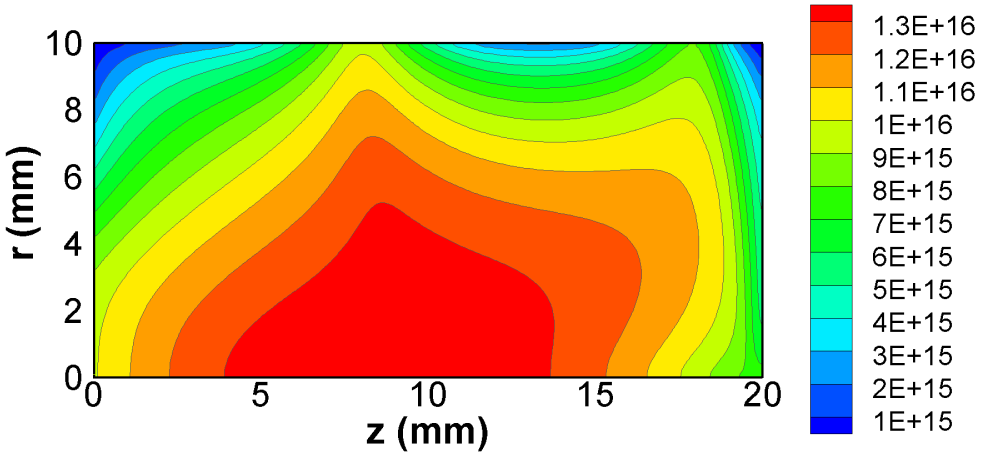

Figure 3.20: Reference plasma density (m^{-3}) obtained with a 400×200 uniform mesh. The density values are compared to numerical solutions to estimate the error.

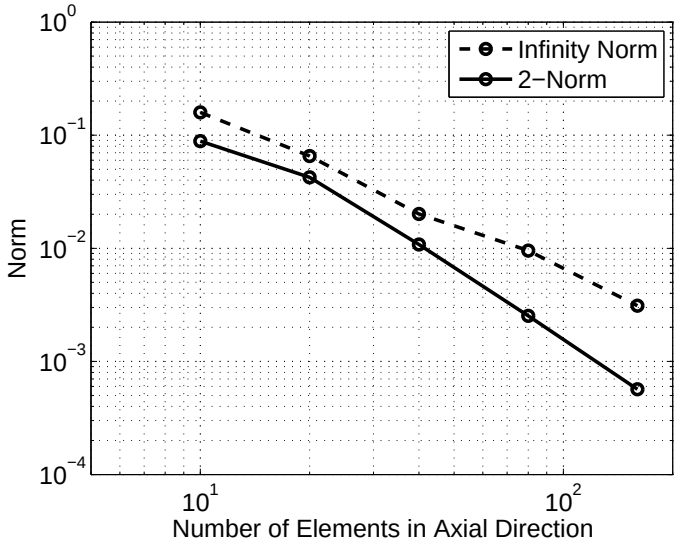

Figure 3.21: Infinity norm and 2-norm of error in the computational solution.

First, convergence of the solution is checked by varying the resolution of a uniform mesh. In contrast to the previous study shown in Fig. 3.19, the convergence behavior is more predictable; the order of accuracy is approximately second order as shown in Fig. 3.21. The convergence study for a MFA mesh is not performed here since the solution of the mesh is very sensitive to quality of the near-boundary elements, and a monotonic convergence behavior is difficult to obtain just as in the previous study. The difference in the convergence rate compared to the previous study may be attributed to the numerical diffusion. In the previous study, the error due to the numerical diffusion is dominant as a result of the enforced condition of $M_\perp = 0$, causing the overall error to be persistent. Larger errors were seen along the lines of magnetic field when the degree of misalignment was greater (see Fig. 3.18(a)). Figure 3.22 shows the difference in the computed density obtained with 28×14 and 400×200 uniform meshes. Here, the difference values are normalized by the maximum density. The error due to the numerical diffusion seems to be relaxed in this study. Since the perpendicular mobility is finite, the diffusion in the perpendicular direction naturally occurs, resulting in mixing and canceling of errors in space. As a result, the error distribution is smoothed out within the entire domain with decreased maximum error ($||\tilde{n}||_\infty$). Therefore, the relationship between the error and the degree of misalignment is not clearly seen anymore. Even within the region where the mesh is well-aligned with the magnetic field, the error is observed to

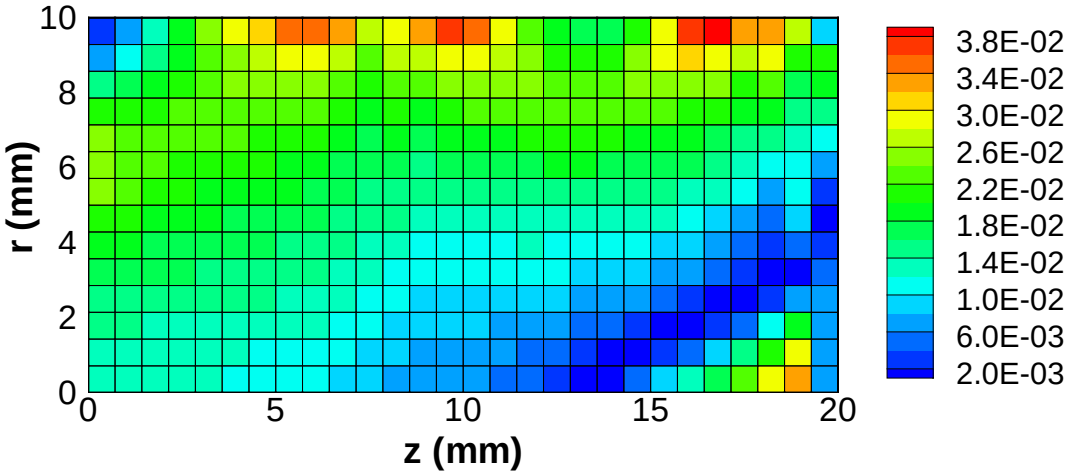

Figure 3.22: Difference in the solutions using the 28×14 and 400×200 uniform meshes. The difference values are normalized by the maximum density.

be comparible to the maximum error.

The MFA mesh is generated so that it contains a number of grid elements comparable to the uniform mesh shown in Fig. 3.22. The errors are obtained for the MFA meshes at different generation phases to clearly show the effect of each process. First, the baseline mesh is generated with the stretching parameters of $\alpha_\psi = 1.5$ and $\alpha_\phi = 0.9$ and the numbers of contour levels of $n_\psi = 21$ and $n_\phi = 21$ (Fig. 3.23(a)). Instead of using Eqs. (3.8) and (3.9) to increase the resolution near the domain axis, a simple stretching function similar to Eq. (3.10) is used to determine the contour levels for ψ. The large errors in the mesh is expected because of the poor mesh quality of the near-boundary elements and large element sizes near the domain axis. Then, all the large elements near the domain axis are split into three elements (Fig. 3.23(b)). By splitting the elements, the element sizes become comparable to the neighboring elements, and the errors are reduced in the near-axis region. The third step involves the manipulation of the near-boundary elements by enforcing the element facets intersecting the domain boundary to be orthogonal to the boundary (Fig. 3.23(c)). Although the quality of the near-boundary elements has not been refined at this phase, the process has made a significant improvement in the upstream region. In the region near the downstream boundary, the smoothness of the mesh is still poor. This is due to the existence of a null

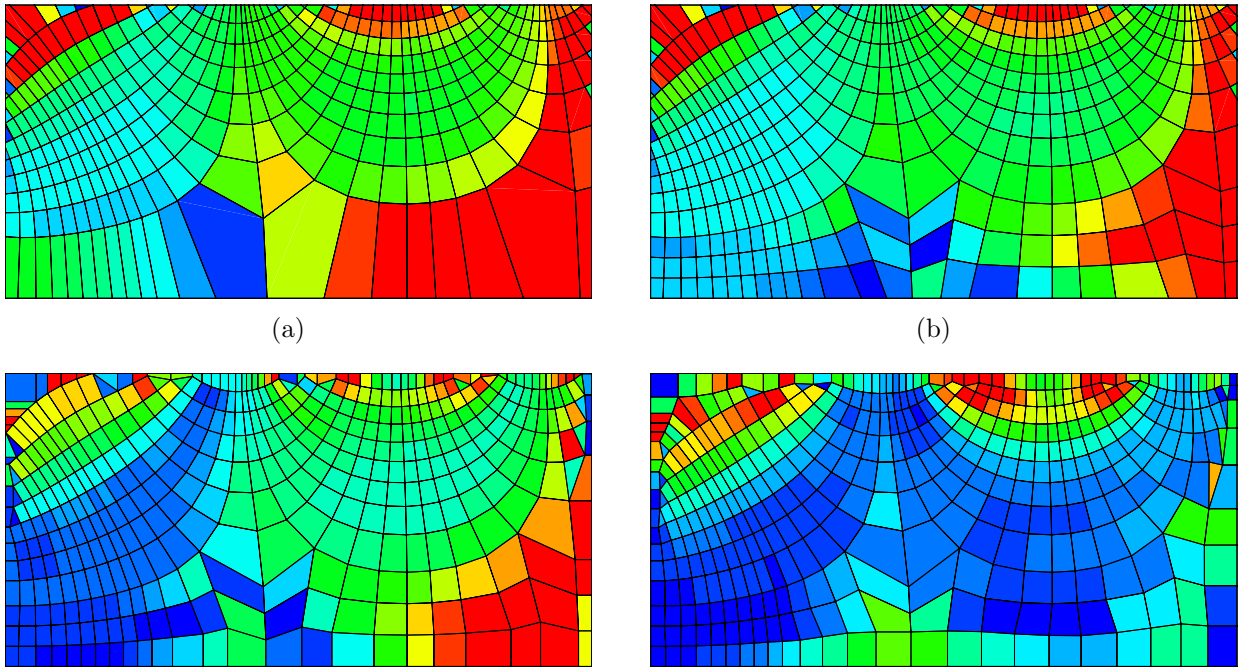

Figure 3.23: Normalized differences in the numerical solutions using the MFA meshes at the different phases of generation process compared with the reference density solution. The contour levels are the same as in Fig. 3.22. (a) Baseline MFA mesh. (b) The near-axis element is split into three elements. (c) The element facet intersecting a boundary is manipulated to be orthogonal to the boundary. (d) The near-boundary nodes are relocated to improve the mesh quality.

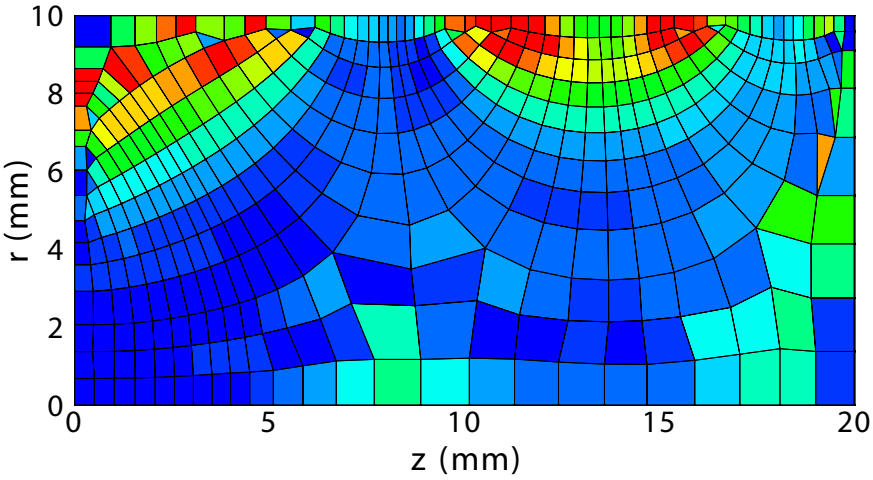

Figure 3.24: Normalized difference in the numerical solution using the final MFA mesh compared with the reference density solution. The contour levels are the same as in Fig. 3.22.

point right before the boundary. The near-boundary mesh quality is improved by moving the near-boundary nodes according to Eq. (3.11) (Fig. 3.23(d)). The errors in the bulk region as well as the near-cusp region are reduced significantly. Finally, the quality of the skewed elements in the other null region are improved by moving two interior nodes along the line of $\psi = 0$ according to Eq. (3.11), which slightly improves the accuracy in the null region (Fig. 3.24). As shown in Fig. 3.24, the overall accuracy using the MFA mesh is improved by an order of magnitude in the bulk and the near-cusp regions when compared with the uniform mesh. However, in the region between the cusps, the errors are inflated. This is not much of concern as the ionizing high-energy electrons rarely reach this region. Consequently, the ion generation rate in the between-cusp region should be much lower than the parameter in the other regions, where we have assumed to be constant throughout the domain for this test case.

While it has been shown that the MFA mesh can be better than the uniform mesh for a ring-cusp discharge configuration, it is still interesting to investigate the cause of the errors in the region between the cusps. Four different parameters that indicate the mesh quality are plotted in Fig. 3.25. The area of each element indicates the relative element size between the elements (Fig. 3.25(a)). The smoothness of each element is an indication of the jump in element size, computed by

$$\text{smoothness} = \left| 1 - \frac{\max(A_k, A_m)}{\min(A_k, A_m)} \right| \tag{3.38}$$

where the subscripts k and m denote the current and neighboring elements, respectively. This quantity is calculated for all the neighboring elements, and the maximum values are plotted in Fig. 3.25(b). The aspect ratio is simply the ratio of the maximum to the minimum facet length (Fig. 3.25(c)). Finally, the skewness plotted in Fig. 3.25(d) is computed by

$$\text{skewness} = \max \left[\frac{\theta_{\max} - \theta_e}{180^\circ - \theta_e}, \frac{\theta_e - \theta_{\max}}{\theta_e} \right] \tag{3.39}$$

where θ is the interior angle of the element, and θ_e is the angle for equiangular polygon (e.g. 60° for a triangle and 90° for a square). Comparing Fig. 3.25 with Fig. 3.24, it is

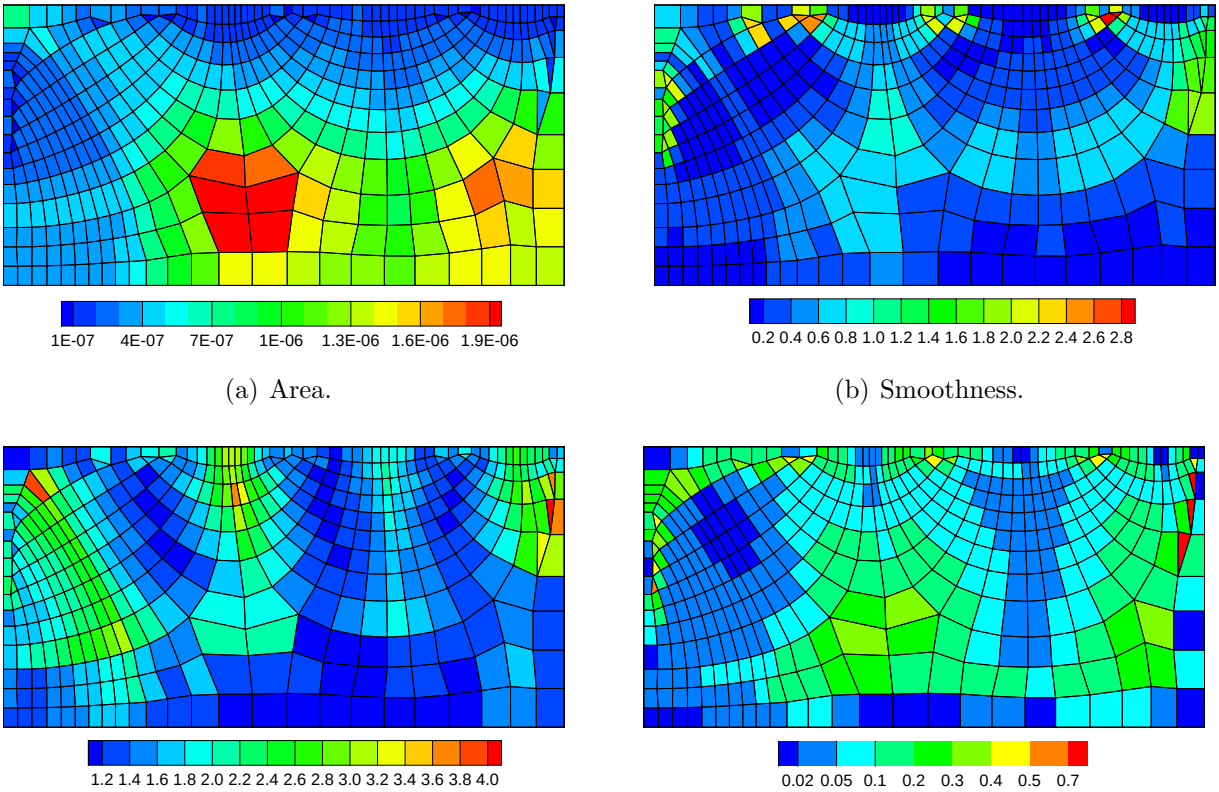

(a) Area.

(b) Smoothness.

(c) Aspect Ratio.

(d) Skewness.

Figure 3.25: Different parameters indicating the quality of elements in a MFA mesh.

readily seen that the larger element size and poor aspect ratio are not the dominant cause of the error. In a simulation of a boundary layer in the fluid dynamics, a stretching mesh with high aspect ratio elements is typically used to increase the resolution near the wall. As long as the direction of the flow is aligned with the mesh, a large aspect ratio is acceptable, which is also the case for the MFA mesh. The element size definitely has some effect to the accuracy but is not as remarkable as the other grid quality indicators. Both the skewness and especially the smoothness seem to have a dominant effect on the accuracy of the solution. Near the wall boundary, the five-sided elements are split into a triangular and a quadrilateral elements. Whenever a triangular element is present, the smoothness in the region becomes undesirable as the less number of facets likely leads to a smaller area compared to the neighboring quadrilateral elements. Those triangular elements are most likely present where the magnetic field intersects with the domain boundary at angles close to 45° with respect to

the direction normal to the boundary. The skewness of these triangular elements is also likely not preferable. The errors resulted from these triangular elements primarily propagates in the direction of the magnetic field, while the errors are also smoothed in the perpendicular direction. As a result, the larger errors are seen in the entire between-cusp regions.

For the problem examined herein, the accuracy achieved with the MFA mesh is approximately ten times better than that obtained with the uniform mesh with a similar number of mesh elements. Since the order of convergence is approximately second order when using a uniform mesh, the same accuracy can be achieved by increasing the resolution by about three times in each direction. This nearly proportionally increases the computational run-time required to solve the plasma diffusion equation. However, one has to remember that the development of the code with the MFA mesh may require significant effort due to its complex mesh structure. Therefore, if the code is already developed to use a structured mesh, there may not be significant enough benefit to re-develop the code for a MFA mesh. Also, it is important to note that, in spite of the complex mesh structure, the numerical implementation can be much simpler if the code is developed only for a MFA mesh. More specifically, the off-diagonal terms in mobility tensor (M_B in Eq. (3.15)) vanish for the MFA mesh, so the gradient along the facet, $\partial Q/\partial s$, does not need to be evaluated. If the near-boundary mesh quality is acceptable such that it does not introduce additional error in the solution, the MFA mesh can only be better compared to the uniform mesh. For design and optimization efforts, the use of a uniform or MFA mesh will depend on the combination of the factors discussed above. A particular and important case where the MFA mesh will be of value is when the magnetic field is to be held relatively constant for low beta plasma, and other parameters (i.e. flow rate, voltages, and currents) are to be varied for different runs. In this way, the user can take advantage of the simplified numerical implementation and shorter run time, while the mesh set up will be of relatively little cost.

3.4 Improved View Factor Method for Neutral Atom Density

In DC-ION, the neutral atom density is computed in the Neutral Atom Sub-Model, utilizing a view factor that is commonly used for a calculation of radiative heat transfer. In radiative heat transfer, a view factor is defined as a fraction of radiation leaving a surface that is intercepted by another surface. The underlying assumption is that the surface is a Lambertian or diffusely reflecting surface so that the reflection is approximately at cosine distribution due to the finite roughness of the surface. The same concept can be applied to neutral atoms such that a flux of atoms intercepted by a segment of the chamber wall is re-emitted diffusely from the surface. Therefore, the chamber wall can also be considered as a source of neutral flux, whereas the direct sources of the neutral gas are the hollow cathode and gas feeds. The view factor here is simply the fraction of the neutral flux from a surface or a direct source intercepted by another surface (e.g. an internal mesh element or a segment of the chamber wall).

The Neutral Atom Sub-Model employs two sets of mesh in addition to the internal mesh as shown in Fig. 3.26. The 2D surface mesh generated along the domain boundaries is only used to find the flux between segments of the chamber wall. Note that only half the chamber, say the azimuthal angles between 0° and 180°, needs to be meshed due to the axisymmetry. The 1D wall mesh is generated along the edges of the internal mesh corresponding to the chamber wall where the internal mesh lies at the plane of 0° or 180°. Each element of the 1D wall mesh, or a line segment ending at two adjacent nodes, can be thought to represent a strip of the chamber wall about the axis of symmetry. The flux re-emitted from the 1D wall mesh element is simply the sum of the fluxes intercepted by the element; these fluxes include the fluxes from all the 2D surface elements and the direct sources. The ions incident to the chamber surfaces are assumed to experience recombination and then be diffusely re-emitted from the surfaces as neutrals. Therefore, the ion flux intercepted by the element is also considered in the re-emitted flux calculation from the 1D wall element. After setting up the conservation equations for all the 1D wall mesh elements, the fluxes from these elements can be computed by solving the linear system of equations. Now, with the fluxes from the wall

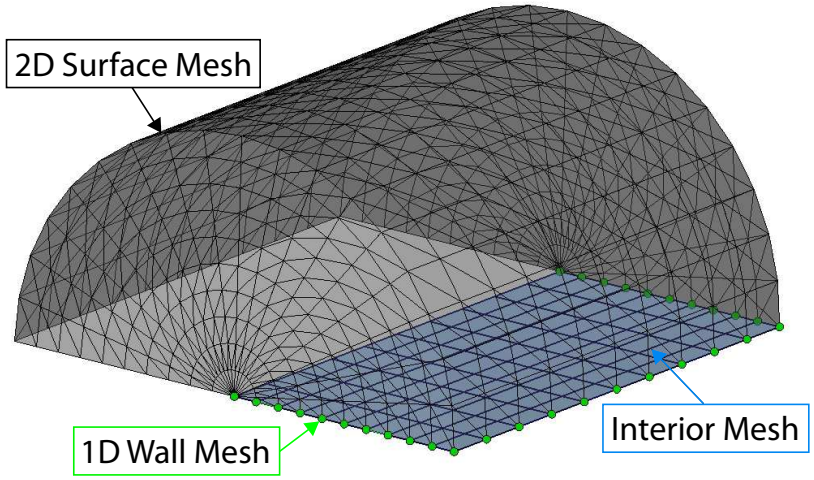

Figure 3.26: Three different meshes are used in the Neutral Atom Sub-Model.

elements and the sources to the interior cells, the neutral density within the domain can be computed. The Neutral Atom Sub-Model also includes the effect of ionization collisions by defining an effective view factor. The view factor method assumes straight paths for the neutral atom trajectories. The mean free paths for elastic collisions including the momentum and charge exchange collisions are comparable to or greater than the device dimensions for a typical electron bombardment ion thruster, implying that the assumed condition is fairly valid. The complete description of the view factor method for the neutral density calculation is provided in Ref. [13].

The view factor method produces a smooth neutral density distribution by the nature of the method. The counterpart of this method is the Monte Carlo method, tracking many neutral atoms from the sources. The Monte Carlo method is most commonly used for neutral density calculations and can easily include the effect of elastic collisions that is neglected in the view factor method. However, it requires tracking of a very large number of particles to obtain a sufficiently accurate and smooth density distribution. On the other hand, the accuracy in the view factor method depends on the resolution of the meshes including the 1D wall mesh and 2D surface mesh. Even with the fine mesh resolution, the computational cost is significantly lower than the Monte-Carlo method; the reduction in the cost can even be by orders of magnitude. Nevertheless, the mesh resolution that can be achieved is limited by

the memory available on the machine. In the original formulation of the view factor method, triangular elements are used for the 2D surface mesh (See Fig. 3.27(a)) due to the readily available formula for the solid angle [191].

$$\tan\left(\frac{\Omega_3}{2}\right) = \frac{\mathbf{s_1} \cdot (\mathbf{s_2} \times \mathbf{s_3})}{1 + \mathbf{s_1} \cdot \mathbf{s_2} + \mathbf{s_2} \cdot \mathbf{s_3} + \mathbf{s_3} \cdot \mathbf{s_1}} = \frac{N}{D} \tag{3.40}$$

where $\mathbf{s}$ is the unit vector from a point to a vertex of the triangular element and subscripts denote the node numbers counted in counterclockwise direction. Except near the axis of symmetry, two triangular element are created simply by splitting a quadrilateral element. Since the two triangular elements do not resolve the curvature of the chamber wall any better than the quadrilateral element, quadrilateral elements should be used in place of triangular elements as shown in Fig. 3.27(b). In this way, the number of elements in the 2D surface mesh is reduced by approximately half without sacrificing accuracy. Furthermore, the computational cost can be reduced significantly due to the fewer number of solid angle calculations. The general formula for the solid angle of polyhedral cones is provided by Mazonka [192].

$$\Omega_4 = 2\pi - \arg \prod_{j=1}^{n} \{b_j c_j - a_j + i d_j\} \tag{3.41}$$

where $a_j = \mathbf{s_{j-1}} \cdot \mathbf{s_{j+1}}$, $b_j = \mathbf{s_{j-1}} \cdot \mathbf{s_j}$, $c_j = \mathbf{s_j} \cdot \mathbf{s_{j+1}}$, $d_j = \mathbf{s_{j-1}} \cdot (\mathbf{s_j} \times \mathbf{s_{j+1}})$. Also, n is the number of vertices and j is the node index in counterclockwise direction and is circular such that $\mathbf{s_{n+1}} = \mathbf{s_1}$ and $\mathbf{s_0} = \mathbf{s_n}$. Using $n = 4$, the solid angle for a quadrilateral element can be determined, while the number of operations turns out to be greater than two solid angles for triangular elements when the formula is applied directly. Instead of using Eq. (3.41), we simply combine the solid angles for the two triangular elements using a few trigonometric identities.

$$\tan\left(\frac{\Omega_4}{2}\right) = \tan\left(\frac{\Omega_{3a} + \Omega_{3b}}{2}\right) = \frac{N_a D_b + N_b D_a}{N_a N_b - D_a D_b} \tag{3.42}$$

The number of operations for Eq. (3.40) and Eq. (3.42) are summarized in Table 3.2. It is readily seen that a single calculation for a quadrilateral element requires significantly less operations compared to twice the operations for a triangular element.

Table 3.2: Number of operations to evaluate Eq. (3.40) and Eq. (3.42).

Operation	Triangular	Quadrilateral
Addition/Subtraction	20	33
Multiplication	37	55
Division	4	5
Square Root	3	4
Tangent	1	1

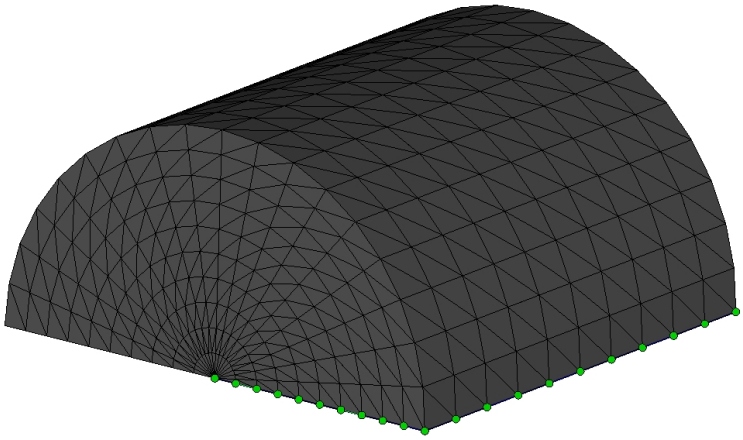

(a)

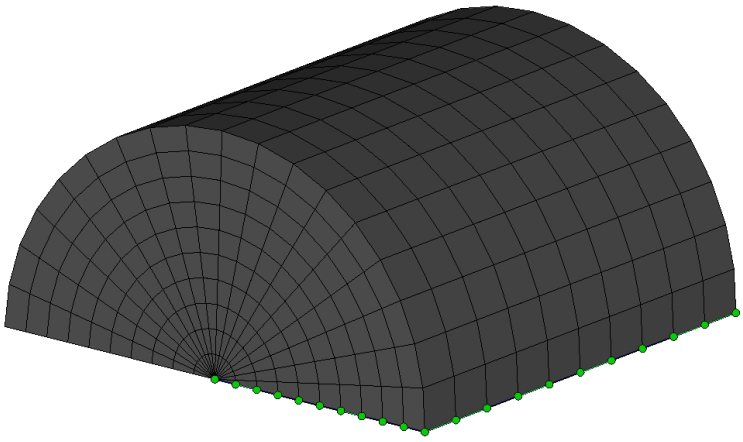

(b)

Figure 3.27: 2D surface meshes with (a) only triangular elements and (b) both triangular and quadrilateral elements.

3.5 Chapter Summary

The 2D/3D hybrid fluid/particle code, DC-ION, has been improved significantly from the original version. The SC model described in Chapter 2 is similar to the Electron Collision Sub-Model. Therefore, the more sophisticated numerical methods used in the SC model can be directly applied to DC-ION. These include the analytical equations for the permanent magnets, the particle weighting algorithm for a non-uniform axisymmetric mesh, and the more realistic electron-atom elastic scattering calculation. This chapter focused on the improved techniques and routines applicable to the other sub-models: the MFA mesh for the Internal Mesh Generator routine, the numerical method for solving the plasma diffusion equation on the MFA mesh for the Ion Diffusion Sub-Model, and the faster and more memory efficient view factor method for the Neutral Atom Sub-Model.

This chapter first provided a detailed numerical procedure to generate a MFA mesh for simulations of a ring-cusp discharge chamber. The MFA mesh generation algorithm worked fairly well in a configuration similar to the existing ring-cusp discharge. The MFA mesh generated from the routine could consist of grid nodes that were attached to more than four elements as a result of the method in treating the null points and the manipulation of the near-boundary elements to improve the grid quality. The numerical method developed to solve the plasma diffusion equation was capable of handling such meshes. The method used the least squares approach for the irregular nodes and singular value decomposition to add more rigorousness. The method was validated against the simple simulation condition without a magnetic field or with a uniform axial magnetic field, providing a second order accurate solution for the specific problem. Then, the MFA mesh and the method for evaluating the diffusion equation were combined to simulate the plasma with perfect anisotropicity by artificially enforcing the zero perpendicular mobility. The combination of the MFA mesh with the numerical method was also applied to the plasma in a ring-cusp discharge-like configuration. A uniform mesh was often susceptible to a numerical diffusion when the grid was unaligned with the magnetic field. Although the MFA mesh reduced the effect of numerical diffusion, it tended to introduce errors due to the poor quality of the mesh near the domain

boundary. In these studies, it was shown that the MFA mesh could provide superior accuracy relative to the uniform mesh within the region of interest, more specifically, in the bulk and the near-cusp regions. This often required an improvement of the near-boundary mesh quality. The mesh quality enhancement method implemented herein was demonstrated to work fairly well with the field configuration examined, while a further improvement may be realized by improving the mesh smoothness near the domain boundary.

For the Neutral Atom Sub-Model, the combination of the triangular and quadrilateral elements was used for the 2D surface mesh that was needed in finding the flux between segments of the chamber wall. The solid angle calculation for the quadrilateral element was simply done by summing the solid angles for two triangular elements. In this way, the required memory was reduced roughly by half. Furthermore, a significant reduction in the number of operations was realized especially for the slow operations such as the tangent, square root, and division functions.

CHAPTER 4

Heavy Species Collision Model for Ion Beam Experiment and Electric Propulsion Devices

Previous chapters covered the numerical models to understand the physics in a discharge chamber where high-energy primary electrons are very important. This chapter now switches the focus to the high-energy ions that are responsible for creating thrust and are important in understanding the plume physics. Much of the content is from the articles *Ion-Neutral Collision Modeling Using Classical Scattering with Spin-Orbit Free Interaction Potential* published in IEEE Transactions on Plasma Science and *Collision Modeling for High Velocity Ions in a Quiescent Gas* presented at 42nd AIAA Plasmadynamics and Lasers Conference, while significant content is added for this thesis.

4.1 Introduction

In plasma devices, different types of ion-atom collisions are possible, including momentum-exchange, resonant and non-resonant charge-exchange, ionization, excitation, superelastic, and radiative collisions [4]. Of these types of interactions, momentum- and resonant charge-exchange collisions are the most important ion-atom collisional mechanisms in electric propulsion and plasma processing devices [193]. Proper modeling of these collisions is required for accurate and predictive modeling of the life and performance of these devices. For example, in the plumes of ion thrusters and Hall-effect thrusters, ions experiencing either of the two collisions are responsible for the ion population found at angles greater than the main beam divergence that can lead to impingement on spacecraft surfaces [79]. Charge-exchange ions created in the plume can also cause erosion of critical thruster components and

can be the primary determinant of thruster life and long duration performance [14,38,39,79].

In an elastic collision, the particle velocities of the collision pair are altered as the energy is transferred between the particles, while the total energy and momentum of the collision pair are conserved. Resonant charge-exchange collision is similar to elastic collision except that one or more electrons are exchanged between the collision pair. Therefore, charge-exchange collisions can be considered to be a subset of elastic collisions [73]. In order to differentiate the two processes, we call the elastic collisions without and with exchanges of an electron MEX and CEX collisions, respectively.

The objective of this investigation is to develop a numerical model that may be used to explore the collisions between xenon ions and atoms at relatively low neutral pressures. The neutral pressure of interest is applicable for electric propulsion as well as plasma processing devices; therefore, the computational technique described herein can be applied to more complex simulations of those devices. The Ion Beam (IB) model employs a domain and boundary condition that match the well-defined "Test Cell" experimental domain as shown in Fig. 4.1 and described in [80]. Using matching domains allows direct comparisons between

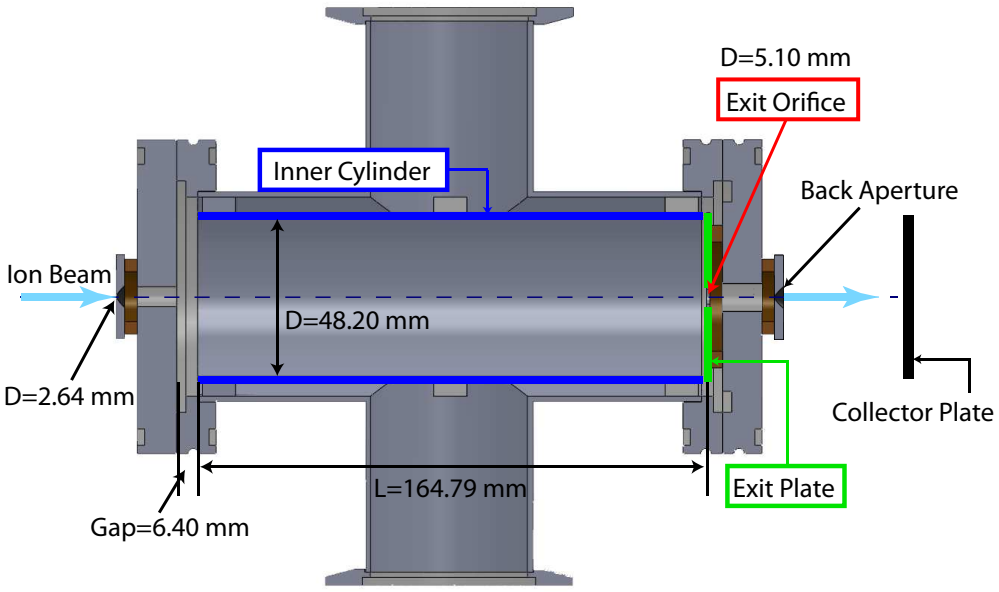

Figure 4.1: Schematic of the ion beam experiment (not to scale) [80]. The Back Aperture plate and the Collector Plate are placed approximately 20 and 220 mm from the Exit Plate, respectively.

computational and experimental results. In the experiment [80], a mono-energetic xenon ion beam of 1500 eV is guided to enter a cylindrical Test Cell, and the currents to the four different electrodes (Inner Cylinder, Exit Plate, Back Aperture, and Collector Plate) are measured. Note that the Inner Cylinder and Exit Plate electrodes are made from stainless steel, the Back Aperture is made from poco carbon, and the Collector Plate is made from graphite. The computational results are compared with these experimental results in order to validate the model. It should also be noted that, to simplify the simulation domain, the model computes the current through the Exit Orifice, and this current is compared with the sum of experimentally measured Back Aperture and Collector Plate currents. The IB model is designed for shorter run-time compared to the high-fidelity model by Giuliano and Boyd [76, 77] so that it can be used as a tool for preliminary computational analyses for the improvement and development of the experiment. This chapter is organized as follows: followed by the survey of literature on methods for approximating ion-atom elastic collisions in Sec. 4.2, the detailed description of the IB model is provided in Sec. 4.3. An analytical model to predict the Exit Orifice current is given in Sec. 4.4. Results comparing the computed and measured electrode currents are presented and discussed in Sec. 4.5. This section also includes the suggestions to the previous collision calculation methods as well as the improvements for the method implemented in the IB model. Finally, this chapter closes with a summary in Sec. 4.6.

4.2 Previous Models with Ion-Atom Elastic Collisions

The MEX and CEX collisions have been implemented in many computational models. For example, Oh [69] developed a quasi-neutral PIC-DSMC model to simulate a plume of a Hall-effect thruster to study the spacecraft-plume interaction. In his model, the MEX collision is approximated using the variable hard sphere (VHS) collision method, in which, the post-collision velocity is determined in the same way as the hard sphere model except that the collision cross-section is assumed to vary depending on the energy of the collision pair. On the other hand, the CEX collision is simulated by simply switching the velocity vectors of the

collision pair, assuming that the collision only occurs at a long-range. In an ion optics code developed at Jet Propulsion Laboratory [14,38,39], the CEX ion trajectories are determined to predict the erosion rate of the ion thruster accelerator grid caused by the CEX ion impact. The initial velocity of the CEX ion is assumed to be approximately the same as the velocity of a neutral atom escaping through the grid aperture. Here, the underlying assumption is that the interaction is in a long-range so that the neutral does not gain momentum when becoming an ion after the CEX collision. Mikellides et al. [79] developed an electrostatic thruster plume model using a Lagrangian fluid model. Their computational results showed good agreement with experimental results for angular dependence of ion energy and flux. In their model, a differential cross-section is used to find a flux between two node points where the cross-section is obtained from the classical scattering theory by only considering the repulsive part of ion-atom interaction potential. Giuliano and Boyd [76, 77] developed a hybrid PIC-DSMC model and used a curve-fit representative of a differential cross-section to perform calculations of post-collision particle velocities. Their differential cross-section is derived from the classical scattering equation with spin-orbit free interaction potential. This potential function is a much more accurate representation as it includes three potential functions in addition to the repulsive part of the potential. Although the use of differential cross-section in the collision calculations has an advantage in speed, the method is limited to mono-energetic incident ion since the differential cross-section differs for different energies. Therefore, the method cannot be applied in a regime where multiple collisions take place.

4.3 Computational Model Description

4.3.1 Overview

The IB model employs the multi-species iterative Monte Carlo method similar to the SC model discussed in Chapter 2, while different species are tracked in the IB model: high-energy primary ions, fast neutral atoms, CEX ions, and secondary electrons emitted from electrodes. Macro-particles, each representing a fraction of the total species current is tracked individually using the leap-frog method [120]. When the primary ion experiences a collision,

the current that undergoes a CEX collision is determined. Then, in addition to the primary ion, a fast neutral and a CEX ion are tracked from the location of collision. After all the particles representing the three species are tracked until they impact any electrode, the secondary electrons emitted from all the electrodes are tracked; their currents are based on the number of high-energy ions and atoms impacting the electrode and corresponding secondary electron yield. In order to find densities for all the species, particles are distributed to computational nodes at every time-step using the density conserving shape function given by Ruyten [128]. Electric potential is calculated by solving Poisson's equation with a finite difference formulation, using space charge distribution computed from particle tracking. The potential solver and particle tracking are run multiple times until the electric potential reaches steady-state. Finally, computed electrode currents as a result of particles impacting the walls are determined and compared with experimental results. A simplified structure of the code is shown in Fig. 4.2.

In the IB model, a high energy ion beam of 1500 eV is assumed to enter the cylindrical Test Cell with a uniform beam profile and without divergence. The beam radius used in the simulation is 1.32 mm, which is about 20 times smaller than the Test Cell radius. Thermal background neutrals of 300 K are assumed in the post-collision velocity calculation. In order to resolve the beam, finer grid size in this region is used with stretching grid size in the radial

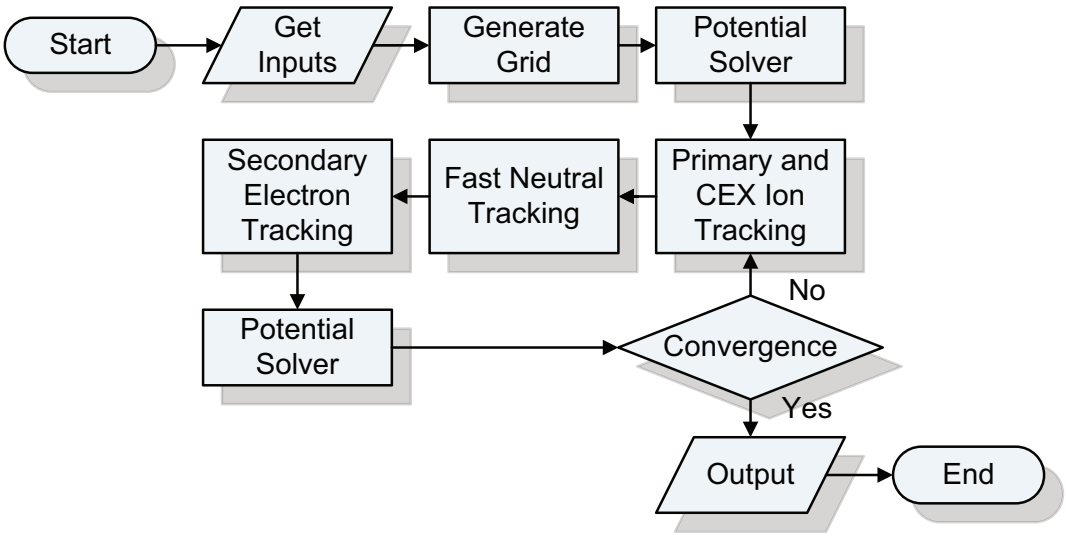

Figure 4.2: Simplified flowchart for the IB model.

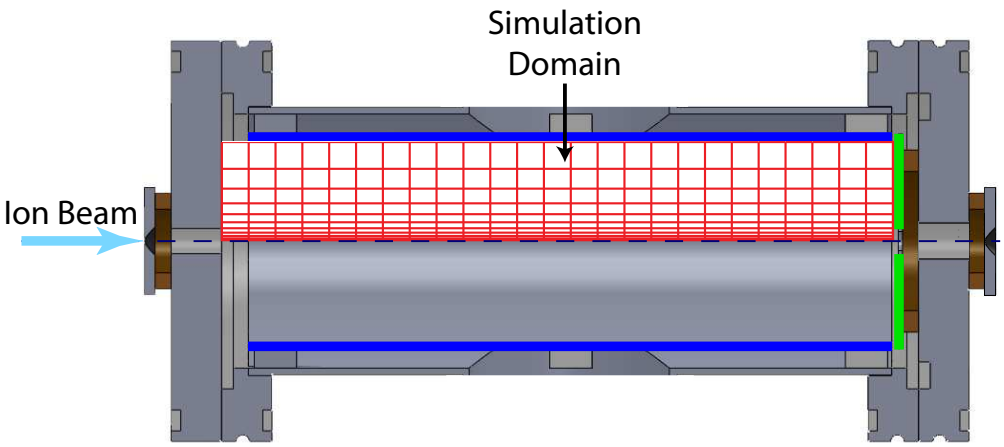

Figure 4.3: Two-dimensional axisymmetric computational domain with a radially stretched grid to simulate the cylindrical "Test Cell" used in Refs. [80]. The actual grid used in the simulation is four times the resolution of the one shown in the figure.

direction as shown in Fig. 4.3.

When no xenon neutral is present in the Test Cell, all primary ions reach the Collector Plate for the case of zero beam divergence. However, as the background neutral pressure is increased, the probability of the primary ions colliding with neutrals increases, and a fraction of the ions experience elastic collisions with neutrals. As a result, the primary ions are deflected at some angles; the scattered high-energy ions are called MEX ions. Here, we refer to all the high-energy ions as primary ions, which includes both the unscattered and MEX ions. During the elastic collisions, the ions can gain electrons from neutrals which most commonly results in slow CEX ions and fast neutrals. Short range Coulomb collisions between ions are less important compared to the two primary types of collisions for the range of ionization levels found in the experiment ($< 10^{-5}\%$), while long range Coulomb interactions are incorporated in the form of electric forces calculated from space charges in the domain. The ionization collision is neglected since the collision cross-section is much smaller than the CEX collision cross-section.

4.3.2 Collision Dynamics

The elastic collisions between ions and neutrals are approximated by using two different collision models depending on the projectile ion energy. At energies greater than 30 eV, we

use a classical scattering model with recently calculated spin-orbit free interaction potential [194,195]. Otherwise, the VHS molecular model is employed [139]. Discussion on the limit of 30 eV is given in Sec. 4.3.6. Most of the calculations for the collisions between the primary ions and the background neutral atoms are done with the classical scattering model since the primary ion energy hardly becomes less than 30 eV even after several collisions. In contrast, the CEX ions have relatively low initial energy, and their energy approaches thermal energy after multiple collisions with background neutrals; thus, the VHS model is employed in most of the collision calculations between the CEX ions and the background neutrals. For collisions between the CEX ions and the background neutrals, the difference in the collision model used does not significantly affect the result because of the large aspect ratio of the Test Cell. In other words, most of the CEX ions impact the long Inner Cylinder wall instead of the Exit Plate no matter which collision model is used.

Miller et al. [196] conducted a guided-ion beam experiment to find Xe^++ Xe symmetric CEX cross-sections as a function of laboratory-frame (LAB) ion energy. They provided a functional form of the CEX cross-section, σ_{CEX}, in Å^2 as

$$\sigma_{\text{CEX}} = 87.3 - 13.6 \log(E) \tag{4.1}$$

where E is the LAB primary ion energy in eV. At an ion energy of 1500 eV, the CEX cross-section is 44.1 Å^2. Several computational models approximate the MEX collision cross-section to be equal to the CEX cross-section, i.e. $\sigma_i = \sigma_{\text{MEX}} + \sigma_{\text{CEX}} \approx 2\sigma_{\text{CEX}}$ where σ_i is the total ion-atom elastic collision cross-section [197, 198]. Instead of using the same approximation, we use the following functional form for σ_i in Å^2.

$$\sigma_i = 300.34 - 44.54 \log(E) \tag{4.2}$$

The total elastic collision cross-section given in Eq. (4.2) represents the cross-section within which the MEX and CEX collisions can take place and is calculated from the charge exchange probability, P_{CEX}, as discussed in detail in Sec. 4.3.5.

During a time-step, Δt, the probability that a particle experiences either a MEX or CEX collision is expressed as

$$P_{\text{total}} = 1 - \exp(-\Delta t \sigma_i v_i n_o) \tag{4.3}$$

Equation (4.3) gives a positive value that is always less than or equal to 1. Whether a collision event takes place is determined by comparing P_{total} with a uniformly probable number, U, between 0 to 1 generated by the random number generator. The random number is updated for every instance it appears in different equations. If $P_{\text{total}} > U$, then the particle experiences either a MEX or CEX collision. The depletion of macro ion current, ΔJ_i, by the CEX collision is approximated by $\Delta J_i = P_{\text{CEX}} J_{i0}$, and the remainder of the particles represented by $J_i = J_{i0} - \Delta J_i$ experience the MEX collisions.

4.3.3 Xe^+ + Xe Interaction Potential

The interaction potentials for Xe^+ + Xe collisions have been calculated with *ab initio* quantum chemistry [194, 199, 200]. In the computational model, four spin-orbit free potentials, Π and Σ potentials with the *gerade* (g) and the *ungerade* (u) states, calculated by Paidarova and Gadea are used [194]. These potentials are shown in Fig. 4.4. Chiu et al. [195] verified that the scattering results are not affected significantly by using the full spin-orbit potentials. The averaged (u,g) pairs of the spin-orbit free potentials are fitted using Morse potential form [195] with the fitting parameters given in Table 4.1.

$$V_{\text{avg}}(r) = D_e(\mathrm{e}^{2b(r_e - r)} - 2\mathrm{e}^{b(r_e - r)}) \tag{4.4}$$

Here, r is the internuclear distance given in atomic units. The statistical weights for Σ and Π potentials, d_Σ and d_Π, are 1/3 and 2/3, respectively. In order to calculate P_{CEX}, the long-range form of the potential is adapted:

$$V(r)_{g,u} = -\frac{\alpha}{2r^4} \pm \frac{A}{2}\mathrm{e}^{-ar} \tag{4.5}$$

where α is the polarizability of the neutral atom and A and a are parameters given in Table 4.2. Then, the exchange energy, ΔV, can be expressed in the exponential form.

$$\Delta V(r) = V_g - V_u = A\mathrm{e}^{-ar} \tag{4.6}$$

Expressing the exchange energy in the exponential form greatly simplifies the calculation of P_{CEX} as discussed in Sec. 4.3.5. The fitting parameters given in Table 4.2 are obtained by minimizing the 2-norm of the difference between the potential values calculated from Eq. (4.6) and tabulated in Ref. [194] at internuclear distances greater than 5 a.u., which covers the long range.

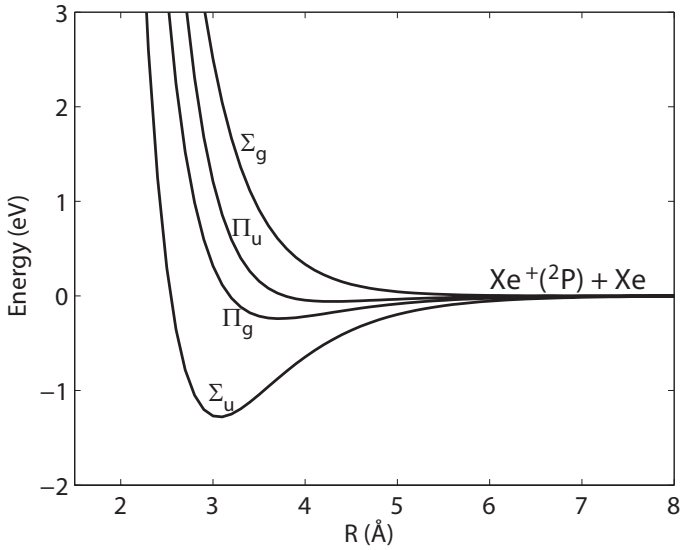

Figure 4.4: Spin-orbit free interaction potential energy curve for $Xe^+(^2P)$+Xe calculated by Paidarova and Gadea [194].

Table 4.1: Morse potential fitting parameters for averaged (u,g) pairs of the spin-orbit free potentials (see [195]). Values are given in atomic units (1 a.u.=27.21 eV=0.529 Å).

Potentials	D_e	b	r_e
$(V_{\Sigma g} + V_{\Sigma u})/2$	0.00585	0.645	7.476
$(V_{\Pi g} + V_{\Pi u})/2$	0.00487	0.677	7.570

Table 4.2: Exponential fitting parameters for exchange energy. Values are given in atomic units (1 a.u. = 27.21 eV = 0.529 Å).

Potentials	A	a
$V_{\Sigma g} - V_{\Sigma u}$	6.81	0.69
$V_{\Pi g} - V_{\Pi u}$	-6.53	0.93

4.3.4 Deflection Function

Referring to Fig. 4.5, the center of mass (CM) deflection angle, χ, can be calculated by the classical approach [201].

$$\chi(b, E_r) = \pi - 2b \int_{R_m(b,E_r)}^{\infty} \frac{dr}{r^2[1 - b^2/r^2 - V(r)/E_r]^{\frac{1}{2}}} \tag{4.7}$$

where b is the impact parameter, E_r is the initial kinetic energy in CM frame given as $E_r = \frac{1}{2} m_r v_r^2$, m_r is the reduced mass given as $m_r = m_1 m_2/(m_1 + m_2)$, v_r is the relative velocity of the collision pair, and $V(r)$ is the sum of the four spin-orbit free potentials with the statistical weights, $V = 1/6(V_{\Sigma u} + V_{\Sigma g}) + 1/3(V_{\Pi u} + V_{\Pi g})$. Subscripts 1 and 2 denote incident and target particles, respectively.

Assuming the target particle is much slower than the incident particle, the LAB and CM deflection angle and energy are related by the following expression:

$$E = 2E_r, \quad \theta = \chi/2 \tag{4.8}$$

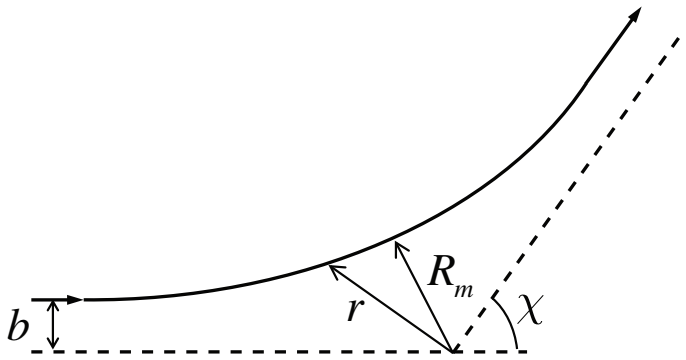

Figure 4.5: Classical scattering trajectory.

The classical turning point or the minimum distance of approach, R_m, is calculated by finding the largest root of the equation.

$$1 - b^2/R_m^2 - V(R_m)/E_r = 0 \tag{4.9}$$

Computing Eq. (4.7) with direct numerical integration can be difficult since the denominator blows up in the limit of $r = R_m$. Instead, Eq. (4.7) is solved by applying Smith's method that uses the Gauss-Mehler formula [202].

$$I = \int_{R_m(b,E_r)}^{\infty} \frac{dr}{r^2[1 - b^2/r^2 - V(r)/E_r]^{\frac{1}{2}}} = \frac{\pi}{nR_m} \sum_{j=1}^{\frac{1}{2}n} f(v_j) \tag{4.10}$$

where

$$v_j = \cos\frac{2j-1}{2n}\pi, \quad f(v_j) = \left[\frac{1 - v_j^2}{1 - V(R_m/v_j) - b^2 v_j^2/R_m^2}\right]^{\frac{1}{2}} \tag{4.11}$$

Figure 4.6 shows the center of mass deflection angle as a function of impact parameter with different center of mass energies. Note that $E_r = 750$ eV corresponds to the primary ion energy ($E = 1500$ eV) used in the ion beam experiment. The deflection function for $E_r = 0.5$ eV has a small minimum at $b \approx 4.9$ Å, which gives a rainbow singularity in the differential cross-section at the rainbow angle corresponding to the minimum deflection angle. A further discussion on the singularity is given in Sec. 4.3.6. Also, the deflection function becomes discontinuous at the critical angle at even lower energies (i.e. orbiting singularity). These singularities are not realistic, and quantum scattering has to be considered [197, 201]. However, at high energies, the deflection is mostly affected by the repulsive part of the potential at long-range so that the deflection function barely has a minimum. In this regime, the classical scattering model is sufficiently accurate to approximate ion-atom collision behavior [197]. For all the energies, the CM scattering angle approaches zero as $b \to \infty$, however, it never actually reaches zero. This implies that the total collision cross-section is unbounded. In applying the model, it is necessary to provide a cut-off impact parameter or deflection angle [139]. For this computational effort, the cut-off or the maximum impact parameters, $b_{\max}$, are chosen from σ_i for the corresponding incident particle energy.

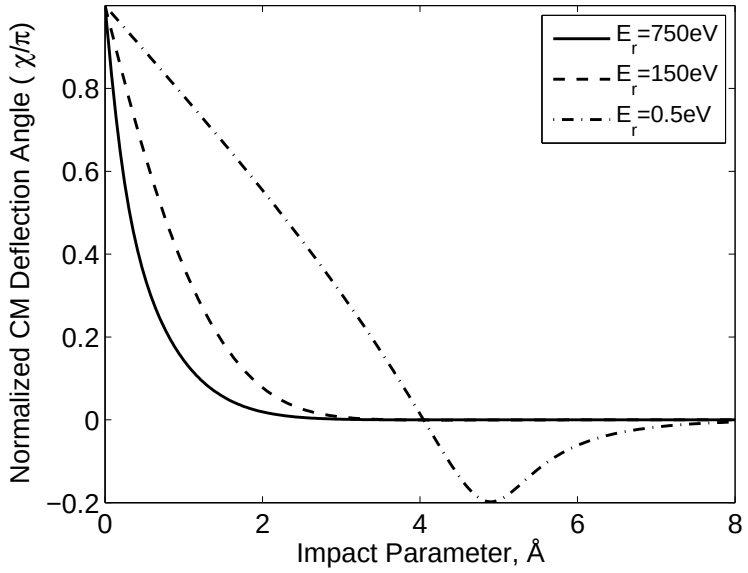

Figure 4.6: Deflection functions computed by the classical scattering equation with the spin-orbit free potential at different CM energies.

At an ion energy of 1500 eV, $b_{\max}$ is 7.11 Å. As long as the deflection angles at $b > b_{\max}$ are very small, the choice of $b_{\max}$ does not significantly affect the elastic scattering of the particles. In other words, by employing a maximum impact parameter, the deflection angle is artificially set to zero for $b > b_{\max}$, where the deflection angle is very small. It is easy to obtain an idea of what fraction of elastically scattered particles reaches the Exit Plate aperture for a single collision condition. Referring to Fig. 4.1, the angle between the Exit Orifice radius and the edge of the beam when entering the Test Cell is $\theta_{cr} = \tan^{-1}[(2.5-1.27)/(153.3+6.4)] = 0.44°$. If the particles experience collisions right at the inlet plane, all the particles deflected with $\theta < \theta_{cr}$ reach the Exit Plate aperture. For the maximum impact parameter chosen in the model, approximately 84% of the particles considered to be experiencing elastic collisions are deflected at $\theta < \theta_{cr}$. Particles can, of course, collide with the background neutrals closer to the Exit Plate than at the inlet plane, therefore, the percentage represents the lower bound. In contrast, if a CEX process takes place, the CEX ions are likely to have very large CM deflection angles when they are created.

Figure 4.7 compares $\chi(b, E_r)$ obtained with classical scattering model with the spin-orbit free potential and the purely repulsive part of the potential ($V_{\Sigma g}$) for an ion energy

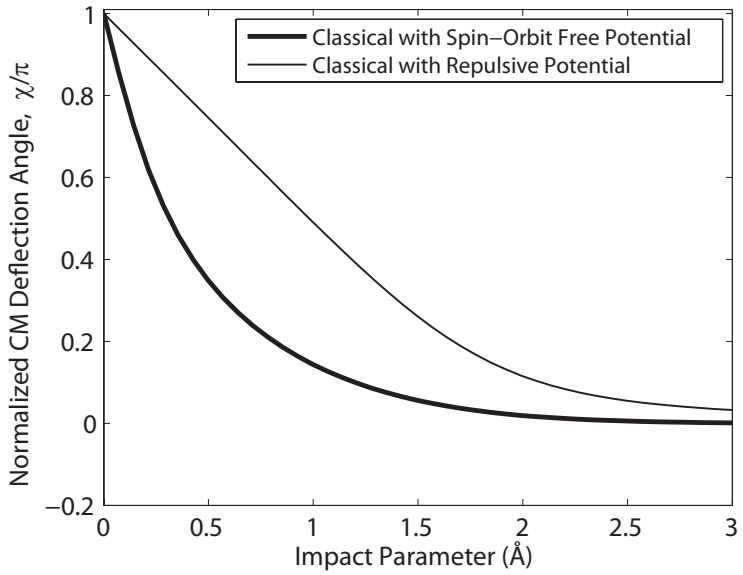

Figure 4.7: Comparison of deflection functions with the spin-orbit free and repulsive part of the potential for the LAB ion energy of 1500 eV.

of 1500 eV. The classical model with the repulsive potential has been applied in a few models [79, 203]. Smaller angle deflections are more likely to take place with the spin-orbit free potential compared to the repulsive potential due to the attractive force that counteracts the repulsive force. At higher energies, the collisions are more affected by the potential at long-range; therefore, the difference between the two potentials becomes smaller at a larger impact parameter since the potential functions asymptote to zero when the collision pair is far apart.

Because of the singularities that appear at low energies, the VHS molecular model [139] is used for low energy incident particles instead of using the quantum scattering. The method is also used in the SC model and is given in Eqs. (2.31) and (2.32). Once the deflection angle is calculated for some impact parameter, the post-collision velocity can be calculated. The details of the post-collision velocity calculation is given in Appendix D.2. In the CEX process, the particles of the collision pair are deflected in the same way as the MEX collision, except that the target particle is now an ion after transferring one or more electrons. Therefore, the CM deflection angle of the newly created CEX ion is simply the angle of the target particle, $\pi - \chi$.

4.3.5 Charge-Exchange Probability

The charge exchange interaction involves a transition to the other potential, (u) or (g), of the same pair (Σ or Π). Therefore, the charge exchange probability is calculated from the difference between the elastic scattering phase shifts, $\Delta\eta$ for *gerade* and *ungerade* states ($\Delta\eta = \eta_g - \eta_u$) at a specific impact parameter [73, 195, 196].

$$\begin{aligned} P_{\mathrm{CEX}}(b) &= \sum_l d_l \sin^2 \Delta\eta_l \\ &= \frac{1}{3}\sin^2 \Delta\eta_\Sigma + \frac{2}{3}\sin^2 \Delta\eta_\Pi \end{aligned} \tag{4.12}$$

According to Marchi and Smith, the phase shift difference at large impact parameters can be approximated by [204, 205]

$$\Delta\eta = -\frac{m_r}{\hbar^2 k}\int_{R_m}^{\infty} \frac{\Delta V(r) dr}{\left[1 - R_m^2/r^2\right]^{1/2}} \tag{4.13}$$

where $\hbar$ is the reduced Planck's constant and k is the wavenumber calculated by $k = \sqrt{2m_r E_r}/\hbar$. For the case in which the exchange energy is expressed in the exponential form, Eq. (4.13) is solved analytically to give [204, 206]

$$\Delta\eta = \frac{A m_r}{k\hbar^2} b K_1(ab) \tag{4.14}$$

where K_1 is the first order Bessel function of the second kind, and A and a are the parameters given in Eq. (4.6) and Table 4.2. The phase shift differences monotonically increase or decrease depending on the sign of A.

Figure 4.8 shows the charge exchange probability for a primary ion energy of 1500 eV. Note that the CEX probability is not shown at $b < 2$ Å since the approximation to the phase shift difference is not valid at small impact parameters. In this region, the CEX probability oscillates rapidly between 0 and 1, and the average value of 0.5 is typically used in computational models. The oscillation between 0 and 1 in the CEX probability continues to about 4 Å, and then its maximum value in the oscillation starts to decrease due to the

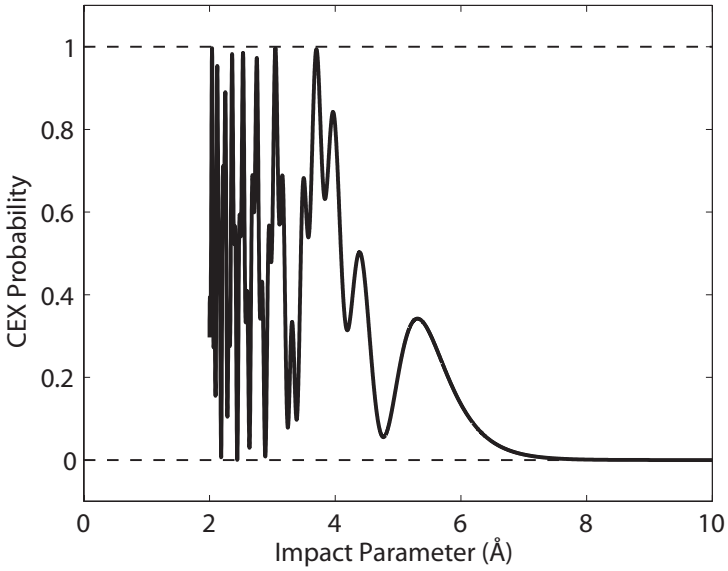

Figure 4.8: Charge exchange probability for the LAB ion energy of 1500 eV.

stronger interaction of Σ potentials.

The CEX cross-section can be calculated from P_{CEX} by [195, 196]

$$\sigma_{\mathrm{CEX}} = 2\pi \int_0^\infty P_{\mathrm{CEX}}(b) b db \tag{4.15}$$

Since the approximation of P_{CEX} at small impact parameters is invalid, the CEX cross-section can be rewritten in the following equation, assuming $P_{\mathrm{CEX}} = 0.5$ at $b < b_0$ [206].

$$\sigma_{\mathrm{CEX}} = 2\pi \int_{b_0}^\infty P_{\mathrm{CEX}}(b) b db + \frac{\pi}{2} b_0^2 \tag{4.16}$$

As shown in Fig. 4.6, the deflection angles of the projectile particle at $b > 2$ Å are very small ($< 3.4°$) at the energy of 1500 eV. Using $b_0 = 2$ Å, the probability of the CEX interaction occurring in the region of $b > 2$ Å can be calculated by dividing the first term of the right-hand side of Eq. (4.16) by σ_{CEX}, which corresponds to approximately 87%. Since the CM deflection angle of the CEX ions is given as $\pi - \chi$, it is readily seen that the CEX ions are deflected at very large angles in the CM frame ($> 176.6°$) if the collision impact parameter is greater than 2 Å. In contrast, the larger CM deflection angles below 2 Å indicate that

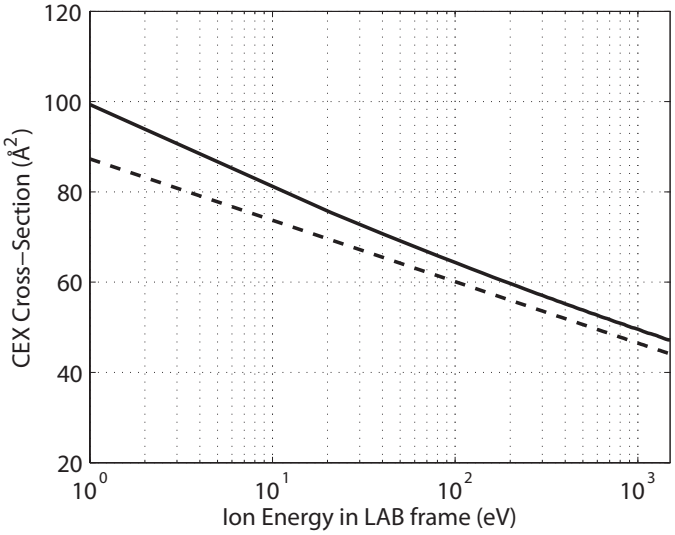

Figure 4.9: Charge exchange cross-sections as a function of LAB energy. Solid line is calculated using Eq. (4.16) and dashed line represents the empirical equation given in Eq. (4.1) [196].

some CEX ions are deflected at smaller angles in the CM frame. Figure 4.9 shows the CEX cross-section as a function of the projectile energy calculated with Eq. (4.1) and Eq. (4.16). The CEX cross-section calculated using the spin-orbit free potential agrees fairly well with the empirical relation. At lower ion energies, the measured cross-section is considerably lower than the theoretical cross-section. The discrepancy is likely due to the potential function that we use in the model. Nevertheless, the cross-section result is within the bounds for the cross-sections predicted using the similar potential functions [196].

In the IB model, the charge exchange probability calculated from Eq. (4.12) is used rather than simply assuming $P_{\mathrm{CEX}} = 0.5$. For this reason, it is necessary to use a total ion-atom collision cross-section that covers the largest impact parameter giving $P_{\mathrm{CEX}} > 0$. Using $\sigma_i = 2\sigma_{\mathrm{CEX}}$ neglects the CEX interaction occurring at the impact parameter greater than $\sqrt{2\sigma_{\mathrm{CEX}}/\pi}$. For each energy, the minimum impact parameter, b_{cr}, is found, which satisfies the condition $P_{\mathrm{CEX}} \approx 0$ for $b > b_{cr}$. Then, Eq. (4.2) is obtained by curve fitting the cross-sections, πb_{cr}^2, at different energies.

4.3.6 Differential Cross-Section

Using the scattering angle in the CM frame, the differential cross-section can be derived [79].

$$I_{\mathrm{CM}}(\chi, E_r) = \left.\frac{d\sigma(\chi)}{d\Omega}\right|_{CM} = \left|\frac{b}{\sin\chi(d\chi/db)}\right| \tag{4.17}$$

Here, $d\chi/db$ can be approximated by using first order difference equations. Taking into account of the backscattered CEX ions, the differential cross-section can be rewritten as follows [195]

$$I_{\mathrm{CM}}(\chi) = (1 - P_{\mathrm{CEX}}(\chi))I_{\mathrm{CM}}(\chi) + P_{\mathrm{CEX}}I_{\mathrm{CM}}(\pi - \chi) \tag{4.18}$$

The first and second terms on the right-hand side of Eq. (4.18) denote the MEX and CEX collision contributions to the total differential cross-section, respectively. If the collision partners have equal mass and the target particle is stationary, the CM differential cross sections can be converted into the LAB reference frame by [79]

$$\left.\frac{d\sigma}{d\Omega}\right|_{\mathrm{LAB}} = \left.\frac{d\sigma}{d\Omega}\right|_{\mathrm{CM}} 4\cos(\chi/2) \tag{4.19}$$

For the CEX collision, the LAB differential cross section is calculated by replacing χ with $\pi - \chi$ in Eq. (4.19).

Figure 4.10 plots LAB cross sections derived using the classical scattering with the spin-orbit free potential and the repulsive part of the potential ($V_{\Sigma g}$) for an LAB ion energy of 1500 eV. In this figure, $P_{\mathrm{CEX}} = 0.5$ is used for simplicity [73], which is a reasonable assumption except near 0 and 90 degrees. The non-symmetric behavior of the solutions about 45 degrees is caused by the transformation from the CM to LAB frame. The two differential cross-sections have a very similar trend in that both potentials lead to a large probability in small angle scattering. It should be noted that the LAB differential cross sections are obtained under the assumption of the stationary target atom. The effect of initial target particle velocity to the post-collision velocity is discussed in detail in Sec. 4.5.3. For the repulsive potential, larger differential cross-sections at intermediate angles indicate relatively larger scattering as shown in Fig. 4.7.

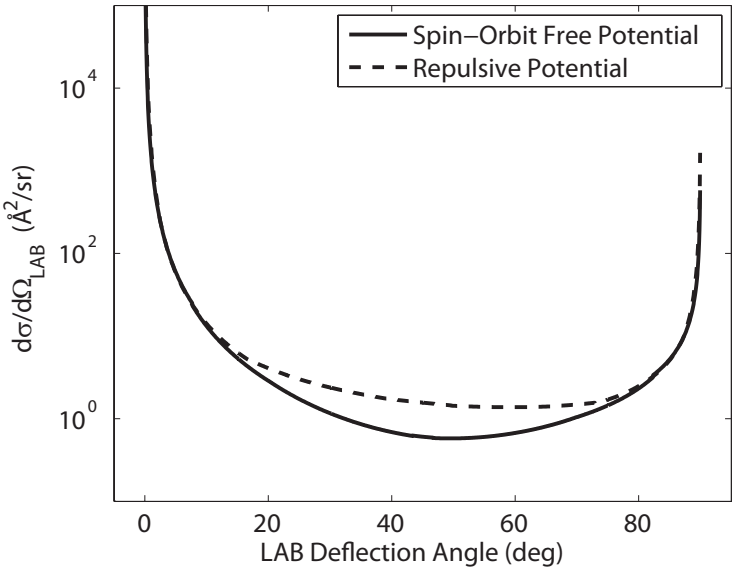

Figure 4.10: LAB differential cross sections for an ion energy of 1500 eV calculated using the classical scattering model with the spin-orbit free potential and the purely repulsive part of the interaction potential.

As noted earlier, the deflection angle is computed using the VHS model below the incident ion energy of 30 eV. This limit is obtained by observing the scattering angle that the rainbow singularity occurs (rainbow angle). As long as there is a inflection point in the deflection function, the singularity is always found in the differential cross-section. The classical scattering theory is not valid near the singularity, and the quantum effect has to be taken into account [197, 201]. As the energy is increased, the rainbow angle becomes smaller, and eventually, the singularity becomes indistinguishable from a glory singularity in which the differential cross-section becomes infinity as approaching zero degree. Figure 4.11 shows the differential cross-sections at the CM energies of 0.5 and 15 eV. Note that these differential cross-sections are obtained without considering the effect of the CEX collision. In Fig. 4.11(a), the singularity occurs at the rainbow angle of 35.5° when using the classical scattering theory, and the discontinuity should be smoothed out with the quantum scattering theory. At the CM energy of 15 eV (Fig. 4.11(b)), the rainbow singularity occurs at the CM angle of $\sim 1°$ ($\theta_{\mathrm{LAB}} \approx 0.5°$). In that region, the accuracy of the deflection angle calculation is not critical in the computational model. In other words, even with an error in the classical

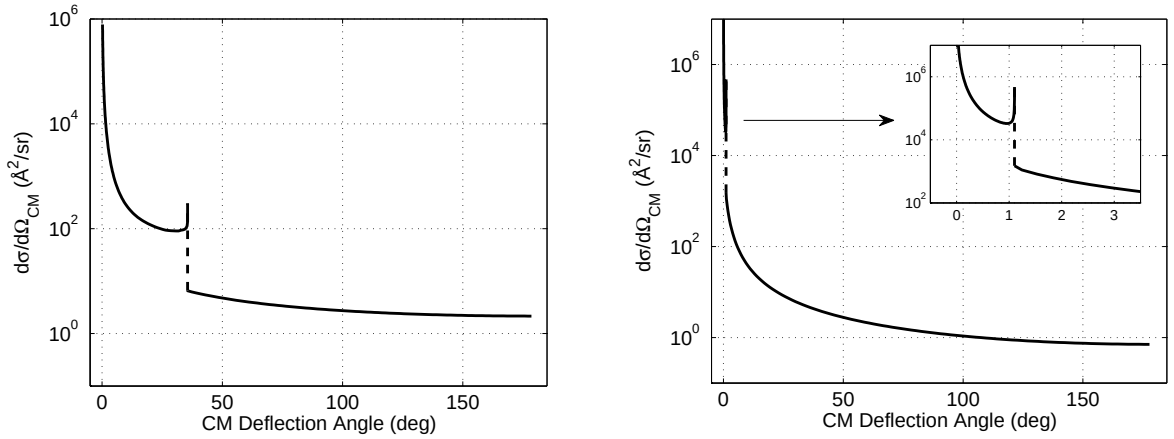

(a) $E_r = 0.5$ eV. (b) $E_r = 15$ eV.

Figure 4.11: Rainbow singularity in the CM differential cross-sections.

theory, the actual deflection angle should be very small anyway. Therefore, we chose 30 eV as the limit. The energy limit does not have to be 30 eV as long as it is not close to the energies that the primary and CEX ions may have. In this way, the collision calculations are consistent for each species, as the primary and CEX ion collisions are generally approximated using the classical scattering and the VHS model, respectively.

4.3.7 Xe + Xe Collisions

As primary ions encounter background neutrals, they may experience CEX collisions, exchanging the charge between the two species. The product of the CEX collisions is high-energy neutral atoms and slow CEX ions. Although the high-energy neutrals do not carry any charge, their impact on the electrode surfaces can cause emissions of secondary electrons due to their high mass and energy. Therefore, it is important to accurately predict the fast neutral atom trajectories to determine the secondary electron current from the electrodes.

Just as the primary ions, the fast atoms can experience MEX collision with the thermal background neutrals. The collision is approximated by the similar method as the ion-atom collision using the classical scattering equation given in Eq. (4.7). In determining collision probability at every time-step, the cross-section computed and tabulated by Phelps [207] is used. The cross-section data are fitted into different forms depending on the relative energy

between the collision pair.

$$\begin{cases} \log(\sigma) &= -0.196\log(E_r) + 2.60 & E_r < 5.9\text{eV} \\ \log(\sigma) &= -0.421(\log(E_r))^2 + 0.815\log(E_r) + 2.07 & 5.9\text{eV} \le E_r < 38.7\text{eV} \\ \sigma &= 915(E_r^{-0.415})(1 + E_r/250)^2)^{0.166} & E_r \ge 38.7\text{eV} \end{cases} \tag{4.20}$$

Here, σ is in Å^2 and E_r is in eV. The fitted total cross-section (Eq. (4.20)) is plotted in Fig. 4.12 together with the tabulated data provided in Ref. [207]. The total cross-section exhibits an oscillatory structure caused by glory scattering [208, 209]. The fitting equation given in Eq. (4.20) resolves the oscillation at the energy around 38 eV while the highly oscillatory region at low energy is not resolved. Even after multiple collisions, the fast neutrals hardly reach that low of energy; therefore, accurate fitting of the cross-section at low energies is not necessary.

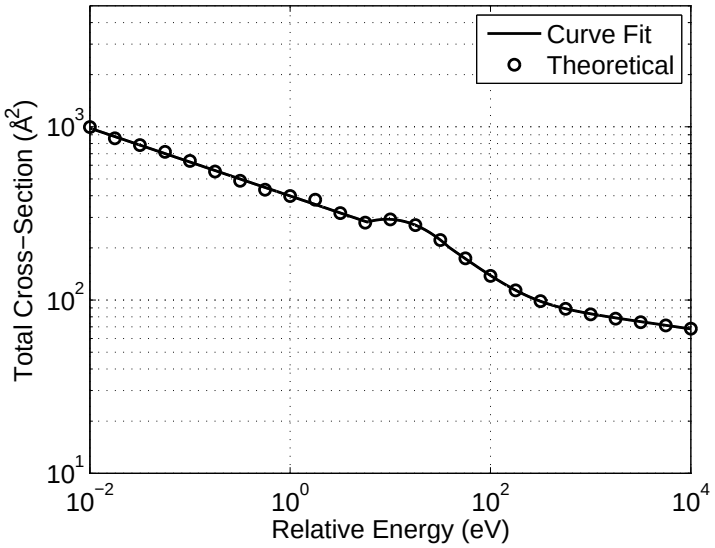

Figure 4.12: Total cross-section for collisions between xenon atoms.

Table 4.3: Parameters for Xe-Xe interaction potential [210].

Parameter	Value
A^*	5.44087277×10^4
α^*	7.52958289
c_6	1.0055522
c_8	0.58359858
c_{10}	0.47378306
β^*	-3.3390428
D	1.114
ε/k (K)	282.8
R_m (Å)	4.3656

In order to determine the post-collision velocity, Xe-Xe interaction potential provided by Dham et al. [210] is used in the classical scattering equation (Eq. (4.7)).

$$V(r) = \varepsilon V^*(x) \tag{4.21}$$

where

$$\begin{aligned} V^*(x) &= A^* \exp(-\alpha^* x + \beta^* x^2) - F(x) \sum_{j=0}^{2} c_{2j+6}/x^{2j+6} \\ F(x) &= \begin{cases} \exp[-(D/x - 1)], & x < D \\ 1, & x \geq D \end{cases} \\ x &= R/R_m \end{aligned} \tag{4.22}$$

Values for the parameters are provided in Table 4.3. The Xe-Xe potential curve given in Eq. (4.21) is a semi-empirical equation fitted into the form of HFD-B2 potential by adjusting the coefficients based on experimental data for various properties.

Figure 4.13 compares the interaction potential curves for Xe-Xe and Xe^+-Xe elastic collisions used in the model. The potential curves for the two collisions are very similar as shown in Fig. 4.13(a). However, the Xe-Xe potential starts to deviate from the Xe^+-Xe potential below internuclear distance of 2 Å. Figure 4.13(b) plots a narrower range of potential energy

to clearly show the difference where the energy becomes negative. It is apparent that the Xe-Xe potential is less negative, indicating lower attractive force. Figure 4.14 shows the deflection functions computed for the Xe-Xe and Xe^+-Xe elastic collisions. The differences in the deflection functions are caused by the slight differences in the potential curve below 2 Å and between 3 to 6 Å. At higher energies, the incident particle can further approach the target particle, and its trajectory is affected significantly more by the potential below 2 Å for small impact parameters. On the other hand, the effect of attractive force becomes more significant at lower energies, causing deflections at negative angles.

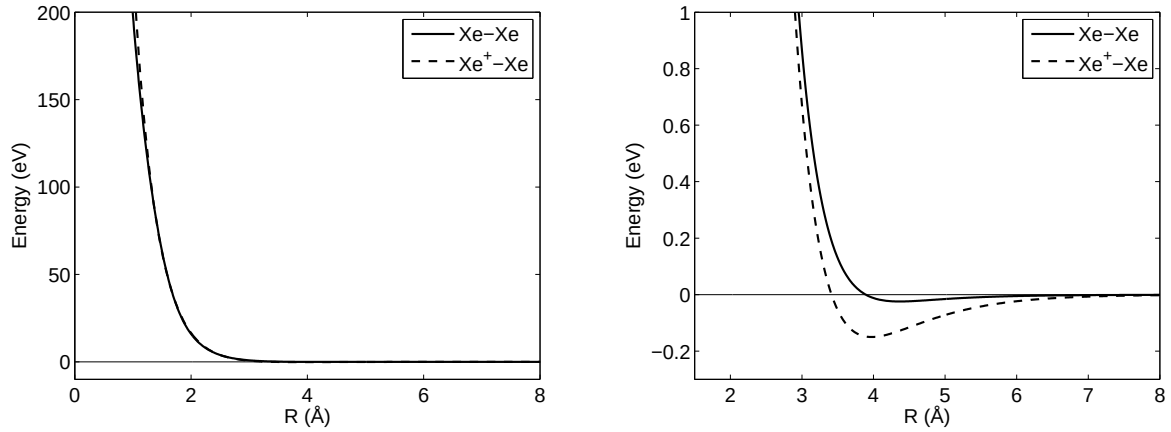

(a) From -10 to 200 eV (b) From -0.3 to 1 eV

Figure 4.13: Interaction potential curves for Xe-Xe and Xe^+-Xe collisions used in the model, displaying different ranges of potential energy.

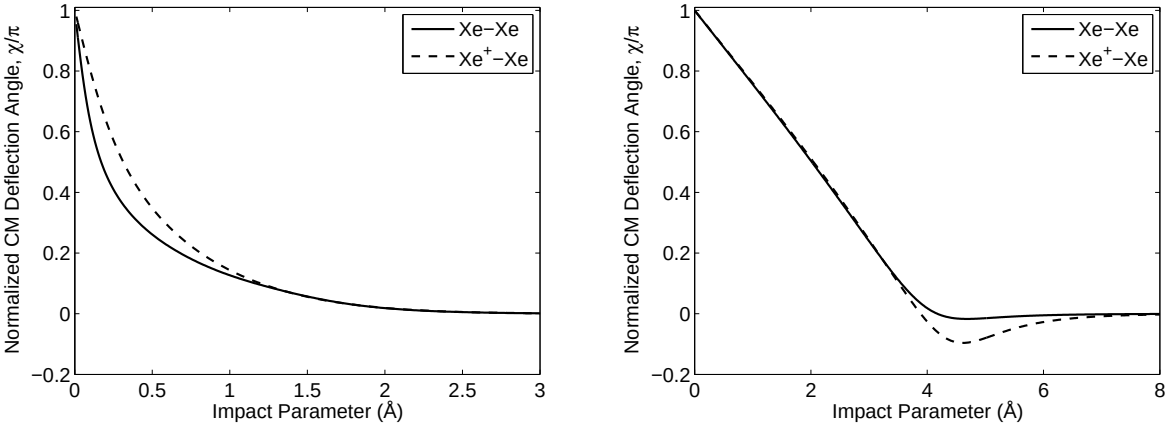

(a) Incident particle energy of 1500 eV (b) Incident particle energy of 2 eV

Figure 4.14: Comparison of deflection functions for Xe-Xe and Xe^+-Xe collisions.

4.3.8 Secondary Electron Emission

With inclusion of only the primary and CEX ions, the computational model was not capable of predicting the electrode currents that agree sufficiently well with the experimental results. Furthermore, more recent data from the ion beam experiment with biased electrodes [211] suggested that the effect of the secondary electrons to the experimental result must be significant. Therefore, the secondary electron emission from the electrode surfaces had to be incorporated in the model.

When particles (ions, atoms, electrons, or photons) with sufficient energy impact a surface and penetrate into the solid by a finite depth, electrons in the solid are excited. These electrons can directly reach the surface or experience multiple collisions with other electrons beforehand. As a result, a finite number of electrons transported to the surface can be emitted from the surface. The number of ejected electrons per incident particle is called secondary electron yield (SEY). For ion induced secondary electron emission, electrons can be excited by two different processes, depending on the incident ion energy [212]. At lower energies, the potential electron emission is the dominant mechanism and can result from either Auger neutralization or Auger deexcitation [212, 213]. The kinetic energy of the incident particle is not required to induce this process. At higher energies, the secondary electron emission is increasingly dominated by the kinetic electron emission where the kinetic energy of incident particle is transferred to the electrons. The two excitation processes can only occur at an energy greater than the threshold that is a function of the minimum energy required to free an electron, U_m [212]. After the threshold for kinetic emission, SEY generally increases with energy at energies below 10 keV. Therefore, in the experiment to be simulated, primarily the primary ions and fast atoms are responsible for the electron emission from the electrodes. At the incident ion energy of approximately 1500 eV, both the electron excitation mechanisms can be significant. On the other hand, electron excitation is solely due to KE process for atom induced electron emission since neutral atoms do not carry any potential energy [212, 214].

Potential Electron Emission The potential emission only occurs when the internal energy is larger than twice the minimum energy required to free an electron, U_m, where U_m can be approximated to be equal to the work function (W_ϕ) for metals [212]. The contribution of potential emission to ion-induced electron emission can be approximated by the simple equation given by Kishinevskii [215].

$$\gamma_p = \frac{0.2}{E_F}(0.8E_i - 2W_\phi) \tag{4.23}$$

where γ_p is the SEY due to potential emission, E_F is the Fermi-energy of the target material, and E_i is ionization energy of the incident ion. For the combination of xenon ion and stainless steel, the SEY due to potential emission is approximated to be 0.016. Here, the value is obtained using the Fermi energy for iron ($E_F = 11.1$ eV), the work function for stainless steel ($W_\phi = 4.4$ eV), and the ionization energy for xenon ($E_i = 12.13$).

Kinetic Electron Emission Extensive research has been done to gather experimental data and formulate theories or semi-empirical relations for kinetic electron emission. Many of theories are valid for certain combination of ion and target material in limited energy [216]. These theories, including classical theory by Sternglass [217] and more rigorous theory by Schou [218], predict the SEY to be directly proportional to the inelastic stopping power (dE/dx) and are only valid for high energy ions. For protons above the energy of 10 keV, the ratio of SEY to dE/dx holds constant for various target material [219], indicating that the classical theories are valid for the combination of ions and target materials. However, the assumption of the direct proportionality between SEY and dE/dx does not hold for heavy ions especially at lower energies (< 50 eV) [220]. More recent semi-empirical equation provided by Winter et al. [221] using the theory proposed by Lorincik et al. [222] may possibly

be applied to the xenon ion at the energy of interest.

$$\gamma_{KE} = 2\xi\rho^2 V^2 \left\{ \exp\left(\frac{-\pi W_\phi}{2\gamma v}\right) - \sqrt{\pi}\sqrt{\frac{\pi W_\phi}{2\gamma v}}\mathrm{erfc}\left(\sqrt{\frac{\pi W_\phi}{2\gamma v}}\right) + \frac{\pi\gamma v}{6\varepsilon_0}\left[\exp\left(-\frac{W_\phi}{\varepsilon_0}\right)\sqrt{\pi}\sqrt{\frac{W_\phi}{\varepsilon_0}}\mathrm{erfc}\left(\sqrt{\frac{W_\phi}{\varepsilon_0}}\right)\right]\right\} \tag{4.24}$$

where v is the incident particle velocity, ρ is the electronic density of states at the Fermi energy, and V is the scattering matrix element. Here, ξ, γ, and ε_0 are fitting parameters. Unlike the other theories, this theory is based on a many-electron mechanism, assuming that electron excitation takes place locally within the impact zone through electron-electron interaction [221,222]. The SEY data for kinetic emission as a function of inverse of impact ion velocity are fitted fairly well for xenon and gold ions colliding with a clean gold surface [221]. Unfortunately, Eq. (4.24) cannot be applied for our system because of scarce data available for the combination of xenon ion and stainless steel at the energy of interest.

Total Ion Induced Secondary Electron Yield As described above, none of the existing theory is sufficient to predict the SEY value for the combination of 1500 eV xenon ion and stainless steel. Furthermore, there exist no experimental data for SEY in our system. Therefore, we simply conducted a parametric study by using different SEY values and comparing the results with our experimental data. In doing this, it was necessary to determine at least an order of magnitude for SEY applicable to the experimental condition. First, we gathered SEY data for xenon ions impacting various metals as shown in Fig. 4.15. At the impact energy of 1500 eV, the SEY values for all the metals except molybdenum are on the order of 10^{-2} electrons/ion. Now, we need to determine where the SEY for stainless steel lies in Fig. 4.15. The SEY data for sodium and cesium ions impacting on aluminum and stainless steel are provided by Martel and Olson [223]. For impact energy of 20 keV, SEY values are 20.0, 22.5, 37.4, and 32.5 electrons/ion for $Na^+ \rightarrow$ Al, $Na^+ \rightarrow$ SS, $Cs^+ \rightarrow$ Al, and $Cs^+ \rightarrow$ SS, respectively. Here, stainless steel is denoted by SS. These data suggest that the SEY values for aluminum and stainless steel should be on the same order of magnitude. Furthermore, the SEY data provided by Ray and Barnett [224] for low-energy (0-5 keV) proton impact on

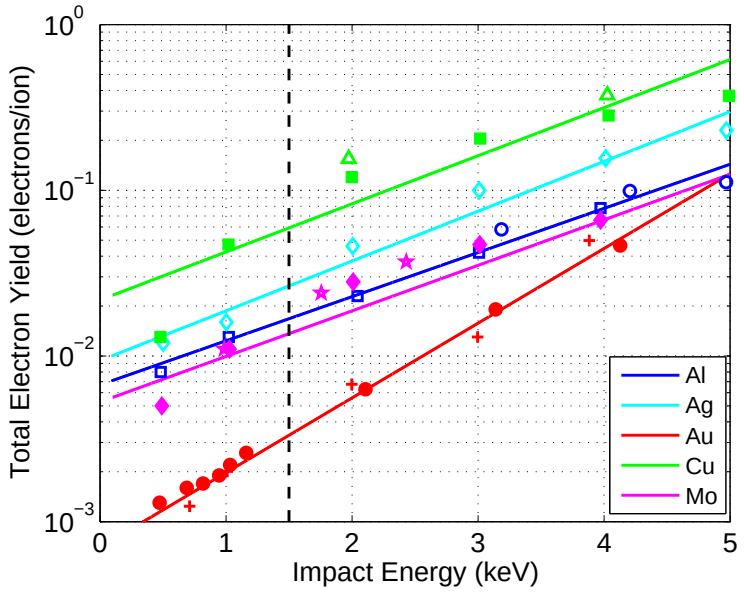

Figure 4.15: Total secondary electron yield under bombardment with xenon ion on clean aluminum (○ [220], □ [225]), silver (◊ [225]), gold (● [226],+ [227]), copper (■ [225],△ [228]), and molybdenum (⧫ [225],★ [229]). Solid lines are exponential fits to the data for energy between 0.5 and 5 keV.

various metals suggest that the SEY for stainless steel and molybdenum should be similar. Since the yields for aluminum and molybdenum are similar for the energy of 1.5 keV, the SEY for xenon ion impact on clean stainless steel is expected to be approximately 10^{-2} electrons/ion.

While conducting the parametric study for different SEY values on the order of 10^{-2} electrons/ion, it was found that the value was too small to provide simulation results in sufficient agreement with the experimental data. The SEY is required to be at least one order of magnitude larger than the value we expected initially. This can easily be explained in terms of oxidation and contamination of the electrode surfaces. The Test Cell electrodes were made from scrap piece of stainless steel that had been exposed to atmosphere for days/months and possibly been contaminated. When conducting an experiment, the electrodes were never cleaned while cleaning of the surface could have been achieved by sputtering or flash-heating [213]. As found in many literature [213, 214, 230, 231], the change in total yield due to oxidation/contamination of the surface is a well-known phenomena. As found by Walton et al. [231], the electron yield under bombardment of sodium ion on stainless steel increased

with the degree of oxygen exposure for impact energy lower than 500 eV. The increase in SEY was up to 100 times. Furthermore, Alonso et al. [230] showed that SEY from oxidized stainless steel target under bombardment with various ions was up to 10 times larger than from clean stainless steel for the impact energy between 1.5 and 30 keV. Therefore, we can expect the true yield for our system to be somewhere between 10^{-1} and 1 electrons/ion.

Total Atom Induced Secondary Electron Yield Although xenon ions and atoms have essentially the same mass, the yield from a target surface can be different. Excitation of electron due to potential emission does not occur for neutral atoms as they do not carry potential energy [212, 214]. Furthermore, the yield due to the kinetic emission is found to be generally lower for neutral atoms than for charged ions at low energies [213]. Lakits et al. [227] provided an analytical formula for ratio of yields for bombardment by neutral and charged projectiles.

$$\frac{\gamma^o}{\gamma^+} = \frac{(1 - F_0^\infty)(1 - k) + k(1 + y)}{(1 - F_0^\infty)(1 - k) + k + y} \tag{4.25}$$

where y is defined as x_0/L, x_0 is the e-folded length, L is the electron escape length, F_0^∞ is the equilibrium charge state fractions, and k is the screening factor. Equation (4.25) is derived by assuming a lower inelastic stopping power for neutral atoms due to screening of the proton charge. This results in a further penetration into the solid, and therefore, a lower electron yield. In the limit of low energy, Eq. (4.25) reduces to the following expression.

$$\frac{\gamma^o}{\gamma^+} \approx \frac{k(1 + y)}{k + y} \tag{4.26}$$

Although Eq. (4.26) seems to be extremely simple, the appropriate inputs for k and y are not precisely known, especially for our system where no data are available. Lakits et al. [227] also provided experimental data for various ions and atoms impacting on gold (Fig. 4.16). For all the atoms, the ratio of SEY by atoms to SEY by ions, γ^o/γ^+, was generally in the range of 0.75 to 0.95 as shown in Fig. 4.17. For simplicity, we used the average value of 0.85 for the ratio of yields in conducting a parametric study.

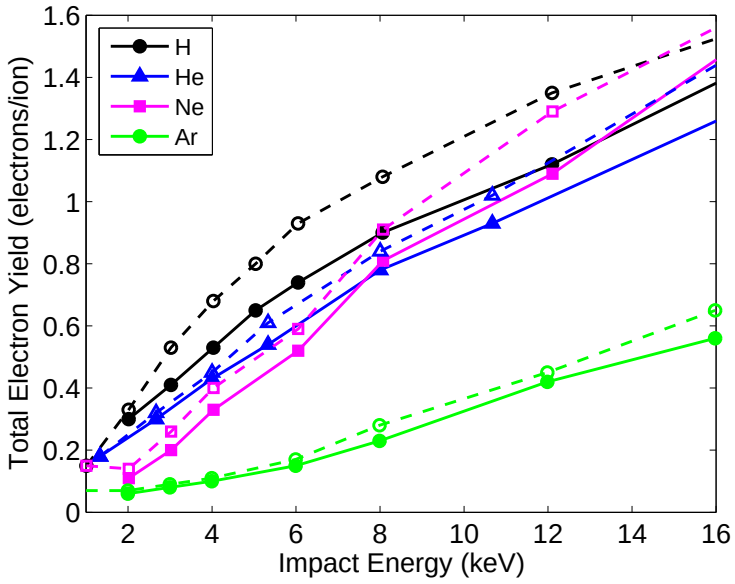

Figure 4.16: Total secondary electron yield under bombardment with various ions and atoms on clean gold (Reproduced from [232]). Open markers are for ions and filled markers are for neutral atoms.

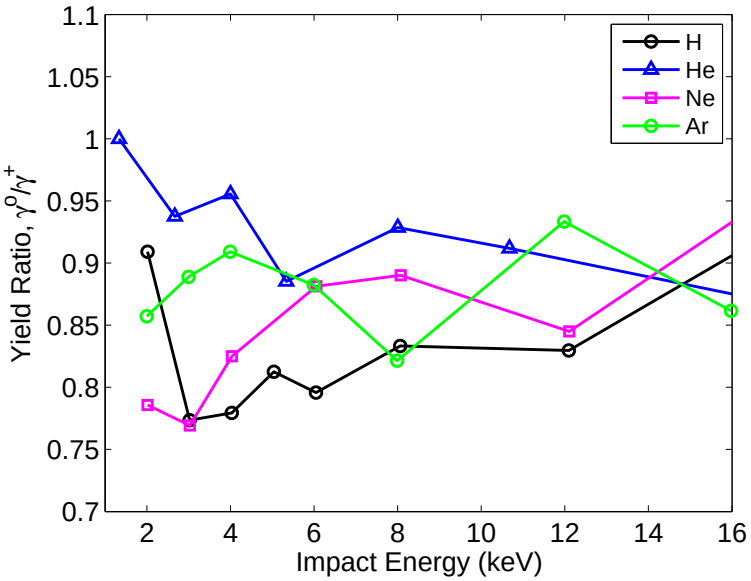

Figure 4.17: Secondary electron yield ratio under bombardment by various neutral atoms and their ions (Reproduced from [232]).

Dependence of Total Yield with Angle of Incidence Total secondary yield generally increases with incident angle with respect to surface normal. At larger angles, the penetration depth from the surface becomes smaller so that it is easier for the excited electrons to reach the surface and being ejected into vacuum. For incident angle less than 70°, an empirical relation has been obtained from experimental data for heavy ions [233–236]:

$$\gamma(\theta) = \gamma(0) \cos^{-f} \theta \tag{4.27}$$

Here, f is a parameter ranging from 0.5 to 1.5. The parameter depends on the impact energy, the combination of incident particle and target material, and the angle of incident [213]. In spite of the empirical relation, we neglected the dependence with incident angle for several reasons. First, no experimental data are available to determine the parameter, f. Second, the aspect ratio of Test Cell is very large, and the high-energy particles generally impact the Exit Plate at small angles with respect to the surface normal. The SEY from the Inner Cylinder is not as significant as the SEY from the Exit Plate because of much larger high-energy particle flux to the Exit Plate. Third, the computational run-time will be too large if we keep track of incident angles for all high-energy particles. Lastly, an accurate prediction of the dependence with the incident angle is not so important as the total yield at normal incidence is not precisely known.

Angular Distribution of Emitted Electrons The angular distribution of emitted secondary electrons is generally accepted to be at cosine distribution [212, 213].

$$\frac{d\gamma}{d\Omega}(\theta) = \frac{d\gamma}{d\Omega}(0) \cos(\theta) \tag{4.28}$$

where θ is the ejection angle of secondary electron with respect to the surface normal. The ejection is most probable in the direction perpendicular to the surface, and the probability decreases with increasing angle. The angular distribution is found to be independent of projectile incident angle [213]. Furthermore, no dependence on the azimuthal angle has been observed [213]. The cosine distribution for the electron emission is used in the model.

Energy Spectra of Emitted Electrons The energy distribution of the secondary electrons from metals by ion bombardment exhibits the peak that lies below an energy of 10 eV (typically $2 - 4$ eV) [226, 237, 238]. The peak is due to the cascade process between the electrons within the solid [239, 240]. With increasing energy, the intensity rapidly rises up to the cascade peak and then decreases relatively gradually. This feature is the most dominant in the energy spectra. Additional distinct peaks may be seen at different energies, but the intensity is much less than the cascade peak [239]. These peaks are the results of other processes such as Auger electron emission, autoionisation, and plasmon decay [221]. In spite of the improved understanding in secondary electron emission mechanisms, there are no experimental data or semi-empirical relations that can be applied to our system. In addition, the precise knowledge of the secondary electron energy is not required since the secondary electron trajectories are expected to be close to straight paths due to the very low potential in the domain. Therefore, we assumed in the computational model that the emitted electrons are mono-energetic at 4 eV; This value is within the range of typical energy that the cascade peak lies.

4.4 Analytical Model for Exit Orifice Current

A simple analytical solution for the Exit Orifice current (approximately the sum of Back Aperture and Collector Plate currents) derived in this section is used as a tool for a sanity check of the computational model. A flux Γ' of the beam ions traveling a distance of dx can be expressed in terms of initial flux Γ, neutral density n_o, and the collision cross-section σ [141].

$$\Gamma' = \Gamma(1 - n_o \sigma dx) \tag{4.29}$$

Then, the change of Γ with distance is

$$\frac{\Gamma' - \Gamma}{dx} = \frac{d\Gamma}{dx} = -n_o \sigma \Gamma \tag{4.30}$$

Integrating Eq. (4.30), the ion beam current at any distance, x, is calculated.

$$J = J_0 \exp(-n_o \sigma x) \tag{4.31}$$

where J is given as $J = e\Gamma A$. Equation (4.31) can be used to predict the total current through the Exit Orifice. If we assume that the ions experiencing both MEX and CEX collisions are deflected at large enough angles, then the cross section in Eq. (4.31) is simply $\sigma = \sigma_i \approx 2\sigma_{\text{CEX}}$. However, the deflection functions given in Sec. 4.3.4 predict very high probability of small angle scattering due to the elastic collisions, and a very large fraction of the primary ions experiencing the MEX collisions is essentially "unscattered" (i.e., the primary ions will pass through the Exit Orifice). For this reason, we find $\sigma = \sigma_{\text{CEX}}$ to be the appropriate cross-section in Eq. (4.31). The implication of using σ_{CEX} is that all the MEX ions reach the Exit Orifice while all the CEX ions do not reach the Exit Orifice. Of course, this description is not exactly true but approximates the reality the best.

4.5 Results and Discussion

4.5.1 Electrode Currents

Exit Orifice Figure 4.18 shows currents through the Exit Orifice (the sum of the Back Aperture and Collector Plate currents), predicted by the IB model, the analytical model, and measured in the ion beam experiment [80]. For this Exit Orifice current result, we neglected the effect of the secondary electron emission. Note that the current values are normalized by the sum of currents measured at all the electrodes to clearly show the trends in collisionality as discussed in Refs. [80]. At very low pressure, most of the primary ions reach the Exit Orifice without experiencing any collision. As the pressure is increased, an increasing number of primary ions diverge from the beam because of the MEX and CEX collisions, and the current reaching the Exit Orifice is decreased exponentially as predicted by Eq. (4.31). It can be seen in Fig. 4.18 that the results from the IB model and the analytical model with $\sigma = \sigma_{\mathrm{CEX}}$ agree well with the experimental result. Here, we used σ_{CEX} from our calculation rather than the empirical equation given in Eq. (4.1) (see Fig. 4.9) to better compare with

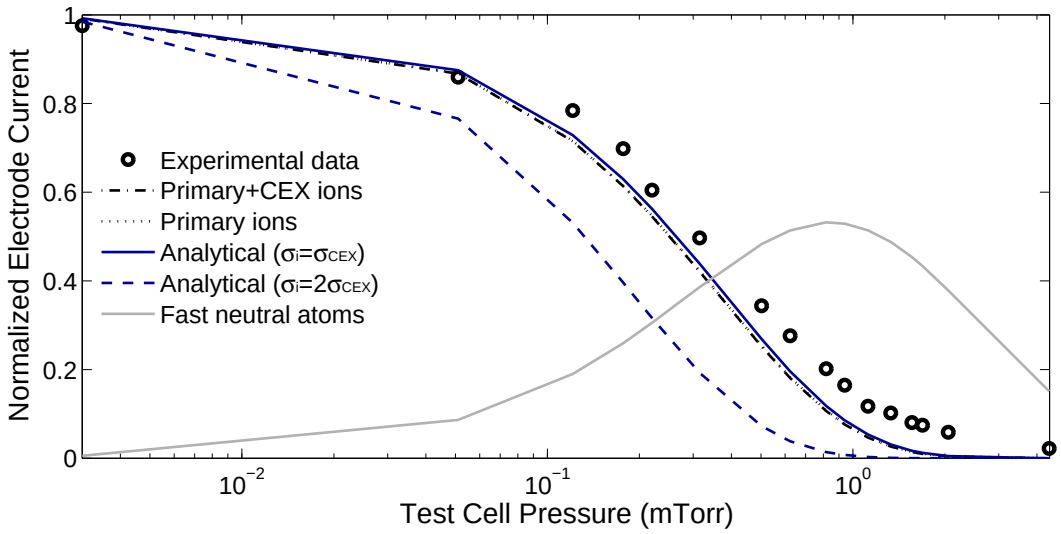

Figure 4.18: Current through the Exit Orifice. The current values are normalized by the sum of charged particle currents to all electrodes. The fast neutral current is normalized by the current (particle/s) equivalent to the sum of charged particle currents (C/s) to all electrodes.

the computational result. The slight disagreement with the experimental result can be attributed to our calculation of the CEX cross-section. The calculation of the CEX cross-section is sensitive to the interaction potential function, which is not known perfectly. Even with a slight adjustment of the cross-section, the analytical solution never matches better at the pressure of $\sim 10^0$ mTorr. Around the pressure, the high-energy neutral current to the electrode happens to be higher than at other pressures. This suggests that the discrepancy is due to the secondary electron emission that we did not take into account of for the Exit Orifice. The secondary electrons emitted from Back Aperture and Collector Plate can be collected at other surfaces, simply raising the current measured at these electrodes.

The analytical model with $\sigma = \sigma_{\mathrm{CEX}}$ predicts slightly higher currents than the currents predicted by the IB model. Although the classical scattering model predicts a very large probability in small angle scattering, the MEX ions can be deflected at relatively larger angles. On the other hand, while the initial CM velocity of the newly created CEX ion is most likely be at large angle, the LAB velocity can be at small angle depending on initial velocity of the target neutral atom. The discrepancy between computational and analytical results simply means that the IB model predicts slightly more larger-angle scattered MEX ions compared to very small-angle scattered CEX ions. It is clearly seen that the analytical model with $\sigma = 2\sigma_{\mathrm{CEX}}$ is far off from the other results because it neglects effectively "unscattered" MEX ions (the MEX ions with very small deflection angles) in the electrode current.

Inner Cylinder and Exit Plate Figures 4.19 and 4.20 plot normalized currents predicted by the IB model and measured during the ion beam experiment at the Inner Cylinder and the Exit Plate, respectively. Different species currents are added incrementally to clearly show the contribution by each species. With inclusion of more species, the computed electrode currents generally become closer to the experimental results, and the simulation results with $\gamma = 0.4$ agree fairly well with the experimental results.

As seen in Fig. 4.19, the MEX ion current to the Inner Cylinder is almost negligible. On the other hand, a significant fraction of the MEX ions impact the Exit Plate as shown in Fig. 4.20. Although the classical scattering model predicts a high probability in small

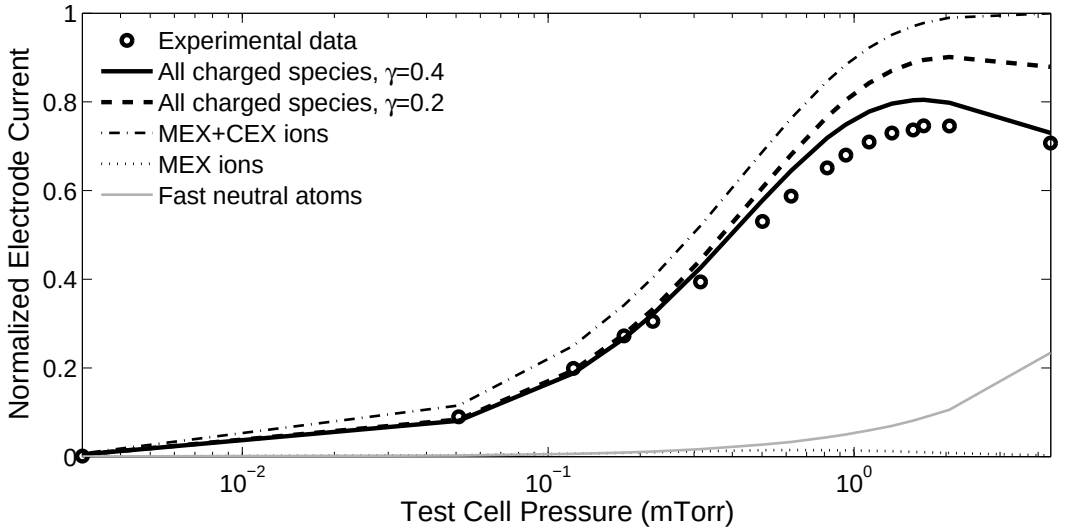

Figure 4.19: Normalized electrode current at the Inner Cylinder. The current values are normalized by the sum of charged particle currents to all electrodes. The fast neutral current is normalized by the current (particle/s) equivalent to the sum of charged particle currents (C/s) to all electrodes.

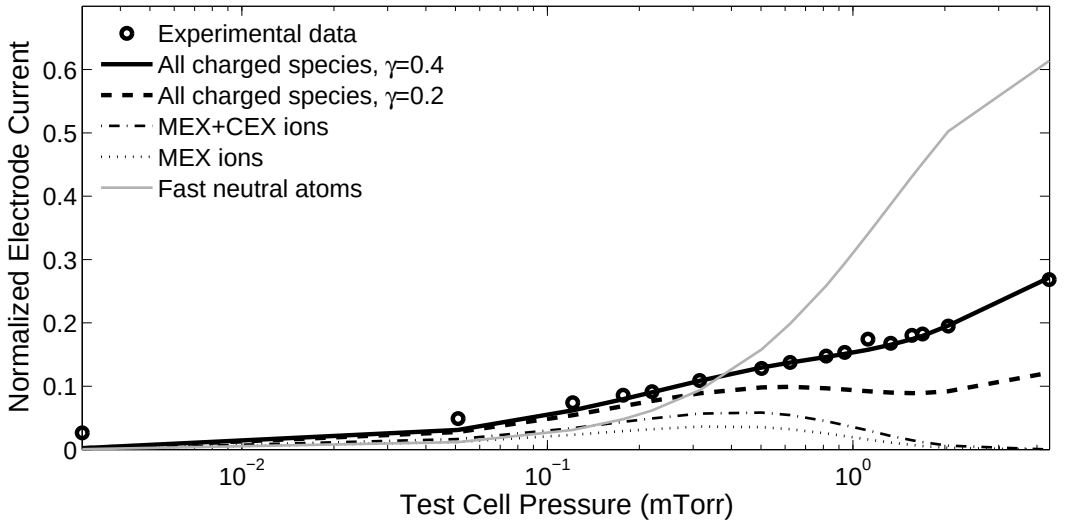

Figure 4.20: Normalized electrode current at the Exit Plate. The current values are normalized by the sum of charged particle currents to all electrodes. The fast neutral current is normalized by the current (particle/s) equivalent to the sum of charged particle currents (C/s) to all electrodes.

angle scattering, some fraction of the MEX ions can be deflected at larger angles. However, the deflection is mostly not large enough to impact the Inner Cylinder. One might expect increasing population of large-angle scattered MEX ions at higher pressures. However, the probability of CEX collision increases with pressure as well, and the MEX ions can experience the CEX collision on the way to an electrode, resulting in a reduction of the overall MEX ion population as shown in Fig. 4.21.

The CEX ions are the main contributor to the Inner Cylinder current due to their large scattering angles and the large aspect ratio of the Test Cell. The initial increase is primarily due to the rapid rise in the CEX ion population as shown in Fig. 4.21. Even with the large aspect ratio of the test cell, a significant fraction of CEX ions contributes to the Exit Plate current. This is due to the small angle scattered CEX ions (and CEX ions at moderate angles created near the Exit Plate). The classical scattering model predicts small angle scattering for the MEX ions, which implies that the deflection of the CEX ions are mostly at large angles in the CM frame. However, since the post-collision speed is comparable to the initial target speed, the velocity distribution of CEX ions becomes nearly isotropic after the transformation of the velocity into the LAB frame, increasing the CEX ion population

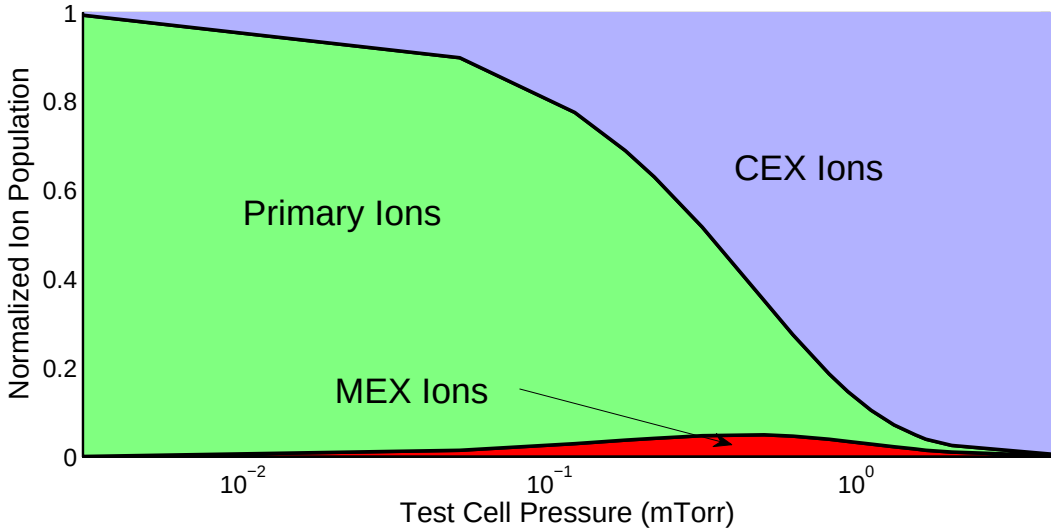

Figure 4.21: Types of ions before impacting the electrodes. Primary ions include effectively "unscattered" ions that experience MEX collision but are at very small angle such that they pass through the Exit Orifice.

at small angles with respect to the incident particle velocity. A further discussion on the importance of initial target velocity is given later in Sec. 4.5.3.

At higher pressures, the effect of secondary electrons becomes increasingly prominent. This effect can be seen in both the Inner Cylinder and the Exit Plate currents. As discussed in Sec. 4.3.8, the high-energy ion and neutral atom impacts on the electrode surfaces can cause the secondary electron emission, while the thermal atoms and the slow CEX ions typically do not have the energy beyond the threshold for the secondary electron emission. It turns out that electron emission by the fast neutral impact starts to dominate at the pressure greater than 10^{-1} mTorr. The contribution of MEX ions eventually becomes negligible at high pressures as a result of the reduction in the overall MEX ion population due to the CEX collisions. The maximum MEX ion population lies approximately at the pressure of 4×10^{-1} mTorr. This pressure corresponds to the value when the mean free path of CEX collisions becomes equivalent to the Test Cell length; past the pressure value, each ion experiences more than one CEX collision events on average. On the contrary, the number of fast neutrals increases exponentially with the number of CEX ions. The particle counts for fast neutrals and CEX ions at a given pressure are the same since the product of a single CEX collision event is one fast neutral atom and one CEX ion. Therefore, the total number of particles that induce secondary electron emission increase with the Test Cell pressure. Since those particles (MEX ions and fast neutral atoms) mostly impact the Exit Plate, the overall effect is a rise in the Exit Plate current and a reduction in the Inner Cylinder current. As indicated by relatively low fast neutral current, the secondary electron emission from the Inner Cylinder electrode is not as significant.

Effect of Beam Divergence The effect of beam divergence to the computational results is briefly examined by conducting a sensitivity study on the beam divergence to see if the simulation results are improved by inputting some reasonable divergence angles. During the experiment [80], an accurate measurement of the ion beam divergence angle was not possible with the experimental set-up. Before reaching the Test Cell, the beam ions experience multiple deflections to be guided into the Test Cell. These deflections can significantly alter

the divergence of the beam. The divergence angle can also be altered with the Test Cell pressure, as the neutral atoms can leak from the Test Cell and collide with the ion beam before entering the Test Cell. As long as the beam does not impinge the Exit Plate directly, the simulation results do not change significantly from the case with no beam divergence. Also, the direct impingement of the beam is not likely as seen in the trends in Figs. 4.18 and 4.20. In addition, it is found that the beam ion density is so low that the space charges do not affect the beam significantly, and the space charge contributions to the beam divergence is minimal. Therefore, the beam divergence is not significant, and the effect can be neglected.

4.5.2 Current Density Profiles along Electrodes

Figures 4.22 and 4.23 plot the computed current density as a function of position along the Inner Cylinder and the Exit Plate at the background xenon pressure of 0.22 mTorr, respectively. In addition to the ion current densities, the current density values for the secondary electrons ejected from the Exit Plate and collected at the Inner Cylinder are plotted. At the pressure of 0.22 mTorr, the ratio of the Test Cell length to the CEX collision mean free path is approximately 0.5, indicating half of the beam ions experience a single CEX collision event. As discussed above, the Inner Cylinder current is dominated by the slow CEX ions. Neglecting the sections near the upstream and downstream edges, the CEX ion current density generally decreases as approaching the Exit Plate. On the other hand, both the primary and CEX ions contribute to the Exit Plate current. At the pressure of 0.22 mTorr, the high-energy and slow CEX ions as well as the secondary electron emission current are of the same order except at a small radius. For all the species, the current densities decrease with radius. Most of the secondary electron current emitted from the Exit Plate is collected at the Inner Cylinder, reducing the total current measured at the electrode. It turns out that the secondary electrons are mostly collected at the section of the Inner Cylinder close to the Exit Plate.

At relatively low pressure, the CEX ions are almost entirely created within the ion beam, and their initial velocity distribution is nearly isotropic. The effect of initial target particle

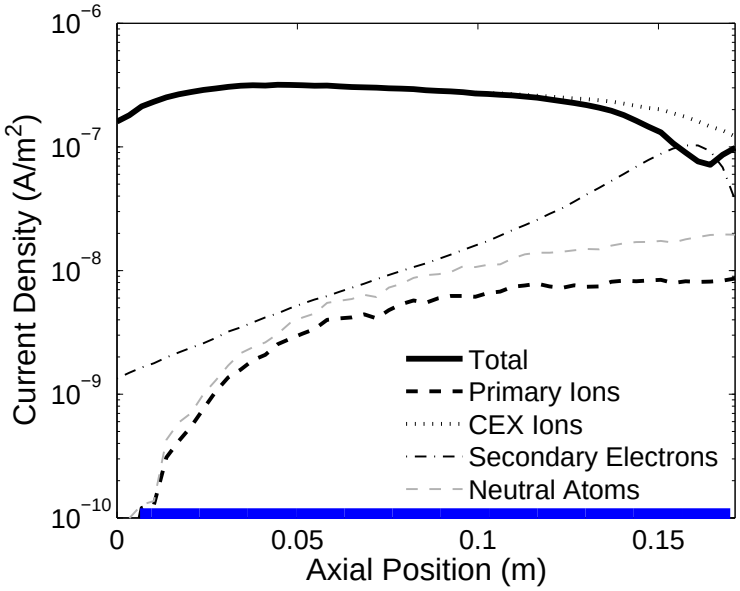

Figure 4.22: Current density along the radius of the Test Cell at background neutral pressure of 0.22 mTorr. Thick solid line along abscissa axis represents the Inner Cylinder. For neutral atoms, the current density (particle/s m^2) is expressed in terms of equivalent singly charged particle current (A/m^2). For secondary electrons, current density collected at the electrode is shown.

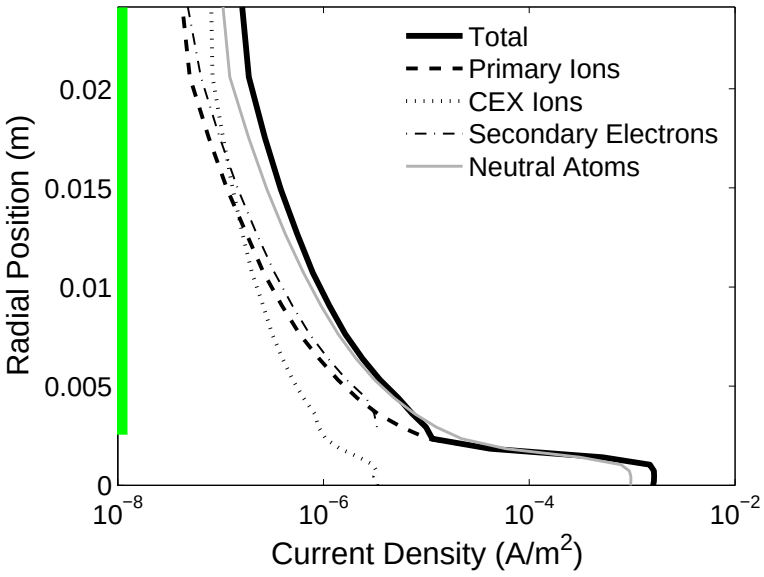

Figure 4.23: Current density along the downstream end of the Test Cell at background neutral pressure of 0.22 mTorr. Thick solid line along ordinate axis represents the Exit Plate. For neutral atoms, the current density (particle/s m^2) is expressed in terms of equivalent singly charged particle current (A/m^2). For secondary electrons, current density emitted from the electrode is shown.

velocity distribution to the post collision velocity is discussed in Sec. 4.5.3. For the sake of discussion, we will use a simplified description such as an isotropic velocity distribution for CEX ions and that the CEX ions are created at the centerline in order to explain the features of the CEX ion current density profiles. For the Inner Cylinder, the current density profile generally decreases toward downstream in the middle section away from the edges; this profile is due to the ion beam current attenuation by the CEX collisions. If the background neutral density is uniform throughout the domain, the CEX ion generation rate must be proportional to the ion beam current. Since the ion beam current is attenuated according to Eq. (4.31), the CEX ion generation rate also decreases exponentially along the path of the ion beam. A similar but slightly modified CEX ion profile should be seen at the Inner Cylinder as the CEX ions simply follow nearly straight paths from their origins to the electrodes at the pressure of interest. The decreasing currents at the upstream and downstream edges are due to the absence of the forward and backward CEX ion fluxes, respectively. The current density is proportional to the flux of the CEX ions perpendicular to the surface. Therefore, at the Exit Plate, the current density decreases with increasing radial position since the angles between the centerline axis and the impact position become larger. When the CEX ions are initiated farther downstream, the change in the angle becomes more dramatic with the radial position.

The electric field caused by the space charges in the beam does not significantly affect the shape of the beam itself because of its low ion density ($< 5 \times 10^{11}$ m^{-3}). As shown in Fig. 4.24, the maximum potential is approximately 0.08 V, which indicates that the potential energy is much smaller than the primary ion energy. Similarly, the second electron emission energy is assumed to be 4 eV, that is much larger than the maximum electric potential. Therefore, both the high-energy ions and secondary electrons are not significantly affected by the electric field, and they follow approximately straight paths. However, the majority of the CEX ions have energies on the same order of magnitude as the potential energy due to the high probability of large angle scattering in CM frame. The CEX ions initially heading toward the Exit Plate can be deflected toward the Inner Cylinder due to the radial electric field. Thus, the electric field acts to reduce the CEX ion current at the Exit Plate.

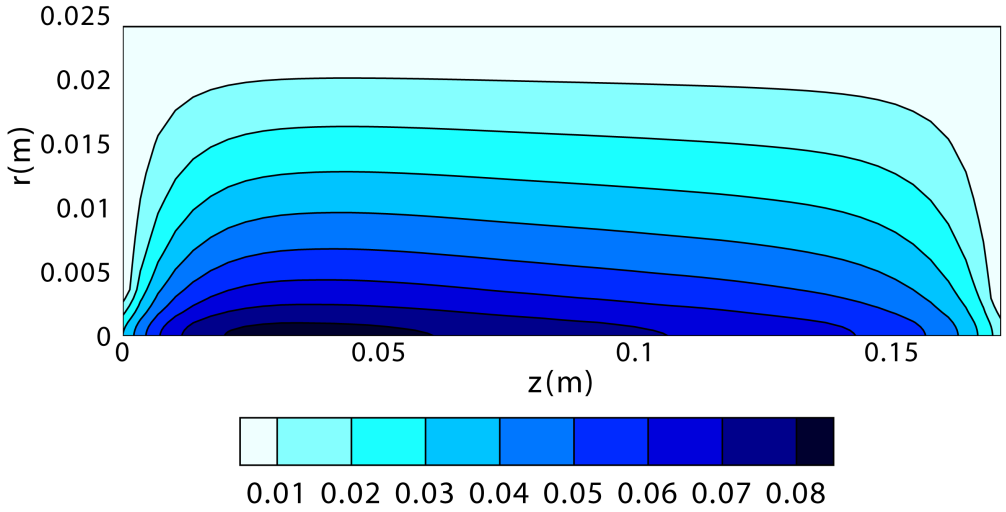

Figure 4.24: Contour of electric potential at background neutral pressure of 0.22 mTorr. The bottom boundary of the contour plot corresponds to the axis of symmetry of the Test Cell.

The secondary electron current density emitted from the Exit Plate is proportional to the sum of high-energy ion and neutral fluxes based on the assumptions made for our secondary electron model. Therefore, as expected, the profile for the secondary electrons ejection is very similar to the profiles for the high-energy species as shown in Fig. 4.23. The secondary electron collection profile at the Inner Cylinder may not seem reasonable at the first glance. A cosine distribution is used for the secondary electron ejection angle, and the distribution has the highest probability normal to the emission surface while the probability decreases with increasing angle. Solely based on the emission distribution, one may expect a higher flux, Γ, to furthest upstream location of the Inner Cylinder. However, the impact angle, θ, with respect to the collection surface normal has to be taken into account in estimating the current density profile. Considering this angle, the projected area, $A_p = A\cos\theta$, from the point on the Exit Plate to the Inner Cylinder is the largest at the furthest downstream (closest to the Exit Plate) of the Inner Cylinder. Therefore, the current density peaks when the flux times the projected area integrated along the emission surface becomes the maximum according to $j = q\Gamma A_p/A = q\Gamma\cos\theta$.

4.5.3 Importance of Initial Target Particle Velocity

In previous models such as the PIC-DSMC model developed by Giuliano and Boyd [76, 77], the curve-fit representation of the LAB differential cross-section was used to determine the post-collision velocities of the collision pair. The differential cross-section is not well defined at the extreme angles of 0 and 90° (see Fig. 4.10), and they assumed the differential cross-section to be constant around those angles [76, 198]. The assumption results in a very high probability in the CEX ion scattering at approximately 90°. Here, we will investigate the assumption and provide an improved description of the CEX ion velocity distribution when the CEX ions are created.

Figure 4.25 shows the LAB-frame post-collision CEX ion deflection angle with respect to the direction of the incident particle velocity for different pre-collision velocity distributions. Three pre-collision velocity distributions are investigated: (1) Stationary, (2) Unidirectional, in the direction of the incident particle, and (3) Isotropic distributions. For all the cases, the incident ion and target neutral speeds are assumed to be $47,000$ and 220 m/s, respectively. These speeds correspond to the speed of 1500 eV xenon ion and the mean velocity of xenon neutral at room temperature. At the impact parameter of 0 Å, the collision is head on, and the CEX ion is deflected in the same direction as the incident ion for all cases. The deflection angles for the three cases are very similar up to the impact parameter of 1 Å, monotonically increasing to reach the deflection angle of $\sim 76°$. Above the impact parameter, the deflection angles for the three cases start to deviate.

For the stationary neutral case, the deflection angle asymptotes to 90° at large impact parameters. If this assumption is used in our system, most CEX ions would be directed almost normal to the Inner Cylinder electrode. The deflection angle for this case is equivalent to computing the deflection angle from the curve-fit equations for LAB differential cross-section [76,198]. In order to apply the differential cross-section for our system, it is necessary to reconstruct the LAB differential cross-section including the effect of target neutral velocity or use the CM differential cross-section and transform the coordinate system from the CM to LAB frame.

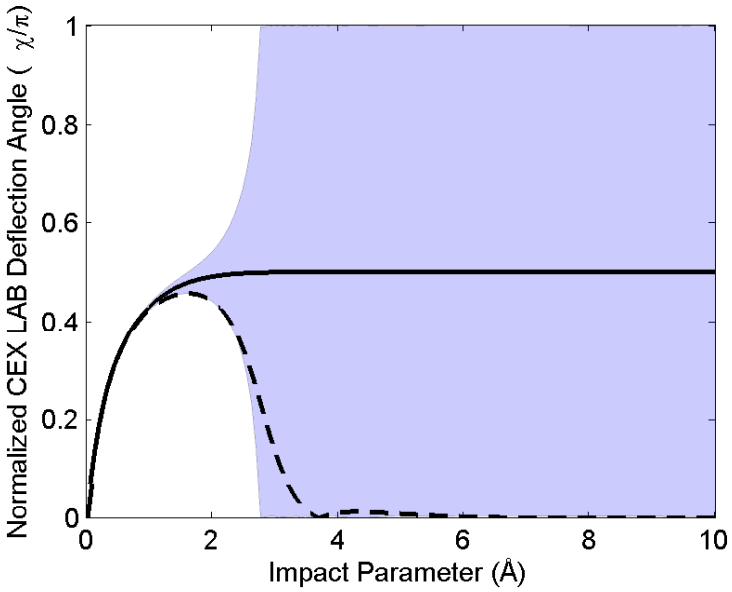

Figure 4.25: Laboratory-frame CEX ion deflection angle with respect to the direction of incident particle velocity. Solid and dashed lines represent cases with (1) stationary atoms and (2) atoms moving in the same direction as the incident primary ions, respectively. Light blue area represents possible range of CEX ion deflection angle for collisions with (3) thermal neutral atoms.

The second case with unidirectional target neutral atoms is a fair approximation for neutrals in ion thruster plumes; the ions accelerated through the grids collide with neutral atoms escaping from the discharge chamber. The deflection angle asymptotes to 0° at large impact parameters. In the JPL-developed ion optics code [14, 38, 39], it is assumed that all the CEX ions are born at the velocity in a direction normal to the grid surface. However, at the impact parameter below approximately 3.5 Å, the CEX ions are deflected at significant angles. Refering to Fig. 4.27, this corresponds to about 40% of the CEX ions, thus the assumption is not entirely true. It should be noted that, in the ion thruster ion optics code, the CEX ion trajectories are not strongly sensitive to the initial velocity due to the large gradient in the electric potential.

The third case, the target neutral atom velocity at the isotropic distribution, best approximates the condition in our system. At the impact parameters greater than approximately 2.8 Å, the CEX ions can be deflected at any angle, as indicated by the blue region covering the entire range of angles in Fig. 4.25. As shown in Fig. 4.26, the normalized post-collision

CEX ion speed asymptotes to 1, meaning that the target particle does not gain any momentum from the CEX collision when the impact parameter is large enough. Now, referring to Fig. 4.27, the CEX collisions with no momentum gain correspond to approximately 70%. Therefore, the CEX collision treatment by simply switching the velocity vector of the collision pair is a fair approximation as done in the DSMC model developed by Oh [69]. In other words, for 70% of the CEX collisions, we can simply switch the charge between the collision pair to approximate the collision event. Keep in mind that the rest (30% of the CEX ion population) gains momentum significantly. Therefore, the precise treatment of the CEX collision event as done in the model is necessary for our system.

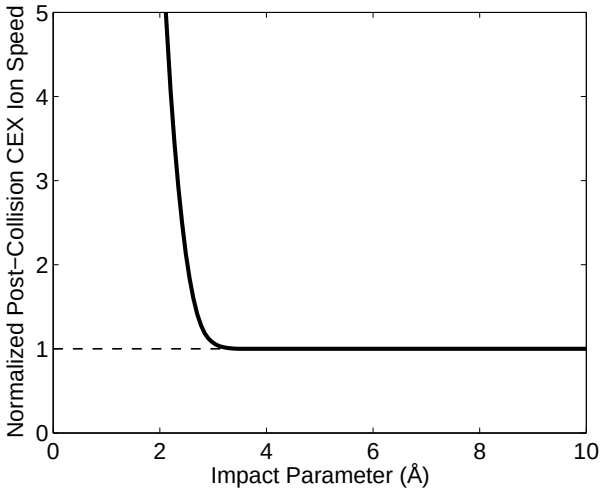

Figure 4.26: Post-collision CEX ion speed normalized to the thermal speed.

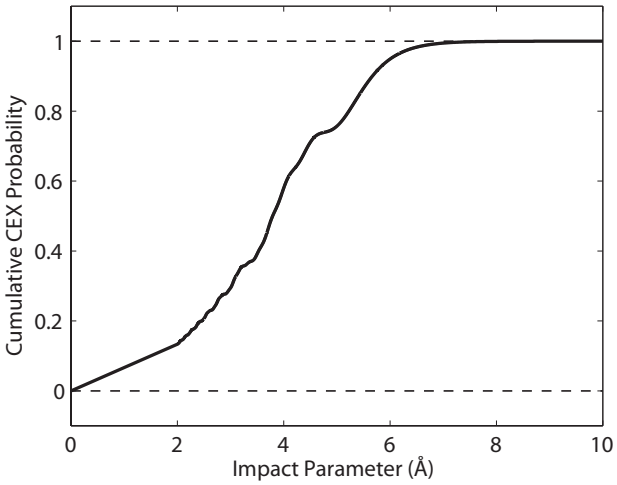

Figure 4.27: Cumulative CEX collision probability as a function of impact parameter.

4.5.4 Improved Collision Calculation Method

With the knowledge gained from Sec. 4.5.3, we can improve the elastic collision calculations that were used in previous models and also in our model. As noted earlier, Guiliano and Boyd [76, 77] used the LAB differential cross-section that was derived assuming that the xenon atom is stationary [73]. However, we have shown that the assumption made for initial target particle velocity significantly affects the post-collision velocity of the CEX ions. The incorporation of the target atom velocity can be done with a simple modification to the calculation procedure. In this procedure, as described in Refs. [73, 76, 77], the momentum exchange collision cross-section, σ_{MEX}, is assumed to equal σ_{CEX} so that $\sigma_i = \sigma_{\mathrm{MEX}} + \sigma_{\mathrm{CEX}} \approx 2\sigma_{\mathrm{CEX}}$. This is a fair approximation since the impact parameter corresponding to $2\sigma_{\mathrm{CEX}}$ is 5.3 Å at 1500 eV, and the CM deflection angle is already very small at the impact parameter as seen in Fig. 4.6. In addition, it is assumed that $P_{\mathrm{CEX}} = 0.5$, noting that P_{CEX} is highly oscillatory ranging from 0 to 1 at small impact parameters. Although the probability curve becomes less oscillatory when the impact parameter is in the range of 3 to 6 Å (Fig. 4.8), the deflection angle is already small and the accurate determination of the angle is unnecessary. Therefore, 50 % probability in the CEX collision would result in a similar result while it simplifies the collision calculation significantly. The modification we propose is to use a curve-fit equation for the CM deflection function in Eq. (D.13) instead of the LAB differential cross-section, and then, transform the coordinate system from the CM to the LAB frame according to Appendix D.2. By fitting the deflection functions shown in Fig. 4.6 with polynomials, we can get equations that can be used to determine the CM deflection angle at a given impact parameter.

$$\chi = \begin{cases} \sum_{k=0}^{n} A_k b^k & b \le b_{\mathrm{cut}} \\ 0, & b > b_{\mathrm{cut}} \end{cases} \tag{4.32}$$

where A_i is the coefficients, n is the order of polynomial, and b_{cut} is the cut off impact parameter. These values are given in Table 4.4 for the incident xenon ions at energies of 1500 and 300 eV. Once we determine that the elastic collision takes place by using $\sigma_i = 2\sigma_{\mathrm{CEX}}$ in Eq. (4.3), the impact parameter is found by equating $b/b_{\max}$ to a random number between 0 and 1 where $b_{\max} = \sqrt{\sigma_i/\pi}$. Although the method described herein is relatively simple,

Table 4.4: Polynomial fitting parameters for deflection functions at the incident ion energies of 300 and 1500 eV. The impact parameter, b, and the CM deflection angle, χ, are in the units of Å and degree, respectively.

E (eV)	n	b_{cut} (Å)	A_0	A_1	A_2	A_3	A_4	A_5	A_6
300	4	3.5504	180	145.13	31.715	1.0433	-0.6998	-	-
1500	6	3.2173	180	-399.42	451.66	-297.88	111.37	21.602	1.6811

this method can only be applied when each ion experiences a single MEX collision event, which may be the case for the Hall thruster plumes. After the first collision, significant MEX ion population would not have the energy of ~ 1500 eV, and the curve-fit equations are no longer accurate.

In the ion beam experiment, the method described above can only be applied for relatively low pressures ($\lessapprox 4 \times 10^{-1}$ mTorr). For this reason, we solve the basic classical scattering equation to determine the post-collision velocity, enabling the deflection angle calculations for incident particle energies below 1500 eV. The method we have implemented in the IB model is slower than the method described above because of the larger number of operations for each collision calculation and more frequent collision calculation due to the large elastic collision cross-section given in Eq. (4.2). The computational time can be reduced greatly if we know when the computation of the deflection angle is necessary. In other words, we can skip the deflection angle calculation when the angle is very small. This can be accomplished by finding an effective elastic collision cross-section, $\sigma_{\text{el,eff}}$, from the deflection functions at different energies.

$$\sigma_{\text{el,eff}} = 62.3 - 13.4 \log(E) \tag{4.33}$$

Equation (4.33) is formulated by finding the impact parameter corresponding to the angle of 1° as shown in Fig. 4.28. In other words, if the projected distance between the centers of the collision pair is within the effective cross-section, the CM deflection angle is greater than 1°. Equation (4.33) coincides to be very similar to the empirical formula for σ_{CEX} given by Miller [196] (Eq. (4.1)) except that $\sigma_{\text{el,eff}}$ is roughly 25 Å^2 lower than σ_{CEX}. This indicates that, if we were to exclude the very small angle scattering ($\leq 1°$) from the MEX collision, the

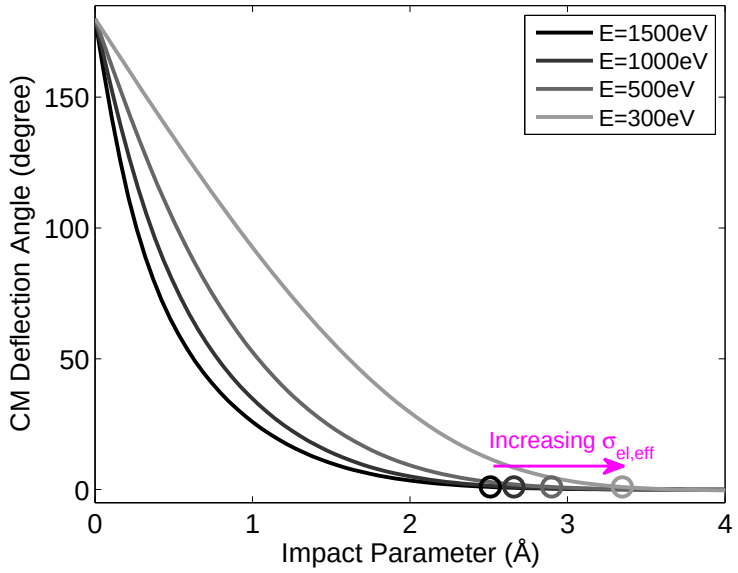

Figure 4.28: Deflection functions at different energies. Circles indicate the impact parameters corresponding to the deflection angle of 1°. The impact parameter values are used to formulate the effective elastic collision cross-section.

MEX cross-section is always smaller than the CEX collision cross-section. Similar formulas for $\sigma_{\text{el,eff}}$ can be obtained by choosing different cut-off angles, depending on the required resolution for small angle scattering and allowable computational run time. At sufficiently high energies, the deflection function generally monotonically decreases as it asymptotes to zero. However, at low energies, the attractive force becomes dominant, and the deflection function may possess a minima with negative deflection angle (see Fig. 4.6). The minima would not be resolved when using Eq. (4.33), as the cut-off impact parameter is located before the minima. Nevertheless, this is not the case above 30 eV where we find the classical scattering theory to be valid except at very small angles $< 1°$.

The improved method suggested herein is rather simpler than the method we implemented in the IB model. The simplified flowchart for this method is shown in Fig. 4.29. As it was done in the previous models (the collision calculation using the differential cross-section), we can use the same simplifications such as $\sigma_i = 2\sigma_{\text{CEX}}$ and $P_{\text{CEX}} = 0.5$. First, we determine if any collision happens by comparing P_{total} with a random number, U_1, at each time-step. If $P_{\text{total}} > U_1$, next, we determine if the collision involves a significant momentum

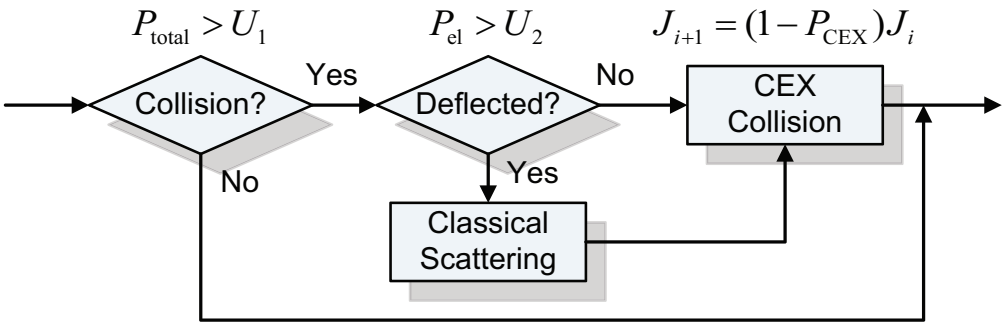

Figure 4.29: Flowchart for the improved collision calculation algorithm.

exchange by comparing $P_{\text{el}} = \sigma_{\text{el,eff}}/\sigma_i$ with another random number, U_2. When $P_{\text{el}} > U_2$, the post-collision velocities of the collision pair are determined using the classical scattering equation and following the procedure described in Appendix D.2. Otherwise, no calculation for deflection angle is performed. Finally, the primary ion current is halved according to $P_{\text{CEX}} = 0.5$.

Figure 4.30 illustrates the difference between the original method and the improved method using the classical scattering equation. The pink area represents σ_{CEX}, and the areas are the same for both the methods. In the improved method, the area for σ_{CEX} is rectangular as P_{CEX} is taken to be constant at the value of 0.5. In this way, the calculation of P_{CEX} (Eq. (4.12)) is completely eliminated. As discussed above, this is justified by the fact that the deflection angle is already very small in the region where the actual curve for P_{CEX} becomes less oscillatory. The relative computational time for collision calculations can be estimated by comparing $\sigma_{\text{el,eff}}$ to σ_i that we used in the IB model (Eq. (4.2)). These cross-sections are represented by the blue areas in Fig. 4.30 and plotted in Fig. 4.31 for comparison. At the energy of 1500 eV, $\sigma_{\text{el,eff}}$ and σ_i are 20 and 172 Å, respectively. When the impact parameter is within the bound corresponding to those cross-sections, the classical scattering equation is evaluated to determine the deflection angle. Therefore, we can expect the reduction in run time required for collision calculations to be approximately 86 %. Furthermore, the deflection angle calculation is less frequent compared to the previous methods using the differential cross-sections as $\sigma_{\text{el,eff}}$ is smaller than $2\sigma_{\text{CEX}}$ as shown in Fig. 4.31.

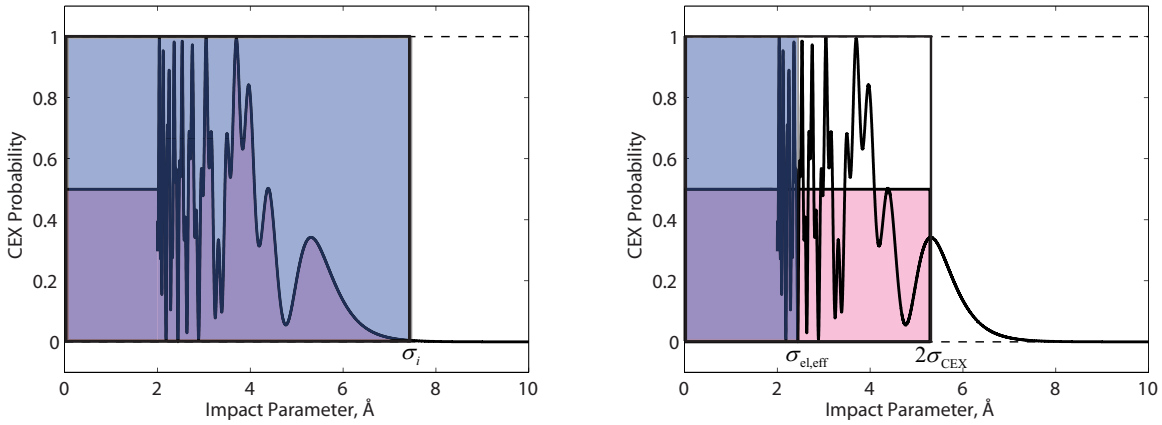

(a) Original method.

(b) Improved method.

Figure 4.30: Representative cross-sections superimposed to the charge exchange probability plot for the original and improved methods. When the impact parameters are within the blue area, the deflection angle is determined by solving the classical scattering equations. The pink area represents the CEX probability used for these methods.

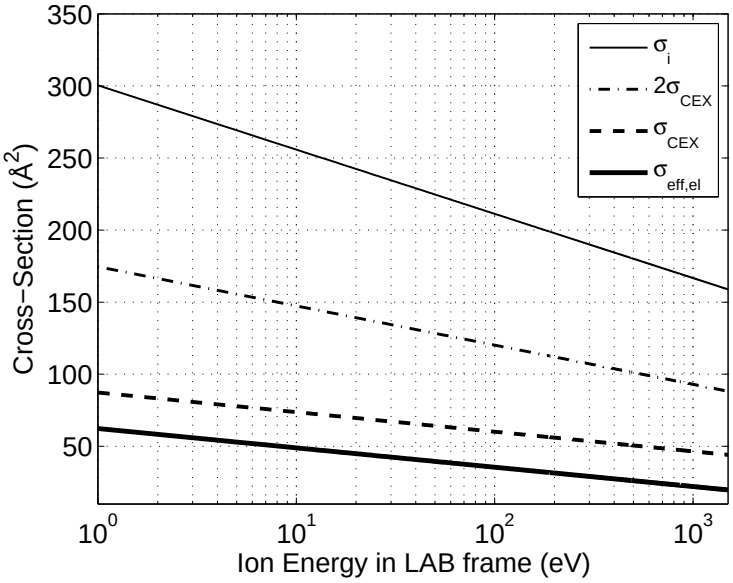

Figure 4.31: Xenon ion-atom collision cross-sections relevant to the collision calculation methods.

4.6 Chapter Summary

The IB model has been developed to investigate collisional behavior of heavy plasma species and is compared to the results of a well-characterized simple ion beam experiment [80]. The collision mechanism implemented in the simulation was elastic collision, which included both the MEX and CEX collisions. The ion scattering due to the elastic collision was approximated by the classical scattering model with spin-orbit free potential and the VHS model. For neutral atoms, the HFD-B2 potential, similar to the ion-atom potential, was used to determine the scattering angles. Poisson's equation was solved computationally to calculate the electric potential in the computational domain. Four different species including primary and CEX ions, high-energy neutral atoms, and secondary electrons were tracked independently, and their trajectories were computed. The currents at different electrodes predicted by the simulation were compared with the results from the ion beam experiment.

The simulation results agreed fairly well with the experimental results when the ion-induced and the atom-induced secondary electron yields were assumed to be 0.4 and 0.34 electrons/ion, respectively. These values were within the expected values for xenon ions and atoms incident to oxidized or contaminated stainless steel surfaces. Generally, the high-energy ions and atoms impacted the Exit Plate while the CEX ions impacted the Inner Cylinder due to the large aspect ratio of the Test Cell and the forward scattering distribution predicted by the classical scattering equation. As a result, the secondary electrons emitted from the Exit Plate were collected to the Inner Cylinder, resulting in an increased Exit Plate current and a decreased Inner Cylinder current. The electron emission due to the high-energy neutral atom impact became increasingly dominant at higher pressures compared to the ion-induced emission. This was due to the increasing probability of the CEX collision that resulted in a decreased population of the high-energy ions in the Test Cell. Furthermore, it was found that the pre-collision target atom velocity significantly affects the post-collision CEX ion velocity distribution. Many computational models assumed the target atom velocity to be stationary, which lead to very large-angle scattering for the CEX ions. This approximation could not be applied to our simulation as the background neutral

was essentially thermal. Appropriate pre-collision velocity distribution for the target neutral atoms lead to the post-collision velocity distribution that was almost isotropic.

The gained understanding of the CEX ions has lead to an improvement to the collision calculation method implemented in the model. In this method, the scattering calculation is performed much less frequently, which is enabled by defining an effective elastic collision cross-section, a cross-section for incident particles scattering at angles greater than some cut-off angle. This method would reduce the time required for collision calculations by 88 % compared to the original method. Furthermore, unlike the methods used in the previous models, this method can take particles at different energies, allowing the simulations at higher pressures where high-energy particles experience multiple collisions.

CHAPTER 5

Conclusions and Future Work

Three independent models have been developed from scratch or improved from an existing model; many of the methods implemented in these models can be directly applied to models for different parts of an ion thruster. The Single Cusp (SC) model is developed in an effort to gain further understanding of the cusp confinement of a weakly ionized plasma near an anode surface, focusing on the near-cusp region in a discharge chamber of an ion thruster (Chapter 2). A few components of the discharge chamber model (DC-ION) are improved from the original version (Chapter 3). Unlike the SC model, DC-ION aids in obtaining the macroscopic picture of the plasma behavior in the discharge chamber. Lastly, the Ion Beam (IB) model is developed to investigate the collisional mechanisms in the ion beam experiment conducted at UCLA [80] (Chapter 4). The numerical methods for heavy species collisions can be implemented in the plume models for an ion thruster as well as a Hall thruster. This chapter reiterates the main conclusions drawn from these models and provides recommendations for future work for these models.

5.1 Single Cusp Model

The SC model was applied to different plasma conditions produced by an electron gun or a hollow cathode in various magnetic field configurations. Starting from an electron plasma in a single cusp configuration, complexity was added by improving the confinement by adding ring cusps and introducing xenon gas. Due to the limit in the operating condition for the electron gun, the plasma density could not be high enough such that the Debye length is comparable to the plasma volume. In these conditions for a sparse plasma, the model

obtained the loss width scaled as the geometric mean of the gyroradii, similar to the loss width measured by Leung et al. [90] and Bosch and Merlino [91, 92] for a weakly ionized plasma. However, the loss mechanism was not exactly the same; for the specific plasma condition of low density, the majority of ions were created near the cusp and were immediately accelerated electrostatically toward the cusp, while the plasma electrons were confined in the domain and experienced multiple collisions to diffusion radially outward and thus increase the loss width. In a similar configuration, the computational and experimental results suggested that the primary electron loss structure was strongly affected by the upstream magnetic field configuration. Since the region of plasma generation correlates with the primary electron density, it might be possible that the loss structure of plasma species was also influenced by the upstream field configuration, whereas the conventional theory predicted the loss width based solely on the local magnetic field. Unfortunately, the SC model was unable to produce reliable results for the case of a weakly ionized plasma, and the similarity of the loss mechanisms for the sparse and the weakly ionized plasmas could not be obtained.

In order to make the SC model more useful, the structure of the model should be changed to be similar to the standard PIC model; the electric potential should be computed every several advancement steps for the charged species. In this way, the problem of extremely unstable behavior of the model can be mitigated by slowly changing the overall potential profile. The SC model contains most of the important components in converting the model; a slight change in the code structure would produce the PIC model. Even after the conversion of the model, a significant amount of work would probably be required since PIC models are typically computationally very expensive and can suffer from the convergence issue. The run-time can be reduced by using the combination of MPI and graphics processing unit (GPU) computing and running on a cluster computer. The domains can be split and assigned to different processes using MPI and particle operations (i.e. advancement, weighting, interpolation, etc) can be done using GPUs. In addition, several numerical approaches to enhance the convergence can be used; these include artificial mass ratio, artificial permittivity factor, and smoothing implemented in several PIC models [25, 159, 160, 241, 242].

5.2 Discharge Model

The initial objective of this effort was to use the DC-ION code developed by Wirz and Katz [13, 24] to address the design and optimization challenges of miniature to micro discharges on the order of 3 cm to 1 cm in diameter. To this end, significant improvements to the model were necessary due to the scaled-down dimension of the domain. While many improvements were made for the Electron Collision Sub-Model as discussed in Chapter 2, Chapter 3 focused on the MFA generation routine for the Internal Mesh Generator together with an advanced method to solve the plasma diffusion equation using a MFA mesh for the Ion Diffusion Sub-Model.

The numerical method was first applied to the simplest condition with a magnetic field: a uniform field with density of zero at the domain boundaries. A uniform mesh was automatically aligned with the field in this configuration. The convergence of the solution was second order as expected. Then, the method was applied to a single cusp configuration with zero perpendicular mobility, and the results using both the uniform and MFA mesh were compared. In this problem, the uniform mesh provided more preferable results, while the convergence for the two meshes were approximately first order. In the uniform mesh, numerical diffusion error was clearly seen along the direction of magnetic fields. For the MFA mesh, it was found that the misalignment of the field with the domain boundaries introduced an error, propagating in the direction of the field. It was also found that a slight adjustment of the boundary cells significantly affected the degree of error. The last test case more resembled the field configuration in the ring-cusp discharge chamber. Finite perpendicular mobilities were used in this test, smoothing out the errors in both the parallel and perpendicular directions and yielding the second order convergence of the overall solution. When using the MFA mesh, it was shown that the errors could be controlled by improving the smoothness of the mesh near the domain boundaries, providing a more accurate solution compared to the solution with the uniform mesh. However, the degree of accuracy was not as superior as expected.

The significance of the MFA mesh in the discharge chamber field configuration has not

been confirmed at this point. Whenever there is a field intersecting with the boundary at angles between 0° and 90°, the MFA mesh does not provide a significantly accurate solution. The degree of accuracy that can be achieved with the MFA mesh can be achieved by increasing the resolution of the uniform mesh. However, it may still be possible to improve the MFA mesh generation routine by properly controlling the near-boundary elements. The smoothness of the mesh from a triangular element to a quadrilateral element is typically poor, so dealing with the triangular element may be the next step. As an alternative method, one may keep the portion of the elements outside the domain and use the cut-cell method to deal with the domain boundary.

5.3 Ion Beam Model

A parametric study on the secondary electron yield was performed, and the results from the IB model showed very good qualitative and quantitative agreement with the experimental results when the yield of 0.4 was used; the value was within the range of possible yield values for the oxidized and contaminated stainless steel electrode surface. A further analysis on the post-collision velocity for the ion-atom collision revealed that the pre-collision velocity of the target atom could not be ignored in determining the post-collision CEX ion velocity, even when the incident particle was much faster than the target particle. Many of the plasma thruster plume models either used a low-order collision calculation method (e.g. the VHS method) or assumed that the target atoms were initially stationary. Furthermore, it was observed that the range of impact parameters that resulted in a significant momentum exchange was much smaller than the range for which the CEX interaction was possible. From these observations, an improved collision calculation algorithm was developed by defining an effective elastic collision that provided scattering of angles greater than some small value. The cross-section was significantly smaller than the value typically used to approximate the elastic collision-section, thus leading to much less frequent calculations of collisions while retaining the higher-order method.

In order to further understand the experimental results, the IB model should either in-

clude a self-consistent secondary electron model or use experimentally measured parameters for the secondary electron emission. These are not easy tasks as the electrode surface is not well-characterized. Another path to take can be to compare against the experimental results with biased electrode potential [211]. In improving the current model, the new collision calculation algorithm can be implemented. The updated model should produce results very similar to the ones provided in this thesis. Further improvement in accuracy may be realized by utilizing more accurate interaction potentials such as the ones provided in Refs. [200,243], while these could significantly increase the number of mathematical operations. Finally, a greater advantage in using the new collision method can be realized by developing a faster method in evaluating the classical scattering equation; in this way, the new method can be applied to more intense models such as DSMC simulations.

APPENDIX A

Useful Geometric Algorithms

A.1 Point inside a Convex Polygon

At every time-step of particle tracking, we need to determine which node element the particle resides in to distribute the particles and compute particle densities at grid cells. This is done with the algorithm described here. The algorithm is also used to determine if the particle is still inside the computational domain. The algorithm starts by checking if the particle location (x_p, y_p) is within the smallest rectangular box (dashed box in Fig. A.1) containing the element by simply comparing the maximum and the minimum vertex positions with the particle location. This calculation effectively eliminates the elements that are far from the particle location. Once it is determined that the particle is within the rectangular box, the next step is to determine if the particle is within the element (gray polygon shown in Fig. A.1). For each element vertex, we use two vectors ($\vec{x}_{i,p}$ and $\vec{x}_{i,i+1}$) originated from the vertex (x_i, y_i) to the particle location and the next vertex in counter-clockwise direction (x_{i+1}, y_{i+1}). If the particle is within the element, the cross-product of the two vectors must be positive.

$$\vec{x}_{i,i+1} \times \vec{x}_{i,p} = (x_p - x_i)(y_{i+1} - y_i) - (y_p - y_i)(x_{i+1} - x_i) > 0 \tag{A.1}$$

This must be true for the other vertices as well.

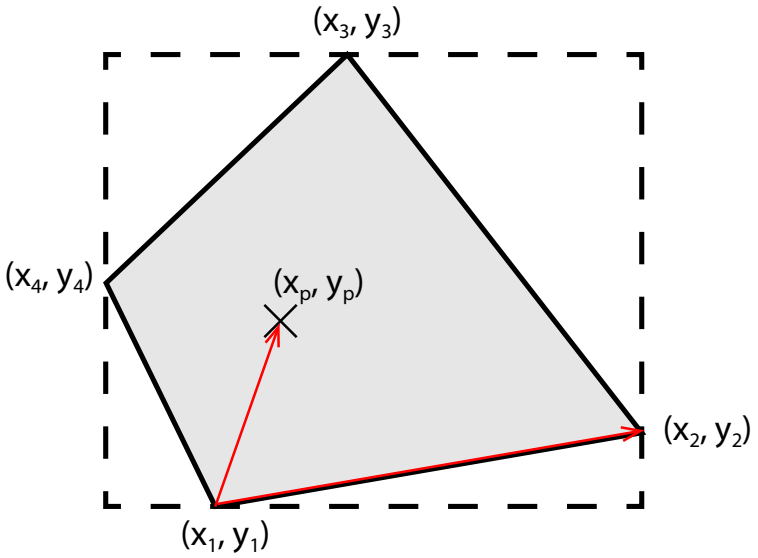

Figure A.1: Schematic of an algorithm for a point inside a convex polygon.

A.2 Intersection of Two Lines

In PIC simulations, particle trajectories can only be determined at finite time-steps. Particles are tracked until they are outside the domain, and the exact time and location that particles impact the boundaries need to be determined. The final time can be computed by approximating the trajectory between a single time-step to be simply a straight line and finding the intersection point with the boundary. An efficient algorithm for determining line intersections involves two steps: the first step checks if the two lines intersect, and the second step determines the intersection point. For the two lines (Line A and Line B) to intersect, the following four conditions must be satisfied.

1. Any point on Line A is inside the smallest rectangular box containing Line B
2. Line A and Line B are not parallel
3. Two end points on Line A are in the opposite side across Line B
4. Two end points on Line B are in the opposite side across Line A

The first two conditions can be easily determined and are illustrated in Fig. A.2. By the third and fourth conditions alone, it can be concluded that the two lines intersect. However, the first two conditions are used to quickly eliminate cases that are not applicable. The last

two conditions are checked using the property of cross-product. Consider four points (A_1, A_2, B_1, and B_2) corresponding to the end points of the two lines as shown in Fig. A.3. Then, the last two conditions are mathematically expressed as

$$\text{sign}\left(\overrightarrow{A_1A_2} \times \overrightarrow{A_1B_1}\right) = \text{sign}\left(\overrightarrow{A_1A_2} \times \overrightarrow{A_1B_2}\right) \tag{A.2}$$

$$\text{sign}\left(\overrightarrow{B_1B_2} \times \overrightarrow{B_1A_1}\right) = \text{sign}\left(\overrightarrow{B_1B_2} \times \overrightarrow{B_1A_2}\right) \tag{A.3}$$

Once the two lines are determined to intersect, the intersection point can be easily found.

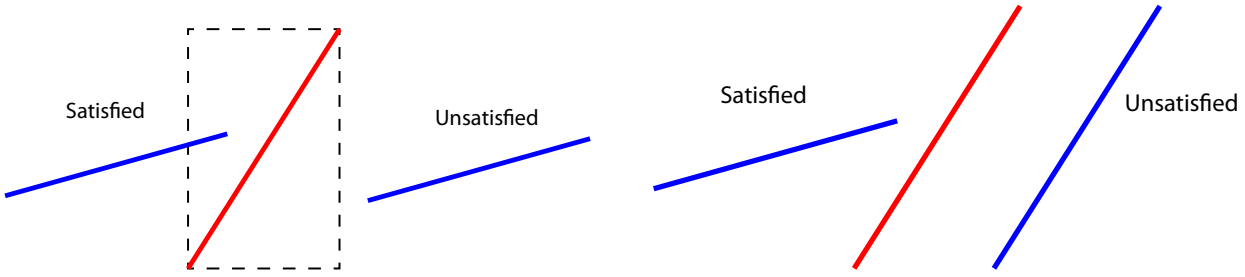

(a) Condition 1 (b) Condition 2

Figure A.2: Conditions for quickly eliminating non-intersecting cases.

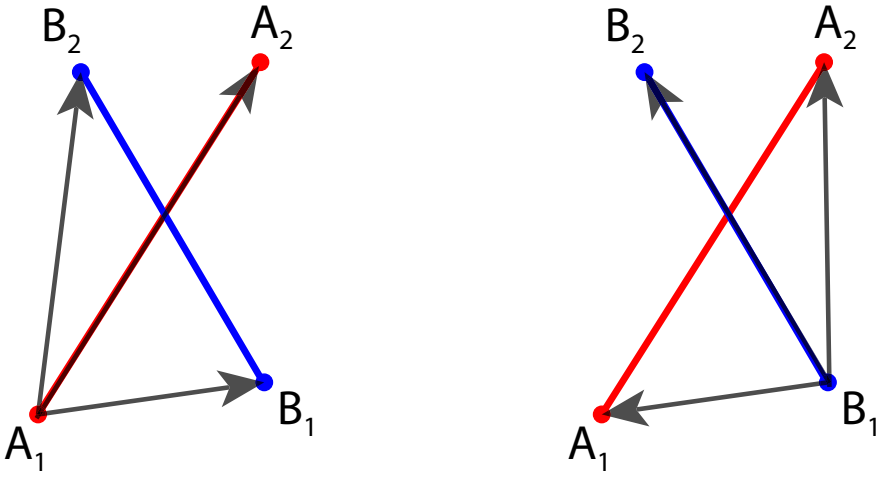

(a) Condition 3 (b) Condition 4

Figure A.3: Conditions for actually determining if two lines intersect. Cross-products are used in these calculations.

A.3 Intersection of a Line with a Surface

In the Neutral Atom Sub-Model of DC-ION, a neutral atom path is approximated to be straight, assuming that a rate of collision is insignificant. While the elastic collision is neglected in the formulation, the effect of ionization collision is incorporated by depleting the neutral flow (particle/s) along its path. The ionization rate is computed in the Electron Collision Sub-Model and is stored as a cell-centered quantity that is averaged over the corresponding cell. In order to deplete the neutral flow accordingly, it is necessary to determine the path length through a given cell; this is done by first computing the intersections of the neutral path to the cell boundaries. DC-ION uses a 2D axisymmetric grid in z-r plane to simulate 3D domain. Therefore, cell boundaries are essentially lines of cell edges that are revolved about the axis of symmetry. The resulting surfaces can either be annuli, shells, or truncated cones.

A ray of neutral path starting from a point (x_1,y_1,z_1) and ending at a point (x_2,y_2,z_2) can be parametrized as

$$\begin{pmatrix} x \\ y \\ z \end{pmatrix} = \left[\begin{pmatrix} x_2 \\ y_2 \\ z_2 \end{pmatrix} - \begin{pmatrix} x_1 \\ y_1 \\ z_1 \end{pmatrix} \right] t + \begin{pmatrix} x_1 \\ y_1 \\ z_1 \end{pmatrix}, \quad 0 \leq t \leq 1 \tag{A.4}$$

This parametric equation is used to determine conditions for neutral paths intersecting cell edges.

A.3.1 Annulus

When the cell edge is parallel to the r-axis, the surface resulted from revolving the line becomes an annulus. In the limit that the inner radius approaches zero, an annulus becomes a disk. Therefore, the formulation described here is applicable to both the annulus and disk. Let the axial position of the annulus be z_a and the inner and outer radii be r_{a1} and r_{a2}, respectively. Then, whether the ray passes through the infinite plate at $z = z_a$ is determined

by the parameter t.

$$t = \frac{z_a - z_1}{z_2 - z_1} \tag{A.5}$$

If t is not in the range of 0 and 1, the ray cannot intersect with the annulus. Now, the radius that the ray passes through the infinite plane has to be in the range of $r_{a1} \leq r \leq r_{a2}$ for the intersection condition. Here, r is given as

$$\begin{aligned} r^2 &= x^2 + y^2 \\ &= [(x_2 - x_1)t + x_1]^2 + [(y_2 - y_1)t + y_1]^2 \end{aligned} \tag{A.6}$$

A.3.2 Shell

When the cell edge is parallel to z-axis, the revolved line becomes a shell. Letting r_s be the radius of the shell and starting from an equation of a circle ($x^2 + y^2 = r_s^2$), an equation for t can be derived by substituting x and y in the parametric equation Eq. (A.4).

$$At^2 + Bt + C = 0 \tag{A.7}$$

where

$$\begin{aligned} A &= (x_2 - x_1)^2 + (y_2 - y_1)^2 \\ B &= 2(x_2 - x_1)x_1 + 2(y_2 - y_1)y_1 \\ C &= x_1^2 + y_1^2 - r_s^2 \end{aligned}$$

Solving the quadratic equation, if $0 \leq t \leq 1$ is satisfied, then it is possible that the ray intersects with the shell. Plugging in t to $z = (z_2 - z_1)t + z_1$, the intersection condition is satisfied if $z_{s1} \leq z \leq z_{s2}$ where z_{s1} and z_{s2} correspond to the ends of the shell.

A.3.3 Truncated Cone

Let the ends of a cell edge to be at $(z_{c1},\, r_{c1})$ and $(z_{c2},\, r_{c2})$. If the cell edge is not parallel to any axis ($z_{c1} \neq z_{c2}$ and $r_{c1} \neq r_{c2}$), then the surface resulted from revolving the line about the axis of symmetry becomes a truncated cone. Imagine a full cone extended from the truncated cone to include a cone apex. The first condition to check is if the ray intersects with the full cone. The implicit equation for the cone is given by

$$x^2 + y^2 = c^2(z_{\text{apex}} - z)^2 \tag{A.8}$$

where z_{apex} is the apex of the full cone and c is the slope of the line.

$$z_{\text{apex}} = z_{c1} - r_{c1}\frac{z_{c2} - z_{c1}}{r_{c2} - r_{c1}}, \quad c = \frac{r_{c1} - r_{c2}}{z_{c2} - z_{c2}} = \frac{r_{c1}}{z_0 - z_{c1}}$$

Plugging in the parametrized expressions for x, y, and z in Eq. (A.4), a quadratic equation similar to the one for the shell can be obtained.

$$At^2 + Bt + C = 0 \tag{A.9}$$

where

$$A = (x_2 - x_1)^2 + (y_2 - y_1)^2 - c^2(z_2 - z_1)^2$$
$$B = 2(x_2 - x_1)x_1 + 2(y_2 - y_1)y_1 - 2c^2(z_2 - z_1)(z_1 - z_0)$$
$$C = x_1^2 + y_1^2 - c^2(z_1 - z_0)^2$$

Again, if $0 \leq t \leq 1$ is satisfied, then it is possible that the ray intersects with the full cone. Now, it is necessary to check if the intersection is within the section of the truncated cone. Plugging in t to $z = (z_2 - z_1)t + z_1$, the intersection condition is satisfied if $z_{c1} \leq z \leq z_{c2}$.

APPENDIX B

Data Structure for Computational Mesh

B.1 Data Structure

Both the SC model and the MFA mesh routine use data structures for an unstructured mesh in which the connectivity is explicitly stored with the mesh. Two separate data structures (node and cell data structures) are used to store the grid information and plasma parameters associated with the cell. The node data structure stores information of the cells that are touching the node. The cell data structure stores information of nodes corresponding to the cell vertices, surrounding cells, and face areas. For an adaptive mesh, additional information is required including grid level and subdivided cell number. Other parameters including electric potential, species densities, generation rate densities, and electric field are also stored in the cell data structure. Information stored in the data structures is summarized in Tables B.1 and B.2 for the case of the adaptive mesh.

In the data structures, data are stored in sequential manner. For the adaptive mesh, the information stored in the data structures starts from the data of the initial uniform grid generated throughout the domain. Then, as the grid refinement is performed, the cell data associated with the grid level is stacked onto the stored data. Finally, boundary cells are generated based on the interior grid, and the information is contained at the end of the data structures. An example of cell data allocation is shown in Figs. B.1 to B.3 for an adaptive regular mesh. For a MFA mesh, the data structure only contains the internal (parent) and boundary cell information.

Table B.1: Information stored in node data structure.

Name	Description
nNode	Total number of nodes - stored in node(1)%nNode
iNode	Node number
nCell	Number of cells associated with the node
iCell(4)	Adjacent cell number stored by position (1:SW, 2:SE, 3:NE, 4:NW)
nType	Node type (0: interior node, 1-4: boundary)
x(2)	Node location [m] ($x(1) = z$, $x(2) = r$)

Table B.2: Information stored in cell data structure.

Name	Description
nCell	Total number of cells - stored in cell(1)%nCell
iCell	Cell number
nNode	Number of nodes along the cell edges
iNode(8)	Node number associated with cell vertices (1:SW, 2:SE, 3:NE, 4:NW, 5:S, 6:E, 7:N, 8:W)
level	Level of subdivision
parCell	Parent cell number
subCell(4)	Subdivided cell number
nextCell(8)	Adjacent cell number
area(8)	Face area
x(2)	Cell center location [m] ($x(1) = z$, $x(2) = r$)
vol	Volume of the cell
phi	Potential at cell centered location [V]
E(3)	Electric field [V/m] ($E(1) = Ez$, $E(2) = Er$, $E(3) = \|E\|$)
np	Primary electron density [#/m^3]
ne	Plasma electron density [#/m^3]
ni	Ion density [#/m^3]
no	Neutral density [#/m^3]
nigen	Ion generation rate density [#/m^{3}s]
negen	Plasma electron generation rate density [#/m^{3}s]
Ti	Ion temperature [eV]
Te	Plasma electron temperature [eV]
aPot(6)	Spline coefficients for electric field calculation

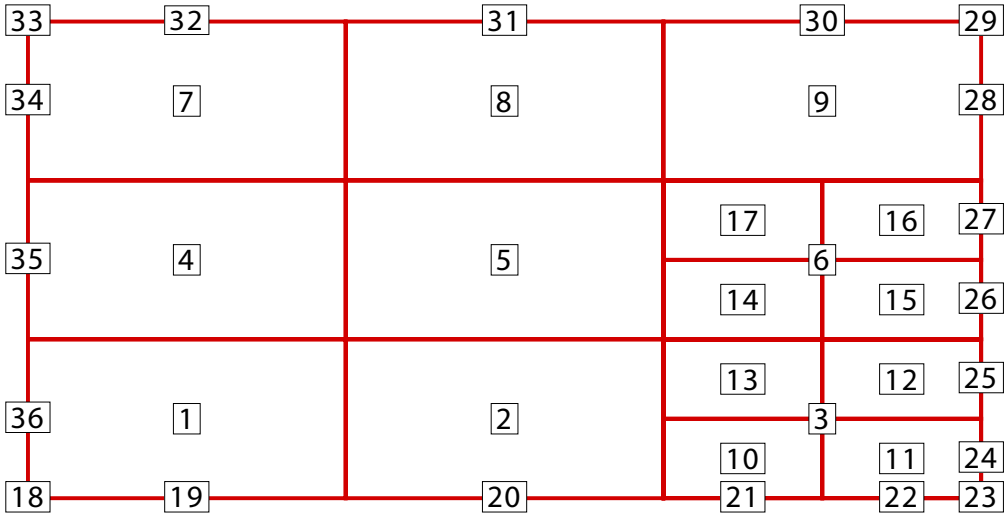

Figure B.1: Example of an adaptive regular mesh with cell numbers.

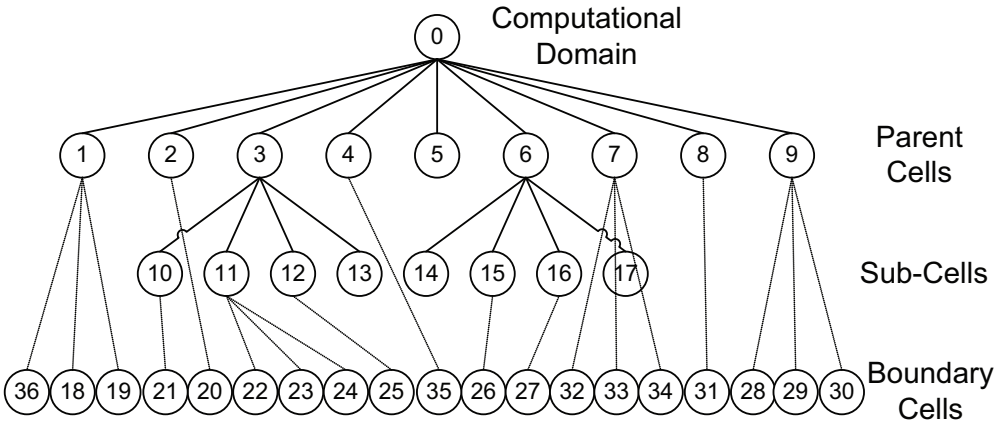

Figure B.2: Tree structure representing the adaptive regular mesh shown in Fig. B.1.

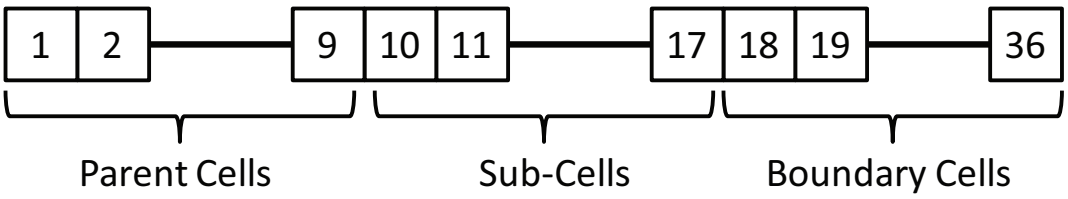

Figure B.3: Example of sequential allocation of cell numbers.

B.2 Numbering System

When using an unstructured data structure, it is necessary to use a numbering rule consistent throughout the program to easily access the grid information. For an adaptive mesh, each node has three to four cells touching the node while each cell has four to eight nodes on its cell boundary. Also, each cell has four faces corresponding to the cell boundaries. These data are numbered in a counterclockwise order as illustrated in Fig. B.4. Whenever grid refinement is performed, five additional nodes are generated for each parent cell. Then, a cell next to a finer grid will have additional nodes that need to be stored. This node information is stored according to Fig. B.4(c). For a MFA mesh, the first vertex of a cell is determined by the distance from the origin, and the other vertices are numbered in a counterclockwise order.

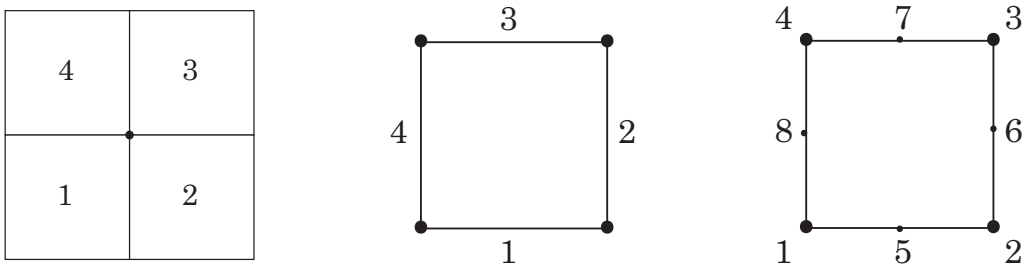

(a) Node to adjacent cells. (b) Cell to cell faces. (c) Cell to nodes.

Figure B.4: Numbering convention used in the model.

B.3 Connectivity

Unlike in a structured grid, the cell information is stored in a vector of data structures even though the grid is generated in two dimensions. For this reason, cell connectivity or how the cell is positioned relative to other cells has to be explicitly specified. One complexity arisen from an adaptive regular grid is that the number of the cells across a face of the current element can be more than one. If the subdivision level of the neighboring cell is greater than the current element grid level, then there are two cells across the cell face as illustrated in Fig. B.5(a). Therefore, two cell numbers have to be stored for this case. In addition, most

of the nodes are touching four cells, but some nodes have only 3 neighboring cell if the node lies on coarse/fine grid interface as shown in Fig. B.5(b). For a MFA mesh, a node can be attached to more than four cells as discussed in Sec. 3.3.2.

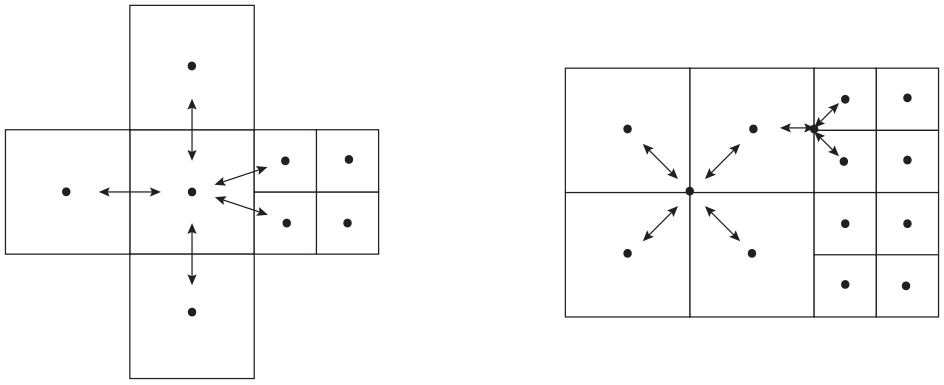

(a) Cell-cell connectivity.

(b) Node-cell connectivity.

Figure B.5: Connectivity between nodes and cells.

APPENDIX C

Magnetic Field Equations

C.1 Magnetic Dipole

Although a single magnetic dipole field is not an accurate representation of the field induced by a permanent magnet especially near the magnet, the dipole field is still implemented in the computational models. The benefit of the dipole equation is in its simplicity, allowing a very quick evaluation of the magnetic field. Therefore, dipoles can be used for quick validations of other important components of the models such as the methods to integrate the equation of motion of a particle. Multiple dipoles can also be used to approximate a field induced by a single permanent magnet. Furthermore, the dipole field is comparable to the permanent magnet field very far from the magnet.

The magnetic field induced by a magnetic dipole is given as

$$\mathbf{B} = \frac{\mu_0}{4\pi}\left[\frac{3\mathbf{n}(\mathbf{n}\cdot\mathbf{m}) - \mathbf{m}}{|\mathbf{x} - \mathbf{x_m}|^3}\right] \tag{C.1}$$

where μ_0 is the permeability of free space, $\mathbf{m}$ is the magnetic dipole moment, $\mathbf{n}$ is a unit vector in the direction $\mathbf{x}$, and $\mathbf{x_m}$ is the position of the dipole. The components of magnetic field in r-z coordinates are given by

$$B_r = \frac{\mu_0 m}{4\pi}\frac{3rz}{(r^2+z^2)^{5/2}} \tag{C.2}$$

$$B_z = \frac{\mu_0 m}{4\pi}\frac{2z^2 - r^2}{(r^2+z^2)^{5/2}} \tag{C.3}$$

Here, m is the magnitude of $\mathbf{m}$.

C.2 Axially Magnetized Cylindrical Magnet

An analytical calculation of a magnetic field induced by a permanent magnet is a quite difficult task as it involves complex integration in the limit of the magnet volume. However, software such as *Maple* and *Mathematica* can be utilized to evaluate the integral to obtain the field solution. Ravaud et al. [111] obtained an analytical equation for magnet field induced by a cylindrical magnet using *Mathematica* in their recently published paper. Their formula was still very complicated, involving the incomplete elliptic integral of third kind with imaginary numbers which was not trivial to solve. Here, the cylindrical permanent magnet equation is obtained from the equation for a magnetic field induced by an axially magnetized ring magnet provided by Babic and Akyel [112]. In the limit when the inner radius of the ring magnet reduces to zero, the equation reduces for a cylindrical magnet.

Let r_m be a radius of a cylindrical magnet, z_1 and z_2 be the position of the ends along the magnet axis, and the magnetization M be in a direction from surface 1 to 2. Then, the magnetic field induced by the magnet is given as

$$B_z = \frac{\mu_0 M}{4}\sum_{k=1}^{2}(-1)^{k-1}\Big\{c_{1k}K(m_k) - c_{2k} + s_{1k}s_{2k}\big[1-\Lambda(\theta_{1k},m_k)\big] - s_{1k}\big[1-\sin(\theta_{2k})-\sin(\theta_{3k})+\Lambda(\theta_{2k},m_k)\big]\Big\} \tag{C.4}$$

$$B_r = \frac{\mu_0 M}{2\pi}\sum_{k=1}^{2}(-1)^{k}\left(\frac{a_k^2 - 2rr_m}{ra_k}K(m_k) - \frac{a_k}{r}E\left(m_k\right)\right) \tag{C.5}$$

Here, $K(m)$, $E(m)$, and $\Lambda(\theta, m)$ are the complete elliptic integral of the first and second kind and the Heuman's Lambda function, respectively, defined in Appendix C.7. The method in computing those elliptic integrals are also described in Appendix C.7. The parameters, m_k, a_k, c_{1k}, c_{2k}, θ_{1k}, θ_{2k}, θ_{3k}, s_{1k}, and s_{2k} are defined in Table C.1. The implementation has been validated with the analytical equation along the magnet axis as well as along some radius from the axis given in Ref. [111]. Along the magnet axis, the axial magnetic field equation can be found elsewhere, and Eq. (C.4) reduces to the equation in the limit of $r = 0$.

Table C.1: Definition of parameters used in the analytical magnetic field equation for a cylindrical magnet.

Parameter	Definition
m_k	$4rr_m/a_k^2$
a_k	$\sqrt{(r+r_m)^2+(z-z_k)^2}$
b_k	$\sqrt{r^2+(z-z_k)^2}$
c_{1k}	$4(z-z_k)b_k/\left[\pi a_k(r+b_k)\right]$
c_{2k}	$2(z-z_k)/(r+b_k)$
h_k	$2r/(r+b_k)$
θ_{1k}	$\sin^{-1}\left(\sqrt{(1-h_{1k})(1-m_k)}\right)$
θ_{2k}	$\sin^{-1}\left(\lvert z-z_k\rvert/(r+b_k)\right)$
θ_{3k}	$\sin^{-1}\left(\sqrt{1-h_{1k}}\right)$
s_{1k}	$\mathrm{sign}(z-z_k)$
s_{2k}	$\mathrm{sign}(b_k-r_m)$

C.3 Block Magnet

In a ring cusp ion thruster, multiple block magnets are placed along the circumference of the discharge chamber to increase the primary electron confinement. Let W_m, L_m, and H_m be half the width, length, and height of the block magnet, corresponding to dimensions along x, y, and z axes, respectively. Assuming a constant magnetization, M, in a direction of z-axis, the magnetic field induced by a block magnet is expressed as [113]

$$B_x = \frac{\mu_0 M}{4\pi}\sum_{k=1}^{2}\sum_{l=1}^{2}\sum_{m=1}^{2} s_{klm}\log\left(y_l+\sqrt{x_k^2+y_l^2+z_m^2}\right) \tag{C.6}$$

$$B_y = \frac{\mu_0 M}{4\pi}\sum_{k=1}^{2}\sum_{l=1}^{2}\sum_{m=1}^{2} s_{klm}\log\left(x_k+\sqrt{x_k^2+y_l^2+z_m^2}\right) \tag{C.7}$$

$$B_z = -\frac{\mu_0 M}{4\pi}\sum_{k=1}^{2}\sum_{l=1}^{2}\sum_{m=1}^{2} s_{klm}\frac{x_k}{|x_k|}\frac{z_m}{|z_m|}\tan^{-1}\left(\frac{|x_k|\cdot y_l}{|z_m|\cdot\sqrt{x_k^2+y_l^2+z_m^2}}\right) \tag{C.8}$$

where μ_0 is the permeability of free space, $s_{klm}=(-1)^{k+l+m}$, $x_k = x+(-1)^k W_m/2$, $y_l = y+(-1)^l L_m/2$, and $z_m = z+(-1)^m H_m/2$. Note that these equations assume the center of the magnet as origin.

C.4 Axially Magnetized Ring Magnet

The field induced by a ring magnet is found to be fairly accurate for the approximation of the field induced by multiple block magnets creating a ring cusp, especially far from the magnets [186]. Although the axisymmetric field masks the 3-dimensional effect near the ring cusp, the approximation is convenient when solving for stream function and scalar potential as described in Sec. 3.3.2.

The analytical expression for the magnetic field created by a permanent ring magnet was recently obtained by Ravaud et al. [114]. Their derivation was based on a coulombian model in which the permanent magnet was represented by two planes with magnetic charges of opposite signs. The expression included incomplete elliptic integral of the third kind. Babic and Akyel [112] then improved the expression by removing the incomplete elliptic integral of the third kind and expressing over complete elliptic integrals of the first kind, $K(m)$ and and Heuman's Lambda function, $\Lambda_0(\theta, m)$. For the ring magnet, let the length be l, the inner radius be r_1, and the outer radius be r_2. Also, let the center of the magnet be the origin, and the magnetization, M, be be parallel to z-axis. Then, the magnetic field at a given location (z, r) is given as

$$\begin{aligned} B_z &= B_z^+ - B_z^- \\ B_r &= B_r^+ - B_r^- \end{aligned} \tag{C.9}$$

where

$$\begin{aligned} B_z^{\pm}(z,r) = \frac{\mu_0 M}{2\pi} \sum_{n=1}^{2} (-1)^{n-1} \Bigg\{ & \frac{\sqrt{m_n^{\pm}} z^{\pm} \sqrt{r^2 + (z^{\pm})^2}}{\sqrt{r r_n}(\sqrt{r^2 + (z^{\pm})^2} + r)} K(m_n^{\pm}) \\ & + \frac{\pi}{2} \text{sign}(z^{\pm}) \text{sign}(\sqrt{r^2 + (z^{\pm})^2} - r_n)[1 - \Lambda_0(\theta_{1n}^{\pm}, m_n^{\pm})] \\ & + \frac{\pi}{2} \text{sign}(z^{\pm})[1 - \Lambda_0(\theta_{2n}^{\pm}, m_n^{\pm})] \Bigg\} \end{aligned} \tag{C.10}$$

$$B_r^{\pm}(z,r) = \frac{\mu_0 M}{\pi} \sum_{n=1}^{2} (-1)^{n-1} \frac{1}{\sqrt{m_n^{\pm}}} \sqrt{\frac{r_n}{r}} \left[E(m_n^{\pm}) - \left(1 - \frac{m_n^{\pm}}{2}\right) K(m_n^{\pm}) \right] \tag{C.11}$$

and

$$z^{\pm} = z \mp l/2, \quad m_n^{\pm} = k_n^{\pm 2} = \frac{4rr_n}{(r+r_n)^2 + z^{\pm}}, \quad h_1^{\pm} = \frac{2r}{\sqrt{r^2 + (z^{\pm})^2} + r},$$
$$\theta_1^{\pm} = \sin^{-1}\sqrt{\frac{1-h_1^{\pm}}{1-m_n^{\pm}}}, \quad \theta_2^{\pm} = \sin^{-1}\frac{|z^{\pm}|}{\sqrt{r^2 + (z^{\pm})^2} + r}$$

C.5 Radially Magnetized Ring Magnet

Similar to the axially magnetized ring magnet, we use the analytical equations provided by Babic and Akyel [112]. For the ring magnet, let the length be l, the inner radius be r^+, and the outer radius be r^-. Also, let the center of the magnet be the origin, and the magnetization, M, be in radially outward direction. Then, the magnetic field at a given location (z, r) is given as

$$\begin{aligned} B_z &= B_z^+ - B_z^- \\ B_r &= B_r^+ - B_r^- \end{aligned} \tag{C.12}$$

where

$$B_z^{\pm}(z,r) = \frac{\mu_0 M}{2\pi}\sum_{n=1}^{2}(-1)^{n-1}\sqrt{m_n^{\pm}}\sqrt{\frac{r^{\pm}}{r}}K(m_n^{\pm}) \tag{C.13}$$

$$B_r^{\pm}(z,r) = -\frac{\mu_0 M}{4\pi}\sum_{n=1}^{2}(-1)^{n-1}\sqrt{\frac{r^{\pm}}{r}}\left[2\frac{t_n k_n^{\pm}}{r+r^{\pm}}K(m_n^{\pm}) + \pi\sqrt{\frac{r^{\pm}}{r}}\text{sign}(r-r^{\pm})\text{sign}(t_n)\left\{1-\Lambda_0(\theta_n^{\pm}, m_n^{\pm})\right\}\right] \tag{C.14}$$

and

$$m_n^{\pm} = k_n^{\pm 2} = \frac{4rr^{\pm}}{(r+r^{\pm})^2 + t_n^{\pm}}, \quad \theta_n^{\pm} = \sin^{-1}\sqrt{\frac{1-h^{\pm}}{1-k_n^{\pm 2}}}, \quad t_1 = z - l/2, \quad t_2 = z + l/2$$

C.6 Current Loop

Let the current through the loop be denoted as I, the radius of the current loop be r_l, and the axial position of the loop be z_l. The magnetic field induced by a current loop at a given location (z, r) is given as [244]

$$\begin{aligned} B_z &= \frac{\mu_0 I}{2\pi\sqrt{r^{*2}+z^{*2}}}\left[K(m)+\left(\frac{2r_l r^*}{[r^{*2}+z^{*2}](1-m)}-\frac{1}{1-m}\right)E(m)\right] \\ B_r &= -\frac{\mu_0 I z^*}{2\pi\sqrt{r^{*2}+z^{*2}}}\left[\frac{K(m)}{r}-\frac{E(m)}{r(1-m)}+\frac{2aE(m)}{[r^{*2}+z^{*2}](1-m)}\right] \end{aligned} \tag{C.15}$$

where r^* and z^* are defined as $r^* = r + r_l$ and $z^* = z + z_l$, respectively. $K(m)$ and $E(m)$ are the complete elliptic integrals of the first and second kind, respectively. The parameter, m, is the square of the elliptic modulus, and is given as $4rr_l/(r^{*2} + z^{*2})$. Evaluation of Eq. (C.15) is relatively expensive since the equation involves elliptic integrals. Therefore, it is impractical to compute Eq. (C.15) for each turn of the coil. Instead, the current coil is approximated with multiple current loops that are evenly spaced within the volume of the coil. Although the approximation would not provide an accurate solution very near the coil, the magnetic field solution within the region of interest, especially near the centerline, is sufficiently accurate (less than 1% error with several current loops).

C.7 Evaluation of Elliptic Integrals

The incomplete elliptic integrals of the first, second, and third kind are defined as

$$F(\theta, m) = \int_0^\theta \frac{1}{\sqrt{1-m\sin(\Theta)^2}}d\Theta \tag{C.16}$$

$$E(\theta, m) = \int_0^\theta \sqrt{1-m\sin(\Theta)^2}d\Theta \tag{C.17}$$

$$\Pi(n, \theta, m) = \int_0^\theta \frac{1}{1-n\sin^2\Theta}\frac{d\Theta}{\sqrt{1-m\sin^2\Theta}} \tag{C.18}$$

respectively, where m is the square of elliptic modulus and n is the characteristic. The complete elliptic integrals are the special case of the incomplete elliptic integrals where

$\theta = \pi/2$.

$$K(m) = F(\pi/2, m) \tag{C.19}$$

$$E(m) = E(\pi/2, m) \tag{C.20}$$

$$\Pi(n, m) = \Pi(n, \pi/2, m) \tag{C.21}$$

The Heuman's lambda function can be expressed in terms of elliptic functions

$$\Lambda(\theta, m) = \frac{2}{\pi}\left\{K(m)E(\theta, 1-m) - (K(m) - E(m))F(\theta, 1-m)\right\} \tag{C.22}$$

Since the calculation of the magnetic field occurs very frequently in the SC model, accuracy and speed in evaluating the elliptic integrals are critical. The elliptic integrals can be evaluated with different methods including direct numerical integration, descending Landen transformation, ascending Landen transformation, and the process of the arithmetic-geometric mean. In the SC model, we utilize two separate methods depending on the arguments of the elliptic integrals: Fukushima's fast computation method and Carlson's method.

C.7.1 Fukushima's Fast Computation Method

For standard domain of elliptic parameters, $0 < m < 1$ (and $0 < \theta < \pi/2$ for an incomplete elliptic integrals), we utilize Fukushima's fast computation methods for $K(m)$ [116], $E(m)$ [116], and $F(\theta, m)$ [117]. The fast method for $E(\theta, m)$ proposed by Fukushima [118] has not been implemented.

Fukushima proposed a method to solve the complete elliptic integrals of the first and second kind, utilizing series expansions [116]. For $m < 0.9$, both the integrals are calculated using the piecewise polynomials obtained by the Taylor series expansions around m_0.

$$K(m) \approx \sum_{j=0}^{J_K} K_j (m - m_0)^j, \quad E(m) \approx \sum_{j=0}^{J_E} E_j (m - m_0)^j \tag{C.23}$$

These polynomials are obtained separately for 10 different intervals: [0,0.1), [0.1,0.2), [0.2,0.3),

[0.3,0.4), [0.4,0.5), [0.5,0.6), [0.6,0.7), [0.7,0.8), [0.8,0.85), and [0.85,0.9). The zero point of the expansions, m_0, are simply the midpoints of these intervals. The coefficients, K_j and E_j, and the order of polynomials, J_K and J_E, can be found in Ref. [116]. For $0.9 \leq m \leq 1.0$, $K(m)$ is computed by Innes formula [245] that uses the nome $q(m')$, and $E(m)$ is computed by a formula improved from Innes formula to reduce the degree of round-off error. Here, the complementary elliptic parameter is defined as $m' \equiv 1 - m$.

$$K(m) = -\log q' \frac{K(m')}{\pi} \tag{C.24}$$

$$E(m) = \frac{1}{K(m')} \left(\frac{\pi}{2} + K(m) H(m') \right) \tag{C.25}$$

where $H(m)$ is defined as $H(m) \equiv K(m) - E(m)$. Both q and H are solved via series expansions with the coefficients provided in Ref. [116].

$$q(m) \approx \sum_{j=0}^{J_q} q_j (m)^j, \quad H(m) \approx \sum_{j=0}^{J_H} H_j (m - m_0)^j \tag{C.26}$$

The incomplete elliptic integrals of the first kind is computed by utilizing the Jacobian elliptic functions, $\mathrm{sn}(u, m)$ and $\mathrm{cn}(u, m)$. Assuming that input arguments are within the ranges $0 < \theta < \pi/2$ and $0 < m < 1$, $F(\theta, m)$ is computed by either of the four equations.

$$F(\theta, m) = \begin{cases} \mathrm{sn}^{-1}(s, m) & \text{if } \theta \leq \theta_s \\ K(m) - \mathrm{sn}^{-1}(z, m) & \text{else if } z^2 \leq y_s \\ \mathrm{cn}^{-1}(c, m) & \text{else if } c > w \\ K(m) - \mathrm{cn}^{-1}(w, m) & \text{otherwise} \end{cases} \tag{C.27}$$

where

$$s \equiv \sin\theta, \quad z \equiv \frac{\sin\theta_c}{\sqrt{m_c + m \sin^2\theta_c}}, \quad c \equiv \sin\theta_c, \quad w \equiv \frac{\sqrt{m_c}\sin\theta}{\sqrt{1 - m\sin^2\theta}} \tag{C.28}$$

Here, y_s and θ_s are chosen to be 0.9 and 1.249, respectively. The efficient algorithms in computing the inverse functions of $\mathrm{sn}(u, m)$ and $\mathrm{cn}(u, m)$ are provided in Ref. [117].

C.7.2 Carlson's Method

For other elliptic integrals as well as $K(m)$, $E(m)$, and $F(\phi, m)$ in non-standard domain of elliptic parameters, we evaluate Carlson's elliptic integrals and use the simple relationship with the standard elliptic integrals [115].

$$F(\theta, m) = \sin\theta R_F(\cos^2\theta, 1 - m\sin^2\theta, 1) \tag{C.29}$$

$$E(\theta, m) = F(\theta, m) - \frac{1}{3}m\sin^3\theta R_D(\cos^2\theta, 1 - m\sin^2\theta, 1) \tag{C.30}$$

$$\Pi(\theta, n, m) = F(\theta, m) - \frac{1}{3}n\sin^3\theta R_J(\cos^2\theta, 1 - m\sin^2\theta, 1, 1 + n\sin^2\theta) \tag{C.31}$$

where R_F, R_D, and R_J are the Carlson's elliptic integral of the first, second, and third kind, respectively. The functions for the Carlson's elliptic integrals are available in various numerical libraries such as International Mathematics and Statistics Library (IMSL) and also in Ref. [115].

C.8 Transformation between Inertial and Magnet Reference Frame

All of the equations provided in this appendix represent the magnetic fields in the magnet reference frame. In order to apply the equations for the case of the magnet unaligned with the inertial coordinate, it is necessary to perform an appropriate coordinate transformation between the inertial and magnet reference frame. In the discharge configuration, multiple block magnets are placed around the circumference of a cylindrical chamber with the directions of magnetization along z- or r-axis. Therefore, the transformation is often required for the block magnets but not for the other magnets if they are aligned with the domain axis. Let $\hat{m}$ be the unit vector in the direction of magnetization, and α be the angle between x-axis and the center of the magnet. Here, the axial and radial directions are only considered for the magnetization vector such that $\hat{m} = m_z\hat{z} + m_r\hat{r}$. Then, the transformation from inertial

$(\hat{x},\hat{y},\hat{z})$ to magnet reference frame $(\hat{x}',\hat{y}',\hat{z}')$is given as

$$\begin{pmatrix} \hat{x}' \\ \hat{y}' \\ \hat{z}' \end{pmatrix} = \begin{bmatrix} m_z \cos\alpha & m_z \sin\alpha & -m_r \\ -\sin\alpha & \cos\alpha & 0 \\ m_r \cos\alpha & m_r \sin\alpha & m_z \end{bmatrix} \begin{pmatrix} \hat{x} \\ \hat{y} \\ \hat{z} \end{pmatrix} \tag{C.32}$$

where $\sqrt{m_z^2 + m_r^2} = 1$. The inverse transformation can be done by multiplying both sides by inverse of the matrix.

$$\begin{pmatrix} \hat{x} \\ \hat{y} \\ \hat{z} \end{pmatrix} = \begin{bmatrix} m_z \cos\alpha & -\sin\alpha & m_r \cos\alpha \\ m_z \sin\alpha & \cos\alpha & m_r \sin\alpha \\ -m_r & 0 & m_z \end{bmatrix} \begin{pmatrix} \hat{x}' \\ \hat{y}' \\ \hat{z}' \end{pmatrix} \tag{C.33}$$

The magnetic field in the inertial coordinate system is computed by first transforming the position vector to the magnet reference frame using Eq. (C.32), then computing the magnetic field in the magnet reference frame, and finally transforming the magnetic field in the inertial coordinate using Eq. (C.33).

APPENDIX D

Supplemental Details for Particle Simulations

D.1 Particle Loading and Injection

In the SC model, the ions and plasma electrons are generated through inelastic collisions between primary electrons and neutral atoms. The initial positions of these particles are assumed to be uniformly distributed within a given cell and are determined using a random number. The velocity distribution is assumed to follow the Maxwell-Boltzmann distribution. The distribution for a single component of velocity is given by

$$f_v(v_k) = \left(\frac{m}{2\pi kT}\right)^{1/2} \exp\left(-\frac{mv_k^2}{2kT}\right) \tag{D.1}$$

where k denotes directions such as x, y, and z. The speed distribution, $f(v)$ in 3D can be derived by equating both sides of the following equation.

$$\int_{-\infty}^{\infty}\int_{-\infty}^{\infty}\int_{-\infty}^{\infty} f_v(v_x)f_v(v_y)f_v(v_z)dv_x dv_y dv_z = \int_v f(v)dv \tag{D.2}$$

where $v^2 = v_x^2 + v_y^2 + v_z^2$. The speed distribution in 3D is computed by taking $dv_x dv_y dv_z = v^2 \sin\theta dv d\theta d\phi$ and working out Eq. (D.2) for $0 \leq \theta \leq \pi$ and $0 \leq \phi \leq 2\pi$.

$$f(v) = 4\pi \left(\frac{m}{2\pi kT}\right)^{3/2} v^2 \exp\left(-\frac{mv^2}{2kT}\right) \tag{D.3}$$

Similarly, the speed distribution in 2D is computed by taking $dv_x dv_y = v d\phi$ and working out Eq. (D.2) for $0 \leq \phi \leq 2\pi$.

$$f(v) = 2\pi \left(\frac{m}{2\pi kT}\right) v \exp\left(-\frac{mv^2}{2kT}\right) \tag{D.4}$$

The particle velocity can be determined from the normalized cumulative distribution function in any dimension and equating to a random number, U.

$$F(v) = \frac{\int_0^v f(v)dv}{\int_0^\infty f(v)dv} = U_s \tag{D.5}$$

The SC model determines the initial velocity of newly created ions and electrons using the Box-Muller method [120]; the method takes advantage of the fact that an expression for $F(v)$ can be obtained explicitly when using the 2D speed distribution function. By inverting the resulting expression, the radial component of the velocity $v_r = \sqrt{v_x^2 + v_y^2}$ is obtained in terms of U_s.

$$v_r = v_t \sqrt{-\ln U_s} \tag{D.6}$$

where $v_t = \sqrt{2kT/m}$. Then, the x and y components of the velocity are simply $v_x = v_r \cos\alpha$ and $v_y = v_r \sin\alpha$, respectively, where α is determined by another random number, U_α, according to $\alpha = 2\pi U_\alpha$. The z component of the velocity is computed in the same manner. Here, the fourth component resulted from the Box-Muller method is simply discarded. The direction of the initial velocity is assumed to be equally probable in all directions (i.e. isotropic).

In contrast to the ions and plasma electrons, the distribution for the primary electrons is dependent on the type of source. For an electron flood gun used in the preliminary study of cusp physics, it is fair to assume that the primary electrons are monoenergetic due to the specification of narrow energy bounds. The source is later replaced with a hollow cathode to achieve a higher plasma density due to the limitation in the electron gun operating pressure. Within the hollow cathode, the electrons are initially at Maxwellian distribution, while they are accelerated by the applied discharge voltage as entering the simulation domain; the resultant distribution is the half-Maxwellian [246]. The half-Maxwellian energy distribution

function is given as

$$f_{\mathrm{HM}}(\alpha) = \frac{2}{E(\alpha_0)}\alpha(\alpha - \alpha_0)\exp(-\alpha^2), \quad \alpha > \alpha_0 \tag{D.7}$$

where $$\alpha = \sqrt{\frac{E_p}{T_p}}, \quad \alpha_0 = \sqrt{\frac{V_p}{T_p}}, \quad E(\alpha_0) = \int_{\alpha_0}^{\infty} \exp(-x^2)dx = \frac{\sqrt{\pi}}{2}\left(1 - \mathrm{erf}(\alpha_0)\right)$$

Here, T_p is the primary electron temperature within the hollow cathode before being accelerated, V_p is the voltage that the electrons are accelerated through (i.e. the plasma potential with respect to the cathode potential), and E_p is the energy of the primary electron entering the simulation domain. Similarly to Eq. (D.5), the energy of each primary electron is determined by utilizing the cumulative distribution function and a random number, U_p.

$$F_p(\alpha) = \frac{\int_{\alpha_0}^{\alpha} f_{\mathrm{HM}}(\alpha)d\alpha}{\int_{\alpha_0}^{\infty} f_{\mathrm{HM}}(\alpha)d\alpha} = U_p \tag{D.8}$$

Both the numerator and denominator in Eq. (D.5) can be evaluated analytically.

$$\int_{\alpha_0}^{\alpha} f_{\mathrm{HM}}(\alpha)d\alpha = \frac{\sqrt{\pi}}{4}\left[\mathrm{erf}(\alpha) - \mathrm{erf}(\alpha_0)\right] - \frac{1}{2}(\alpha - \alpha_0)\exp(-\alpha^2) \tag{D.9}$$

$$\int_{\alpha_0}^{\infty} f_{\mathrm{HM}}(\alpha)d\alpha = \frac{\sqrt{\pi}}{4}\left[1 - \mathrm{erf}(\alpha_0)\right] \tag{D.10}$$

Equation (D.8) is an implicit equation such that the determination of α cannot be evaluated directly. For a given U_p, α that satisfies the equation is obtained utilizing a root-finding algorithm.

D.2 Determination of Post-Collision Velocity

Because of the range of pressures used in the simulations presented in this dissertation, the gas is dilute enough that each collision can be considered to involve only two particles. During an elastic collision, it is assumed that the net translational energy of the collision pair is conserved. The velocities after the elastic (and CEX) collisions are calculated using

conservation equations for linear momentum and energy.

$$\mathbf{v_1^*} = \frac{m_1\mathbf{v_1} + m_2\mathbf{v_2}}{m_1 + m_2} + \frac{m_2}{m_1 + m_2}\mathbf{v_r^*} \tag{D.11}$$

$$\mathbf{v_2^*} = \frac{m_1\mathbf{v_1} + m_2\mathbf{v_2}}{m_1 + m_2} - \frac{m_1}{m_1 + m_2}\mathbf{v_r^*} \tag{D.12}$$

where superscript $*$ denotes post-collision, and subscripts 1 and 2 represent incident and target particles, respectively. Let the pre-collision relative velocity be v_r and the corresponding reference frame be denoted by $(\hat{x}', \hat{y}', \hat{z}')$. Then, the post-collision relative velocity v_r^* can be calculated simply by the following expression, assuming v_r is aligned with z'-axis.

$$\mathbf{v_r^*} = v_r \begin{pmatrix} \sin\chi\cos\gamma \\ \sin\chi\sin\gamma \\ \cos\chi \end{pmatrix}^T \begin{pmatrix} \hat{x}' \\ \hat{y}' \\ \hat{z}' \end{pmatrix} \tag{D.13}$$

Here, χ is the center of mass deflection angle and γ is the azimuthal angle. The transformation between the inertial and pre-collision relative velocity reference frames can be done by

$$\begin{pmatrix} \hat{x}' \\ \hat{y}' \\ \hat{z}' \end{pmatrix} = \begin{bmatrix} \cos\alpha\cos\beta & \sin\alpha\cos\beta & -\sin\beta \\ -\sin\alpha & \cos\alpha & 0 \\ \cos\alpha\sin\beta & \sin\alpha\sin\beta & \cos\beta \end{bmatrix} \begin{pmatrix} \hat{x} \\ \hat{y} \\ \hat{z} \end{pmatrix} \tag{D.14}$$

where α and β are the angles between the two reference frame given by

$$\begin{aligned} \sin\alpha &= v_{ry}/\sqrt{v_{rx}^2 + v_{ry}^2} \quad \cos\alpha = v_{rx}/\sqrt{v_{rx}^2 + v_{ry}^2} \\ \sin\beta &= \sqrt{v_{rx}^2 + v_{ry}^2}/v_r \quad \cos\beta = v_{rz}/v_r \end{aligned} \tag{D.15}$$

Given the pre-collision velocities of both incident and target particles, the post-collision velocities of the two particles can be calculated using (D.11)-(D.15) once χ and γ are determined. Because any value for γ is equally probable, γ is chosen simply by $\gamma = 2\pi U_1$ where U_1 is a random number. Similarly, b is determined with another random number U_2, $b = b_{\max}\sqrt{U_2}$.

D.3 Primary Electron Equilibration Rate Constant

The original velocity distribution of primary electrons is altered as a result of Coulomb collisions with plasma electrons. After multiple encounters, the velocity distribution eventually becomes Maxwellian, and the primary electron population can no longer be treated separately from plasma electron population. The time for primary electrons to reach the equilibrium velocity distribution is approximated by Spitzer energy exchange time, t_E [247].

$$t_E = \frac{v^3}{4A_D G(x_G)} \tag{D.16}$$

where v is the primary electron speed, x is the ratio of v to the root mean square two-dimensional velocity of plasma electrons, and A_D is the diffusion constant. Here, A_D and x are defined by

$$A_D = \frac{1}{2\pi\varepsilon_0^2}\frac{e^4 n_s \ln\Lambda}{m_e^2}, \quad x = v\sqrt{\frac{m_e}{2k_B T_e}} \tag{D.17}$$

where k_B is the Boltzmann constant, and T_e is the plasma electron temperature. The function $G(x)$ is defined in terms of the error function.

$$G(x) = \frac{\mathrm{erf}(x) - x\cdot\mathrm{erf}(x)'}{2x^2} = \frac{\mathrm{erf}(x) - \frac{2}{\sqrt{\pi}}x\exp(-x^2)}{2x^2} \tag{D.18}$$

Using these relations, the primary electron equilibration rate constant can be found by

$$K_{slow} = \frac{1}{n_s t_E} \tag{D.19}$$

Equation (D.19) is used to compute the depletion of primary electron current as a result of equilibration with the plasma electrons.

References

[1] Goebel, D. M. and Katz, I., *Fundamentals of Electric Propulsion: Ion and Hall Thrusters*, John Wiley & Sons, New York, 2008.

[2] Covello, F., "Application of Electrical Propulsion for an Active Debris Removal System: a System Engineering Approach," *Advances in Space Research*, Vol. 50, 2012, pp. 918–931.

[3] Garrigues, L. and P, C., "Electric Propulsion: Comparisons between Different Concepts," *Plasma Physics Controlled Fusion*, Vol. 53, No. 124011, 2011.

[4] Jahn, R. G., *Physics of Electric Propulsion*, Dover Publications, Inc., 2006.

[5] Martinez-Sanchez, M. and Pollard, J. E., "Spacecraft Electric Propulsion–An Overview," *Journal of Propulsion and Power*, Vol. 14, No. 5, 1998, pp. 688–699.

[6] Choueiri, E. Y., "A Critical History of Electric Propulsion: The First Fifty Years (1906–1956)," *40th AIAA/ASME/SAE/ASEE Joint Propulsion Conference & Exhibit*, Fort Lauderdale, Florida, 2004, pp. 1–21, AIAA 2004–3334.

[7] Sovey, J. S., Rawlin, V. K., and Patterson, M. J., "Spacecraft Electric Propulsion–An Overview," *Journal of Propulsion and Power*, Vol. 17, No. 3, 2001, pp. 517–526.

[8] Jahn, R. G. and Choueiri, E. Y., "Electric Propulsion," *in Encyclopedia of Physical Science and Technology*, Vol. 5, Academic Press, New York, 2002, pp. 125–141.

[9] Frisbee, R. H., "Advanced Space Propulsion for the 21st Century," *Journal of Propulsion and Power*, Vol. 19, No. 6, 2003, pp. 1129–1154.

[10] Oh, D. Y. and Goebel, D. M., "Performance Evaluation of an Expanded Range XIPS Ion Thruster System for NASA Science Missions," *42nd AIAA/ASME/SAE/ASEE Joint Propulsion Conference & Exhibit*, Sacramento, California, 2006, pp. 1–12, AIAA 2006–4466.

[11] Kuninaka, H., Nishiyama, K., Funaki, I., Shimizu, Y., Yamada, T., and Kawaguchi, J., "Assessment of Plasma Interactions and Flight Status of the HAYABUSA Asteroid Explorer Propelled by Microwave Discharge Ion Engines," *IEEE Transactions on Plasma Science*, Vol. 34, No. 5, 2006, pp. 2125–2132.

[12] Brophy, J. R., Marcucci, M. G., Ganapathi, G. B., Gates, J., Garner, C. E., Klatte, M., Lo, J., Nakazono, B., and Pixler, G., "Implementation of the Dawn Ion Propulsion System," *41st AIAA/ASME/SAE/ASEE Joint Propulsion Conference & Exhibit*, Tucson, Arizona, 2005, pp. 1–17, AIAA 2005–4071.

[13] Wirz, R. E., *Discharge Plasma Processes of Ring-Cusp Ion Thrusters*, Ph.D. thesis, California Institute of Technology, Pasadena, California, 2005.

[14] Wirz, R. E., Sullivan, R., Przybylowski, J., and Silva, M., "Hollow Cathode and Low-Thrust Extraction Grid Analysis for a Miniature Ion Thruster," *International Journal of Plasma Science and Engineering*, Vol. 2008, 2008, pp. 1–11.

[15] Vincenti, W. G. and Kruger, C. H., *Introduction to Physical Gas Dynamics*, Krieger Publishing Company, Malabar, Florida, 1965.

[16] Arakawa, Y. and Yamada, T., "Monte Carlo Simulation of Primary Electron Motions in Cusped Discharge Chambers," *21st International Electric Propulsion Conference*, Orlando, Florida, 1990, AIAA 1990–2654.

[17] Mahalingam, S. and Menart, J. A., "Primary Electron Modeling in the Discharge Chamber of an Ion Engine," *38th AIAA/ASME/SAE/ASEE Joint Propulsion Conference & Exhibit*, Indianapolis, Indiana, 2002, pp. 1–17, AIAA 2002–4262.

[18] Deshpande, S. S., Mahalingam, S., and Menart, J. A., "Computational Study of Primary Electrons in the Cusp Region of an Ion Engines Discharge Chamber," *40th AIAA/ASME/SAE/ASEE Joint Propulsion Conference & Exhibit*, Fort Lauderdale, Florida, 2004, pp. 1–14, AIAA 2004–4109.

[19] Deshpande, S. S., Ogunjobi, T., and Menart, J. A., "Computational Study of Magnet Placement on the Discharge Chamber of an Ion Engine," *41st AIAA/ASME/SAE/ASEE Joint Propulsion Conference & Exhibit*, Tucson, Arizona, 2005, pp. 1–14, AIAA 2005–4254.

[20] Ogunjobi, T. A. and Menart, J. A., "Computational Study of Ring-Cusp Magnet Congurations that Provide Maximum Electron Connement," *42nd AIAA/ASME/SAE/ASEE Joint Propulsion Conference & Exhibit*, Sacramento, California, 2006, pp. 1–21, AIAA 2006–4489.

[21] Bennett, W., Ogunjobi, T., and Menart, J. A., "Computational Study of the Effects of Cathode Placement, Electron Energy, and Magnetic Field Strength on the Confinement of Electrons," *43rd AIAA/ASME/SAE/ASEE Joint Propulsion Conference & Exhibit*, Cincinnati, Ohio, 2007, pp. 1–13.

[22] Arakawa, Y. and Ishihara, K., "A Numerical Code for Cusped Ion Thrusters," *22nd International Electric Propulsion Conference*, Viareggio, Italy, 1991, pp. 1–6, IEPC 1991–118.

[23] Wirz, R. E. and Katz, I., "A Preliminary 2-D Computational Model of an Ion Thruster Discharge Chamber," *39th AIAA/ASME/SAE/ASEE Joint Propulsion Conference & Exhibit*, Huntsville, Alabama, 2003, pp. 1–10, AIAA 2003–5163.

[24] Wirz, R. E., "Computaitonal Modeling of a Miniature Ion Thruster Discharge," *41st AIAA/ASME/SAE/ASEE Joint Propulsion Conference & Exhibit*, Tucson, Arizona, 2005, pp. 1–10, AIAA 2005–3887.

[25] Mahalingam, S., *Particle Based Plasma Simulation for an Ion Engine Discharge Chamber*, Ph.D. thesis, Wright State University, Dayton, Ohio, 2007.

[26] Mahalingam, S. and Menart, J. A., "Particle-Based Plasma Simulations for an Ion Engine Discharge Chamber," *Journal of Propulsion and Power*, Vol. 26, No. 4, 2010.

[27] Mahalingam, S. and Menart, J. A., "Fully Coupled Electric Field/PIC-MCC Simulation Results of the Plasma in the Discharge Chamber of an Ion Engine," *47th AIAA/ASME/SAE/ASEE Joint Propulsion Conference & Exhibit*, San Diego, California, 2011, pp. 1–24, AIAA 2011–6071.

[28] Hirakawa, M. and Arakawa, Y., "Plasma Particle Simulation in Cusped Ion Thrusters," *24th International Electric Propulsion Conference*, Moscow, Russia, 1993, pp. 1–7, IEPC 1993–242.

[29] Hirakawa, M. and Arakawa, Y., "Particle Simulation of Plasma in Electric Propulsion Thrusters," *Journal of the Japan Society for Aeronautical and Space Sciences*, Vol. 45, No. 523, 1997, pp. 444–452, (in Japanese).

[30] Sandonato, G. M., Barroso, J. J., and Montes, A., "Magnetic Confinement Studies for Performance Enhancement of a 5-cm Ion Thruster," *IEEE Transactions on Plasma Science*, Vol. 24, No. 6, 1996, pp. 1319–1329.

[31] Arakawa, Y. and Wilbur, P. J., "Finite Element Analysis of Plasma Flows in Cusped Discharge Chambers," *Journal of Propulsion and Power*, Vol. 7, No. 1, 1991, pp. 125–128.

[32] Brophy, J. R., *Ion Thruster Performance Model*, Ph.D. thesis, Colorado State University, Fort Collins, Colorado, 1984.

[33] Brophy, J. R. and Wilbur, P. J., "Simple Performance Model for Ring and Line Cusp Ion Thrusters," *AIAA Journal*, Vol. 23, No. 11, 1985, pp. 1731–1736.

[34] Jonell, M., Menart, J., and Mahalingam, S., "Particle-Based Plasma Simulation of the NEXT Ion Engine," *45th AIAA/ASME/SAE/ASEE Joint Propulsion Conference & Exhibit*, Denver, Colorado, 2009, pp. 1–16, AIAA 2009–4818.

[35] Goebel, D. M., Katz, I., Ziemer, J., Brophy, J. R., Polk, J. E., and Johnson, L., "Electric Propulsion Research and Development at JPL," *41th AIAA/ASME/SAE/ASEE Joint Propulsion Conference & Exhibit*, Tucson, Arizona, 2005, pp. 1–12, AIAA 2005–3535.

[36] Sengupta, A., "Magnetic Confinement in a Ring-Cusp Ion Thruster Discharge Plasma," *Journal of Applied Physics*, Vol. 105, No. 093303, 2009, pp. 1–10.

[37] Goebel, D. M., Wirz, R. E., and Katz, I., "Analytical Ion Thruster Discharge Performance Model," *Journal of Propulsion and Power*, Vol. 23, No. 5, 2007, pp. 1055–1067.

[38] Brophy, J., Katz, I., Polk, J. E., and Anderson, J. R., "Numerical Simulations of Ion Thruster Accelerator Grid Erosion," *38th AIAA/ASME/SAE/ASEE Joint Propulsion Conference & Exhibit*, Indianapolis, Indiana, 2002, pp. AIAA 2002–4261.

[39] Anderson, J. R., Katz, I., and Goebel, D., "Numerical Simulation of Two-Grid Ion Optics Using a 3D Code," *40th AIAA/ASME/SAE/ASEE Joint Propulsion Conference & Exhibit*, Fort Lauderdale, Florida, 2004, pp. 1–14, AIAA 2004–3782.

[40] Wirz, R. E., Anderson, J. R., Goebel, D. M., and Katz, I., "Decel Grid Effects on Ion Thruster Grid Erosion," *IEEE Transactions on Plasma Science*, Vol. 2, No. 5, 2008, pp. 2122–2129.

[41] Nakayama, Y. and Wilbur, P. J., "Numerical Simulation of Ion Beam Optics for Multiple-Grid Systems," *Journal of Propulsion and Power*, Vol. 19, No. 4, 2003, pp. 607–613.

[42] Farnell, C. C., *Performance and Lifetime Simulation of Ion Thruster Optics*, Ph.D. thesis, Colorado State University, Fort Collins, Colorado, 2007.

[43] Arakawa, Y. and Nakano, M., "An Efficient Three-Dimensional Optics Code for Ion Thruster Research," *32nd AIAA/ASME/SAE/ASEE Joint Propulsion Conference & Exhibit*, Lake Buena Vista, Florida, 1996, AIAA 1996–3198.

[44] Nakano, M. and Arakawa, Y., "Ion Thruster Lifetime Estimation and Modeling Using Computer Simulation," *27th International Electric Propulsion Conference*, Pasadena, California, 1999, IEPC 1999–145.

[45] Nakano, M., "Three-Dimensional Simulations of Grid Erosion in Ion engines," *Vacuum*, Vol. 83, 2009, pp. 82–85.

[46] Funaki, I., Nakano, M., Kajimura, Y., Miyasaka, T., Nakayama, Y., Hyakutake, T., Wada, M., Kenmotsu, T., Muramoto, T., Kuninaka, H., and Shinohara, I., "A Numerical Tool for Lifetime Evaluation of Ion Thruster's Ion Optics," *47th AIAA/ASME/SAE/ASEE Joint Propulsion Conference & Exhibit*, San Diego, California, 2011, pp. 1–12, AIAA 2011–5734.

[47] Funaki, I., Watanabe, H., Nakano, M., Kajimura, Y., Miyasaka, T., Nakayama, Y., Kuninaka, H., and Shinohara, I., "Numerical Lifetime Evaluation of Ion Thruster's IOn Optics using the JIEDI Tool," *48th AIAA/ASME/SAE/ASEE Joint Propulsion Conference & Exhibit*, Atlanta, Georgia, 2012, pp. 1–11, AIAA 2012–3797.

[48] Becker, R. and Herrmannsfeldt, W. B., "IGUN – A Program for the Simulation of Positive Ion Extraction Including Magnetic Fields," *Review of Scientific Instruments*, Vol. 63, No. 4, 1992, pp. 2756–2758.

[49] Tartz, M., Hartmann, E., and Neumann, H., "Evolution of Extraction Grid Erosion with Operation Time," *40th AIAA/ASME/SAE/ASEE Joint Propulsion Conference & Exhibit*, Fort Lauderdale, Florida, 2004, pp. 1–6, AIAA 2004–3787.

[50] Okawa, Y. and Takegahara, H., "Particle Simulation on Ion Beam Extraction Phenomena in an Ion Thruster," *26th International Electric Propulsion Conference*, Kitakyushu, Japan, 1999, pp. 1–8, IEPC 1999–146.

[51] Okawa, Y., Takegahara, H., and Tachibana, T., "Numerical Analysis of Ion Beam Extraction Phenomena in an Ion Thruster," *27th International Electric Propulsion Conference*, Pasadena, California, 2001, pp. 1–10, IEPC 2001–97.

[52] Kafafy, R. and Wang, J., "A HG-IFE-PIC Simulation Model for Ion Thruster Optics Plasma Flow," *36th AIAA Plasmadynamics and Lasers Conference*, Toronto, Canada, 2005, pp. 1–11.

[53] Kafafy, R., *Immersed Finite Element Particle-In-Cell Simulations of Ion Propulsion*, Ph.D. thesis, Virginia Polytechnic Institute and State University, Blacksburg, Virginia, 2005.

[54] Wang, J., Polk, J., Brophy, J., and Katz, I., "Three-Dimensional Particle Simulations of Ion-Optics Plasma Flow and Grid Erosion," *Journal of Propulsion and Power*, Vol. 19, No. 6, 2003, pp. 1192–1199.

[55] Crofton, M. W. and Boyd, I. D., "The Origins of Accelerator Grid Current: Analysis of T5-Grid Test Results," *35th AIAA/ASME/SAE/ASEE Joint Propulsion Conference & Exhibit*, Los Angeles, California, 1999, pp. 1–10, AIAA 1999–2443.

[56] Emhoff, J. W. and Boyd, I. D., "Perveance and Beamlet Expansion Modeling of the NEXT Ion Engine," *29th International Electric Propulsion Conference*, Princeton, New Jersey, 2005, pp. 1–12.

[57] Emhoff, J. W., *Simulation of Ion Optics Using Particle-In-Cell and Treecode Methods*, Ph.D. thesis, University of Michigan, Blacksburg, Virginia, 2005.

[58] Pollard, J., Diamant, K. D., Khayms, V., Werthman, L., King, D. Q., and DeGrys, K. H., "Ion Flux, Energy, Charge-State Measurements for the BPT-4000 Hall Thruster," *37th AIAA/ASME/SAE/ASEE Joint Propulsion Conference & Exhibit*, Salt Lake City, Utah, 2001, AIAA 2001–3351.

[59] Boyd, I. D., "A Review of Hall Thruster Plume Modeling," *38th Aerospace Sciences Meeting & Exhibit*, Reno, Nevada, 2000, pp. 1–19, AIAA 2000–0466.

[60] Roy, R. I. S., *Numerical Simulation of Ion Thruster Plume Backflow for Spacecraft Contamination Assessment*, Ph.D. thesis, Massachusetts Institute of Technology, Cambridge, Massachusetts, 1995.

[61] Roy, R. I. S., Hasting, D. E., and Taylor, S., "Three-Dimensional Plasma Particle-in-Cell Calculations of Ion Thruster Backflow Contamination," *Journal of Computational Physics*, Vol. 128, 1996, pp. 6–18.

[62] Wang, J., Cao, Y., Kafafy, R., Pierru, J., and Decyk, V. K., "Simulations of Ion Thruster Plume-Spacecraft Interactions on Parallel Supercomputer," *IEEE Transactions on Plasma Science*, Vol. 34, No. 5, 2006, pp. 2148–2158.

[63] Kafafy, R. and Cao, Y., "Modelling Ion Propulsion Plume Interactions with Spacecraft in Formation Flight," *The Aeronautical Journal*, Vol. 114, No. 1157, 2010, pp. 417–426.

[64] Brieda, L., Kafafy, R., Pierru, J., and Wang, J., "Development of the DRACO Code for Modeling Electric Propulsion Plume Interactions," *40th AIAA/ASME/SAE/ASEE Joint Propulsion Conference & Exhibit*, Fort Lauderdale, Florida, 2004, pp. 1–21, AIAA 2004–3633.

[65] Brieda, L., *Development of the DRACO ES-PIC Code and Fully-Kinetic Simulation of Ion Beam Neutralization*, Master's thesis, Virginia Polytechnic Institute and State University, Blacksburg, Virginia, 2005.

[66] Brieda, L., Van Gilder, D., and Wang, J., "Modeling Ion Beam Neutralization and Near-Thruster Plume Interactions," *29th International Electric Propulsion Conference*, Princeton, New Jersey, 2005, pp. 1–12, IEPC 2005–270.

[67] Brieda, L., *Multiscale Modeling of Hall Thrusters*, Ph.D. thesis, The George Washington University, Washington D. C., 2012.

[68] Oh, D. Y. and Hastings, D. E., "Computational Modeling of Expanding Plasma Plumes in Space Using a PIC-DSMC Algorithm," *Proceedings of the 25th International Electric Propulsion Conference*, Cleveland, Ohio, 1997, pp. 1082–1089, IEPC 1997-179.

[69] Oh, D., *Computational Modeling of Expanding Plasma Plumes in Space Using a PIC-DSMC Algorithm*, Ph.D. thesis, Massachusetts Institute of Technology, 1997.

[70] Celik, M., Santi, M., Cheng, S., Martinez-Sanchez, M., and Peraire, J., "Hybrid-PIC Simulation of a Hall Thruster Plume on an Unstructured Grid with DSMC Collisions," *28th International Electric Propulsion Conference*, Toulouse, France, 2003, pp. 1–10, IEPC 2003–134.

[71] Cheng, S., Santi, M., Celik, M., Martinez-Sanchez, M., and Peraire, J., "Hybrid PIC-DSMC Simulation of a Hall Thruster Plume on Unstructured Grids," *Computer Physics Communications*, Vol. 164, 2004, pp. 73–79.

[72] Van Gilder, D. B., Font, G. I., and Boyd, I. D., "Hybrid Monte Carlo-Particle-in-Cell Simulation of an Ion Thruster Plume," *Journal of Propulsion and Power*, Vol. 15, 1999, pp. 530–538.

[73] Boyd, I. D. and Dressler, R. A., "Far Field Modeling of the Plasma Plume of a Hall Thruster," *Journal of Applied Physics*, Vol. 92, No. 4, 2002, pp. 1764–1774.

[74] Boyd, I. D. and Yim, J. T., "Modeling of the Near Field Plume of a Hall Thruster," *Journal of Applied Physics*, Vol. 95, No. 9, 2004, pp. 4575–4584.

[75] Boyd, I. D., "Numerical Simulation of Hall Thruster Plasma Plumes in Space," *IEEE Transactions on Plasma Science*, Vol. 34, No. 5, 2006, pp. 2140–2147.

[76] Giuliano, P. N. and Boyd, I. D., "Effects of Detailed Charge Exchange Interactions in DSMC-PIC Simulation of a Simplified Plasma Test Cell," *32nd International Electric Propulsion Conference*, 2011, pp. 1–10, IEPC 2011–112.

[77] Giuliano, P. N. and Boyd, I. D., "Analysis of a Plasma Test Cell Including Non-Neutrality and Complex Collision Mechanisms," *48th AIAA/ASME/SAE/ASEE Joint Propulsion Conference & Exhibit*, Atlanta, Georgia, 2012, pp. 1–13, AIAA 2012–3736.

[78] Fife, J. M., Gibbons, M. R., Hargus, W. A., Van Gilder, D. B., Kirtley, D. E., and Johnson, L. K., "3-D Computation of Surface Sputtering and Redeposition due to Hall Thruster Plumes," *28th International Electric Propulsion Conference*, Toulouse, France, 2003, pp. 1–7, IEPC 2003–0136.

[79] Mikellides, I., Katz, I., Kuharski, R., and Mandell, M., "Elastic Scattering of Ions in Electrostatic Thruster Plumes," *Journal or Propulsion and Power*, Vol. 21, No. 1, 2005, pp. 111–118.

[80] Wirz, R. E., Chu, L., Patino, M., Mao, H.-S., and Araki, S. J., "Well-Characterized Plasma Experiments for Validation of Computational Models," *32nd International Electric Propulsion Conference*, Wiesbaden, Germany, 2011, pp. 1–12, IEPC 2011–122.

[81] Martinez-Sanchez, M. and Ahedo, E., "Magnetic Mirror Effects on a Collisionless Plasma in a Convergent Geometry," *Physics of Plasmas*, Vol. 18, No. 033509, 2011.

[82] Conversano, R. and Wirz, R. E., "CubeSat Lunar Mission Using a Miniature Ion Thruster," *47th AIAA/ASME/SAE/ASEE Joint Propulsion Conference & Exhibit*, San Diego, California, 2011, pp. 1–19, AIAA 2011–6083.

[83] Conversano, R. and Wirz, R. E., "Mission Capability Assessment of CubeSats Using a Miniature Ion Thruster," *AIAA Journal of Spacecraft and Rockets*, Vol. 50, No. 5, 2013, pp. 1035–1046.

[84] Heidt, H., Puig-Suari, J., Moore, A. S., Nakasuka, S., and Twiggs, R. J., "CubeSat: A New Generation of Picosatellite for Education and Industry Low-Cost Space Experimentation," *Proceedings of the Utah State University Small Satellite Conference*, Logan, Utah, 2001, pp. 1–19, SSC00–V–5.

[85] Wirz, R. E., Mueller, J., Gale, M., and Marrese, C., "Miniature Ion Engines for Precision Formation Flying," *40th AIAA/ASME/SAE/ASEE Joint Propulsion Conference & Exhibit*, Fort Lauderdale, Florida, 2004, pp. 1–9, AIAA 2004–4115.

[86] Martin, S., Scharf, D., Wirz, R. E., Lay, O., McKinstry, D., Mennesson, B., Purcell, G., Rodriguez, J., Scherr, L., Smith, J. R., and Wayne, L., "Design Study for a Planet-Finding Space Interferometer," *Proceedings of IEEE Aerospace Conference*, Big Sky, Montana, 2008, pp. 1–19.

[87] Spalding, I., "Cusp Containment," *Advances in Plasma Physics*, Vol. 4, 1971, pp. 79.

[88] Kitsunezaki, A., Tanimoto, M., and Sekiguchi, T., "Cusp Confinement of High-Beta Plasmas Produced by a Laser Pulse from a Freely-Falling Deuterium Ice Pellet," *Physics of Fluids*, Vol. 17, No. 10, 1974, pp. 1895–1902.

[89] Hershkowitz, N., Leung, K. N., and Romesser, T., "Plasma Leakage through a Low-Beta Line Cusp," *Physical Review Letters*, Vol. 35, No. 5, 1975, pp. 277–280.

[90] Leung, K. N., Hershkowitz, N., and MacKenzie, K. R., "Plasma Confinement by Localized Cusps," *Physics of Fluids*, Vol. 19, No. 1045, 1976.

[91] Bosch, R. A. and Merlino, R. L., "Confinement of a Potassium Plasma in a Spindle Cusp magnetic field," *Journal of Applied Physics*, Vol. 60, No. 9, 1986, pp. 3056–3067.

[92] Bosch, R. A. and Merlino, R. L., "Confinement Properties of a Low-Beta Discharge in a Spindle Cusp Magnetic Field," *Physics of Fluids*, Vol. 29, No. 6, 1986, pp. 1998–2006.

[93] Christensen, T., Hershkowitz, N., and Leung, K. N., "Mass Scaling of Permanent Magnet Line Cusp Plasma Leaks," *IEEE Transactions on Plasma Science*, Vol. PS-5, No. 1, 1977.

[94] Fujita, T., Ohnuma, T., and Adachi, S., "Plasma States in a Cylindrical Cusp-Shaped Magnetic Field Composed of a Permanent Magnet Array," *Plasma Physics*, Vol. 23, No. 11, 1981, pp. 1019–1026.

[95] Kozima, H., Kawamoto, S., and Yamagiwa, K., "On the Leak Width of Line- and Point-Cusp Magnetic Fields," *Physics Letters A*, Vol. 86, No. 6,7, 1981, pp. 373–375.

[96] Hubble, A. A. and Foster, J. E., "Plasma Collection Width Measurements in a 10-cm Ring Cusp Discharge Chamber," *44th AIAA/ASME/SAE/ASEE Joint Propulsion Conference & Exhibit*, Hartford, Connecticut, 2008, pp. 1–18, AIAA 2008–4639.

[97] Matlock, T., Lozano, P., and Martinez-Sanchez, M., "Discharge Chamber Wall Flux Measurements in a Diverging Cusped-Field Thruster," *ESA/A3F Space Propulsion Conference*, San Sebastián, Spain, 2010, pp. 1–8.

[98] Pechacek, R. E., Greig, J. R., Raleigh, M., Koopman, D. W., and DeSilva, A. W., "Measurement of the Plasma Width in a Ring Cusp," *Physical Review Letters*, Vol. 45, No. 4, 1980, pp. 256–259.

[99] Kogashi, S., Sato, K. N., and Sekiguchi, T., "Behaviour of Laser-Produced High-β Plasmas in a Splindle-Cusp Magnetic Container," *Journal of Physics D: Applied Physics*, Vol. 11, 1978, pp. 1057–1072.

[100] Anukaliani, A. and Selvarajan, V., "Loss of Plasma Scaling with Magnetic Field, Pressure and Discharge Current in a CUSP Confined Plasma," *The European Physical Journal: Applied Physics*, Vol. 15, 2001, pp. 199–206.

[101] Horiike, H., Akiba, M., Ohara, Y., Okumura, Y., and Tanaka, S., "Cusp Width and Power Flow Study at a High Power Magnetic Multipole Ion Source," *Physics of Fluids*, Vol. 30, No. 10, 1987, pp. 3268–3275.

[102] Haines, M. G., "Plasma Containment in Cusp-Shaped Magnetic Fields," *Nuclear Fusion*, Vol. 17, No. 4, 1977, pp. 811–858.

[103] Koch, C. and Matthieussent, G., "Collisional Diffusion of a Plasma in Multipolar and Picket Fence Devices," *Physics of Fluids*, Vol. 26, No. 2, 1983, pp. 545–555.

[104] Bosch, R. A. and Gilgenbach, R. M., "Leak Width Resulting from Plasma Diffusion in a Magnetic Cusp," *Physics Letters A*, Vol. 128, No. 8, 1988, pp. 437–438.

[105] Morishita, T., Ogasawara, M., and Hatayama, A., "Estimate of Cusp Loss Width in Multicusp Negative Ion Source," *Review of Scientific Instruments*, Vol. 69, No. 2, 1998, pp. 968–970.

[106] Fukano, A., Mizuno, T., Hatayama, A., and Ogasawara, M., "Estimation of the Cusp Loss Width in Negative-Ion Sources," *Review of Scientific Instruments*, Vol. 77, No. 3, 2006, pp. 03A524 1–4.

[107] Knorr, G. and Willis, D., "Leak Width of a Cusp-Confined Plasma," *Zeitschrift fuer Naturforschung. Teil A: Physik, Physikalische Chemie, Kosmophysik*, Vol. 37, No. 8, 1982, pp. 780–785.

[108] Knorr, G. and Merlino, R. L., "The Role of Fast Electrons for the Confinement of Plasma by Magnetic Cusps," *Plasma Physics and Controlled Fusion*, Vol. 26, No. 2, 1984, pp. 433–442.

[109] Marcus, A. J., Knorr, G., and Joyce, G., "Two-Dimensional Simulation of Cusp Confinement of a Plasma," *Plasma Physics*, Vol. 22, 2000, pp. 1015–1027.

[110] Takekida, H. and Nanbu, K., "Particle Modeling of Plasma Confinement by a Multipolar Magnetic Field," *Journal of Physics D: Applied Physics*, Vol. 37, 2004, pp. 1800–1808.

[111] Ravaud, R., Lemarquand, G., Babic, S., Lemarquand, V., and Akyel, C., "Cylindrical Magnets and Coils: Fields, Forces, and Inductances," *IEEE Transactions on Magnetics*, Vol. 46, No. 9, 2010, pp. 3585–3590.

[112] Babic, S. and Akyel, C., "Improvement in the Analytical Calculation of the Magnetic Field Produced by Permanent Magnet Rings," *Progress In Electromagnetics Research*, Vol. 5, 2008, pp. 71–82.

[113] Engel-Herbert, R. and Hesjedal, T., "Calculation of the Magnetic Stray Field of a Uniaxial Magnetic Domain," *Journal of Applied Physics*, Vol. 97, No. 7, 2005, pp. 074504.

[114] Ravaud, R., Lemarquand, G., Lemarquand, V., and Depollier, C., "Analytical Calculation of the Magnetic Field Created by Permanent-Magnet Rings," *IEEE Transactions on Magnetics*, Vol. 44, No. 8, 2008, pp. 1982–1989.

[115] Press, W. H., Teukolsky, S. A., Vetterling, W. T., and Flannery, B. P., *Numerical Recipes in FORTRAN: The Art of Scientific Computing*, Cambridge University Press, Cambridge, 2nd ed., 1992.

[116] Fukushima, T., "Fast Computation of Complete Elliptic Integrals and Jacobian Elliptic Functions," *Celestial Mechanics and Dynamical Astronomy*, Vol. 105, No. 4, 2009, pp. 305–328.

[117] Fukushima, T., "Fast Computation of Incomplete Elliptic Integral of First Kind by Half Argument Transformation," *Numerische Mathematik*, Vol. 116, No. 4, 2010, pp. 687–719.

[118] Fukushima, T., "Precise and Fast Computation of of a General Incomplete Elliptic Integral of Second Kind by Half and Double Argument Transformations," *Journal of Computational and Applied Mathematics*, Vol. 235, 2011, pp. 4140–4148.

[119] Boris, J. P., "Relativistic Plasma Simulations-Optimization of a Hybrid Code," *Proceedings of the 4th Conference of Numerical Simulation of Plasmas*, Washington DC, 1970, pp. 3–67.

[120] Birdsall, C. K. and Langdon, A. B., *Plasma Physics via Computer Simulation*, IOP Publishing Ltd., 1991.

[121] Mao, H.-S. and Wirz, R. E., "Comparison of Charged Particle Tracking Methods for Non-Uniform Magnetic Fields," *42nd AIAA Plasmadynamics and Lasers Conference*, Honolulu, Hawaii, 2011, pp. 1–9, AIAA 2011–3739.

[122] Cornet, C. and Kwok, D. T., "A New Algorithm for Charge Deposition for Multiple-Grid Method for PIC Simulations in r-z Cylindrical Coordinates," *Journal of Computational Physics*, Vol. 225, No. 1, 2007, pp. 808–828.

[123] Kwok, D. T. and Cornet, C., "Numerical Simulation of Metal Plasma Immersion Ion Implantation (MePIIID) on a Sharp Cone and a Fine Tip by a Multiple-Grid Particle-in-Cell (PIC) Method," *IEEE Transactions on Plasma Science*, Vol. 34, No. 5, 2006, pp. 2434–2442.

[124] Santos, R., "Implementation of the Kinetic Bohm Condition in a Hall Thruster Hybrid Code," *45th AIAA/ASME/SAE/ASEE Joint Propulsion Conference & Exhibit*, Denver, Colorado, 2009, pp. 1–11, AIAA 2009–4913.

[125] Ahedo, E. and Escobar, D., "Two-Dimensional Modeling of the Hall Thruster Discharge," Tech. rep., E. T. S. I. Aeronauticos Universidad Politecnica De Madrid Spain, September 2007.

[126] Vazquez, P. A. and Castellanos, A., "Weighting of Charge in PIC Codes for Unstructured Meshes in Cylindrical Coordinates: Application to Charged Jets," *IEEE Conference on Electrical Insulation and Dielectric Phenomena*, Nashville, Tennessee, 2005, pp. 1–4.

[127] Larson, D., Hewett, D. W., and Langdon, A. B., "Correction Factors for PIC Accumulation on Radial Grids," *Computer Physics Communications*, Vol. 90, 1995, pp. 260–266.

[128] Ruyten, W., "Density-Conserving Shape Factors for Particle Simulations in Cylindrical and Spherical Coordinates," *Journal of Computational Physics*, Vol. 105, No. 2, 1993, pp. 224–232.

[129] Verboncoeur, J., "Symmetric Spline Weighting for Charge and Current Density in Particle Simulation," *Journal of Computational Physics*, Vol. 174, No. 1, 2001, pp. 421–427.

[130] Gibson, J. C., Lun, D. R., Allen, L. J., McEachran, R. P., Parcell, L. A., and Buckman, S. J., "Low-Energy Electron Scattering from Xenon," *Journal of Physics B: Atomic, Molecular and Optical Physics*, Vol. 31, 1998, pp. 3949–3964.

[131] Nishimura, H., Matsuda, T., and Danjo, A., "Elastic Scattering of Electrons from Xenon," *Journal of the Physical Society of Japan*, Vol. 56, No. 1, 1987, pp. 70–78.

[132] Register, D. F., Vuskovic, L., and Trajmar, S., "Elastic Electron Scattering Cross Sections for Xe in the 1–100 eV Impact Energy Region," *Journal of Physics B: Atomic, Molecular and Optical Physics*, Vol. 19, 1986, pp. 1685–1697.

[133] Linert, I., Mielewska, B., King, G. C., and Zubek, M., "Differential Cross Sections for Elastic Electron Scattering in Xenon in the Energy Range from 5 eV to 10 eV," *Physical Review A*, Vol. 76, No. 032715, 2007.

[134] Cho, H., McEachran, R. P., Buckman, S. J., Fillpovic, D. M., Pejcev, V., Marinkovic, B. P., Tanaka, H., Stauffer, A. D., and Jung, E. C., "Absorption Effects in Intermediate Energy Elastic Electron Scattering from Xenon," *Journal of Physics B: Atomic, Molecular and Optical Physics*, Vol. 39, 2006, pp. 3781–3790.

[135] Adibzadeh, M. and Theodosiou, C. E., "Elastic Electron Scattering from Inert-Gas atoms," *Atomic Data and Nuclear Data Tables*, Vol. 91, 2005, pp. 8–76.

[136] Yuan, J. and Zhang, Z., "Application of the Quasirelativistic Approach to Low-Energy Electron-Atom Scattering: Xe," *Atomic Data and Nuclear Data Tables*, Vol. 24, 1991, pp. 275–285.

[137] Okhrimovskyy, A., Bogaerts, A., and Gijbels, G., "Electron Anisotropic Scattering in Gases: A Formula for Monte Carlo Simulations," *Physical Review E*, Vol. 65, No. 037402, 2002.

[138] Surendra, M., Graves, D. B., and Jellum, G. M., "Self-Consistent Model of a Direct-Current Glow Discharge: Treatment of Fast Electrons," *Physical Review A*, Vol. 41, No. 2, 1990.

[139] Bird, G. A., *Molecular Gas Dynamics and the Direct Simulation of Gas Flows*, Clarendon Press, Oxford, 1994.

[140] Dalgarno, A., McDowell, M. R. C., and Williams, A., "The Mobilities of Ions in Unlike Gasses," *Philosophical Transactions of the Royal Society of London. Series A, Mathematical and Physical Science*, Vol. 250, No. 982, 1958, pp. 411–425.

[141] Chen, F. F., *Introduction to Plasma Physics and Controlled Fusion Volumn 1: Plasma Physics*, Springer, New York, 2nd ed., 2006.

[142] Hayashi, M., *Bibliography of Electron and Photon Cross Sections with Atoms and Molecules Published in the 20th Century: Xenon*, National Institute for Fusion Science (Japan), 2003, NIFS–DATA–72.

[143] Subramanian, K. P. and Kumar, V., "Total Electron Scattering Cross Sections for Argon, Krypton and Xenon at Low Electron Energies," *Journal of Physics B: Atomic, Molecular and Optical Physics*, Vol. 20, 1987, pp. 5505–5515.

[144] Szmytkowski, C. and Maciag, K., "Absolute Electron-Scattering Total Cross Section Measurements for Noble Gas Atoms and Diatomic Molecules," *Physica Scripta*, Vol. 54, 1996, pp. 271–280.

[145] Zecca, A., Karwasz, G., Brusa, R. S., and Grisenti, R., "Absolute Total Cross Section Measurements for Intermediate-Energy Electron Scattering: IV. Kr and Xe," *Journal of Physics B: Atomic, Molecular and Optical Physics*, Vol. 24, 1991, pp. 2737–2746.

[146] Wagenaar, R. W. and de Heer, F. J., "Total Cross Sections for Electron Scattering from Ar, Kr and Xe," *Journal of Physics B: Atomic, Molecular and Optical Physics*, Vol. 18, 1985, pp. 2021–2036.

[147] Kobayashi, A., Fujiki, G., Okaji, A., and Masuoka, T., "Ionization Cross Section Ratios of Rare-Gas Atoms (Ne, Ar, Kr and Xe) by Electron Impact from Threshold to 1 keV," *Journal of Physics B: Atomic, Molecular and Optical Physics*, Vol. 35, 2002, pp. 2087–2103.

[148] Rejoub, R., Lindsay, B. G., and Stebbings, R. F., "Determination of the Absolute Partial and Total Cross Sections for Electron-Impact Ionization of the Rare Gases," *Physical Review A*, Vol. 65, No. 042713, 2002.

[149] Rapp, D. and Englander-Golden, P., "Total Cross Sections for Ionization and Attachment in Gases by Electron Impact: I. Positive Ionization," *Journal of Physics B: Atomic, Molecular and Optical Physics*, Vol. 43, No. 5, 1965, pp. 1464–1479.

[150] Mason, N. J. and Newell, W. R., "Determination of Electron-Xenon Total Excitation Cross-Sections, from Threshold to 100 eV, from Experimental Values of Townsend's α," *Journal of Physics B: Atomic, Molecular and Optical Physics*, Vol. 16, 1983, pp. 581–589.

[151] Mason, N. J. and Newell, W. R., "Total Cross Sections for Metastable Excitation in the Rare Gases," *Journal of Physics B: Atomic, Molecular and Optical Physics*, Vol. 20, 1987, pp. 1357–1377.

[152] de Heer, F. J., Jansen, R. H., and van der Kaay, W., "Total Cross Sections for Electron Scattering by Ne, Ar, Kr and Xe," *Journal of Physics B: Atomic, Molecular and Optical Physics*, Vol. 12, 1979, pp. 979–1002.

[153] Kaur, S., Srivastava, R., McEachran, R. P., and Stauffer, A. D., "Electron Impact Excitation of the $np^5(n+1)p$ States of Ar ($n = 3$), Kr($n = 4$), and Xe ($n = 5$) atoms," *Journal of Physics B: Atomic, Molecular and Optical Physics*, Vol. 31, 1998, pp. 4833–4852.

[154] Ester, T. and Kessler, J., "Absolute Elastic and Inelastic Electron Scattering Cross Sections for Xenon in the 15–100 eV Impact-Energy Region," *Journal of Physics B: Atomic, Molecular and Optical Physics*, Vol. 27, 1994, pp. 4295–4308.

[155] Martin, D. F. and Cartwright, K. L., "Solving Poisson's Equation Using Adaptive Mesh Refinement," Tech. rep., University of California, Berkeley, 1996.

[156] Johansen, H. and Colella, P., "A Cartesian Grid Embedded Boundary Method for Poisson's Equation on Irregular Domains," *Journal of Computational Physics*, Vol. 147, No. 1, 1998, pp. 60–85.

[157] Martin, D. F., "A Cell-Centered Adaptive Projection Method for the Incompressible Euler Equations," *Journal of Computational Physics*, Vol. 163, No. 2, 2000, pp. 271–312.

[158] Batishchev, O., "Adaptive RRC Algorithm for SOL Plasma Simulation," *American Physical Society, Division of Plasma Physics Meeting*, New Orleans, Louisiana, 1998.

[159] Fox, J. M., *Advances in Fully-Kinetic PIC Simulations of a Near-Vacuum Hall Thruster and Other Plasma Systems*, Ph.D. thesis, Massachusetts Institute of Technology, 2007.

[160] Verboncoeur, J., "Particle Simulation of Plasmas: Review and Advances," *Plasma Physics and Controlled Fusion*, Vol. 47, 2005, pp. A231–A260.

[161] Boeschoten, F., "Review of Experiments on the Diffusion of Plasma across a Magnetic Field," *Journal of Nuclear Energy. Part C, Plasma Physics*, Vol. 6, No. 4, 1964, pp. 339–388.

[162] Jackson, J. D., *Classical Electrodynamics*, Wiley, New York, 3rd ed., 1999.

[163] Wirz, R. E., J, A. S., and Dankongkakul, B., "Near-Surface Cusp Confinement for Weakly Ionized Plasma," *48th AIAA/ASME/SAE/ASEE Joint Propulsion Conference & Exhibit*, Atlanta, Georgia, 2012, pp. 1–15, AIAA 2012–3948.

[164] Dankongkakul, B., Araki, S. J., and Wirz, R. E., "Influence of Upstream Field Structure on Primary Electron Loss for a Permanent Magnet Cusp," *49th AIAA/ASME/SAE/ASEE Joint Propulsion Conference & Exhibit*, San Jose, California, 2013, pp. 1–12, AIAA 2013–3963.

[165] Dankongkakul, B., Araki, S. J., and Wirz, R. E., "Magnetic Field Structure Influence on Primary Electron Cusp Losses for Micro-Scale Discharges," *Physics of Plasmas*, Vol. 21, No. 043506, 2014, pp. 1–7.

[166] Krall, N. A. and Trivelpiece, A. W., *Principles of Plasma Physics*, McGraw-Hill, Inc, New York, 1973.

[167] Simon, A., "Ambipolar Diffusion in a Magnetic Field," *Physical Review*, Vol. 98, Apr 1955, pp. 317–318.

[168] Anderson, D. V., "Axisymmetric Multifluid Simulation of High Beta Plasmas with Anisotropic Transport Using a Moving Flux Coordinate Grid," *Journal of Computational Physics*, Vol. 17, 1975, pp. 246–275.

[169] Meier, E. T., Lukin, V. S., and Shumlak, U., "Spectral Element Spatial Discretization Error in Solving Highly Anisotropic Heat Conduction Equation," *Computer Physics Communications*, Vol. 181, 2010, pp. 837–841.

[170] Mikellides, I. G., Katz, I., Hofer, R. R., and Goebel, D. M., "Hall-Effect Thruster Simulations with 2-D Electron Transport and Hydrodynamic Ions," *31st International Electric Propulsion Confernce*, Ann Arbor, Michigan, 2009, pp. 1–23, IEPC 2009–114.

[171] Mikellides, I. G., Katz, I., Hofer, R. R., Goebel, D. M., de Grys, K., and Mathers, A., "Magnetic Shielding of the Channel Walls in a Hall Plasma Accelerator," *Physics of Plasmas*, Vol. 18, No. 033501, 2011.

[172] Wirz, R. E. and Katz, I., "2-D Discharge Chamber Model for Ion Thrusters," *40th AIAA/ASME/SAE/ASEE Joint Propulsion Conference & Exhibit*, Fort Lauderdale, Florida, 2004, pp. 1–18, AIAA 2004–4107.

[173] Kainz, A., Weimann, G. H., Kamelander, G., and Batishchev, O. V., "ITER-like Fusion Devices Plasma Behavior Simulation: Enhancement utilizing Adaptive Mesh Application," *27th EPS Conference on Controlled Fusion and Plasma Physics*, Vol. 24B, Budapest, 2000, pp. 348–351.

[174] de Rover, M., Cardozo, N. J. L., and Montvai, A., "Motion of Relativistic Particles in Axially Symmetric and Perturbed Magnetic Fields in a Tokamak," *Physics of Plasmas*, Vol. 3, No. 12, 1996, pp. 4478–4488.

[175] Runov, A. M., Reiter, D., Kasilov, S. V., Heyn, M. F., and Kernbichler, W., "Monte Carlo Study of Heat Conductivity in Stochastic Boundaries: Application to the TEXTOR Ergodic Divertor," *Physics of Plasmas*, Vol. 8, No. 3, 2001, pp. 916–930.

[176] Runov, A. M., Kasilov, S., Riemann, J., Borchardt, M., Reiter, D., and Schneider, R., "Benchmark of the 3-Dimensional Plasma Transport Codes E3D and BoRiS," *Contributions to Plasma Physics*, Vol. 42, No. 2-4, 2002, pp. 169–174.

[177] Feng, Y., Sardei, F., Grigull, P., McCormick, K., Kisslinger, J., Reiter, D., and Igitkhanov, Y., "Transport in Island Divertors: Physics, 3D Modelling and Comparison to First Experiments on W7-AS," *Plasma Physics Controlled Fusion*, Vol. 44, 2002, pp. 611–625.

[178] Feng, Y., Sardei, F., and Kisslinger, J., "A Simple Highly Accurate Field-Line Mapping Technique for Three-Dimensional Monte Carlo Modeling of Plasma Edge Transport," *Physics of Plasmas*, Vol. 12, No. 052505, 2005, pp. 1–7.

[179] Frerichs, H. G., *Three-Dimensional Plasma Transport in Open Chaotic Magnetic Fields: A Computational Assessment for Tokamak Edge Layers*, Ph.D. thesis, Rheinisch-Westflische Technische Hochschule Aachen University, Aachen, Germany, 2010.

[180] Tongue, B. H., "On Obtaining Global Nonlinear System Characteristics Through Interpolated Cell Mapping," *Physica*, Vol. 28D, 1987, pp. 401–408.

[181] Brieda, L. and Keidar, M., "Development of the Starfish Plasma Simulation Code and Update on Multiscale Modeling of Hall Thrusters," *48th AIAA/ASME/SAE/ASEE Joint Propulsion Conference & Exhibit*, Atlanta, Georgia, 2012, pp. 1–30, AIAA 2012–4015.

[182] Marchand, R. and Dumberry, M., "CARRE: a Quasi-Orthogonal Mesh Generator for 2D Edge Plasma Modelling ," *Computer Physics Communications*, Vol. 96, 1996, pp. 232–246.

[183] Marchand, R., Lu, J. Y., Kabin, K., and Rankin, R., "Unstructured Meshes and Finite Elements in Space Plasma Modelling: Principles and Applications," *Advanced Methods for Space Simulations*, edited by H. Usui and Y. Omura, Terrapub, Tokyo, 2007, pp. 111–143.

[184] Abdullaev, S. S., "On Mapping Models of Field Lines in a Stochastic Magnetic Field," *Nuclear Fusion*, Vol. 44, 2004, pp. S12–S27.

[185] Wirz, R. E. and Katz, I., "Plasma Processes of DC Ion Thruster Discharge Chambers," *41st AIAA/ASME/SAE/ASEE Joint Propulsion Conference & Exhibit*, Tucson, Arizona, 2005, pp. 1–25, AIAA 2005–3690.

[186] Mao, H.-S., *Plasma Structure and Behavior of Miniature Ring-Cusp Discharges*, Ph.D. thesis, University of California, Los Angeles, Los Angeles, California, 2013.

[187] Atkinson, K. E., *An Introduction to Numerical Analysis*, John Wiley & Sons, New York, 1989.

[188] Berzins, M., "Mesh Quality: A Function of Geometry, Error Estimates or Both?" *Engineering with Computers*, Vol. 15, 1999, pp. 236–247.

[189] Knupp, P. M., "Algebraic Mesh Quality Metrics," *SIAM Journal of Scientific Computing*, Vol. 23, No. 1, 2001, pp. 193–218.

[190] Knupp, P. M., "A Method for Hexahedral Mesh Shape Optimization," *International Journal for Numerical Methods in Engineering*, Vol. 58, 2003, pp. 319–332.

[191] Van Oosterom, A. and Strackee, J., "The Solid Angle of a Plane Triangle," *IEEE Transactions on Biomedical Engineering*, Vol. BME-30, No. 2, 1983, pp. 125–126.

[192] Mazonka, O., "Solid Angle of Conical Surfaces, Polyhedral Cones, and Intersecting Spherical Caps," Cornell University Livrary Archive, arXiv:1205.1396v2, 2012.

[193] Dressler, R. A. and Chiu, Y.-H., "Quantifying Plasma Collision Processes in Xenon Powered Electric Propulsion Systems," *AIP Conference Proceeding on 27th International Symposium on Rarefied Gas Dynamics*, 2011, pp. 1065–1072.

[194] Paidarova, I., "Accurate Ab Initio Calculation of Potential Energy Curves and Transition Dipole Moments of the Xe_2 Molecular Ion," *Chemical Physics*, Vol. 274, 2001.

[195] Chiu, Y.-H., Dressler, R. A., Levandier, D. J., Houchins, C., and Ng, C. Y., "Large-Angle Xenon Ion Scattering in Xe-Propelled Electrostatic Thrusters: Differential Cross Sections," *Journal of Physics D: Applied Physics*, Vol. 41, 2008, pp. 165503.

[196] Miller, J. S., Pullins, S. H., Levandier, D. J., Chiu, Y.-H., and Dressler, R. A., "Xenon Charge Exchange Cross Sections for Electrostatic Thruster Models," *Journal of Applied Physics*, Vol. 91, No. 3, 2002, pp. 984–991.

[197] Katz, I., Jongeward, G., Davis, V., Mandell, M., Mikellides, I., Boyd, I., Arbor, A., Kannenberg, K., and King, D., "A Hall Effect Thruster Plume Model Including Large-Angle Elastic Scattering," *37th AIAA/ASME/SAE/ASEE Joint Propulsion Conference & Exhibit*, Salt Lake City, Utah, 2001, pp. 1–16, AIAA 2001–3355.

[198] Scharfe, M. K., Koo, J., and Azarnia, G., "DSMC Implementation of Experimentally-Based Xe^++ Xe Differential Cross Sections for Electric Propulsion Modeling," *AIP Conference Proceeding on 27th International Symposium on Rarefied Gas Dynamics*, Vol. 298, 2011, pp. 1085–1090.

[199] Amarouche, M., Durand, G., and Malrieu, J. P., "Structure and Stability of Xe_n^+ Clusters," *Journal of Chemical Physics*, Vol. 88, No. 2, 1988, pp. 1010–1018.

[200] Barata, J. A. S. and Conde, C. A. N., "Calculation of Drift Velocities and Diffusion Coefficients of Xe^+ Ions in Gaseous Xenon," *IEEE Transaction on Nuclear Science*, Vol. 52, No. 6, 2005, pp. 2889–2894.

[201] Child, M. S., *Molecular Collision Theory*, Academic Pres Inc., London, 1974.

[202] Smith, F. J., "The Numerical Evaluation of the Classical Angle of Deflection and of the J.W.K.B. Phase Shift," *Physica*, Vol. 30, 1964, pp. 497–504.

[203] Araki, S. J. and Wirz, R. E., "Collision Modeling for High Velocity Ions in a Quiescent Gas," *42nd AIAA Plasmadynamics and Lasers Conference*, Honolulu, Hawaii, 2011, pp. 1–10, AIAA 2011–3740.

[204] Marchi, R. P. and Smith, F. T., "Theory of Elastic Differential Scattering in Low-Energy He^++ He Collisions," *Physical Review A*, Vol. 139, No. 4, 1965, pp. 1025–1038.

[205] Smith, F. J., "Oscillations in the Caesium and Rubidium Resonant Charge Transfer Cross Sections," *Physics Letters*, Vol. 20, No. 3, 1966, pp. 271–272.

[206] Pullins, S. H., Dressler, R. A., Torrents, R., and Gerlich, D., "Guided-Ion Beam Measurements of Ar^++ Ar Symmetric Charge-transfer Cross Sections at Ion Energies Ranging from 0 . 2 to 300 eV," *Zeitschrift fur Physikalische Chemie*, Vol. 214, No. 9, 2000, pp. 1279–1297.

[207] Phelps, A. V., Private Communication, http://jila.colorado.edu/~avp/collision_data/.

[208] Van Den Biesen, J. J. H., Hermans, R. M., and Van Den Meijdenberg, C. J. N., "Experimental Total Collision Cross Sections in the Glory Region for Noble Gas Systems," *Physica*, Vol. 115A, 1982, pp. 396–439.

[209] Roberts, T. D., Cronin, A. D., Kokorowski, D. A., and Pritchard, D. E., "Glory Oscillations in the Index of Refraction for Matter Waves," *Physical Review Letters*, Vol. 89, No. 20, 2002.

[210] Dham, A. K., Meath, W. J., Allnatt, A. R., Aziz, R. A., and Slaman, M. J., "XC and HFD-B Potential Energy Curves for Xe-Xe and Related Physical Properties," *Chemical Physics*, Vol. 142, 1990, pp. 173–189.

[211] Patino, M. I., Chu, L. E., and Wirz, R. E., "Ion-Neutral Collision Analysis for a Well-Characterized Plasma Experiment," *48th AIAA/ASME/SAE/ASEE Joint Propulsion Conference & Exhibit*, Atlanta, Georgia, 2012, pp. 1–12, AIAA 2012–4119.

[212] Depla, D. and Mahieu, S., *Reactive Sputter Deposition*, Springer Series in Materials Science Volume 209, Springer, Berlin, 2008.

[213] Hasselkamp, D., Rothard, H., Groeneveld, K.-O., Kemmler, J., Varga, P., and Winter, H., *Particle Induced Electron Emission II*, Springer Tracts in Modern Physics, Volume 123, Springer, Berlin, 1992.

[214] Phelps, A. V. and Petrovic, Z. L., "Cold-Cathode Discharges and Breakdown in Argon: Surface and Gas Phase Production of Secondary Electrons," *Plasma Sources Science Technology*, Vol. 8, 1999, pp. R21–R44.

[215] Kishinevskii, L. M., "Estimation of Electron Potential Emission Yield Dependence on Metal and Ion Parameters," *Radiation Effects*, Vol. 19, 1973, pp. 23–27.

[216] Krebs, K. H., "Recent Advances in the Field of Ion-Induced Kinetic Electron Emission from Solids," *Vacuum*, Vol. 33, No. 9, 1983, pp. 555–563.

[217] Sternglass, E. J., "Theory of Secondary Electron Emission by High-Speed Ions," *Physical Review*, Vol. 108, No. 1, 1957.

[218] Schou, J., "Transport Theory for Kinetic Emission of Secondary Electrons from Solids," *Physical Review B*, Vol. 22, No. 5, 1980.

[219] Janni, J. F., "Proton Range-Energy Tables, 1 keV–10 GeV, Energy Loss, Range, Path Length, Time-of-Flight, Straggling, Multiple Scattering, and Nuclear Interaction Probability. Part II. For 92 Elements," *Atomic Data and Nuclear Data Tables*, 1982, pp. 341.

[220] Alonso, E. V., Baragiola, R. A., Ferron, J., Jakas, M. M., and A, O.-F., "Z_1 Dependence of Ion-Induced Electron Emission from Aluminum," *Physical Review B*, Vol. 22, No. 1, 1980.

[221] Winter, H., Eder, H., Aumayr, F., Lorincik, J., and Sroubek, Z., "Slow-Ion Induced Electron Emission from Clean Metal Surfaces: "Subthreshold Kinetic Emission" and "Potential Excitation of Plasmons"," *Nuclear Instruments and Methods in Physics Research B*, Vol. 182, 2001, pp. 15–22.

[222] Lorincik, J., Sroubek, Z., Eder, H., Aumayr, F., and Winter, H., "Kinetic Electron Emission from Clean Polycrystalline Gold Induced by Impact of Slow C^+, N^+, O^+, Ne^+, Xe^+, and Au^+ Ions," *Physical Review B*, Vol. 62, No. 23, 2000.

[223] Martel, J. G. and Olson, N. T., "Ion Bombardment Induced Photon and Secondary Electron Emission," *Nuclear Instruments and Methods*, Vol. 105, 1972, pp. 269–275.

[224] Ray, J. A. and Barnett, C. F., "Secondary Electron Emission of Metals Bombarded with 120-eV to 5-keV Protons," *Journal of Applied Physics*, Vol. 42, No. 8, 1971, pp. 3260–3261.

[225] Carlston, C. E., Magnuson, G. D., Mahadevan, P., and Harrison, D. E., "Electron Ejection from Single Crystals Due to 1- to 10-keV Noble-Gas Ion Bombardment," *Physical Review A*, Vol. 139, No. 3, 1965, pp. 729–736.

[226] Alonso, E. V., Alurralde, M. A., and Baragiola, R. A., "Kinetic Electron Emission from Solids Induced by Slow Heavy Ions," *Surface Science*, Vol. 166, 1986, pp. L155–L160.

[227] Lakits, G., Aumayr, F., Heim, M., and Winter, H., "Threshold of Ion-Induced Kinetic Electron Emission from a Clean Metal Surface," *Physical Review A*, Vol. 42, No. 9, 1990, pp. 5780–5783.

[228] Ding, L., McGrath, C., Woolsey, J. M., Shah, M. B., McCullough, R. W., and Geddes, J., "Potential and Kinetic Electron Emission by Xe^+ and Xe^{10+} Ions on Clean Polycrystalline Copper," *Physica Scripta*, Vol. T80, 1999, pp. 234–235.

[229] Ferron, J., V, A. E., Baragiola, R. A., and Oliva-Florio, A., "Electron Emission from Molybdenum under Ion Bombardment," *Journal of Physics D: Applied Physics*, Vol. 14, 1981, pp. 1707–1719.

[230] Alonso, E. V., Baragiola, R. A., Ferron, J., and Oliva-Florio, A., "Electron Emission from Inconel Under Ion Bombardment," *Radiation Effects*, Vol. 45, No. 1–2, 1979, pp. 119–122.

[231] Walton, S. G., Tucek, J. C., Champion, R. L., and Wang, Y., "Low Energy, Ion-Induced Electron and Ion Emission from Stainless Steel: The Effect of Oxygen Coverage and the Implications for Discharge Modeling," *Journal of Applied Physics*, Vol. 85, No. 3, 1999, pp. 1832–1837.

[232] Lakits, G., Arnau, A., and Winter, H., "Slow-Particle-Induced Kinetic Electron Emission from a Clean Metal Surface: A Comparison for Neutral and Ionized Projectiles," *Physical Review B*, Vol. 42, No. 1, 1990, pp. 15–24.

[233] Ferron, J., V, A. E., Baragiola, R. A., and Oliva-Florio, A., "Dependence of Ion-Electron Emission from Clean Metals on the Incidence Angle of the Projectile," *Physical Review B*, Vol. 24, No. 8, 1981, pp. 4412–4419.

[234] Svensson, B. and Holmn, G., "Electron Emission from Ion-Bombarded Aluminum," *Journal of Applied Physics*, Vol. 52, 1981, pp. 6928–6933.

[235] Jacobsson, H. and Holmen, G., "The Dependence of Si and $Si0_2$ Electron Emission on the Angle of Ion Incidence," *Journal of Applied Physics*, Vol. 74, 1993, pp. 6397–6400.

[236] Wittmaack, K., "Electron Emission and Ion Reflection from Mg, Al and Si Bombarded with 1–10 keV O^+ and Ne^+ at Impact Angles between 0° and 84°," *Nuclear Instruments and Methods in Physics Research B*, Vol. 115, 1996, pp. 288–291.

[237] Hagstrum, H. D., "Auger Ejection of Electrons from Tungsten by Noble Gas Ions," *Physical Review*, Vol. 96, No. 2, 1954, pp. 325–335.

[238] Ferron, J., V, A. E., Baragiola, R. A., and Oliva-Florio, A., "Ion-Electron Emission: The Effect of Oxidation," *Surface Science*, Vol. 120, 1982, pp. 437–434.

[239] Lai, S. Y., Briggs, D., Brown, A., and Vickerman, J. C., "The Relationship Between Electron and Ion Induced Secondary Electron Imaging: A Review With New Experimental Observations," *Surface and Interface Analysis*, Vol. 8, 1986, pp. 93–111.

[240] Bajales, N., Montoro, S., Goldberg, E. C., Baragiola, R. A., and Ferron, J., "Identication of Mechanisms of Ion Induced Electron Emission by Factor Analysis," *Surface Science*, Vol. 579, 2005, pp. L97–L102.

[241] Szabo, J. J., *Fully Kinetic Numerical Modeling of a Plasma Thruster*, Ph.D. thesis, Massachusetts Institute of Technology, Cambridge, Massachusetts, 2001.

[242] Gildea, S. R., *Development of the Plasma Thruster Particle-in-Cell Simulator to Complement Empirical Studies of a Low-Power Cusped-Field Thruster*, Ph.D. thesis, Massachusetts Institute of Technology, Cambridge, Massachusetts, 2012.

[243] Zehnder, O., Mastalerz, R., Reiher, M., Merkt, F., and Dressler, R. A., "On the R-dependence of the spin-orbit coupling constant : Potential energy by high-resolution photoelectron spectroscopy functions of Xe 2 and ab initio quantum chemistry," *Journal of Chemical Physics*, Vol. 128, No. 234306, 2008, pp. 1–13.

[244] Kuns, K., "Calculation of Magnetic Field Inside Plasma Chamber," Tech. rep., UCLA, 2007.

[245] Innes, R. T. A., "Jacobi's Nome (q) in Astronomical Tables and Formulae," *Monthly Notices of the Royal Astronomical Society*, Vol. 62, 1902, pp. 494–503.

[246] Medicus, G., "Theory of Electron Collection of Spherical Probes," *Journal of Applied Physics*, Vol. 32, 1961, pp. 2512–2520.

[247] Spitzer, L. J., *Physics of Fully Ionized Gases*, Interscience, New York, 2nd ed., 1962.